

Interfaces between relativistic hydrodynamics and transport for the dynamical description of heavy ion collisions

Dissertation
zur Erlangung des Doktorgrades
der Naturwissenschaften

vorgelegt beim Fachbereich Physik
der Johann Wolfgang Goethe-Universität
in Frankfurt am Main

von Dmytro Oliinychenko
aus Dnepropetrowsk

Frankfurt 2017
(D30)

vom Fachbereich Physik (13) der
Johann Wolfgang Goethe-Universität als Dissertation angenommen.

Dekan: Prof. Owe Philipsen

Gutachter: Prof. Hannah Petersen, Prof. Marcus Bleicher

Datum der Disputation:

Zusammenfassung

Diese Arbeit basiert auf folgenden Publikationen:

- “Systematic Investigation of Negative Cooper-Frye Contributions in Heavy Ion Collisions Using Coarse-grained Molecular Dynamics” [1]
- “Cooper-Frye Negative Contributions in a Coarse-Grained Transport Approach” [2]
- “Deviations of the Energy-Momentum Tensor from Equilibrium in the Initial State for Hydrodynamics from Transport Approaches” [3]
- “Influence of kinematic cuts on the net charge distribution” [4]
- “Particle production and equilibrium properties within a new hadron transport approach for heavy-ion collisions” [5]
- “Forced canonical thermalization in a hadronic transport approach at high density” [6]
- “Effective dynamical coupling of hydrodynamics and transport for heavy-ion collisions” [7]

Die Dichte des Atomkerns ist für alle Kerne annähernd gleich und beträgt rund $\rho_0 = 0.16 \text{ fm}^{-3} = 2.7 \cdot 10^{17} \frac{\text{kg}}{\text{m}^3}$. Unsere normale Raumtemperatur ist im Vergleich zu nuklearen Energieniveaus so klein, dass man sie für Atomkerne als annähernd Null betrachten kann. Es gibt allerdings Orte im Universum, an denen sich Kernmaterie in einem extremen Zustand befindet. Zum Beispiel kann die Dichte beim Kollaps von Typ II Supernovae bis zu $4\rho_0$ betragen, im Zentrum von Neutronensterne sogar bis zu $9\rho_0$ und wenige Mikrosekunden nach dem Urknall war die Materie nicht nur extrem dicht, die Temperatur war auch höher als 10^{12} K. In den 1970er Jahre wurde theoretisch vorhergesagt, dass bei solchen Temperaturen und Dichten die gewöhnlichen Protonen und Neutronen nicht mehr existieren können. Ein neuer Zustand der Materie werde erzeugt, das sogenannte Quark-Gluon-Plasma (QGP).

Das QGP kann man experimentell in hoch-energetischen Kollisionen von schweren Ionen untersuchen, was manchmal "Urknall im Labor" genannt wird. Eine Reihe von Experimenten an Ionenbeschleunigeranlagen sind der Erforschung der QGP-Physik und der Materie bei extremen Dichten und Temperaturen gewidmet. Diese Beschleuniger sind der RHIC (Relativistic Heavy Ion Collider) in Brookhaven bei New York, der LHC (Large Hadron Collider) in Genf, sowie auch die zukünftige Beschleunigeranlage FAIR (Facility for Antiproton and Ion Research) an der GSI (Gesellschaft für Schwerionenforschung) in Darmstadt, NICA (Nuclotron-based Ion Collider fAcility) in Dubna (Russland) und JPARK-HI in Japan. Dort werden verschiedene Ionen auf ultrarelativistische Energien beschleunigt und zur Kollision gebracht. Die Ergebnisse dieser Kollisionen erlauben es, die Eigenschaften der stark wechselwirkenden Materie zu erforschen. Eine der wichtigsten Fragen der Schwerionenforschung heutzutage ist, ob es einen Phasenübergang zwischen hadronischer Materie und QGP gibt und falls ja, bei welcher Temperatur und Dichte dieser erfolgt. Wenn es einen Phasenübergang gibt, stellt sich auch die Frage, welcher Ordnung er ist und wo der kritische Punkt liegt. Durch Variation der Kollisionsenergie kann man verschiedene Punkte des Phasendiagramms erreichen. Man erwartet, dass der kritische Punkt bei mittleren Energien, $E_{\text{lab}} \simeq 20\text{--}200 \text{ A GeV}$, beobachtet werden kann. Die zukünftigen Experimente, und auch das Beam Energy Scan Program am RHIC, arbeiten in diesem Energiebereich, um den kritischen Punkt zu untersuchen. Das macht die detaillierte Simulation von Schwerionenkollisionen bei mittleren Energien aktuell und interessant.

Heutzutage gibt es zwei Arten von dynamischen mikroskopischen Modellen zur Beschreibung von Schwerionenkollisionen: Relativistische Hydrodynamik und Transportsimulationen. Modelle, die Hydrodynamik und Transporttheorie in ihrem jeweiligen Anwendungsbereich verbinden, werden als Hybrid-Modelle bezeichnet. Hydrodynamik beschreibt experimentelle Observablen besonders gut bei hohen Kollisionsenergien. Ein lokales thermodynamisches Gleichgewicht, welches notwendig für die Anwendbarkeit relativistischer Hydrodynamik ist, wird bei hoher Energie schnell erreicht und lange erhalten. Das System ist groß und dicht genug, sodass die mittlere freie Weglänge viel kleiner als die Systemgröße ist und für eine erhebliche Zeit erhalten bleibt. Im Gegensatz dazu ist hadronischer Transport bei kleinen Energien anwendbar, kalibriert und relativ gut verstanden. Welche Methode kann man für die mittlere Energie wählen? Sind die typische Näherungen und Vermutungen der Hybrid-Modelle noch gültig im mittleren Energiebereich? Diese Näherungen werden in dieser Arbeit untersucht und beurteilt. Zusätzlich wird eine neue Simulationsmethode vorgestellt, die es erlaubt, manche Annahmen wegzulassen.

Eine wichtige Annahme von Hybrid-Modellen ist eine schnelle lokale Thermalisierung im gesamten Volumen der Reaktion. Bei hoher Energie ist die schnelle Annäherung zum thermischen Gleichgewicht gut erforscht und begründet (obwohl die Diskussion darüber, welcher Thermalisierung-Mechanismus dominiert, noch sehr aktiv ist). Bei mittleren Energien ist die Annäherung zum Gleichgewicht weniger gut erforscht. Allerdings ist die Nähe zum lokalen thermischen Gleichgewicht eine notwendige Bedingung für die Anwendbarkeit von Hydrodynamik. Ist das Gleichgewicht bei mittleren Energien überhaupt erreicht? Wenn ja, wie schnell? Auf diese Fragen wird hier mit Hilfe eines Transport-Modells UrQMD (Ultra-relativistic Quantum Molecular Dynamics) sowie des sogenannten "coarse-graining"-Verfahrens eingegangen. Hierfür wird der Energie-Impuls-Tensor $T^{\mu\nu}$ für jeden Punkt des kartesischen Gitters bestimmt, das sich über das ganze System erstreckt. Mittels $T^{\mu\nu}$ wird die Abweichung vom Gleichgewicht bestimmt. Der wichtigste Beitrag zum Ungleichgewicht ist die Anisotropie von $T^{\mu\nu}$. Das Gleichgewicht wird nie im gesamten System erreicht, jedoch ist ab einer bestimmten Zeit $t_{iso}(E_{lab}, b, \sigma)$ ein ausreichendes Volumen genug isotropisiert, um Hydrodynamik anwenden zu können. Dabei ist E_{lab} die kinetische Energie des Projektils pro Nukleon, b der Stoßparameter, der die Zentralität der Kollision charakterisiert, und σ ist ein Ausschmierung-Parameter des coarse-graining-Verfahrens. Die gefundene Abhängigkeit (für eine Vielzahl der Transport-Simulationen, ermittelt im coarse-graining-Verfahren) lässt sich näherungsweise mit der folgenden Formel beschreiben: $t_{iso} = 2R(E_{lab}/2m_N)^{-1/2} + \alpha\sigma$.

Hybrid-Modelle verwenden Hydrodynamik im Bereich hoher Dichten und Transport-Simulationen im Bereich niedriger Dichten. Der Übergang zwischen diesen zwei Verfahren beruht auf bestimmten Näherungen und Annahmen. Man vermutet, dass dieser Übergang sehr schnell ist und auf einer Hyperfläche erfolgt. Die hydrodynamischen Gleichungen werden im ganzen Vorwärtslichtkegel gelöst und die Hyperfläche wird nur aus der Hydrodynamik a posteriori bestimmt, nicht dynamisch aus kombinierten Hydrodynamik und Transporttheorie Gleichungen. Die Teilchen werden aus der Hydrodynamik gemäß der Cooper-Frye-Formel produziert und anschließend im Rahmen der Transporttheorie beschrieben. Sie können nicht in den hydrodynamischen Bereich zurückkehren und rückstoßen. Diese Näherungen führen zu negativen Beiträgen der Cooper-Frye-Formel. Bei hohen Energien sind diese Beiträge vernachlässigbar, aber bei mittleren Energien wurden sie nie systematisch untersucht. In dieser Arbeit werden die negative Cooper-Frye-Beiträge in Gold-Gold Kollisionen bei $E_{lab} = 5-160$ A GeV für verschiedene Hadronen in verschiedenen kinematischen Regionen mithilfe des "coarse-grained" Transport-Modells UrQMD bestimmt. Diese Rechnung

nimmt ein thermisches Gleichgewicht auf der Hyperfläche an. Die größten negative Beiträge liegen für Pionen bei mittlerer Rapidität vor und machen nicht mehr als 15% aus. In Transport-Modellen kann man auch explizit die Teilchen zählen, welche die Hyperfläche von außen nach innen überqueren — das entspricht den negativen Cooper-Frye-Beiträgen ohne Annahme eines Gleichgewichts. In dieser Arbeit wird gezeigt, dass diese negativen Beiträge im Nichtgleichgewicht erheblich kleiner sind als im Gleichgewicht.

Die negativen Cooper-Frye-Beiträge vermeidet man in einem neuen Modell, das in dieser Arbeit konstruiert wird. In gewöhnlichen Transport-Modellen im Bereich hoher Dichten wird eine Thermalisierung künstlich erzwungen, was intensiven Mehr-Teilchen-Kollisionen oder der Bildung des Quark-Gluon-Plasmas entspricht. Dieses Verfahren wurde mit dem Transport-Modell SMASH implementiert und getestet. Drei Algorithmen der Thermalisierung wurden verglichen und der neuentwickelte “biased Becattini-Ferroni” Algorithmus erwies sich als ausreichend zuverlässig und effizient. In einem kontrollierten Szenario einer expandierenden Kugel wurde gezeigt, dass SMASH mit erzwungener Thermalisierung die Expansionsgeschwindigkeit und die Energiedichte zwischen Hydrodynamik und Transporttheorie aufweist. Bei der Simulation von Schwerionenkollisionen mit diesem Modell wurden folgende Beobachtungen gemacht: im Vergleich zum Transport wird mehr Seltsamkeit erzeugt, der mittlere transversale Impuls wird aufgrund der Druckisotropisierung erhöht und Bereiche hoher Dichten leben länger. Alle diese Merkmale sind den Hybrid-Modellen ähnlich, aber ohne die oben genannten Nachteile. Insgesamt führt die erzwungene Thermalisierung zu den erwarteten Ergebnissen.

Im Rahmen dieser Doktorarbeit wurde auch ein erheblicher Beitrag zur Entwicklung des SMASH-Modells selbst geleistet, insbesondere was Nukleon-Nukleon-Potentiale, Fermi-Bewegung, Pauli-Blockierung, Thermodynamik und Detaillierte Balance betrifft. Das relativistische Transport-Modell SMASH ist für Simulationen der Kollisionen von Ionen, Protonen oder anderen Hadronen geeignet. Ein gesamter Kollisionsprozess wird als eine Sequenz von elementaren $2 \rightarrow 2$ Kollisionen, Zerfällen, Resonanz-Bildungen und Teilchen-Propagation simuliert. Die Potentiale beeinflussen die Trajektorien der Teilchen während der Propagation und sind für Schwerionenkollisionen niedriger Energien (z.B. für Simulationen des FOPI Experiments an der GSI in Darmstadt) besonders wichtig. Bei solchen Energien ist es auch wichtig die Quanteneffekte für Fermionen, die Pauli-Blockierung und Fermi-Bewegung in einem Atomkern zu berücksichtigen. Zusätzlich zu diesen Effekten wurde das oben genannte

“coarse-graining“-Verfahren in SMASH implementiert. Das hat die oben beschriebenen Simulationen mit erzwungener Thermalisierung ermöglicht.

Zusammengefasst lauten die wichtigsten Resultate dieser Arbeit:

- Entwicklung eines neuen Modells mit erzwungener Thermalisierung im Bereich hoher Dichten. Diese Thermalisierung entspricht intensiven Mehr-Teilchen-Kollisionen oder der Bildung des Quark-Gluon-Plasmas.
- Systematische Beurteilung der negativen Cooper-Frye-Beiträge in Schwerionenkollisionen im Energiebereich $E_{\text{lab}} = 5\text{--}160 A \text{ GeV}$. Die negativen Cooper-Frye Beiträge limitieren die Präzision der Hybrid-Modelle in diesem Bereich.
- Analyse der lokalen Thermalisierungsgrade in Schwerionenkollisionen im Energiebereich $E_{\text{lab}} = 5\text{--}160 A \text{ GeV}$.
- Erheblicher Beitrag zu der Entwicklung des Transport-Modells SMASH.

Contents

1. Motivation	1
1.1. Introduction	2
1.1.1. Atoms and atomic nuclei	2
1.1.2. Elementary particles	3
1.1.3. Hadrons and color confinement	5
1.1.4. Quark-gluon plasma	8
1.1.5. Phase diagram of strongly-interacting matter	10
1.1.6. Big bang and neutron stars	12
1.1.7. Structure of the thesis	13
1.2. Heavy-ion collision experiments	14
1.3. Heavy-ion collisions theory	18
1.3.1. Quantum chromodynamics	19
1.3.2. Other field-theoretical approaches	21
1.3.3. Statistical approaches	23
1.3.4. Hydrodynamic approaches	25
1.3.5. Transport approaches	28
1.3.6. Hybrid approaches	31
2. Interfaces between hydrodynamics and transport	35
2.1. Coarse-graining	35
2.1.1. Energy-momentum tensor of a point-like particle	37
2.1.2. Energy-momentum tensor of a wavepacket	39
2.1.3. Final expressions for coarse-graining	42
2.2. Fluidization	42
2.2.1. Overview of fluidization in current hybrid models	44
2.2.2. Consistency of $T^{\mu\nu}$ and j^μ with hydrodynamics	47
2.2.3. Multicomponent ideal hadron gas equation of state	50
2.3. Particlization with Cooper-Frye formula and negative particle numbers	51

3. Deviation of $T^{\mu\nu}$ from equilibrium in Au+Au collisions at $E_{\text{lab}} = 5\text{--}160 A$ GeV	54
3.1. Methodology to quantify off-equilibrium contributions in $T^{\mu\nu}$ and j^μ	54
3.2. Sensitivity to statistics, grid spacing and smearing	56
3.3. Results	60
3.3.1. Pressure anisotropy	61
3.3.2. Off-diagonality of $T^{\mu\nu}$ in the local rest frame	64
3.3.3. Relative velocity between Landau and Eckart frames	65
3.3.4. The effect of momentum-space cuts	66
3.4. Summary and discussion	67
4. Cooper-Frye contributions in Au+Au collisions at $E_{\text{lab}} = 5\text{--}160 A$ GeV	69
4.1. Methodology	69
4.2. Sensitivity to internal parameters and fulfillment of conservation laws	72
4.3. Magnitude of negative Cooper-Frye contributions estimated from the coarse-grained transport approach	74
4.4. Summary and discussion	80
5. SMASH transport approach: implementation and testing	82
5.1. Degrees of freedom	83
5.1.1. Hadrons in SMASH	83
5.1.2. Hadron spectral function	84
5.1.3. Resonance width	86
5.1.4. Strings	89
5.2. Initial conditions	89
5.2.1. Nucleus-nucleus collisions	89
5.2.2. Infinite matter (periodic box) calculations	94
5.3. Interactions	95
5.3.1. Collisions	95
5.3.2. Decays	100
5.3.3. Detailed balance	100
5.3.4. Potentials	109
5.3.5. Pauli blocking	113
5.4. Thermodynamics in the SMASH transport approach	116
5.4.1. Thermodynamic quantities from coarse-grained SMASH	116
5.4.2. SMASH equation of state	120

6. Interpolating between hadronic transport and hydrodynamics using forced canonical thermalization	122
6.1. Performing forced canonical thermalization in SMASH	124
6.2. Thermal box - testing the sampling algorithm	127
6.3. Interpolating between transport and hydrodynamics	134
6.4. Discussion	140
7. Summary	142
A. Glossary	144
A.1. Units and conventions	144
A.2. Abbreviations	144
B. Sampling two Poissonian integers A and B with fixed $N = A - B$	146
C. Hadrons and the SU(3) group	148
Acknowledgements	153
Bibliography	155
Lebenslauf	176

Chapter 1.

Motivation

The cosmological standard model of the universe traces history back to the Big Bang — an event that created a lot of very dense and hot matter, which immediately started to cool and expand. In the first microseconds after the Big Bang the temperature was so high that no atoms could exist. The universe was filled with radiation and a special state of matter known as quark-gluon plasma. Remarkably, today it is possible to create quark-gluon plasma in the laboratory by colliding heavy ions at ultra-relativistic energies.

The major goal of several modern experiments is to study the properties of the quark-gluon plasma and to understand its transition to the usual hadronic matter. Since the quark-gluon plasma is created in heavy ion collisions for only approximately 10^{-22} seconds it is impossible to observe it directly. Conclusions about the initial stages of heavy ion collisions need to be drawn from the debris measured in the detector. Theoretical models and simulations of heavy ion collisions are required to understand the initial stages of these collisions from the measured produced particles.

This thesis is devoted to a particular kind of simulations: transport and hydrodynamical simulations as well as their fusion, which play a big role in the interpretation of the experimental results. Hydrodynamical approaches are especially successful at high collision energies, while hadronic transport approaches are particularly useful at low energies. Currently one of the most prominent tasks of heavy ion collisions experiments is the quest for a critical point and the investigation of the phase transition between ordinary hadronic matter and the quark-gluon plasma. This transition is expected at intermediate energies (see Table 1.2 for the convention of “low”, “intermediate” and “high” energies adopted in the thesis). The goal of this thesis is to

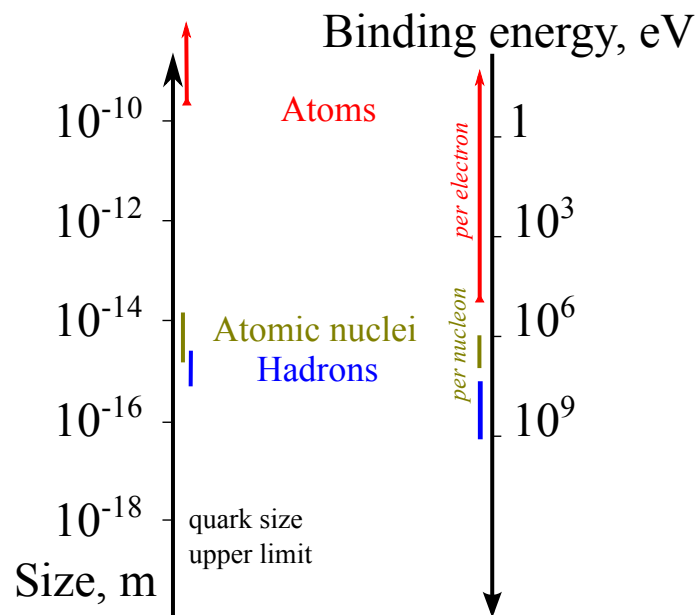


Figure 1.1.: Size and energy scales from atoms to quarks. This thesis deals in the range of atomic nuclei and hadrons.

investigate the possibilities and consequences of applying relativistic hydrodynamics and transport approaches at intermediate beam energies.

In the following sections some basic vocabulary of heavy ion collisions is briefly introduced: hadrons, baryons, mesons; quarks, gluons and quark-gluon plasma, color confinement, etc. More comprehensive explanations can be found in textbooks, for example [8]. Besides the brief introduction to the field, the goal of this chapter is to demonstrate the motivation of the thesis, its relevance and its position in the more general context of heavy ion collision studies.

1.1. Introduction

1.1.1. Atoms and atomic nuclei

Heavy ions are the atoms of heavy elements (from Fe to U) with some or even all of the electrons stripped off. Descending from larger to smaller length scale, the physics of energetic heavy ion collisions involves atoms, atomic nuclei, hadrons, quarks and gluons. The relevant spatial scales range from the atomic scale of order 10^{-10} m down to 10^{-16} m as shown in the left part of Figure 1.1. The binding energy scales are demonstrated in the right part of Fig. 1.1 and range from eV to GeV per bound object.

The existence of atoms is of common knowledge nowadays, so atoms seem to be a good starting point to discuss physics on smaller scales. Disassembling any macroscopic object to smaller and smaller parts one will inevitably arrive at atoms of one of the elements from the Mendeleev's periodic table: hydrogen, carbon, oxygen, nitrogen, sulfur, iron, or any other of more than 110 elements. First introduced by ancient Greek philosophers Democritus and Leucippus as purely theoretical objects, today atoms can be directly observed in the electron microscope, moreover even manipulations with individual atoms are possible.

Starting from Rutherford experiments (Nobel prize in chemistry 1908) it is known that atoms have a dense nucleus, which is 1000 times smaller than the whole atom, but contains 99.9 % of its mass. The nucleus of size 1 – 10 fm consists of nucleons (electrically charged protons and neutral neutrons) bound together with energies from 1 to 8 MeV per nucleon. Even the electrons in the inner shells of heavy elements are bound by at most 0.1 MeV per electron, so electrons can be detached from a nucleus without destroying the nucleus itself. Initial ionization is experimentally achieved by using strong electric fields, further ionization - by accelerating the ions and letting them fly through thin stripping foils.

Protons, neutrons and electrons exist as well as individual particles. Protons and electrons are stable outside of atoms (their measured average lifetime upper bounds are larger than the age of the Universe). Neutrons live around 880 s in average, decaying into a proton, electron and anti-neutrino. The fact that all kinds of atoms consist of only 3 particles - protons, neutrons and electrons - is indeed very satisfying, but it has turned out that the whole particle zoo is much richer. Hundreds of short-living particles were discovered during the past century in cosmic rays and in high-energy proton-proton, proton-electron, electron-positron and other collisions in particle accelerator experiments. The variety of discovered particles has posed the question, which of them are fundamental and how they can be classified.

1.1.2. Elementary particles

Presently the above mentioned classification questions are answered by the Standard Model of particles and interactions [10]. Few particles are considered to be elementary - by definition this means they are point-like and do not have excited states. Elementary particles can still be unstable and decay into other elementary particles. They are characterized by mass, electric charge and spin - an intrinsic form of angular

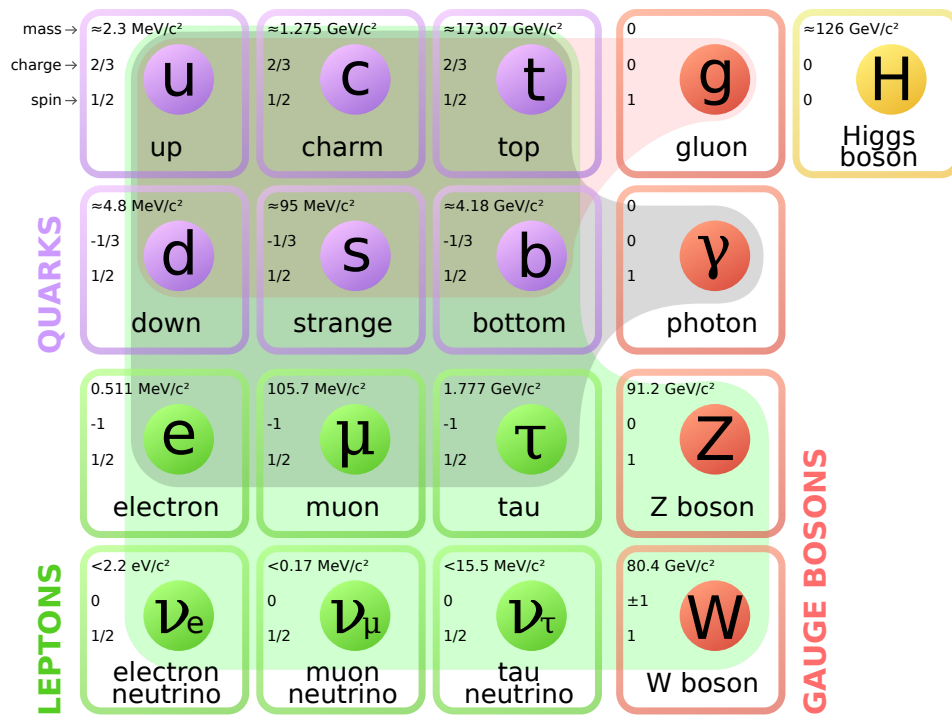


Figure 1.2.: Elementary particles of the Standard Model, their properties and interactions [9].

momentum measured in units of \hbar . In Figure 1.2 all elementary particles are listed together with their properties according to our present knowledge.

Depending on the spin, particles are classified into fermions (spin $\frac{1}{2}$, $\frac{3}{2}$, $\frac{5}{2}$, etc) and bosons (spin 0, 1, 2, etc). The difference between bosons and fermions is however not limited just to numerical values of spin. It has a very deep implication, manifested as the spin-statistics theorem: two fermions are not allowed to be in the same quantum state (this rule is also referred to as Pauli exclusion principle), while any number of bosons can be in the same quantum state. It is due to Pauli’s principle that electrons in atoms cannot reside on one orbital, but create structures of orbitals that give elements their chemical properties. It also plays a role in atomic nuclei, because protons and neutrons are fermions. So are the quarks, of which they are composed of.

In the Standard Model there are 12 fermions, 4 bosons with spin 1 and the Higgs boson with spin 0. All the interactions between fermions are described as an exchange with a boson, that is why the bosons of the Standard Model are also called force carriers. The exchange of a gluon g corresponds to the strong interaction, the exchange of W^\pm or Z bosons is the weak interaction and exchange of a photon γ describes the electromagnetic interaction. The Higgs boson was introduced as a mathematical

construction necessary to provide the W^\pm and Z bosons mass, which could not be introduced directly without violating gauge symmetry. In 2012 the Higgs boson was discovered as a physical particle. In 2013 a Nobel prize was awarded to Englert and Higgs, who predicted the Higgs boson in 1964.

All 12 fermions in Fig. 1.2 can interact weakly, i.e. exchange W^\pm or Z bosons. However, only 6 of them interact strongly, i.e. exchange gluons. The strongly-interacting fermions are called *quarks*, the rest are called *leptons*. Leptons include electron, muon, tau-lepton and neutrinos. For every fermion there is also an antiparticle, which has identical mass and spin, but opposite electric charge. The first 3 columns of the table in Fig. 1.2 are called generations. One can notice that particles in each generation are heavier than in the previous. This remains an observed fact and has no underlying theoretical explanation. Lighter three quarks, u , d and s , are often referred to as "light quarks", the rest are "heavy quarks". The type of quark, one of the six possible, is also called flavour.

This thesis is devoted almost exclusively to the quark sector and the strong interaction. The weak and electromagnetic interactions can be neglected for the purposes of this thesis, because on the time scales of order $100 \text{ fm}/c \simeq 10^{-22} \text{ s}$, which are relevant for heavy ion collisions, strong interactions are much more intense than all the other interactions. For example, it takes around 10^{-24} s to form a pion in a proton-proton collision via strong interaction, 10^{-17} s for it to decay via electromagnetic interaction and 10^{-8} s to decay via weak interaction. On the one hand, this allows to simulate heavy ion collisions neglecting electromagnetic and weak interactions. On the other hand, it makes photons and dileptons useful penetrating probes, which are emitted once and do not rescatter during the hadronic fireball evolution.

1.1.3. Hadrons and color confinement

So far, quarks and gluons were introduced as elementary particles subjected to the strong interaction. In the following their property called "color" is introduced and their bound states are discussed.

In general any particles may form bound states, if their interaction is attractive. For example e^- and e^+ can form positronium, e^- and μ^+ also form a bound state, connected by the electromagnetic interaction. There are no known bound states produced purely by weak interaction, although conjectured heavy neutrinos from

extensions of the Standard Model would form a bound state [11]. In contrast, strong interaction forms a plethora of bound states, called *hadrons*.

Not every combination of quarks and antiquarks appears as a bound state in nature. Experimentally known are only $q\bar{q}$ states called *mesons* and qqq states called *baryons*. Explaining the absence of states like qq or $qq\bar{q}$ involves a property of quark called "color". It is unrelated to the spectrum of reflected or transmitted light called color in our daily life, but there is an analogy that will be explained further. Quark color has 3 eigenvalues, often denoted as r , g and b . The number of colors $N_c = 3$ and the necessity to introduce it is justified by several reasons:

- Experimentally known hadrons like $\Delta^{++}(uuu)$ or $\Omega^-(sss)$ would be forbidden by the Pauli principle, if the only quantum number of quarks was the spin. The measured spin of Δ^{++} is $3/2$, which implies that every u quark that it is composed of has spin projection $1/2$. So without additional quantum numbers all u -quarks are in the same quantum state, which violates Pauli principle. With color Δ^{++} and Ω^- are allowed by Pauli principle, because every quark is in a different color state.
- A number of experiments have measured the ratio of produced hadrons to $\mu^-\mu^+$ pairs in e^-e^+ collisions, $R = \frac{\sigma(e^+e^- \rightarrow \text{hadrons})}{\sigma(e^+e^- \rightarrow \mu^+\mu^-)}$. This ratio is proportional to N_c and measurements indicate $N_c = 3$.
- If one takes the standard model with an arbitrary number of colors N_c , then it would be non-renormalizable because of the so-called axial anomaly in the electroweak sector. The anomaly is only canceled for $N_c = 3$. As a side note, this anomaly cancellation also requires that fermions are grouped into quark-lepton families.
- All the hadrons found in nature are invariant under transformations in the color space, or in mathematical terms, hadrons are singlet representations of the SU(3) group (more details are given in the appendix C). Here the analogy with our daily life color comes into play: like red, green and blue superimposed result in white, colored quarks compose "colorless" hadrons. Here "colorless" actually means that hadrons do not change - are invariant - under the SU(3) transformations in color space. It turns out (see appendix C for details) that combinations qqq , $q\bar{q}$, $q\bar{q}q\bar{q}$, $qqq\bar{q}\bar{q}$ have singlet representations of SU(3) group and thus can be colorless,

while combinations like $qq\bar{q}$, qq , $qqqq$ or single quarks cannot be colorless by any means.

The observed existence of only colorless objects in nature is often referred to as *color confinement* or simply confinement, because the color is confined inside of hadrons. To acknowledge the role of color, the microscopic quantum field theory describing the strong interaction is called quantum chromodynamics (see section 1.3.1 for details). In addition to baryons and mesons color confinement allows many other combinations of quarks, including the pentaquark $qqqq\bar{q}$. Remarkably, in 2015 two kinds of pentaquarks were discovered by the LHCb collaboration at the Large Hadron Collider at CERN [12].

Confinement implies that no single free quark can be observed. This statement has been tested experimentally by multiple experiments [13], measuring the cross-section for the inclusive reaction

$$pp \rightarrow q(\bar{q})X.$$

The best upper limit for the cross-section of such a reaction is currently set by the CMS collaboration and constitutes $\sigma < 2.3 \times 10^{-40} \text{ cm}^2$. This has to be compared to the total pp cross-section, which is of order 100 mb or 10^{-25} cm^2 . This implies that if single quarks are produced in pp collisions then at the maximum average rate of 10^{-15} per collision. So far no single quark was observed.

Quantum chromodynamics (QCD) explains confinement in the following way. From the lattice formulation of QCD one can obtain a phenomenological quark-antiquark potential

$$V(r) = -\frac{\alpha}{r} + \kappa r, \quad (1.1)$$

which grows with distance. If one tries to separate a quark and an antiquark and pull them apart, their interaction energy is large enough to produce a new quark-antiquark pair out of vacuum. So, instead of a separated quark and antiquark one obtains two mesons. This explanation does not provide a full understanding of confinement. For example, it is still unclear under which conditions quarks are not confined.

QCD predicts that at high collision energy the interaction between quarks becomes small. This phenomenon is called asymptotic freedom (see section 1.3.1). The

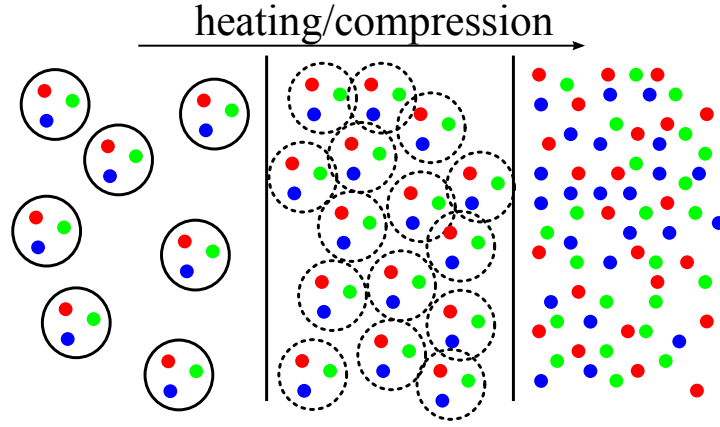


Figure 1.3.: Hadrons with confined color turn into a gas of quarks with deconfined color at heating and/or compression.

asymptotic freedom implies that there is a possibility to obtain deconfined quarks at sufficiently high temperature and density.

1.1.4. Quark-gluon plasma

As mentioned before, it follows from asymptotic freedom of QCD that very hot and/or very dense matter consists of almost non-interacting quarks. It was suggested [14] that by heating and compressing matter in high-energy heavy ion collisions one obtains an almost ideal gas of *deconfined* quarks. The naive illustrative picture of this is shown in Figure 1.3.

Asymptotic freedom was established theoretically in the framework of zero-temperature field theory for the interaction of two quarks. In a heavy ion collision the physics is significantly different: the size of the system is much larger than the size of a single nucleon and one can therefore speak of the formation of a medium. Will the asymptotic freedom hold in the thermal bath created by the medium? This question was answered by Eduard Shuryak in 1978 in the one-loop approximation. He computed the gluon propagator and the potential between two quarks in the thermal medium of temperature T [15]:

$$V(r) = \frac{Q}{4\pi r} e^{-mr} \quad (1.2)$$

$$m^2 = \frac{1}{3} g^2 (N_c + N_f/2) T^2 \quad (1.3)$$

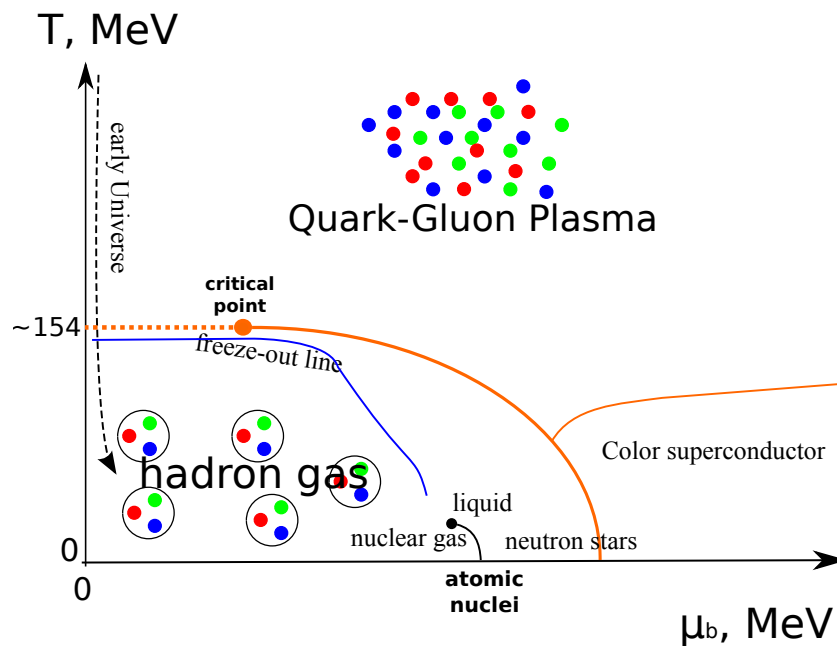


Figure 1.4.: Schematic phase diagram of strongly-interacting matter.

This potential is similar to the Debye screening potential in a classical plasma, therefore the hot and dense medium of quarks was called quark-gluon plasma. It has been produced experimentally at the Relativistic Heavy Ion Collider (RHIC) in 2000 [16–19]. Additionally it has been shown that the quark-gluon plasma behaves like a fluid with a very low viscosity [20–22]. Low viscosity implies that the QGP obtained in Au+Au collisions at RHIC is strongly-coupled, in contrast to an earlier picture of a weakly-coupled gas (see [23] for a review of this paradigm shift).

What are the physical properties of the quark-gluon plasma? How and under which conditions does the transition from hadronic matter to the quark-gluon plasma occur? Is there a phase transition or only a smooth cross-over? If phase transition then of which order? Is there a critical point and if yes, where is it located and what are the critical indices? Are there additional phases? These are some of the questions that motivate modern heavy ion collision experiments and theoretical investigations. Many of these questions are directly related to the phase diagram of the strongly-interacting matter.

1.1.5. Phase diagram of strongly-interacting matter

One of the most important tasks of modern heavy-ion collision experiments is to study the phase diagram of strongly-interacting matter [24]. A sketch of the theoretical and experimental knowledge about the phase diagram is given in Figure 1.4 in terms of temperature T and baryon chemical potential μ_b . The chemical potential refers to the energy increase of the system after adding one baryon, it also characterizes the asymmetry between baryons and antibaryons. At $\mu_b = 0$ the energies needed to add a baryon or an antibaryon to the system are identical and therefore baryon and antibaryon numbers are equal. At high μ_b baryons are strongly preferred.

Strictly speaking, the diagram can have two additional axes, isospin chemical potential μ_{I3} and strangeness chemical potential μ_s . On this diagram, it is assumed that $\mu_s = \mu_{I3} = 0$. Non-zero isospin chemical potential is important for neutron stars, because it characterizes the asymmetry between protons and neutrons, which is significant in these cosmological systems. More important for heavy ion collisions is the transition between hadron gas and quark-gluon plasma. At high collision energies approximately equal amounts of baryons and antibaryons are produced, so μ_b is small. The region of $\frac{\mu_b}{T} \leq 2$ is covered by lattice QCD calculations [25–27], which conclude that in this region there is no phase transition, only a smooth cross-over. The value of the pseudocritical temperature where the chiral susceptibility has its maximum is $T_c = 153$ MeV [28–30]. Unfortunately, lattice QCD is limited to the vicinity of $\mu_b = 0$ due to the sign problem [31].

At non-zero μ_b a first-order phase transition is predicted by multiple models and phenomenological studies (see summaries in [32] and [33]). A first order phase transition occurs in massless two-flavour QCD [34,35] as well as in the two flavour linear sigma model and Nambu-Jona-Lasinio model [36], in a model based on the statistical bootstrap [37] and in a model with an effective potential for two-flavour massive QCD [38]. However, none of these models can be described as fully realistic. The point where the first order phase transition ends and cross-over starts is called critical point. In the vicinity of the critical point multiplicity fluctuations become large [39,40]. At RHIC and at NA61 experimental measurements of multiplicity fluctuations are ongoing to locate the critical point. Future FAIR, NICA and J-PARC facilities have search and possibly studies of the critical point as a part of their motivation (see more in section 1.2).

The nuclear matter liquid-gas phase transition with its own critical point around $T_c^{\text{nucl}} \approx 20$ MeV was studied both theoretically and experimentally in ion collisions [41,42]. There are many indications in favor of a phase transition. These include temperature saturation over a broad range of energies, flattening of the caloric curves, sudden opening of the high fragment multiplicity channel, the onset of collective expansion, the abnormally high partial energy fluctuations, the bimodal distribution of exclusive observables, and the finite size and Fisher scalings. However, the numerical value of the critical point still has a large uncertainty and even the discovery of the transition is still debatable.

The color superconductor phase was theoretically predicted at very large baryon densities and low temperatures [43,44]. At these high densities, possibly occurring in the cores of neutron stars, gluons acquire large mass, as quarks form a condensate and massive excitations over condensate dominate physics, so that "QCD at high densities and low temperatures may in many ways be much more similar to QCD at low densities than to a weakly coupled quark-gluon plasma" [45].

The chemical freeze-out line results from an attempt to quantify features of the phase diagram from the experimental side [46]. By definition chemical freeze-out is the instant, when inelastic number-changing hadronic reactions cease, because of the expansion of the system, and hadron multiplicities are fixed, "frozen". The thermal (also called "hadron resonance gas") model postulates simultaneous sharp chemical freeze-out for all hadron species. Despite this rough approximation, this model provides a surprisingly good description of hadron multiplicities in heavy ion collision for collision energies ranging from a few GeV per nucleon pair to 2.76 TeV [46–48]. Temperature T^{FO} and chemical potential μ_b^{FO} at the chemical freeze-out are parameters of thermal models extracted from fitting multiplicities at each experimental collision energy. Lattice QCD studies hint that the freeze-out curve lies near the phase transition curve for low μ_b [49].

Different parts of the phase diagram are studied with different theoretical approaches and it is an important task to connect them. Describing different parts of the phase diagram in a unified approach would allow to connect properties of neutron stars, heavy ion collision experiments at high energies and measurements of the nuclear phase transition.

1.1.6. Big bang and neutron stars

The physics of hadrons and quark-gluon plasma has deep connections to cosmology, in particular to the early universe evolution and to neutron stars. Our universe is known to be uniform on a very large scale of 100 Mpc, but it is extremely non-uniform on a smaller scale. Indeed, the density of neutron star is 40 orders of magnitude larger than the density of cosmic voids. It is suggested that the phase transition from a hot quark-gluon plasma to hadrons during the first microseconds after the Big Bang could be partly responsible for such a non-uniformity. For example, in [50] lumps of quark matter floating in the Universe are suggested and in [51] the impact of the QCD transition on inhomogeneities in the baryon to photon ratio is studied.

After the Big Bang the universe was extremely hot, small and was cooling and expanding [52], similarly to the fireball in heavy ion collisions, although the initial temperature was higher - of order 10^{18} GeV at Plank time of 10^{-43} s in contrast to initial temperatures of several hundred MeV in heavy ion collisions. At 10^{-7} s the Universe has already reached conditions testable in modern heavy ion collisions experiments. Of course, between the universe and ion collisions there are differences in geometry. The expansion of the universe was spherical, while heavy ion collisions have a collision axis. However, due to the formation of a quark-gluon plasma, similarities in expansion and cooling and also in the sequence of freeze-out processes heavy ion collisions are sometimes called the Little Bang.

Hadronic and quark-gluon plasma physics are also related to neutron stars and conjectured quark stars [53]. Neutron stars are remnants of type II supernovae explosion, typically detected as millisecond radio pulsars. They can neither be too light, otherwise they would be destroyed by centrifugal force; nor too heavy to avoid collapse into a black hole. Observed neutron stars have masses approximately between 1 and 2 solar masses and radius from 10 to 20 kilometers [54]. Simultaneous precise measurements of mass, radius and rotation period of neutron stars would put stringent constraints on the nuclear equation of state at high densities. For example, precise measurements of the masses of PSR J1614-2230 ($M = 1.97 \pm 0.04 M_{Sun}$) and PSR J0348-0432 ($M = 2.01 \pm 0.04 M_{Sun}$) [55, 56] have excluded many quark matter equations of state, which could not produce such heavy neutron stars. Nevertheless, there is still enough room for stars with quark core [57, 58]. Astrophysical measurements of neutron stars probe the lower temperature and high density region of the phase diagram in Fig. 1.4 and are thus complementary to heavy ion collision studies.

1.1.7. Structure of the thesis

Going from atoms to neutron stars, the introductory part of this thesis has outlined the general motivation driving heavy ion collision experiments and theoretical calculations all over the world. Section 1.2 overviews the experimental studies of heavy ion collisions and demonstrates substantial interest on intermediate energies, where the search of the critical point is or will be performed. Section 1.3 constitutes a brief overview of theory related to heavy ion collisions. This is necessary to show the inter-relations between different theoretical approaches and to introduce transport, hydrodynamical and hybrid approaches, which play a big role in this thesis.

Chapter 2 contains a mathematical part of methodology necessary for the next parts. It provides a detailed description of the coarse-graining method, fluidization and particlization - the interfaces between hydrodynamics and transport, studied in this work.

The assumptions behind hydrodynamical and hybrid approaches that were fulfilled at high energies may become challenging at intermediate energies. The first of these assumptions is rapid thermalization over the whole fireball volume in heavy ion collisions. The local thermalization at energies $E_{\text{lab}} = 5 - 160$ GeV per nucleon ($\sqrt{s_{NN}} = 3-17$ GeV) is studied in a coarse-grained transport approach in chapter 3. The degree of thermalization is estimated by quantifying local deviations of energy-momentum tensor and baryon four-current in the Landau rest frame from the thermal equilibrium. chapter 3 is based on publication [3].

Another assumption adopted by hydrodynamical and hybrid approaches at high energies is that particles emitted from the region of hydrodynamical evolution cannot return back and cause feedback to hydrodynamics. Neglecting of this feedback is typically manifested as so-called "negative Cooper-Frye contributions" - negative numbers of particles emitted from certain regions of the phase-space. At high energies at midrapidity they are negligible. Does this hold for intermediate energies? This question is investigated in chapter 4 based on publication [1].

Chapter 5 (based on [5]) introduces the SMASH transport approach, which was used for the following computations. In chapter 6 (based on [6]) a novel approach to simulate hydrodynamical regime at high density avoiding negative Cooper-Frye contributions is suggested and tested. This approach is based on performing forced canonical thermalization in the high-density region of the pure hadronic transport. Chapter 7 summarizes the main results of this work.

1.2. Heavy-ion collision experiments

An important part of the motivation for this thesis stems from ongoing and planned heavy ion experimental programs. That is why in this section a short overview of heavy ion experiments is given. Only experiments with the relativistic beam of kinetic energy $E_{\text{lab}} > 1$ GeV per nucleon are considered. This condition cuts off heavy ion programs devoted to nuclear physics, such as heavy ion experiments in Saclay (France), Uppsala (Sweden), East Lansing (USA) or RIKEN experiment (Japan). In the world there is only a limited number of accelerators operating at $E_{\text{lab}} > 1$ GeV per nucleon, the information about them is summarized in table 1.1. They are all synchrotrons with a beam revolving continuously in a circular beam pipe. Typically multiple experiments are taking advantage of the beam.

Pioneering experiments in heavy ion collisions were performed in the 1970ies at Bevalac at Lawrence Berkley Laboratory (LBL) in the US and at Synchrophasotron in Dubna (Russia). They managed to create compressed nuclear matter and study its properties. The most important results of Bevalac include studies of the equation of state of nuclear matter [72], collective phenomena [73,74] and low-mass dileptons [75]. Synchrophasotron studied cumulative effect, HBT-correlations [76] and nuclear multifragmentation [77]. These experiments were operating at beam energies below 2 GeV per nucleon. In 1990 SIS18 started to operate in the same energy regime. SIS18 experiments FOPI and KaoS have performed systematic studies of pion production [78], strangeness production [79,80] (including subthreshold production of Σ -baryon [81] and ϕ -meson [82]) and collective flow studies [83]. HADES continues these studies [84] and extends them to investigations of dilepton production [85,86]. Hadronic transport approaches were successfully applied to describe the results of experiments at Bevalac and SIS18.

Beam energies of $E_{\text{lab}} = 2 - 14.5$ GeV ($\sqrt{s_{NN}} = 2.7 - 5.5$ GeV) were covered by the Alternating Gradient Synchrotron (AGS) at Brookhaven National Laboratory, first colliding lighter ^{16}O and ^{28}Si nuclei and then heavier ^{197}Au nuclei. Exclusive particle spectra [87–89] were measured for π^{\pm} , K^{\pm} , p , \bar{p} , Λ , $\bar{\Lambda}$ and ϕ . Directed (v_1) [90] and elliptic (v_2) flow [91] were investigated. Pion interferometry [92] allowed to extract the produced fireball size. The overall conclusion was that “there is no evidence for any onset of new behavior beyond hadronic scattering as the beam energy or centrality is changed” [93], because the results of AGS were well-reproduced by the hadronic transport models RQMD and ARC [93]. Another conclusion was that

Table 1.1.: Summary of heavy ion accelerators at energy $E_{\text{lab}} > 1$ GeV. Operation time is given only for heavy ion period: e.g. Bevalac started operation in 1960, but heavy ion program was initiated in 1971. Note that only accelerated projectile ions are listed in the table, but not target ions.

Accelerator	Place	Lab.	Time	E_{beam} [GeV]	$\sqrt{s_{NN}}$ [GeV]	Projectile ions	HI Experi- ments	Refs.
Bevalac	Berkley USA	BNL	1971-1993	0.4 - 2.1	2 - 2.7	O, C, Ne, Fe, Xe, U	Plastic Ball, Streamer chamber, EOS, DLS	[59,60]
Synchro- Phasotron	Dubna Russia	JINR	1970-2003	0.1 - 4.5	1.9 - 3.5	d - Si		[61]
Nuclotron			1993-now	0.1 - 4.5	1.9 - 3.5	d - Xe, Au	BM@N	[62,63]
NICA			2023-	2 - 5.5	4 - 11	d - Au	MPD	[64,65]
SIS18	Darmstadt Germany	GSI	1990-now	0.1 - 2	1.9 - 2.7	d - Au, π	FOPI, HADES, KaoS	[66]
SIS100(300)			2022-	< 14 (44)	< 5.5 (9.2)	d - U, π	CBM, PANDA, NUSTAR	[66]
AGS	Brookhaven USA	BNL	1980-1999	2 - 14.5	2.7 - 5.5	O, Si, Au	E802, E859, E866, E917, E814, E877, E810, E891, E895, E910	[66,67]
RHIC			2000-now	3.85 - 100	7.7 - 200	Au, Cu, U, d	STAR, PHENIX, PHOBOS, BRAHMS	[68]
SPS	Geneva Switzerland	CERN	1983-now	20 - 200	6.3 - 19.4	O, S, In, Pb	NA35, CERES(NA45), NA49, NA57, NA60, WA98, NA61 (SHINE)	[66,69]
LHC			2008-now	1380 (Pb)	2760 (PbPb) 5400 (pPb)	Pb	ALICE, AT- LAS, CMS, LHCb	[70]
MR	Tsukuba Japan	JPARC	2024-	1 - 19	2 - 6.2	d - U		[71]

the produced particle multiplicities correspond to thermal equilibrium in the grand-canonical ensemble [94], which turns out to be true also for higher collision energies.

At the Super Proton Synchrotron (SPS) at CERN a sequence of experiments was carried out using oxygen, sulfur and lead beams at $E_{\text{lab}} = 20\text{-}200$ GeV per nucleon corresponding to $\sqrt{s_{NN}} = 6.4\text{-}19.4$ GeV. At the highest SPS energy NA35 experiment reached the theoretically required energy density for quark-gluon plasma formation in S+S collisions [69]. The goal of the later experiments in a larger Pb+Pb system was to look for the onset of quark-gluon plasma formation by decreasing collision energy. The experiments NA45, NA50 and WA98 measured low-mass dielectron spectra [95], dimuon spectra [96] and direct photons [97]. NA57 has measured multistrange hadron production [98]. Very extensive and systematic measurements of hadron production were conducted by NA49 experiment [99]. Overall, big attention at SPS was devoted to electromagnetic and strange particle observables as potential signals of the quark-gluon plasma formation. Among these signals are "Kink, Step and Horn" [100, 101]: a sharp maximum in the $\frac{K^+}{\pi^+}(\sqrt{s})$ (Horn), sudden change in the number of pions per participant (Kink) and a plateau in the \sqrt{s} dependence of inverse slope parameter of the kaon transverse momentum spectra (step). Hadronic transport models were unable to describe the Horn and especially the Step [102]. This is consistent with the hypothesis of quark-gluon plasma observation, although does not serve as unambiguous evidence. NA61, the successor of NA49 experiment, is now operating at the same energies that NA49, but with a broader range of collision system sizes [103]. NA61 also puts more attention to measuring hadron multiplicity fluctuations.

The Relativistic Heavy Ion Collider (RHIC) at Brookhaven National Laboratory started its operation in 2000 using AGS as a preaccelerator. The beam time at RHIC is dedicated almost completely to heavy ion collisions (there is also a polarized proton collision program). Unlike all the previous experiments, RHIC is a collider. Initially experiments at a center of mass collision energy of $\sqrt{s_{NN}} = 200$ GeV and 130 GeV per nucleon were conducted. Later the Beam Energy Scan program was launched with the motivation to find the critical point of the phase diagram (see Fig. 1.4) and the collision energy was systematically decreased down to 7.7 GeV at the cost of beam luminosity [68]. The smallest experiment at RHIC, PHOBOS, has measured global observables, including charged particle multiplicities, in a large window of rapidity [104]. BRAHMS, PHENIX and STAR have performed systematic measurements of hadronic spectra [105, 106], collective flow of identified hadrons [107, 108], jet quenching, heavy flavour, fluctuations and correlations in large Au+Au/Cu+Cu and in small d+Au systems. The

spectra and elliptic flow of identified particles at low transverse momentum is well-described by ideal relativistic hydrodynamics [109–111], as well as by hydrodynamics with hadronic afterburner [112]. This led to the statement that a nearly ideal fluid was created at RHIC [16–19]. Viscous relativistic hydrodynamics was applied to describe the RHIC $v_2(p_T)$ data [20–22] and it was shown that an extremely low viscosity to entropy density ratio $\frac{\eta}{s}$ from 0.08 to 0.2¹ is preferred by data. The applicability of hydrodynamics, early thermalization, high v_2 and low η/s signal that a strongly-interacting fluid is produced at RHIC. Additional convincing arguments that this fluid is indeed the quark-gluon plasma were jet quenching [113] and the scaling of v_2 with the number of constituent quarks [114, 115] (although constituent quark scaling being a signature of quark-gluon plasma is debatable [116]). Currently, the RHIC beam energy scan is focused on the search of the critical point and therefore event-by-event fluctuations of conserved charges became important observables [117].

The Large Hadron Collider (LHC), which started its operation in 2010, has contributed significantly to the field of heavy ion collisions. LHC makes use of a specialized detector ALICE (A Large Ion Collider Experiment) dedicated to heavy ion collisions, but also CMS (Compact Muon Solenoid), ATLAS (A Toroidal LHC Apparatus) and LHCb play significant role in heavy ion measurements. LHC, in addition to its main $p + p$ program, is colliding $Pb + Pb$ at $\sqrt{s_{NN}} = 2.76$ TeV, as well as $p + Pb$ at $\sqrt{s_{NN}} = 5$ TeV. With energy an order of magnitude higher than at RHIC, there is no doubt in the literature that the quark-gluon plasma is produced at LHC. HBT correlation measurements (see [76] for explanation of the method) show that the hot and dense fireball at LHC is larger than at RHIC and leaves longer until decoupling [118]. Fourier harmonics of $\frac{dN}{d\phi}$ were measured up to v_6 and are well-described by hydrodynamics. Jet quenching turned out to be smaller than at RHIC consistently with perturbative QCD predictions. The biggest surprise from LHC was that the smaller systems like $p + Pb$ or high-multiplicity $p + p$ were exhibiting large v_2 and were described well by hydrodynamics, which seems to be consistent with the production of quark-gluon plasma.

Future experiments are dedicated to the search of the critical point of strongly interacting matter and a possible phase transition between hadrons and quark-gluon plasma. The future accelerators are FAIR (Facility for Antiproton and Ion Research, includes SIS100 accelerators) [119] at GSI (Gesellschaft für Schwerionenforschung) in Darmstadt, Germany; NICA (Nuclotron-based Ion Collider fAcility) [65] at JINR in

¹Dimensionless since $k_B = \hbar = c = 1$ is used, in SI has dimension $\frac{k_B}{\hbar}$.

Collision energy	\sqrt{s} [GeV]	Accelerators
“Low”	$\lesssim 4.5$	Bevalac, Nuclotron, SIS, AGS
“Intermediate”	$\approx 5 - 20$	SPS, RHIC (BES), FAIR, NICA, JPARC
“High”	$\gtrsim 130$	RHIC, LHC

Table 1.2.: Convention for the naming of energy ranges of relativistic heavy ion collisions.

Dubna, Russia; and JPARC-HI [71] at Japan Proton Accelerator Research Complex (JPARC) in Japan. All of them concentrate on the intermediate or lower energy region, where the critical point and the first-order phase transition are expected. NICA will be a collider using the existing Nuclotron as an injector. This will allow to increase energy to $\sqrt{s} = 4-11$ GeV, accelerating all kinds of ion beams. FAIR will be a major addition to SIS18 accelerator at GSI, operating with fixed target at low energies up to $\sqrt{s} = 4.9$ GeV at a very high beam rate and with possibility of antiproton and rare isotope beams. JPARC-HI energies are $\sqrt{s} = 2-6.2$ GeV and the high beam rate is planned, as for FAIR, of order 10^{11} ions per cycle.

Two observations can be drawn from this brief heavy-ion experiment overview. Firstly, the experimental interest is shifting towards lower and intermediate energies. This is manifested by the RHIC beam energy scan program, NA61 at SPS, as well as future experiments FAIR, NICA and JPARC-HI. Secondly, with some exceptions the results of the low-energy experiments are well-described by hadronic transport approaches and the results of high-energy experiments are well-described by the hydrodynamics. Understanding the results of future experiments at intermediate energies requires extending theoretical approaches calibrated at low and high energies.

The terms “low energy”, “intermediate energy” and “high energy” are frequently used throughout the thesis. The ranges are defined only approximately and are partly motivated by the experimental programs. Table 1.2 summarizes the convention adopted in the text.

1.3. Heavy-ion collisions theory

The theory of heavy ion collisions is rather versatile: the approaches range from completely microscopic and static lattice QCD to macroscopic relativistic hydrodynamics. The theoretical approaches may be divided into four branches as shown in

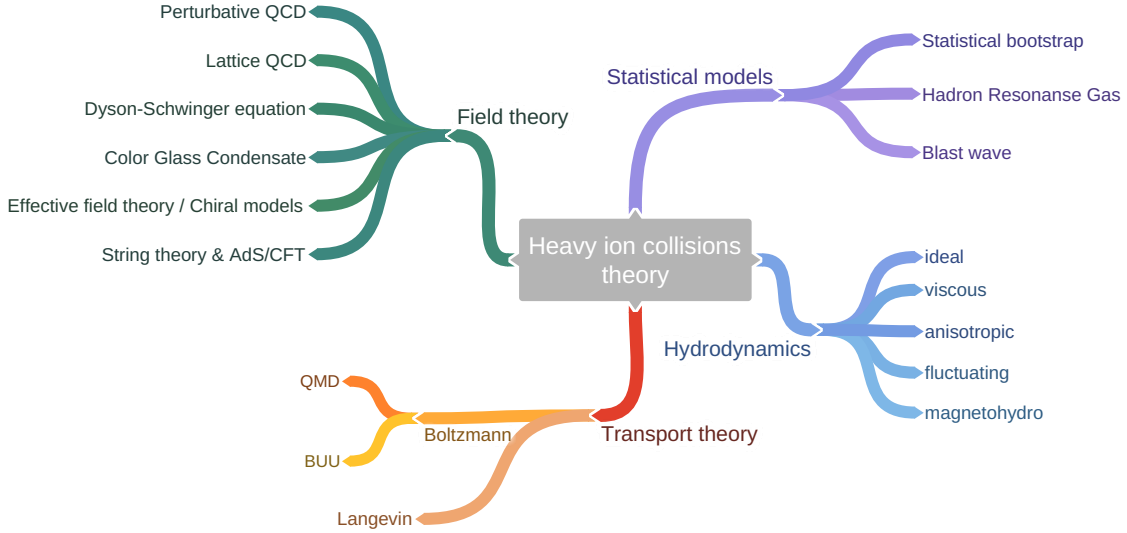


Figure 1.5.: Theoretical approaches to heavy ion collisions.

Fig. 1.5: field-theoretical, transport, hydrodynamical and statistical. This thesis is devoted mainly to transport and hydrodynamical approaches, as well as their fusion called hybrid approaches. That is why the discussion about them is more extensive. The other approaches are just briefly listed here supplied with short descriptions, underlining their connections to hydrodynamics and transport.

1.3.1. Quantum chromodynamics

The modern microscopic theory describing interactions of quarks and gluons is quantum chromodynamics (QCD). Its Lagrangian is composed of interacting quark fields $|\Psi\rangle$, which carry flavor, color and spin indices (therefore $6 \times 3 \times 4$ components) and gluon fields A with Lorentz indices and a color index taking 8 possible values corresponding to the number of SU(3) generators (see appendix C):

$$\mathcal{L} = - \sum_f \bar{\Psi}_f \left[\gamma^\mu \partial_\mu - \frac{i}{2} g \gamma^\mu A_\mu^a \lambda_a - m_f \right] \Psi_f - \frac{1}{4} G_{\mu\nu}^a G_a^{\mu\nu} \quad (1.4)$$

$$G_a^{\mu\nu} = \partial_\mu A_\nu^a - \partial_\nu A_\mu^a + f^{abc} A_b^\mu A_c^\nu \quad (1.5)$$

Here λ_a are the Gell-Mann matrices introduced in appendix C, f^{abc} are SU(3) structure constants, $\left[\frac{\lambda_a}{2}, \frac{\lambda_b}{2} \right] = f^{abc} \frac{\lambda_c}{2}$. Parameters of the QCD Lagrangian are the

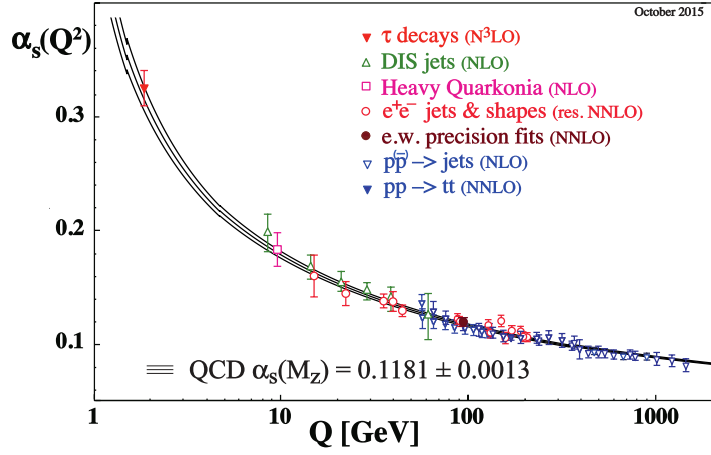


Figure 1.6.: Dependence of strong coupling constant on the energy scale. The decrease of coupling with energy scale is called asymptotic freedom.

quark masses m_f and the interaction constant g . In principle, this Lagrangian contains the full description of strong interactions, but the equations arising after quantizing it are notoriously hard to solve.

QCD is a renormalizable theory [120] and after renormalization the dependence of parameters $g(\mu^2)$ and $m_f(\mu^2)$ emerges, where μ is the energy scale. The first calculation of $g(\mu^2)$ was performed in 1973 by David Gross, Frank Wilczek and David Politzer. They received the Nobel Prize in 2004 for this calculation. Their main result can be expressed as follows [121] in terms of $\alpha_s = \frac{g^2}{4\pi}$:

$$\frac{d\alpha_s}{d \ln(\mu)} = \frac{\alpha_s^2}{\pi} \beta_1 + \left(\frac{\alpha_s^2}{\pi} \right)^2 \beta_2 + \dots \quad (1.6)$$

$$\beta_1 = - \left[\frac{11}{6} N_c - \frac{2}{3} n_f \right] \quad (1.7)$$

Here $N_c = 3$ is the number of colors and $n_f = 6$ is the number of flavors. One can see that β_1 is negative, so the coupling decreases with the energy scale μ . This means that the interaction between quarks at high energies or equivalently at small distances vanishes. This conclusion was confirmed by many scattering experiments, see Figure 1.6. The effect itself is called asymptotic freedom. Although quarks are always confined, asymptotic freedom provides the chance to observe quasi-free quarks. This possibility was an important motivation for heavy ion collisions, until it has been realized that even at the highest LHC energies the quark-gluon plasma is still strongly

coupled. Indeed, the scale μ in Eq. (1.6) is set not by the very high collision energy \sqrt{s} , but by the temperature of the formed medium, which is below 1 GeV.

Besides providing the motivation for heavy ion studies, perturbative QCD is used to compute jet production cross-sections and jet quenching at high p_T in the quark-gluon plasma. Also multiple perturbative calculations were performed for finite-temperature QCD to determine quark-quark potentials in the quark-gluon plasma [122]. Perturbative calculations are useful at high energies, where the strong-coupling constant is small according to the Eq. (1.6). However, when μ decreases the QCD coupling diverges at the scale of $\Lambda_{QCD} \sim 300$ MeV [123]. One of the consequences is that perturbative QCD cannot deal with hadrons. This gap is bridged by lattice QCD, described further and by other field-theoretical approaches described in section 1.3.2.

Lattice QCD is a non-perturbative approach to QCD based on path integrals in a discretized space-time. There are many ways to discretize the QCD action, but all of them should converge to the same results in the continuum limit $a \rightarrow 0$ and $N_\tau \rightarrow \infty$, where a is lattice spacing and N_τ is number of points in Euclidean time. Within lattice QCD the lower lying part of the hadronic spectrum can be computed, but most importantly for heavy ion physics it provides the equation of state of strongly-interacting matter at zero chemical potential. Due to Taylor expansion in $\frac{\mu}{T}$ at $\mu = 0$ the lattice QCD equation of state is available in the region $\frac{\mu_b}{T} \leq 2$ [25–27]. This equation of state is widely used in hydrodynamical approaches. Lattice QCD calculations are extremely computationally demanding, so many simplifying assumptions are often made: large quark masses, massless quarks or small N_τ . Calculations with physical masses in (2+1)-flavor QCD (meaning that two light quarks with equal masses and a strange quark are considered) and with continuum extrapolation are only recently feasible [124].

1.3.2. Other field-theoretical approaches

Field-theoretical approaches are mostly based on the QCD Lagrangian (see Eq. 1.4). As mentioned before, perturbative QCD cannot deal with low-energy phenomena. This gap is partially bridged by non-perturbative Dyson-Schwinger equations involving dressed quark and gluon propagators [125]. They are rigorous, based on QCD and able to capture physics at all energy scales, but unfortunately this is an infinite system of equations that requires truncation. Other approaches covering low-energy physics are effective field theories, where the degrees of freedom are hadrons, not

quarks or gluons [126]. Such approaches are usually based on the concept of chiral symmetry. These approaches are able to predict hadronic cross-sections, decay widths and branching ratios, which then can be inserted as an input to transport models. The disadvantage of effective field theories is that they are non-renormalizable and therefore their precision is limited and the applicability range is restricted to low collision energies. Additionally, every hadron species needs to be inserted should by inserted to the effective theory Lagrangian explicitly, making realistic and detailed calculation extremely elaborate.

While chiral effective theories are applied at low energies, at high energies the effective theory called Color Glass Condensate (CGC) [127, 128] is useful. Proton-proton or nucleus-nucleus collisions involve two energy scales: the large ("hard") scale of the parton-parton collision energy and the small ("soft") scale of inter-parton interactions within the nucleons. The computation of the reaction cross-sections is possible within perturbative QCD for the parton-parton scattering. The soft part is neither accessible by perturbative QCD nor by lattice QCD, so it is encapsulated into the parton distribution functions (PDF) [129, 130] measured mainly by experiments at HERA e^-p collider in Hamburg. PDFs depend on two parameters - the momentum transfer Q^2 and the variable x which corresponds, at lowest order in perturbation theory, to the longitudinal momentum fraction carried by a parton in the hadron. For small x gluon PDFs dominate in the nucleons, so one can say that at small x nucleons consist of a large number of gluons.

CGC is based on the concept of saturation, which can be explained as follows. Schematically one can write a factorization theorem for the hadronic cross-sections:

$$\sigma_{pp} = \int_0^1 dx_1 dx_2 PDF(x_1, Q^2) PDF(x_2, Q^2) \sigma_{partonic} \left(x_1, x_2, Q^2, \alpha_s(\mu^2), \frac{Q^2}{\mu^2} \right) \quad (1.8)$$

The total cross-section should be limited. This follows from unitarity [131] and poses a restriction on the parton distribution function at low x : PDFs should grow not faster than $\mathcal{O}\left(\frac{\log 1/x}{x}\right)$ for small enough x , $x < x_s(Q^2)$ - a phenomenon called saturation. Instead of $x < x_s(Q^2)$ condition for fixed Q^2 one can also introduce $Q^2 > Q_s^2(x)$ condition for a fixed x . These considerations allow the CGC approach to separate small x and large x physics. Within the CGC the nucleons are approximated as a combination of classical gluon fields at small x and valence quarks at large x as sources of these fields. The CGC picture is applicable for the very initial state of heavy

ion collisions, but at time of order Q_s^{-1} the gluon medium becomes dilute and the basic assumption of saturation is no longer reached. A suggested solution is to couple CGC initialization to hydrodynamics [132] or transport approaches [133].

Another set of approaches to the strongly coupled regime inaccessible by perturbative QCD is exploiting dualities between strongly coupled quantum field theories and weakly-coupled gravitational theories, such as the famous AdS/CFT duality [134]. This kind of approach was used to compute the shear viscosity to entropy density ratio $\frac{\eta}{s}$ in a strongly-coupled conformal field theory and find the well-known low value of $\frac{\eta}{s} = \frac{1}{4\pi}$ [135]. The gauge-gravity duality has also been applied to study the approach of fireball in heavy ion collisions to equilibrium [136]. Moreover, the whole heavy ion collision process at high energies can be considered as a dual of two gravitational shock waves colliding [137]. Although very powerful, duality approaches for heavy ion collisions can currently serve only for qualitative insights, since no dual theory of QCD has yet been found.

1.3.3. Statistical approaches

Statistical approaches avoid describing the complex evolution of the fireball in heavy ion collisions. Instead it is assumed that at chemical freeze-out all the hadrons are in thermal and chemical equilibrium at the same temperature T . This allows to describe the fireball at freeze-out as an ideal gas of hadrons and hadronic resonances. The inclusion of resonances as degrees of freedom encapsulates hadron-hadron interactions according to the Bernstein-Dashen-Ma theorem [138]. The latter assumes that hadron interactions proceed via narrow resonances, which is not always true: for example see Fig. 5.5 for pp cross-section, which has no resonant structures. Under the mentioned assumptions in the grand-canonical ensemble for an ideal Boltzmann gas one obtains

$$N_i = \frac{g_i V e^{\mu_i/T}}{2\pi^2} T^3 \left(\frac{m_i}{T}\right)^2 K_2\left(\frac{m_i}{T}\right), \quad (1.9)$$

where N_i is the multiplicity of the hadron species i , g_i is its degeneracy and m_i is its mass. This equation has to be supplied with conservation laws to fix chemical potentials, resonance decays have to be taken into account for comparison with experimental data and various corrections are possible - see [46, 139] for details. The overall model is called Hadron Resonance Gas (HRG) model. Although the HRG model is very simple and its assumptions are rather naive, it describes hadron multiplicities in

heavy ion collisions remarkably well from AGS to LHC energies with three parameters: the temperature T , the baryon chemical potential μ_b and the volume V [46, 140–144]. Hadron Resonance Gas was also applied in the canonical ensemble with respect to strangeness conservation [145–147]. In the canonical ensemble hadron multiplicities in pp collisions [148] and even e^+e^- collisions [149] can be described, although for the latter the description quality is not as high.

The parameters $T(\sqrt{s})$, $\mu_b(\sqrt{s})$ and $V(\sqrt{s})$ extracted from the fits to multiplicities at different collision energies \sqrt{s} exhibit characteristic meaningful patterns. Temperature of freeze-out T increases with collision energy and saturates at around 160 MeV. The chemical potential decreases with collision energy and goes to zero at LHC, while the volume V behaves exactly as the volume extracted from HBT radii - it has a minimum at SPS energies. The saturation of the temperature may be explained by the statistical bootstrap model by Hagedorn [150, 151], which describes hadrons as "bags" being composites of one another. The bootstrap model yields an exponential hadron spectrum and it originally predicted a limiting temperature $T_H \simeq 150\text{-}170$ MeV, above which hadrons cannot exist. This limiting temperature was later reinterpreted as a transition temperature from hadrons to quarks [152]. It is believed that the value at which the freeze-out temperature saturates is the Hagedorn temperature T_H [46].

The Hadron Resonance Gas model only allows to describe hadron multiplicities. To access momentum and rapidity spectra HRG was extended by including the overall motion of the hadron gas. A freeze-out at some predefined hypersurface is performed according to the Cooper-Frye formula [153]. Such models are called blast-wave models. They have the freedom to select the freeze-out hypersurface, so there are several modifications [154–156]. Blast-wave models allow to describe transverse hadronic spectra using a common radial expansion velocity β common for all hadron species as an additional parameter. Generally, blast-wave models are not able to produce higher-order flows: v_2 , v_3 , etc. The description of anisotropic flow requires more involved dynamical approaches.

The temperatures T_{kin} obtained from the blast wave fits to spectra are typically lower than the temperatures T_{chem} from HRG fit of multiplicities. This is because inelastic reactions that change chemical content cease earlier than pseudoelastic and elastic reactions that can only modify spectra. In other words, chemical freeze-out happens earlier, when the temperature of the medium is higher. The kinetic freeze-out, after which the spectra are not modified, occurs later.

1.3.4. Hydrodynamic approaches

In contrast to statistical models, hydrodynamical approaches describe the evolution of the fireball starting from thermalization until the freeze-out. Two necessary applicability conditions of hydrodynamics are that every part of the system is in the vicinity of local thermal equilibrium and the mean free path is much smaller than the system size,

$$l_{mfp} \ll L. \quad (1.10)$$

Typical expansion velocities in heavy ion collisions are comparable to the speed of light, so the hydrodynamical theory must be relativistic. Relativistic hydrodynamics was initiated in 1953 by the works of Landau for multiparticle production in high-energy collisions of proton-proton, proton-nucleus or nucleus-nucleus collisions [157, 158]. The Landau model assumed high collision energy, so that two colliding nuclei are represented as flat disks due to Lorentz contraction. After colliding these two disks stop completely and the resulting flat disk expands longitudinally. The model predicts a Gaussian rapidity spectrum, which was indeed observed at AGS and SPS for the net charge. At higher energies nuclei do not seem to stop as rapidly as the Landau model assumes, but rather pass through each other. This is represented by the flat region of dN/dy at midrapidity. Such a situation is described well by the Bjorken hydrodynamical model [159], which assumes longitudinal boost invariance. The Bjorken model allows to make a simple estimate of the energy density achieved in the collision, which is used to judge by a comparison to the critical energy density of $1 \text{ GeV}/\text{fm}^3$, if the quark-gluon plasma was produced.

Modern approaches (recent overview [160]) go far beyond these approximations. However, the main equations of hydrodynamics, which are nothing else but conservation of energy, momentum and charges, are written in the same form as in the seminal papers of Landau [157, 158]:

$$\partial_\mu T^{\mu\nu} = 0 \quad (1.11)$$

$$\partial_\mu j^\mu = 0, \quad (1.12)$$

where $T^{\mu\nu}$ is the energy-momentum tensor of the fluid and j^μ is a 4-current of conserved charges. What has changed is

- the dimensionality of the problem
- the equation of state (EoS)
- the initial conditions and event-by-event simulations
- the freeze-out conditions
- viscous corrections

In the following these aspects are described in more detail in this order. Transverse expansion is included in (2+1)D and (3+1)D simulation. This is important to describe transverse flow, in particular the dependence of $v_2(p_T)$, where v_2 is the second Fourier harmonics of the azimuthal angle distribution $\frac{dN}{d\phi}$. Unlike the Landau or Bjorken models, these partial differential equations are not analytically solvable and have to be solved numerically.

The equation of state closes the system of hydrodynamic evolution equations, connecting pressure with energy density and conserved charge densities:

$$p = p(\epsilon, n) \tag{1.13}$$

All the properties of the fluid are encoded in the EoS. It is a big advantage of the hydrodynamics that the EoS can be explicitly varied. In this way one can study the implications of the conjectured quark-gluon plasma to hadron gas phase transition on the experimental observables [161]. At low μ_b the EoS is constrained by lattice QCD, but at higher μ_b it can only be conjectured using phenomenological models.

The initial condition for hydrodynamics is the energy density $\epsilon(x, y, z)$ and the baryon density $n_b(x, y, z)$ at a fixed time t or at a fixed proper time $\tau = \sqrt{t^2 - z^2}$, where the z -axis is along the beam direction. Initial conditions play an important role as they provide spatial anisotropies, which then develop into momentum anisotropies v_n measured in experiment. In earlier studies initial conditions were smooth and based on the overlap geometry of the colliding nuclei, see [162] for a review. In recent works they are typically lumpy and generated by microscopic transport models [163–165], Color Glass Condensate approach [166, 167], IP-Glasma [168], Monte Carlo versions of the Kharzeev-Levin-Nardi (MC-KLN) [169, 170] or the Glauber model (MC-Glauber) [171–173]. Some approaches were developed to classify this zoo [174], but the true initial condition is still to be found.

Because of the initial state fluctuations from collision to collision, event-by-event calculations have to be performed. Instead of smooth averaged initial condition and one hydrodynamic evolution one performs many simulations with different initial conditions and then averages results. These approaches are not equivalent, since hydrodynamical equations are nonlinear. Event-by-event simulations are necessary to reproduce the higher flow harmonics, from v_3 up to v_6 [175–177].

The earlier hydrodynamical simulations were stopped at a fixed time or proper time, a so-called isochronous freeze-out. In modern simulations the freeze-out is typically performed at a fixed temperature, energy density or Knudsen number. Freeze-out is discussed in more detail in chapter 4.

In ideal hydrodynamics the energy momentum tensor in the rest frame of the fluid element is written as

$$T_{\text{ideal}}^{\mu\nu} = \begin{pmatrix} \epsilon & 0 & 0 & 0 \\ 0 & p & 0 & 0 \\ 0 & 0 & p & 0 \\ 0 & 0 & 0 & p \end{pmatrix}, \quad (1.14)$$

where ϵ is local energy density and p is pressure. Suppose that the local fluid velocity is $\vec{\beta}$. Then the four-velocity takes the following form

$$u^\mu = (\gamma, \gamma\vec{\beta}), \quad (1.15)$$

where $\gamma = (1 - \beta^2)^{-1/2}$. To boost the energy-momentum tensor to the laboratory frame one multiplies it by Lorentz-matrices:

$$T^{\mu\nu} = \Lambda_\alpha^\mu \Lambda_\beta^\nu T^{\alpha\beta} \quad (1.16)$$

$$\Lambda_\nu^\mu = \begin{pmatrix} \gamma & -\gamma\vec{\beta} \\ -\gamma\vec{\beta} & \delta_{ij} + (\gamma - 1)\frac{\vec{\beta}_i\vec{\beta}_j}{\beta^2} \end{pmatrix} = \begin{pmatrix} u^0 & -u^i \\ -u^i & \delta^{ij} + (1 + u^0)^{-1}u^i u^j \end{pmatrix} \quad (1.17)$$

Therefore, in the laboratory frame

$$T_{\text{ideal}}^{\mu\nu} = \epsilon u^\mu u^\nu - p(g^{\mu\nu} - u^\mu u^\nu), \quad (1.18)$$

where $g^{\mu\nu} = \text{diag}(1, -1, -1, -1)$. In ideal hydrodynamics the four-current is a vector $(n, 0, 0, 0)$, where n is the density, boosted to the laboratory frame:

$$j^\mu = n u^\mu \quad (1.19)$$

Ideal hydrodynamics requires strict local thermodynamic equilibrium and neglects possible dissipative effects. Small departures from local equilibrium and dissipation are taken into account by viscous hydrodynamics. The equations of dissipative relativistic fluid dynamics were first formulated by Eckart [178] and then by Landau and Lifshitz [179]. Both were relativistic generalizations of Navier-Stokes theory and are often referred to as first order theories. It turned out that these generalizations are acausal, i.e. the speed of sound can exceed the speed of light. This was remedied in the Israel-Stewart second order hydrodynamics [180]. Recently a systematic expansion in Knudsen number has been developed [181], which improves on the 14-moment approximation of Israel and Stewart.

Viscous hydrodynamics is applied with great success to simulate heavy ion collisions [22, 182–185]. It allows to describe anisotropic flow from v_2 to v_6 up to $p_T = 2.5$ GeV at RHIC and LHC, extract shear viscosity η/s and bulk viscosity ζ/s and even some attempts to obtain the temperature dependence of η/s from experimental data are being made [164, 186, 187].

A recent development is anisotropic hydrodynamics [188, 189]. Unlike the usual viscous hydrodynamics, which is an expansion near thermal equilibrium, anisotropic hydrodynamics expands around a non-equilibrium anisotropic state. This makes it applicable for the early stages of heavy ion collisions, where the momentum anisotropy is very large and conventional hydrodynamics cannot be applied.

1.3.5. Transport approaches

The most general microscopic approaches to heavy ion collisions that consider non-equilibrium evolution are approaches based on relativistic transport theory [190]. Transport theory is formulated in terms of the one-particle distribution function $f(t, \vec{r}, \vec{p})$, which is nothing else but the density in phase space. Assuming that the

number of particles in a given region of phase space can change only via collisions and decays and neglecting all other sources of correlations one can write

$$\frac{df}{dt} = \frac{\partial f}{\partial t} + \frac{\partial f}{\partial \vec{r}} \frac{p}{E} + \frac{\partial f}{\partial \vec{p}} \vec{\nabla} U = I_{coll}, \quad (1.20)$$

where I_{coll} is an expression called collision integral. This is the non-relativistic classical Boltzmann equation, but it is nevertheless relevant for quantum systems. It can be derived from the quantum BBGKY-hierarchy of equations for the N -particle density matrix, truncating it at the two-particle level and performing a Wigner transformation. This truncation assumes that the density is not too high:

$$\lambda_{\text{Compton}} \ll l_{mfp}, \quad (1.21)$$

where $\lambda_{\text{Compton}} = \frac{hc}{M}$ is the Compton wavelength and $l_{mfp} \simeq (\rho\sigma)^{-1}$ is the mean free path. This defines the limit of applicability for the Boltzmann equation, which can however be overcome by introducing different degrees of freedom. Another assumption made during the truncation is the so-called hypothesis of molecular chaos:

$$f_2(p_1, x_1; p_2, x_2) = f(p_1, x_1)f(p_2, x_2), \quad (1.22)$$

which implies the neglect of all phase space-correlations between particles. The collision integral is written for the classical case as

$$I_{coll} = \int \frac{d^3 p_2}{E_2} \frac{d^3 p'_1}{E_1} \frac{d^3 p'_2}{E'_2} \times W(p, p_2 \rightarrow p'_1, p'_2) \times (f'_1 f'_2 - f f_2). \quad (1.23)$$

In the quantum case, the Boltzmann equation was first formulated by Uehling and Uhlenbeck and therefore the equation is called BUU (Boltzmann-Uehling-Uhlenbeck):

$$I_{coll} = \int \frac{d^3 p_2}{E_2} \frac{d^3 p'_1}{E_1} \frac{d^3 p'_2}{E'_2} \times W(p, p_2 \rightarrow p'_1, p'_2) \times (f'_1 f'_2 (1 + a f)(1 + a f_2) - f f_2 (1 + a f'_1)(1 + a f'_2)). \quad (1.24)$$

Here $a = 1$ for bosons and $a = -1$ for fermions. One can see that the quantum BUU equation differs from the classical Boltzmann only by factors that account for quantum statistics in the collision term.

The physical meaning of Boltzmann or BUU equations is very simple: for a given time interval dt the number of particles in a phase-space cell has changed (left part) as much as the number of particles that entered it from other cells via collisions or decays (right part, gain term) minus the number of particles that escaped to other cells via collisions or decays (right part, loss term). The Boltzmann equation can be written in a manifestly covariant notation:

$$p^\mu \frac{\partial f}{\partial x^\mu} + m \frac{\partial K^\mu f}{\partial p^\mu} = I_{coll}, \quad (1.25)$$

where K^μ is Minkowski-four-force vector. The Boltzmann equation as written above is just for one sort of particles experiencing $2 \rightarrow 2$ elastic collisions. In heavy ion collisions one encounters hundreds of different hadrons, that can also collide inelastically, decay and form resonances. For this case Boltzmann equation turns into a coupled system of equations - as many equations as hadron species. This system is generally solved via Monte-Carlo simulations, where the particles propagate according to the equations of motion obtained from the left hand side of Eq. 1.25 and collide/decay simulating the collision integral.

Depending on the degrees of freedom, there are pure hadronic transport codes, used at low energies [191–195], approaches including hadrons and strings (e.g., RQMD [196], UrQMD [197], HSD [198], JAM [199], GiBUU [200]), only partons (e.g., [201, 202], Zhang Parton Cascade [203], BAMPS [204]) or partons, hadrons and string together, like PHSD [205] or AMPT [206].

Transport simulations are divided into two groups, usually called BUU (Boltzmann-Uehling-Uhlenbeck) and QMD (Quantum Molecular Dynamics), which differ in the treatment of potentials. BUU approaches aim at solving the one-body BUU equations with mean-field potentials depending on the local density. The hypothesis of molecular chaos implies that in BUU approaches all the correlations between particles are destroyed. The QMD approach solves equations of motion for particles with potentials depending on distances and momenta. The QMD approach generates correlations between particles. In the case in which there are no potentials, which is called the cascade mode, QMD and BUU approaches are identical.

Transport approaches are extremely powerful tools to study heavy ion collisions, because they do not require local equilibrium, simulate microscopic interactions and

allow to extract almost any experimentally observable quantity. However, they also have some disadvantages:

- Strictly speaking, transport approaches are only applicable, if the density is low enough, so that Eq. 1.21 is fulfilled.
- A lot of phenomenological input is required. Many resonance cross-sections and branching ratios are not known experimentally. Modeling microscopically the hadronization process is challenging. String formation and fragmentation can be modeled in many possible ways. All this creates considerable differences in the results even between conceptually similar approaches, see e.g. this comparison [207].

1.3.6. Hybrid approaches

As one can see from the applicability conditions for transport approaches (Eq. 1.21) and hydrodynamics (Eq. 1.10), transport tends to be applicable at lower densities and hydrodynamics at higher densities. At the same time, the hydrodynamical equations can be derived from the Boltzmann equation, therefore the regions of applicability of hydrodynamics and transport overlap. This motivated the development of hybrid approaches, which use hydrodynamics at high density and switch to transport at low density, hopefully in the region, where both are applicable. Hybrid approaches are very successful in describing experimental data at highest RHIC and LHC energies [132, 163, 208–214], and for the RHIC beam energy scan [164, 215].

The advantages of hybrid approaches are:

- Theoretical consistency: hydrodynamics and transport are supposed to be applied within their applicability ranges.
- The hadronic rescattering stage improves the description of experimental data compared to pure hydrodynamics, in particular it improves the description of elliptic flow v_2 of identified particles and p_T spectra of protons and Λ [216].
- The equation of state can be studied explicitly.
- There are no uncertainties related to hadronization in the transport simulation. The complex hadronization process is encoded in the equation of state.

These advantages make hybrid approaches excellent simulations at intermediate energies, relevant for RHIC beam energy scan, NICA, FAIR and JPARC. However, in this thesis it is argued that some improvements of hybrid approaches are necessary to perform consistent simulations at intermediate energies. These improvements are connected to the interfaces between the hydrodynamics and transport.

Modern hybrid approaches assume:

1. Fast thermalization and an ideal fluid form of energy-momentum tensor (Eq. 1.18) at the initialization. At high energies these assumptions seem to be justified, however at intermediate energies they are not guaranteed. In chapter 3 these assumptions are verified, testing the deviation of the energy-momentum tensor from ideal fluid form.
2. At the initialization of hydrodynamics the whole space is assumed to be in thermal equilibrium. However, the borders of the fireball never really enter the equilibrated phase. This is cured in the core-corona approach [217], where the core with high energy density is treated by hydrodynamical equations and the low-density corona is propagated with transport. At high energies the corona is negligible, but at intermediate energies it becomes important. It has to be noted that in [217] core and corona are decoupled: particles from the corona cannot feedback to the core. This is in line with the next assumption of hybrid approaches.
3. It is assumed that transport is decoupled from hydrodynamics: particles from transport cannot cause any feedback to hydrodynamical equations. It turns out that this assumption becomes more and more challenging when one moves from higher energies to lower beam energies, as shown in chapter 4.
4. The particlization hypersurface is chosen by hand. Typically, it is a hypersurface of constant energy density or temperature, where it is assumed that both hydrodynamics and transport are applicable. If this assumption is justified then at particlization hypersurface the amount of particles flying into the hydrodynamical region would be consistent with the hydrodynamical expectation. In chapter 4 it is demonstrated that this conjecture is not fulfilled.

I would like to underline that the listed assumptions are well-justified at highest RHIC and LHC energies, where most of the hybrid approaches were applied, but they are challenging at RHIC beam energy scan, NICA, FAIR and JPARC energies.

There is a number of approaches and ideas, which seek for relaxing these assumptions. Anisotropic hydrodynamics [188,189] is applicable for highly anisotropic initial states, which are out of equilibrium in a particular way. As shown in chapter 3, the departure from equilibrium in heavy ion collisions at intermediate energies is mainly due to the pressure anisotropy. This means that anisotropic hydrodynamics is able to relax the first assumption about fast thermalization.

The next assumptions could be relaxed in an approach, in which *coupled* hydrodynamical and transport equations are solved. Attempts to write down the appropriate equations were already performed. Boundary conditions on a sharp hypersurface separating two transport approaches with different distribution functions were formulated in [218]. These conditions are also suitable for the boundary between hydrodynamics and transport. However, it is not enough to formulate the boundary conditions. One also has to supply the rules for how particles thermalize or how they deposit energy entering the hydrodynamical phase.

This was partially addressed in the hydrokinetic approach [219,220], where particles decouple from hydrodynamics continuously governed by rate equations. The decoupling hypersurface is momentum dependent in such a way that particles do not return to the hydrodynamical domain. There is also an approach of a transition layer [221,222], where particle escape probabilities are also governed by rate equations and particles returning to the hydrodynamical domain are integrated out.

An approach, where coupled hydrodynamical and transport equations are solved and the boundary is defined dynamically is not fully developed for the relativistic case. However, the analogous non-relativistic problem often appears in practice and is solved for many different scenarios. A possible example is the simulation of fluid flow with complicated boundary conditions: at the boundary the fluid has to be simulated kinetically and far from the boundary hydrodynamically. This kind of non-relativistic problem is successfully solved using the domain decomposition methods, see for example [223] and references therein. Similar ideas are also used in plasma simulations, see e.g. [224]. An analogous approach for heavy ion collisions would solve many of the problems that appear in the present hybrid models, in particular the problem of negative Cooper-Frye contributions (section 2.3).

In chapter 6 an alternative approach to the problem is suggested. Hadronic transport is applied in the whole space, but in the region of high energy density it is subjected to forced thermalization. This allows to interpolate between transport and

hydrodynamics. Unfortunately, varying the equation of state in this approach is challenging, although possible in principle. Hadrons inside the "hydrodynamical" high-density region need then to be treated as fictitious particles like in the particle-in-cell hydrodynamics [225].

Chapter 2.

Interfaces between hydrodynamics and transport

As one can see from the discussion about hydrodynamical and hybrid models, many uncertainties in the dynamical simulations of heavy ion collision are coming from interfaces between different approaches - for hybrid models this is the construction of the initial state (fluidization) and final state (particlization). In this chapter the actual calculations at these interfaces are discussed to better understand the source of uncertainties and to introduce the methodology used in the next chapters. Some parts of this chapter follow publications [1], [3] and [6].

2.1. Coarse-graining

Coarse-graining is a method to obtain macroscopic variables, such as the rest-frame energy-density, baryon density or velocity of the fluid from the particles in a transport approach. This method is used extensively in chapters 3, 4 and 6, as well as in other works, e.g. [226,227]. An example of coarse-graining is demonstrated in Fig. 2.1, where the microscopic particles from a transport simulation of heavy ion collision are turned into energy-density, pressure and velocity, the macroscopic variables necessary for hydrodynamics.

In the following sections the mathematical expressions for coarse-graining are derived, starting from the energy-momentum tensor and four-currents for a point-like particle, and proceeding with a smeared particle or a wavepacket.

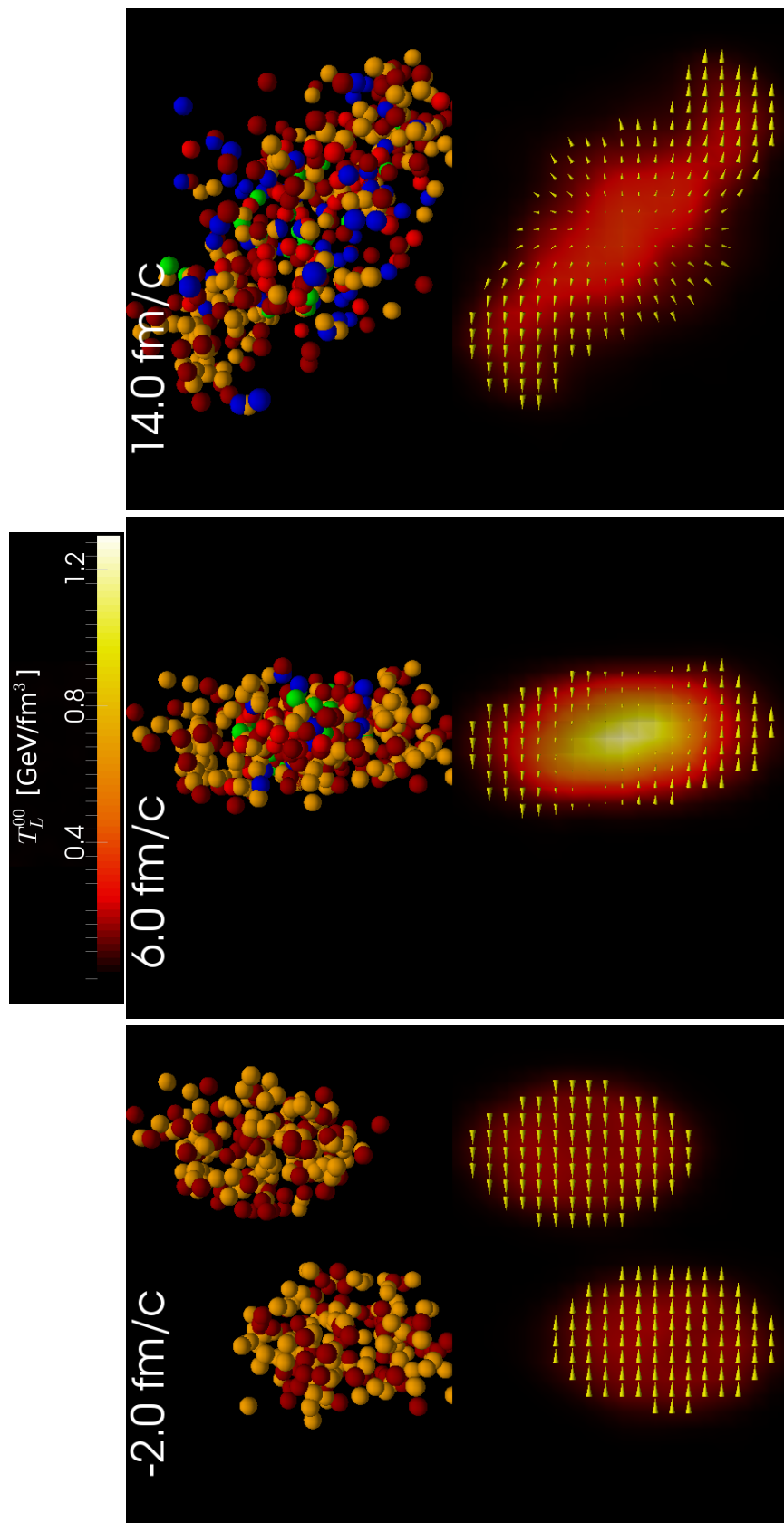


Figure 2.1.: Demonstration of coarse-graining. On the top row is the particle representation of a Au+Au collision at $\sqrt{s} = 3 \text{ GeV}$ and impact parameter $b = 5 \text{ fm}$ from the transport code SMASH. The simulation was performed in the center of mass frame, that is why both nuclei are Lorentz-contracted. Dark-red corresponds to protons, blue to neutrons, yellow to pions, red to Δ s and green to the rest. At the bottom is the coarse-grained picture of the energy-density in the Landau rest frame and Landau velocities in the XZ plane from a SMASH simulation with $N_{test} = 30$.

2.1.1. Energy-momentum tensor of a point-like particle

The expression for the energy-momentum tensor of a single point-like particle is well-known in the literature [228], as well as for particles interacting with fields [229]. Here the derivation is repeated to use it later for the wavepacket.

The action of a point-like particle is

$$S = -m \int_a^b d\tau = -m \int_a^b \sqrt{dx^\mu dx_\mu}. \quad (2.1)$$

Varying the particle trajectory $x^\mu = x^\mu + \delta x^\mu$ with fixed ends one obtains an action variation:

$$\begin{aligned} \delta S &= -m \int_a^b \sqrt{dx^\mu dx_\mu + 2dx^\mu d\delta x_\mu} + m \int_a^b \sqrt{dx^\mu dx_\mu} = \\ &= -m \int_a^b \frac{dx^\mu}{d\tau} d\delta x_\mu = \\ &= m \int_a^b \frac{du^\mu}{d\tau} d\tau \delta x_\mu, \end{aligned} \quad (2.2)$$

where $u^\mu = \frac{dx^\mu}{d\tau}$. Using the expression

$$\frac{du^\mu}{d\tau} = \frac{\partial u^\mu}{\partial x^\nu} \frac{\partial x^\nu}{\partial \tau} = u^\nu \partial_\nu u^\mu \quad (2.3)$$

one can rewrite the action variation as

$$\delta S = m \int_a^b u^\nu \partial_\nu u^\mu d\tau \delta x_\mu. \quad (2.4)$$

In this expression variation of the action depends on the coordinates and velocity of the particle, that will further be marked with index “p”. Now let us rewrite it in terms of continuous medium by adding integration over space-time and a δ -function. The coordinates x^μ are coordinates in space, over which integration is performed.

$$\delta S = m \int dV \int_a^b d\tau \delta^{(4)}(x^\mu - x_p^\mu(\tau)) u^\nu \partial_\nu u^\mu \delta x_\mu. \quad (2.5)$$

The delta-function $\delta^{(4)}(x^\mu - x_p^\mu(\tau))$ allows to change variables depending on x_p^μ to variables dependent on x^μ . Since $\int d\tau \delta(x^0 - x_p^0(\tau)) = \frac{1}{u^0}$, one can rewrite the equation (2.5) in the following form:

$$\delta S = \int dV \partial_\nu T^{\mu\nu} \delta x_\mu, \quad (2.6)$$

where the following notation is used

$$T^{\mu\nu} = m j^\mu u^\nu, \quad (2.7)$$

$$j^\mu = u^\mu \delta^{(4)}(x^\mu - x_p^\mu(\tau)) = \frac{u^\mu}{u^0} \delta^{(3)}(x^i - x_p^i(\tau)). \quad (2.8)$$

Here it was taken into account that $\partial_\mu j^\mu = 0$ due to the equations of motion. It is convenient to rewrite this in terms of the 4-momentum p^μ of the particle:

$$j^\mu = \frac{p^\mu}{p^0} \delta^{(3)}(x^i - x_p^i(\tau)) \quad (2.9)$$

$$T^{\mu\nu} = \frac{p^\mu p^\nu}{p^0} \delta^{(3)}(x^i - x_p^i(\tau)) \quad (2.10)$$

There is a simpler way to obtain the same formulas. One notices from the $T^{\mu\nu}$ of the ideal fluid that for a particle at rest

$$T_{\text{rest}}^{\mu\nu}(\vec{x}) = \text{diag}(m \delta^{(3)}(x^i - x_p^i), 0, 0, 0) \quad (2.11)$$

Notice that the δ -function has dimension of fm^{-3} here. Boosting the energy-momentum tensor with the 4-velocity u^μ using the Lorentz boost matrices from Eq. (1.17) one obtains

$$T^{\mu\nu}(\vec{x}') = \Lambda_0^\mu \Lambda_0^\nu m \delta^{(3)}(x'^i - x_p'^i) \frac{1}{u^0} = \frac{p^\mu p^\nu}{p^0} \delta^{(3)}(x'^i - x_p'^i). \quad (2.12)$$

Note that the necessary $\frac{1}{u^0}$ factor is obtained via the δ -function transformation:

$$d^3 x \delta^{(3)}(x^i - x_p^i) = d^3 x' \delta^{(3)}(x'^i - x_p'^i), \quad (2.13)$$

$$d^3 x = u^0 d^3 x'. \quad (2.14)$$

The primed coordinates x' here are the lab frame coordinates in contrast to the ones in the rest frame. For j^μ the calculation is analogous.

2.1.2. Energy-momentum tensor of a wavepacket

As one can see from Eq. (2.9), for finite numbers of point-like particles the energy-momentum tensor will be non-zero only at the particle positions. For coarse-graining it is desirable that $T^{\mu\nu}$ is continuous in space. That is why the point-like particles are not used directly. Instead they are smeared, which may be physically interpreted as wavepackets in coordinate space.

To introduce a non-pointlike particle one simply replaces the δ -function in space by a smearing kernel $K(\vec{x} - \vec{x}_p, u_p^\mu, \sigma)$, which represents the shape of the wavepacket in the rest frame. The smearing kernel should satisfy three conditions: $K(\vec{r})d^3r$ should be Lorentz scalar, it should be normalized as $\int K(\vec{x} - \vec{x}_p)d^3x = 1$, and it should approach a δ -function when the smearing parameter σ approaches zero. Then transforming from the particle rest frame

$$T_{\text{rest}}^{\mu\nu}(\vec{x}) = \text{diag}(mK(\vec{x} - \vec{x}_p), 0, 0, 0) \quad (2.15)$$

$$j_{\text{rest}}^\mu(\vec{x}) = \text{diag}(K(\vec{x} - \vec{x}_p), 0, 0, 0) \quad (2.16)$$

exactly as it was done with the δ -function, one obtains:

$$j^\mu(\vec{x}') = \frac{p^\mu}{p^0} K(\vec{x}' - \vec{x}'_p(\tau)) \quad (2.17)$$

$$T^{\mu\nu}(\vec{x}') = \frac{p^\mu p^\nu}{p^0} K(\vec{x}' - \vec{x}'_p(\tau)). \quad (2.18)$$

Surprisingly, all current popular choices of K in the literature are such that $K(\vec{r})d^3r$ is not a Lorentz scalar:

- Cell averaging: $K(\vec{x}) = \begin{cases} 1/\Delta V, & \vec{x} \in \Delta V \\ 0, & \text{otherwise} \end{cases}$. Here $K(\vec{x})d^3x$ is not a Lorentz scalar, since the volume ΔV is not contracted.
- Gaussian distribution with Lorentz contraction in z direction: $K(\vec{x}) = N \exp\left(-\frac{x^2 + y^2 + \gamma_z^2 z^2}{2\sigma^2}\right)$ is behaving properly only under boosts in z direction.
- Gaussian in x, y, η coordinates also behaves properly only under boosts in z direction.

Let us derive a simple, not too computationally demanding kernel, which satisfies all aforementioned conditions, in particular $K(\vec{x} - \vec{x}_p)d^3x$ being a Lorentz scalar. In the rest frame of the particle a Gaussian is taken, assuming that the particle is at the origin, $\vec{x}_p = 0$:

$$K_{rf}(\vec{x}) = (2\pi\sigma^2)^{-3/2} \exp(-\vec{x}^2/2\sigma^2) \quad (2.19)$$

Let us now express the rest frame coordinates through coordinates \vec{x}' in the laboratory (computational) frame via the Lorentz boost using the matrix from Eq. (1.17).

$$\begin{pmatrix} t \\ x^i \end{pmatrix} = \begin{pmatrix} u^0 & u^i \\ u^i & \delta^{ij} + (1 + u^0)^{-1}u^i u^j \end{pmatrix} \begin{pmatrix} 0 \\ x'^j \end{pmatrix} \quad (2.20)$$

The time component on the right hand side is zero because the smearing kernel needs to be evaluated at a fixed time in the computational frame, not in the particle rest frame. This derivation is analogous to the standard derivation of the Lorentz contraction, but the direction of contraction is not necessarily along a coordinate axis.

It follows then that

$$x^i = (\delta^{ij} + (1 + u^0)^{-1}u^i u^j)x'^j = x'^i + (1 + u^0)^{-1}u^i(u^j x'^j) \quad (2.21)$$

$$\vec{x}^2 = x^i x^i = \vec{x}'^2 + 2(1 + u^0)^{-1}(u^i x'^i)(u^j x'^j) + (1 + u^0)^{-2}(u^i u^i)(u^j x'^j)^2 = \quad (2.22)$$

$$= \vec{x}'^2 + (u^j x'^j)^2(1 + u^0)^{-1} \left(2 + \frac{(u^i u^i)}{1 + u^0} \right) \quad (2.23)$$

It follows from $u^\mu u_\mu = 1$ that $u^i u^i = u_0^2 - 1$ and

$$(1 + u^0)^{-1} \left(2 + \frac{(u^i u^i)}{1 + u^0} \right) = 1. \quad (2.24)$$

Therefore,

$$\vec{x}^2 = \vec{x}'^2 + (u^j x'^j)^2 \quad (2.25)$$

and the kernel K can be written in the computational frame as

$$K(\vec{x}' - \vec{x}'_p, u_p, \sigma) = \frac{u_0}{(2\pi\sigma^2)^{3/2}} \exp\left(-\frac{\vec{x}'^2 + (\vec{u}\vec{x}')^2}{2\sigma^2}\right) \quad (2.26)$$

This is the kernel used for all calculations throughout this thesis. The factor u_0 was added to ensure $K(x' - x'_p)d^3x' = K_{rest}(x - x_p)d^3x_{rest}$, since $d^3x' = u_0^{-1}d^3x_{rest}$. Let us check explicitly that the normalization condition is fulfilled. Using the Gaussian integral

$$\int \left(\prod_{i=1}^n dx_i\right) e^{-x_i A^{ij} x_j} = \pi^{n/2} (\det A)^{-1/2} \quad (2.27)$$

and the fact that the determinant $\det(\delta_{ij} + u_i u_j) = u_0^2$ one indeed finds that

$$\int K(\vec{x}' - \vec{x}'_p) d^3x' = 1. \quad (2.28)$$

It is not a coincidence that the smearing kernel is correctly normalized. It already follows from the transformation properties, that if it is normalized in one frame, it is normalized in any frame. One can check that this formula turns into the more familiar expression from [230], if the particle velocity is directed along the z-axis and $\vec{u} = \gamma_z(0, 0, \beta_z)$. Since $1 + (\gamma_z \beta_z)^2 = \gamma_z^2$, it follows that $\vec{x}'^2 + (u^j x'^j)^2 = x'^2 + y'^2 + \gamma_z^2 z'^2$ and the coincidence of the expressions is established.

The last thing to check is that the smearing kernel approaches the δ -function at $\sigma \rightarrow 0$. If this is true in the rest frame, it is true in any frame, so is enough to check it at the rest frame. This can be immediately seen from the δ -function limit representation

$$\delta(x) = \lim_{\epsilon \rightarrow 0} \frac{1}{\sqrt{2\pi\epsilon}} e^{-\frac{x^2}{2\epsilon}}. \quad (2.29)$$

Taking this limit for every dimension one obtains

$$\lim_{\sigma \rightarrow 0} K_{rest}(\vec{x} - \vec{x}_p, \sigma) = \delta^{(3)}(\vec{x} - \vec{x}_p). \quad (2.30)$$

Finally one notes that the exponential form of the smearing function is by no means unique. Any normalized function of $\vec{x}'^2 + (u^j x'_j)^2$ can be incorporated given that in some limit it gives the δ -function. The reasons to prefer an exponential are firstly, because it has infinite number of continuous derivatives and secondly, because it

corresponds to the physical background of the Gaussian wavepacket. An alternative smearing kernel could be, for example,

$$K_{\text{alternative}} = \begin{cases} \frac{15u_0}{8\pi\sigma^3} \left(1 - \frac{\vec{x}'^2 + (\vec{u}\vec{x}')^2}{\sigma^2} \right) & |x| < \sigma \\ 0 & |x| > \sigma \end{cases} \quad (2.31)$$

2.1.3. Final expressions for coarse-graining

The derivations from the two previous sections allow to write down the expressions used in this work for the coarse-graining. Suppose that particles for coarse-graining are taken from N_{ev} events (N_{ev} transport simulations). Then the following expressions are valid:

$$T^{\mu\nu}(\vec{r}) = \frac{1}{N_{ev}} \sum_{\text{events}} \sum_i \frac{p_i^\mu p_i^\nu}{p_i^0} K(\vec{r} - \vec{r}_i, u_i) \quad (2.32)$$

$$j^\mu(\vec{r}) = \frac{1}{N_{ev}} \sum_{\text{events}} \sum_i \frac{p_i^\mu}{p_i^0} K(\vec{r} - \vec{r}_i, u_i) \quad (2.33)$$

$$K(\vec{r} - \vec{r}_i, u, \sigma) = \frac{u_0}{(2\pi\sigma^2)^{3/2}} \exp\left(-\frac{(\vec{r} - \vec{r}_i)^2 + (\vec{u} \cdot (\vec{r} - \vec{r}_i))^2}{2\sigma^2}\right) \quad (2.34)$$

$$u^\mu = (u^0, \vec{u}) = \frac{p^\mu}{m} \quad (2.35)$$

These expressions in principle allow to compute the energy-momentum tensor and four-currents on any irregular grid, but in this work only Cartesian grids are used.

2.2. Fluidization

The first interface in hybrid approaches is the transition from transport to fluid, called fluidization. At fluidization microscopic particles with their coordinates and momenta have to be converted into a macroscopic continuous hydrodynamic fields: density, energy density, pressure, etc. In the relativistic case the first step of the fluidization is the construction of the energy-momentum tensor $T^{\mu\nu}$ and four-currents j^μ as describe above. However, it is by no means guaranteed that they have an ideal fluid-dynamical form or that they are close to it. Indeed, transport approaches generally simulate non-equilibrium systems and the $T^{\mu\nu}$ of hydrodynamics is close to equilibrium. The problem of matching a non-equilibrium $T^{\mu\nu}$ to an equilibrium

one is relevant for many approaches that construct their initial state from the discrete degrees of freedom [163–165, 168, 211, 231–233].

This matching problem can be eliminated or minimized by waiting until transport approach reaches equilibrium and only switching to hydrodynamics, when the necessary degree of equilibration is reached. However, it was argued that a good description of experimental data requires rather small initialization times of hydrodynamics ($\tau \leq 0.6$ fm/c at the highest RHIC energy) [234]. The initial state generated by transport at this early time is highly off-equilibrium. Such an initial state is suitable for anisotropic hydrodynamics [188], but in most of the existent approaches it has to be matched to equilibrium state. The matching procedure is not unique and introduces uncertainty to the simulation. To demonstrate this uncertainty the matching procedures applied by different approaches are discussed in section 2.2.1. All the discussed approaches neglect the non-equilibrium part of $T^{\mu\nu}$.

How good is this approximation? This depends on the degree of thermalization at the time of fluidization. One way to quantify the degree of thermalization is given in section 2.2.2. At high energies a number of studies were devoted to understand the approach to equilibrium in heavy ion collisions. It was studied both in strongly-coupled and weakly-coupled field-theoretical models (see [235] for an overview). The strongly coupled ones apply dualities of supersymmetric Yang-Mills gauge theory for calculations in the strong coupling limit [236, 237]. The weakly coupled ones are able to achieve fast thermalization in a weak coupling limit, where colliding nuclei are described in the color-glass condensate framework [127, 238]. The primary effect in CGC leading to fast thermalization is believed to be plasma instabilities, such as the chromo-Weibel instability [239]. Both types of approaches predict considerable momentum space anisotropies at the time, when hydrodynamics is initialized. The aforementioned studies are relevant for high collision energies. At intermediate energies thermalization was studied using transport models [240], where momentum distributions were averaged over a $(5 \times 5 \times 5)$ fm³ central cell. This study investigates global thermalization in a big volume and results in thermalization times much larger than typical starting times for hydrodynamics. At the same time, it is clear that thermalization is a local phenomenon. It is reached faster, where the density is higher and collisions are more intense and probably never reached at the boundary of the fireball. Therefore, in chapter 3 the deviation from equilibrium at intermediate energies is studied locally using a coarse-grained transport approach.

2.2.1. Overview of fluidization in current hybrid models

How do existing approaches perform fluidization, i.e. construct the initial state of hydrodynamics? How is fluidization time chosen? What fluidization procedures are applied (it was mentioned already that the procedure is not unique)? This is discussed in this section.

The modern hybrid models applying fluidization are summarized in Table 2.1. All the shown approaches need to obtain the ideal fluid part of $T^{\mu\nu}$ and j^μ from discrete degrees of freedom (hadrons, partons, strings). The viscous corrections are neglected in all models, even if viscous hydrodynamics is applied for the evolution. The only exception is a recent work by Liu et al. [241], where the initial stage for viscous hydrodynamics is constructed from free streaming partons and viscous corrections are explicitly included.

In the relevant approaches [163–165, 168, 211, 231–233] the fluidization is typically performed either at a constant proper time hypersurface $\tau = \text{const}$ or at a constant center of mass frame time hypersurface $t_{CM} = \text{const}$, see Table 2.1. The constant is often chosen according to the *geometrical criterion* - the time, when nuclei geometrically pass through each other: $t_{CM} = \frac{2R}{\gamma\beta} = 2R(E_{\text{lab}}/2m_N)^{-1/2}$, where R is the radius of the nucleus, $\vec{\beta}$ is the velocity, $\gamma = (1 - \vec{\beta}^2)^{-1/2}$, E_{lab} is laboratory frame kinetic energy per nucleon, and m_N is nucleon mass. This time is taken to be the same for all collision centralities. It was never systematically verified, if the energy-momentum tensor $T^{\mu\nu}$ and four-currents j^μ are close to hydrodynamical form at fluidization. An exception is the work [244], where the fluidization time t_{fl} is chosen such that the entropy per baryon does not change any more at $t > t_{fl}$. The isochronous fluidization has little physical motivation, it is rather a matter of technical convenience. Indeed, a study has appeared recently, where fluidization is not isochronous [245].

There are three ways in the literature to match the $T^{\mu\nu}$ and j^μ to ideal hydrodynamics. The first one is to use only $T^{\mu 0}$, j^0 , assuming that they have ideal fluid form $T_{ideal}^{\mu\nu} = (\epsilon + p)u^\mu u^\nu - pg^{\mu\nu}$, $j_{ideal}^\mu = nu^\mu$, and adding the equation of state $p = p(\epsilon, n)$. The following system of equations is then solved (usually iteratively, for details see [165]):

Model	Initial condition	Hydro	Switching criterion	Smearing kernel	Getting $T_{ideal}^{\mu\nu}$	
UrQMD hybrid [163]	UrQMD cascade	ideal 3+1D, SHASTA	$t_{CM}[\text{fm}/c] = \max(2R\sqrt{\frac{E_{\text{lab}}}{2m_N}}, 1.0)$	Gaussian z-contracted	T^{μ^0}, j^0	
Skokov-Toneev hybrid [231]	Quark-Gluon-String-Model	ideal 3+1D, SHASTA	t_{CM} such that $S/Q_B = \text{const}$	not mentioned	T^{μ^0}, j^0	
EPOS [211]	Strings (Regge-Gribov model)	ideal 3+1D	τ	Gaussian z-contracted	Landau frame	
NeXSPheRIO hybrid [232, 242]	Strings (Regge-Gribov model)	ideal 3+1D, SPH	$\tau = 1 \text{ fm}/c$ [243]	Gaussian in $x, y, \tau\eta$	Landau frame	
Gale et al [168]	IP-glasma	viscous 3+1D, MUSIC	$\tau = 0.2 \text{ fm}/c$ ($\sqrt{s_{NN}} = 2.76 \text{ TeV}$)	not mentioned	Landau frame	
Karpenko hybrid [164]	UrQMD cascade	viscous 3+1D	τ_{geom}	Gaussian with σ_{\perp} and σ_{η}	T^{μ^0}, j^0	
Pang et al hybrid [165]	AMPT	ideal 3+1D, SHASTA	τ	Gaussian with σ_{\perp} and σ_{η}	T^{μ^0}, j^0	
Bhalerao et al hybrid [233]	AMPT	viscous 2+1D, VISH2+1	$\tau = 0.4 \text{ fm}/c$ ($\sqrt{s_{NN}} = 2.76 \text{ TeV}$)	Gaussian in x, y	local frame	CM

Table 2.1.: Fluidization features in different hybrid approaches. Each of these models, including those using viscous hydrodynamics, neglects viscous corrections at fluidization.

$$\begin{cases} T^{00} = (\epsilon + p)\gamma^2 - p \\ T^{0i} = (\epsilon + p)\gamma^2\vec{v} \\ j_B^0 = n\gamma \\ p = p_{EoS}(n, \epsilon) \end{cases} \quad (2.36)$$

The advantage of this method is that it conserves energy and momentum. However, this method supports switching only to ideal fluid $T_{ideal}^{\mu\nu}$, keeping viscous corrections is hardly possible. Even though the switching method conserves energy and momentum, one of the models [165], which employs it, violates conservation laws, because in [165] the whole $T^{\mu\nu}$ is multiplied by a free parameter K , which is then fixed by experimental multiplicities.

A different procedure takes advantage of the Landau matching condition, determining the energy density ϵ and the collective velocity u^μ by solving the eigenvalue problem

$$T^{\mu\nu}u_\nu = \epsilon u^\mu, \quad (2.37)$$

using the fact that u^μ is a timelike eigenvector of $T^{\mu\nu}$ and satisfies $u^\mu u_\mu = 1$. Then the density n is computed as $n = j^\mu u_\mu$. Only after that the pressure is determined from the equation of state. Note that this way is not equivalent to the previous one: here the collective velocity does not depend on the equation of state. This method conserves energy and momentum only if the viscous corrections are kept. If they are neglected (as in [168,211,232]), then conservation laws are violated. For a simple example assume that $u^\mu = \gamma(1, 0, 0, v)$. In this case, the energy density in the computational frame is $\epsilon_{comp} = \gamma^2(\epsilon + v^2 T_L^{33})$, where T_L^{33} can be split into the ideal fluid pressure and a viscous correction. If the correction is neglected, energy conservation is violated.

The third way is applied in [233]. All particles in the cell are boosted to the local center of mass frame, which moves with velocity $\vec{v} = \frac{\sum \vec{p}_i}{\sum E_i}$, where E_i and \vec{p}_i are energy and momentum of the i -th particle. Energy density is computed as $\epsilon(r) = \sum_i E'_i \cdot K(\vec{r} - \vec{r}_i)$, where E'_i is the energy of i -th particle in the local center of mass frame, and K is the smearing kernel. Pressure is determined from the equation of state, local collective velocity is assumed to be equal to \vec{v} . In this method energy and momentum conservation are violated, if the viscous corrections are neglected, as in the previous method.

2.2.2. Consistency of $T^{\mu\nu}$ and j^μ with hydrodynamics

It is important to be able to quantify the deviation of $T^{\mu\nu}$ and j^μ from equilibrium. If the deviation is small enough then one can switch to hydrodynamics. This quantification is discussed here. A non-equilibrium energy-momentum tensor and four-currents can be decomposed as

$$T^{\mu\nu} = T_{ideal}^{\mu\nu} + \pi^{\mu\nu} \quad (2.38)$$

$$j^\mu = j_{ideal}^\mu + q^\mu, \quad (2.39)$$

where $T_{ideal}^{\mu\nu}$ and j_{ideal}^μ are the energy-momentum tensor and the four-currents of conserved charges of an ideal fluid defined by Eqs. (1.18-1.19). Such a decomposition is generally not unique, but depends on the matching conditions. In section 2.2.1 three kinds of matching conditions used in modern hybrid models are discussed.

For the applicability of hydrodynamics it is required that the corrections to the ideal fluid-dynamical form of $T^{\mu\nu}$ and j^μ are not too large:

$$\|\pi^{\mu\nu}\| \ll \|T_{ideal}^{\mu\nu}\| \quad (2.40)$$

$$\|q^\mu\| \ll \|j_{ideal}^\mu\| \quad (2.41)$$

Here $\|A\|$ denotes a norm of tensor A , which satisfies the usual norm definition, for example $\|A^{\mu\nu}\| \equiv A^{\mu\nu} A_{\mu\nu}$. Let us rewrite these conditions in a form convenient for numerical computation. The general expressions for $T^{\mu\nu}$ and j^μ in viscous hydrodynamics (Landau picture) are the following:

$$T^{\mu\nu} = \epsilon_0 u^\mu u^\nu - \Delta^{\mu\nu} (P_0 + \Pi) + \pi^{\mu\nu} \quad (2.42)$$

$$j^\mu = n_0 u^\mu + q^\mu,$$

where Π is the bulk pressure, $\pi^{\mu\nu}$ is the shear stress tensor, n_0 is the conserved quantum number density and q^μ is the diffusion current. The viscous corrections to ideal hydrodynamical $T^{\mu\nu}$ and j^μ are supposed to be small:

$$\|\pi^{\mu\nu}\| \ll \|T^{\mu\nu}\| \quad (2.43)$$

$$\Pi \ll P_0 \quad (2.44)$$

$$\|q^\mu\| \ll n_0 \quad (2.45)$$

From Eqns. 2.42 one obtains

$$\pi^{\mu\nu} = T^{\mu\nu} - \epsilon_0 u^\mu u^\nu + \frac{1}{3} \Delta^{\mu\nu} (T_\alpha^\alpha - \epsilon_0) \quad (2.46)$$

$$P_0 + \Pi = -\frac{1}{3} \Delta_{\mu\nu} T^{\mu\nu} \quad (2.47)$$

$$q^\mu = \Delta_\nu^\mu j^\nu \quad (2.48)$$

One can see that in the Landau rest frame $u_L^\mu = \text{diag}(1, 0, 0, 0)$, $\pi_L^{\mu 0} = 0$, and $q_L^0 = 0$. The non-zero components are written as follows:

$$P_0 + \Pi = \frac{1}{3} (T_L^{11} + T_L^{22} + T_L^{33}) \quad (2.49)$$

$$\pi_L^{ij} = T_L^{ij} - (P_0 + \Pi) \delta^{ij} \quad (2.50)$$

$$q_L^i = -j_L^i \quad (2.51)$$

Let us note that tensor and vector norms are frame-independent, so the consistency conditions for viscous hydrodynamics can be formulated in any frame. In Eqn. (2.43) one can substitute $\|T^{\mu\nu}\|$ by its largest component in the Landau frame: ϵ_0 . Then Eqn. (2.43) will turn into

$$\|T_L^{\mu\nu} - \text{diag}(\epsilon_0, P', P', P')\| \ll \epsilon_0, \quad (2.52)$$

where P' denotes $\frac{1}{3} (T_L^{11} + T_L^{22} + T_L^{33}) = P_0 + \Pi$. The physical meaning of this equation is that the diagonal components of $T^{\mu\nu}$ in the Landau rest frame do not deviate much from P' and simultaneously the off-diagonal components are small compared to ϵ_0 . The condition for q^μ is rewritten as

$$(j_L^1)^2 + (j_L^2)^2 + (j_L^3)^2 \ll (j_L^0)^2. \quad (2.53)$$

Here the physical meaning is that relative velocity between Landau and Eckart frames should be small. To rewrite $\Pi \ll P_0$ one has to add an equation of state $P_0 = p_{EoS}(\epsilon_0, n_0)$ to the system. Then one obtains $P' / p_{EoS}(\epsilon_0, j_L^0) - 1 \ll 1$. Consequently, whether the tensor $T^{\mu\nu}$ is suitable for fluid dynamics or not is also defined by the equation of state from the fluid dynamics itself. The same $T^{\mu\nu}$ can be consistent with viscous hydrodynamics with some equation of state, and may fail when the equation of state is changed. Therefore, we will not study the smallness of bulk corrections further, but leave this for a future study.

The conditions for smallness of the shear stress tensor can be split into two: pressure isotropy and smallness of off-diagonal elements. One has to note that the Landau frame is defined only up to an arbitrary rotation. Locally one can always choose coordinates such that $T_L^{12} = T_L^{23} = T_L^{13} = 0$. However, our coordinates are the global coordinates of the computational frame and therefore non-diagonal components of the $T_L^{\mu\nu}$ are in general non-zero. Therefore,

$$|T_L^{11} - P'| + |T_L^{22} - P'| + |T_L^{33} - P'| \ll \epsilon_0 \quad (2.54)$$

$$|T_L^{12}| + |T_L^{23}| + |T_L^{13}| \ll \epsilon_0 \quad (2.55)$$

To strengthen these conditions, every term is substituted by the right hand side of the inequality $|T_L^{11} - P'| = |T_L^{11} - T_L^{22} + T_L^{11} - T_L^{33}|/3 \leq |T_L^{11} - T_L^{22}|/3 + |T_L^{11} - T_L^{33}|/3$ and ϵ_0 is substituted by P' . In this way, a set of criteria is obtained that is further used for numerical calculations.

$$X \equiv \frac{|T_L^{11} - T_L^{22}| + |T_L^{22} - T_L^{33}| + |T_L^{33} - T_L^{11}|}{T_L^{11} + T_L^{22} + T_L^{33}} \ll 1 \quad (2.56)$$

$$Y \equiv \frac{3(|T_L^{12}| + |T_L^{23}| + |T_L^{13}|)}{T_L^{11} + T_L^{22} + T_L^{33}} \ll 1$$

$$v_{LE} = \sqrt{(j_L^1)^2 + (j_L^2)^2 + (j_L^3)^2} / j_L^0 \ll 1$$

$$Z \equiv \frac{T_L^{11} + T_L^{22} + T_L^{33}}{3 p_{EoS}(\epsilon_0, j_L^0)} - 1 \ll 1$$

In the following X is referred to as pressure anisotropy and Y as off-diagonality. Please note that due to the inequality $|a - b| \leq |a| + |b|$ it is always fulfilled that $X \leq 2$. For ideal fluid dynamics $X = 0$. For Y let us remark that

$$T^{12} \sim \sum \frac{p^1 p^2}{p^0} \leq \frac{1}{2} \sum \frac{p_1^2 + p_2^2}{p^0} \sim \frac{1}{2} (T^{11} + T^{22}) \quad (2.57)$$

Interchanging indices and substituting this into the definition of Y one gets $Y \leq 3$. For an ideal fluid $Y = 0$. The measures X and Y are used in chapter 3 to evaluate the deviation of the $T^{\mu\nu}$ from equilibrium.

2.2.3. Multicomponent ideal hadron gas equation of state

An equation of state is necessary for one of the fluidization methods, described in section 2.2.1, as well as for the forced thermalization method in chapter 6 and for testing the thermodynamical properties of SMASH transport approach in section 5.4.2. For all these purposes a simple ideal hadron gas grand-canonical equation of state is used. This equation of state is widely known in literature (see e.g. [240]) and is given here for reference and completeness.

Suppose that the energy-momentum tensor $T^{\mu\nu}$, baryon four-current j_B^μ and strangeness four-current j_S^μ are constructed from a coarse-grained transport. After their transformation to the rest frame one obtains the rest frame energy density ϵ_{rest} , the baryon density n_B^{rest} and the strangeness density n_S^{rest} . The isospin projection density n_{I3} is not considered, which is justified, because the isospin chemical potential μ_{I3} is typically much smaller than μ_B and μ_S . To find temperature T , baryon chemical potential μ_B and strangeness chemical potential μ_S the ideal hadron gas equation of state is employed throughout this thesis:

$$n_B^{rest} = \frac{T^3}{2\pi^2(\hbar c)^3} \sum g_i B_i \lambda_i z_i^2 K_2(z_i) \quad (2.58)$$

$$n_S^{rest} = \frac{T^3}{2\pi^2(\hbar c)^3} \sum g_i S_i \lambda_i z_i^2 K_2(z_i) \quad (2.59)$$

$$\epsilon^{rest} = \frac{T^4}{2\pi^2(\hbar c)^3} \sum g_i z_i^2 \lambda_i (3K_2(z_i) + z_i K_1(z_i)) , \quad (2.60)$$

where the chemical potential $\mu_i \equiv \mu_B B_i + \mu_S S_i$ corresponds to baryon and strangeness conservation, $z_i \equiv \frac{m_i}{T}$ and fugacity $\lambda_i \equiv \exp\left(\frac{\mu_i}{T}\right)$. Here the sum runs over all hadron species, m_i is the mass of a hadron i , g_i is its spin and isospin degeneracy factor, and B_i and S_i are its baryon number and strangeness. The lists of hadronic species used for the equation of state are slightly different for the investigations in the different chapters, so they are mentioned at the corresponding places. The system of equations (2.58-2.60) is solved with respect to temperature and chemical potentials. Then the equilibrium hadron densities in the rest frame n_i and pressure p are computed as

$$n_i = \frac{T^3}{2\pi^2(\hbar c)^3} g_i \lambda_i z_i^2 K_2(z_i) \quad (2.61)$$

$$p = T \sum n_i \quad (2.62)$$

This equation of state does not take into account the effects of quantum statistics and finite width of the resonances.

2.3. Particlization with Cooper-Frye formula and negative particle numbers

The second important interface is the transition from hydrodynamics to transport, the “particlization”. The particlization is the reverse of the fluidization: macroscopic continuous fields are converted into the microscopic particles. The fluidization is accompanied by the loss of the microscopic information about the system. At the particlization, on the contrary, one has to make an assumption about the underlying microscopic distribution. The most commonly used way of particlization involves Cooper-Frye formula, which receives the underlying momentum distribution in the local rest frame $f(p)$ as an input and computes the number of particles crossing a predefined infinitesimally thin three-dimensional hypersurface Σ . This hypersurface Σ represents a sharp moving boundary between the transport approach and the hydrodynamics. The hypersurface is usually determined a posteriori from the hydrodynamical solution in the whole forward light cone, usually as a hypersurface of constant time, energy density, temperature, or Knudsen number. Particle distributions on an infinitesimal element of hypersurface, $d\Sigma$, are then following from the Cooper-Frye formula:

$$p^0 \frac{d^3 N}{d^3 p} = p^\mu d\sigma_\mu f(p), \quad (2.63)$$

where $d\sigma_\mu$ a normal four-vector of the hypersurface with length equal to the area of the infinitesimal surface element. This formula was obtained by Cooper and Frye [153] with the main feature that it respects four-momentum conservation. Though formula (2.63) is valid for any $f(p)$, the distribution function is usually assumed to be either the boosted thermal distribution $f(p) = f_0(p) = \left[\exp\left(\frac{p^\mu u_\mu - \mu}{T}\right) \pm 1 \right]^{-1}$ (ideal fluid), or a distribution close to the boosted thermal distribution $f(p) = f_0(p) + \delta f(p)$ (viscous fluid), where $\delta f(p)$ is the dissipative correction. Here T , μ and $u^\mu = \gamma(1, \vec{v})$ are temperature, chemical potential and the flow velocity of the fluid, respectively.

There is, however, a conceptual problem with the Cooper-Frye formula. Where the surface is space-like, *i.e.*, its normal vector $d\sigma_\mu$ is space-like, and $p^\mu d\sigma_\mu < 0$ for some \vec{p} .

Thus if $f(p) > 0$ for all p , as is the case for the thermal distribution, $\frac{d^3 N}{d^3 p} < 0$ for some \vec{p} . This can be easily seen in the local rest frame of a space-like surface (which always exists since $v_{surf} < c$ for space-like surfaces), where $p^\mu d\sigma_\mu = \vec{p} \cdot \vec{n}$ and thus $\frac{d^3 N}{d^3 p} < 0$ for momenta directed inward the surface. On the other hand, for those time-like surfaces which normal vector points toward the future (*i.e.*, $d\sigma_0 > 0$), $\frac{d^3 N}{d^3 p} > 0$ for any \vec{p} . This can be also understood as follows: the surface is “escaping” faster than the speed of light, so no particle can cross it inward. (For a summary of the properties of time-like and space-like surfaces, see Table 2.2).

time-like surface	space-like surface
time-like normal	space-like normal
$d\sigma^\mu d\sigma_\mu > 0$	$d\sigma^\mu d\sigma_\mu < 0$
$v_{surf} > c$	$v_{surf} < c$
\exists RF: $d\sigma^\mu = (\pm dx dy dz, 0, 0, 0)$	\exists RF: $d\sigma^\mu = (0, 0, 0, dt dx dy)$
$d\sigma_0 > 0 \Rightarrow \forall p^\mu: p^\mu d\sigma_\mu > 0$	$\exists p^\mu: p^\mu d\sigma_\mu < 0$
$d\sigma_0 > 0 \Rightarrow \forall p^\mu: \frac{d^3 N_{CF}}{d^3 p} > 0$	$\exists p^\mu: \frac{d^3 N_{CF}}{d^3 p} < 0$

Table 2.2.: Properties of surface elements. $g^{\mu\nu} = (1, -1, -1, -1)$. The normal vector is directed toward lower density. RF abbreviates Reference Frame, $\frac{d^3 N_{CF}}{d^3 p}$ denotes particle distribution from the hypersurface element calculated using the Cooper-Frye formula.

If $\frac{d^3 N}{d^3 p}$ is interpreted as a phase-space density, negative values of it are clearly unphysical, but instead of giving a literal phase-space density, the Cooper-Frye formula rather counts the world lines of particles crossing the surface element $d\Sigma$, and assigns positive weight to particles moving “outward” and negative weight to particles moving “inward”. Thus the negative values of $\frac{d^3 N}{d^3 p}$, the so-called negative Cooper-Frye contributions, refer to particles flying inward toward the hydrodynamical region, and which should thus be absorbed back to the fluid.

In pure hydrodynamical models, this poses a problem: Particlization takes place at freeze-out when rescatterings cease, and particles stream freely. Thus, once particles cross the particlization surface, there is nothing from where particles could scatter back toward the surface, and thus there should be no particles flying back. To avoid this problem, one could choose a completely time-like particlization hypersurface, for example a hypersurface of a constant time without any negative contributions. However, it was shown [246] that particle spectra obtained in such an approach are

dramatically different from spectra on a constant temperature hypersurface. Another way is to consider a cut-off distribution [247]: $p^0 \frac{d^3 N}{dp^3} = p^\mu d\sigma_\mu f(p) \ominus (p^\mu d\sigma_\mu)$. Such a prescription violates conservation laws, unless one adjusts temperature, chemical potentials, and flow velocity in the particle distribution $f(p)$ [248, 249].

On the other hand, there is no such a problem in hybrid models. Particlization takes place where rescatterings are abundant, and thus it is natural to have particles flying back to the fluid-dynamical region. The problem is rather a practical one: What does the negative weight of a particle mean when one samples the particle distributions at the particlization surface to create an initial state for the hadron transport? Usually one simply ignores them (see *e.g.* Ref. [230]), which violates conservation laws. An attempt to include these negative weights to the hadron transport was recently made in Ref [250]. Alternatively, if the transition from fluid to transport takes place in a region where hydrodynamics and transport are equivalent, the negative Cooper-Frye contributions coincide with the distribution of particles that backscatter to hydrodynamical region. Thus all one needs to do is to remove these particles from the cascade, but this removing is technically challenging, and the problem remains how to find the region where hydrodynamics and transport lead to equal solutions—assuming that such a region exists at all! Thus the ultimate solution to the problem would be to construct a model, solving coupled hydrodynamical and kinetic equations with the kinetic model providing boundary condition for hydrodynamics. An attempt in this direction was taken by Bugaev [218, 251, 252], but these ideas have not yet been implemented in practice.

Fortunately, at high collision energies, the explosive expansion dynamics keeps the negative contributions on the level of a few percent. The emission of particles from time-like areas of the surface where no negative contributions appear (so-called volume emission) is much larger than the emission from space-like areas (so-called surface emission), and as will be discussed later, large fluid flow velocities reduce negative contributions from space-like surfaces. Nevertheless, there are very few studies that actually quote the values of negative contributions, and investigations at lower collision energies were lacking completely, before the investigation [1], that is presented in chapter 4.

Chapter 3.

Deviation of $T^{\mu\nu}$ from equilibrium in Au+Au collisions at $E_{\text{lab}} = 5\text{--}160 A \text{ GeV}$

The importance to quantify the deviation of the local energy-momentum tensor from equilibrium is discussed in 2.2. This quantification allows to assess the uncertainty arising from neglecting the non-equilibrium part of $T^{\mu\nu}$ at fluidization, an approximation adopted by most of the existing approaches (see section 2.2.1 for details).

Therefore, the following questions are addressed here for Au+Au collisions at $E_{\text{lab}} = 5\text{--}160 A \text{ GeV}$, varying the collision centrality and nuisance parameters:

- How far away are $T^{\mu\nu}$ and j^μ from the ideal fluid form at the time of geometrical overlap — typical fluidization time in many approaches?
- What are the main sources of deviation from equilibrium?
- Is there a better fluidization criterion? Should it depend on centrality?

3.1. Methodology to quantify off-equilibrium contributions in $T^{\mu\nu}$ and j^μ

The calculation is based on the hadronic transport approach called Ultra-relativistic Quantum Molecular Dynamics (UrQMD 3.4) [197, 253], which is similar to the SMASH transport approach described in detail in chapter 5. The degrees of freedom in UrQMD are hadrons, resonances up to a mass of 2.2 GeV and strings and the implemented processes include binary elastic and inelastic scatterings which mainly proceed via resonance formation and decays or string excitation and fragmentation at higher

collision energies. The UrQMD particles move along classical trajectories and scatter according to their free-particle cross-sections. In this study no long range potentials are employed and particle trajectories between collisions are always straight lines. Using UrQMD Au + Au collisions at laboratory frame energies $E_{\text{lab}} = 5, 10, 20, 40, 80$ and 160 A GeV are simulated.

The general procedure for the calculations is:

1. Generate many UrQMD events and coarse-grain them using a 2+1D space-time grid. The space dimensions are chosen to be the event plane xz . A 2+1D grid and not 3+1D is chosen, because observing the behaviour of some quantity on a 2D surface versus time is much easier and informative for a human than observing a quantity on a 3D grid. Additionally, in central collisions due to symmetry the event plane completely characterizes all the volume. The center of mass frame is used as the computational frame in the simulation. In all the following text the time is measured in the center of mass frame. By the UrQMD convention $t = 0$ is the moment when the contracted spheres of the nuclear radius first touch each other in a central collision.
2. Particles from the generated events are used to construct the energy-momentum tensor $T^{\mu\nu}(t, x, z)$ locally for each grid cell as described in section 2.1.3. To compute $T^{\mu\nu}$ only participants are taken into account, i.e. the particles that took part in at least one collision.
3. Transform the constructed energy-momentum tensor in each grid cell to the Landau rest frame according to Eq. (2.37).
4. Verify the weak conditions given by Eqn. (2.56) locally in time and space. The conditions for smallness of pressure anisotropy, off-diagonality, Eckart velocity relative to Landau are tested. The condition for smallness of bulk pressure compared to pressure is ignored, because it depends on the equation of state, which can be different for different models that use fluidization.

This procedure is nothing but the fluidization of hybrid models with the additional quantification of the deviations from equilibrium.

3.2. Sensitivity to statistics, grid spacing and smearing

Before showing the final results, in this section the influence of nuisance parameters is investigated. Let us first consider the influence of the number of Monte-Carlo events used to produce $T^{\mu\nu}$ and j^μ .

The deviations of $T^{\mu\nu}$ in the simulation from the ideal fluid $T_{\text{ideal}}^{\mu\nu}$ can have two distinct reasons. The first one is the deviation of the distribution function $f(\vec{r}, \vec{p})$ in the transport approach from equilibrium, this reason is referred to as physical. The second reason is statistical: due to finite number of particles in the simulation, the distribution function is not sampled exactly.

Let us consider two energy-momentum tensors: calculated from particles $T_{\text{part}}^{\mu\nu}$ and a "true" $T^{\mu\nu}$:

$$T_{\text{part}}^{\mu\nu}(\vec{r}) = \frac{1}{N_{\text{ev}}} \sum_{\text{events}} \sum_i \frac{p_i^\mu p_i^\nu}{p_i^0} K(\vec{r} - \vec{r}_i, p_i) \quad (3.1)$$

$$T^{\mu\nu}(\vec{r}) = \int \frac{p^\mu p^\nu}{p^0} f(\vec{r}, \vec{p}) d^3 p \quad (3.2)$$

Here N_{ev} is the number of events and $K(\vec{r} - \vec{r}_i, p_i)$ is a smearing kernel. The particular form of the kernel is discussed in section 2.1.2. In the limit of $N_{\text{ev}} \rightarrow \infty$

$$\frac{1}{N_{\text{ev}}} \sum_{\text{events}} \sum_i K(\vec{r} - \vec{r}_i, p_i) \xrightarrow{N_{\text{ev}} \rightarrow \infty} \int d^3 p d^3 r' f(\vec{r}', \vec{p}) K(\vec{r} - \vec{r}') \quad (3.3)$$

For the case of a Gaussian kernel and $\sigma \rightarrow 0$, the kernel turns into a δ -function and one retains the "true" $T^{\mu\nu}$. To combine these two limits ($\sigma \rightarrow 0$, $N_{\text{ev}} \rightarrow \infty$) one has to keep enough particles within a volume of size σ^3 . Consequently, to obtain the "true" $T^{\mu\nu}$ in the simulation, one has to take the limit (ρ is the particle number density)

$$\sigma \rightarrow 0, N_{\text{ev}} \rho \sigma^3 \rightarrow \infty \quad (3.4)$$

This creates practical limitations for determining the "true" $T^{\mu\nu}$ in simulations: decreasing σ by a factor of 10 demands increasing the statistics by a factor of 1000! Also see regions with lower density are more demanding with respect to statistics. To get some insights into the effect of statistics, an auxiliary simulation is performed: N

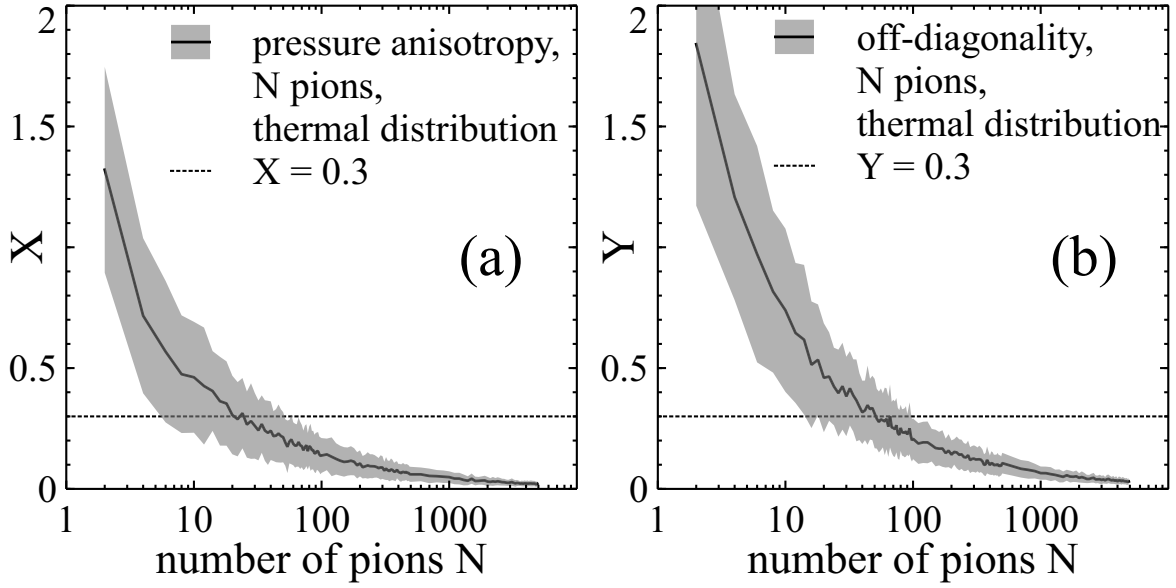


Figure 3.1.: Pressure anisotropy X (panel a) and off-diagonality Y (panel b) of $T^{\mu\nu}$ for particles sampled according to thermal distributions. The effect of statistics on the deviation of energy-momentum tensor from the ideal fluid one is demonstrated.

pions are generated, their momenta being sampled from a thermal distribution with an ad-hoc temperature of $T = 0.2$ GeV, then $\sum \frac{p^\mu p^\mu}{p_0}$ is computed, pressure isotropy X and off-diagonality Y of the energy-momentum tensor from Eq. (2.56) are calculated. The number of pions N was varied and X and Y are plotted versus N . The results can be seen in Fig. 3.1. For every point the simulation was repeated 100 times and the standard deviation is displayed as an error. For the thermal distribution $X = Y = 0$ in the limit of $N \rightarrow \infty$, so Fig. 3.1 demonstrates a pure effect of sampling a finite number of particles.

Fig. 3.1 can be used to specify the number of events needed to reach a good enough approximation to the "true" $T^{\mu\nu}$. For example, for $Y = 0.3$ as an acceptable level, the condition of Eqn. 3.4 becomes $N_{ev}\rho\sigma^3 > 100$. From Fig. 3.1 one can also see that the off-diagonality Y is more sensitive to statistics than the pressure isotropy X .

In the previous paragraph the effect of statistics itself was considered rather as an obstacle to get the physical "true" $T^{\mu\nu}$. However, recently event-by-event simulations gained popularity, where the initial state for hydrodynamics is intentionally constructed from a small number of events to include the fluctuations. Let us see, how the number of events influences deviations of $T^{\mu\nu}$ from the ideal form in heavy ion collisions. The $T^{\mu\nu}$ was computed locally on every point of the grid, and as a

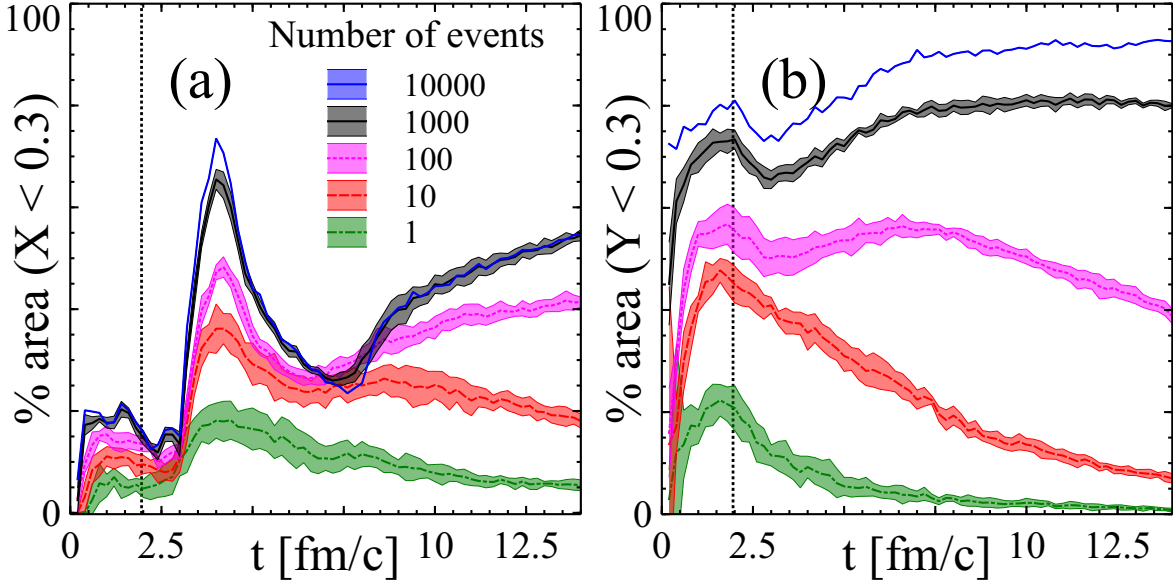


Figure 3.2.: Event plane area percentage, where the pressure isotropy X (panel a) or off-diagonality Y (panel b) does not exceed 0.3 versus time for different number of events N_{ev} used to construct $T^{\mu\nu}$. Number of events $N_{ev} = 1$ corresponds to the event-by-event case. The dotted line marks the geometrical overlap time.

general characteristic the percentage of the event-plane area is chosen, where $X < 0.3$ ($Y < 0.3$). To define the total area numerically, only grid cells, where pressure $p > 10^{-4} \text{ GeV}/\text{fm}^3$ are taken into account. For this example Au+Au collisions at $E = 80A \text{ GeV}$ with the impact parameter $b = 6 \text{ fm}$ are considered. The smearing parameter σ is 0.8 fm. Results are depicted in Fig. 3.2.

One can see that for this given σ 1000 events are enough for X to saturate, so the line for $N_{ev} = 1000$ represents results for the physical pressure isotropy, i.e. due to deviation of $f(\vec{r}, \vec{p})$ in the transport from equilibrium. For Y at $N_{ev} = 10000$ almost all the event area has small off-diagonality, which means that the physical off-diagonality is small. For event-by-event simulations deviations of $T^{\mu\nu}$ from ideal fluid are dominated by statistical effects.

In addition to the effect of statistics the effect of other nuisance parameters was investigated, i.e. the grid spacing and the Gaussian smearing. According to Fig. 3.3, the grid spacing does not influence the results, if taken sufficiently small. This is expected, because the grid does not participate in the simulation or in the calculation of $T^{\mu\nu}$, it only determines the resolution of the $T^{\mu\nu}$ output. The only effect of the grid spacing is on the precision of the area calculation by counting cells, here the resolution

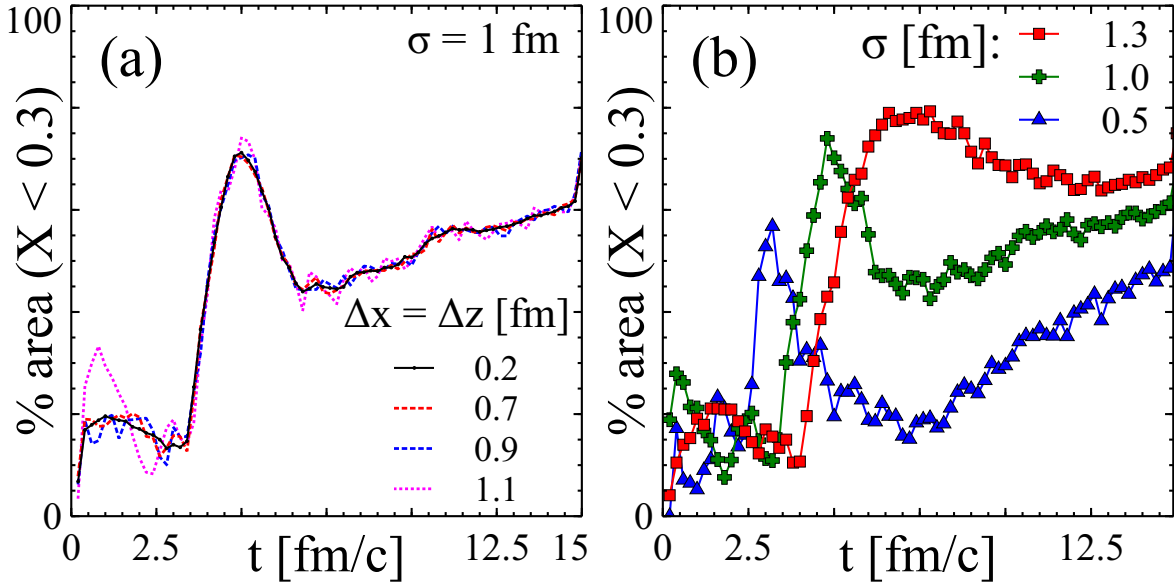


Figure 3.3.: Event plane area percentage, where pressure isotropy X does not exceed 0.3. Au+Au versus time. $E = 80A \text{ GeV}$, centrality $b = 6 \text{ fm}$, number of events $N_{ev} = 1000$. Gaussian smearing σ (right) and grid spacing $\Delta x = \Delta z$ (left) are varied to study sensitivity of results to them.

of the output matters. At early times, it makes some difference, because the total area is small. That is why in the following $\Delta x = \Delta z = 0.6 \text{ fm}$ was chosen. At the same time the Gaussian width σ influences the results very significantly, as it can be seen from Fig. 3.3. The effect of σ is twofold: on the one hand a larger σ means effective increase of statistics. On the other hand, if the pressure anisotropy is large at some space point due to physics, the Gaussian smearing will spread this asymmetry in a $1\text{--}2 \sigma$ radius.

To characterize the influence of σ in a simpler way, t_{iso} versus σ was plotted, where t_{iso} is the earliest time when at least 50% of the area have $X < 0.3$. Let us refer to this time as *isotropization time* as it is further described in the following Section. In Fig. 3.4 this dependence is displayed, the isotropization time is monotonously growing with σ and is approaching the geometrical time for $\sigma \rightarrow 0$. Taking the limit $\sigma \rightarrow 0$ is computationally challenging, because one has to increase statistics as σ^{-3} , as shown previously. Instead a reasonable value $\sigma = 0.8 \text{ fm}$ was chosen and systematic errors were assigned to our results, corresponding to changing σ in the range $(0.6 - 1.0) \text{ fm}$. Another justification for this treatment is that none of the existing models attempts to consider the "physical" limit of $\sigma \rightarrow 0$, $N_{ev}\rho\sigma^3 \rightarrow \infty$, all the models use some fixed width instead.

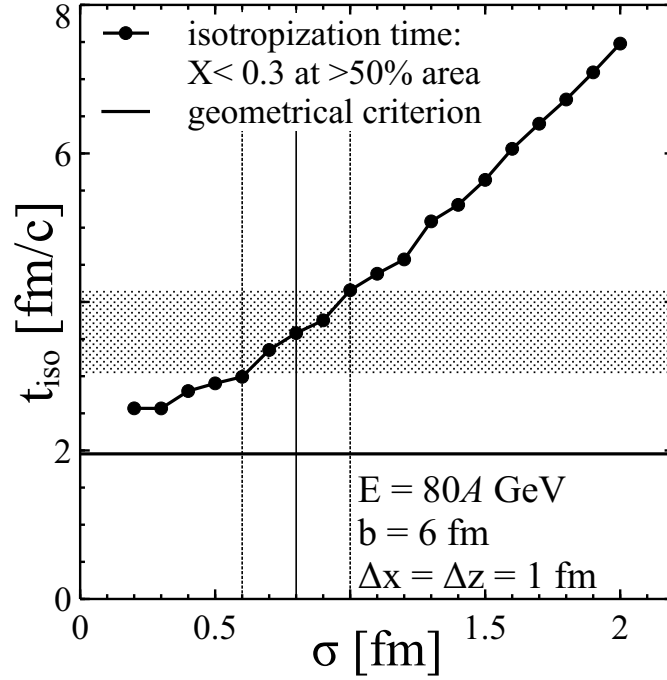


Figure 3.4.: Isotropization time (such time that more than 50% of event plane area have pressure isotropy $X < 0.3$) versus σ .

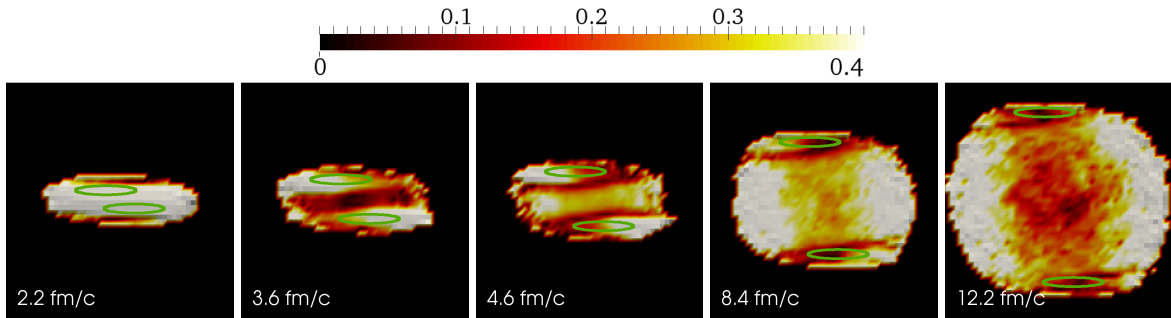


Figure 3.5.: Space-time evolution of the pressure anisotropy $X = \frac{|T_L^{11} - T_L^{22}| + |T_L^{22} - T_L^{33}| + |T_L^{33} - T_L^{11}|}{T_L^{11} + T_L^{22} + T_L^{33}}$ (see color scale above the Fig.) for collision energy $E_{\text{lab}} = 80 A \text{ GeV}$ and impact parameter $b = 6 \text{ fm}$. If the value of X exceeds color map maximum, it is marked with the same color as maximum. Solid lines mark the positions of the nuclei, if they would not interact.

3.3. Results

While in the previous section the effects of nuisance parameters on the energy-momentum tensor generated from particles were studied, here the dependence on physical parameters is considered, namely collision energy and centrality. All the

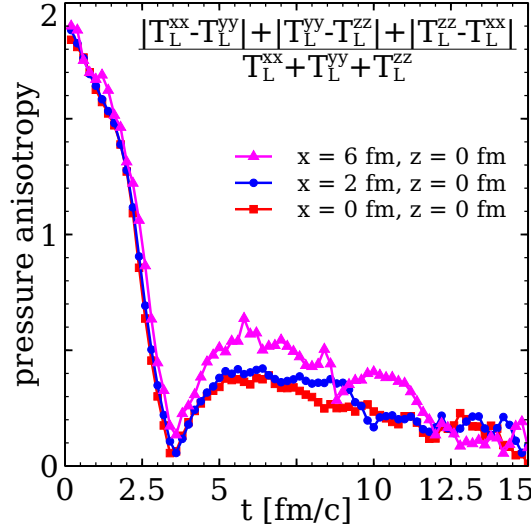


Figure 3.6.: Example for the behaviour of the pressure anisotropy versus time in Au+Au collisions at $E_{\text{lab}} = 80$ A GeV and impact parameter $b = 6$ fm.

following figures are shown for grid spacing $\Delta x = \Delta z = 0.6$ fm, Gaussian smearing $\sigma = 0.8$ fm, and number of events $N_{ev} = 1000$. The smearing kernel is defined as in section 2.1.3.

3.3.1. Pressure anisotropy

The pressure anisotropy X satisfies the following properties: $X \leq 2$ for any tensor and $X = 0$, if and only if $T_L^{11} = T_L^{22} = T_L^{33}$ as it is for an ideal fluid. For viscous hydrodynamics it is necessary that $X \ll 1$. Here $X_{crit} = 0.3$ is considered as a limiting value, when viscous hydrodynamics is still applicable. Changing X_{crit} to 0.4 leaves one with qualitatively the same results and conclusions. Fig. 3.5 gives a qualitative impression of the space-time evolution of the pressure anisotropy. Even though the figure shows a particular energy of $E_{\text{lab}} = 80$ A GeV and centrality $b = 6$ fm, some features are universal for all energies and centralities that were considered:

- On the borders of the expanding system the anisotropy is always high, thus these regions are never consistent with viscous hydrodynamics.
- After some moment of time a relatively isotropized central region rapidly expands and never disappears completely during the time evolution

To make quantitative statements let us consider the evolution of the pressure anisotropy at several points along the x axis ($z = 0$) versus time. This is shown in

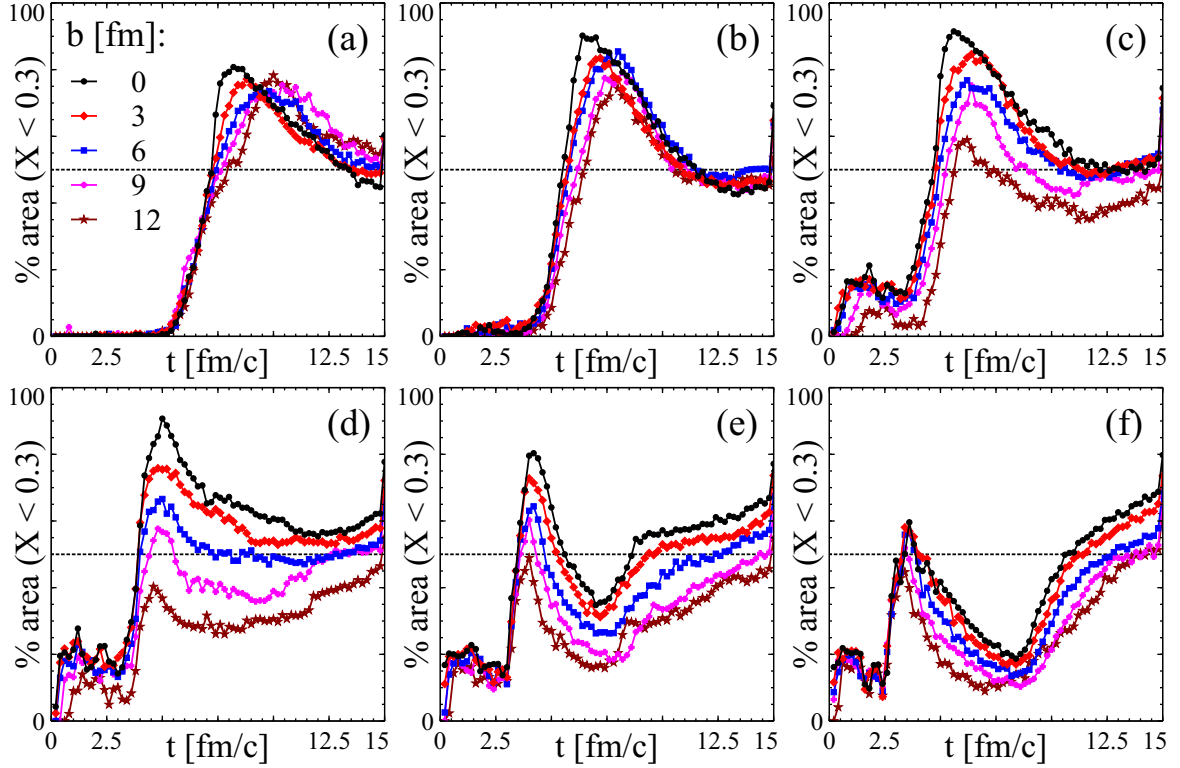


Figure 3.7.: Percentage of area in the event plane, where pressure anisotropy $X < 0.3$, for Au+Au collision energies $E_{\text{lab}} = 5, 10, 20, 40, 80, 160$ A GeV (panels (a) - (f) correspondingly).

Fig. 3.6. One can see that in the beginning the anisotropy is almost maximal, then it rapidly decreases and never rises too much again. As shown in the previous section, $N_{ev} = 1000$ is enough to suppress the anisotropy due to statistics, so the behaviour of X in Fig. 3.6 is dominated by physics. However, the impact of statistical fluctuations can be observed already at $t > 5$ fm/c: X starts to fluctuate in space and time. One can see this both in Fig. 3.5 at later times and in Fig. 3.6.

After looking at the space-time evolution of the anisotropy in 2D as in Fig. 3.5 for different energies, one gets the impression that there is a special moment t_{iso} for each energy and centrality, before which pressures are highly anisotropic in the whole event plane and after which there emerges a considerable isotropic region. To quantify this feeling let us consider the ratio of the area, where $X < 0.3$ to the total area versus time. From Fig. 3.7 one can see that there is indeed a steep rise of the isotropized area at some point in time for every considered energy and centrality. Let us define the *isotropization time* t_{iso} such that more than 50% of the area has $X < 0.3$ at $t = t_{iso}$. The behaviour of this isotropization time versus energy and centrality is compared to the

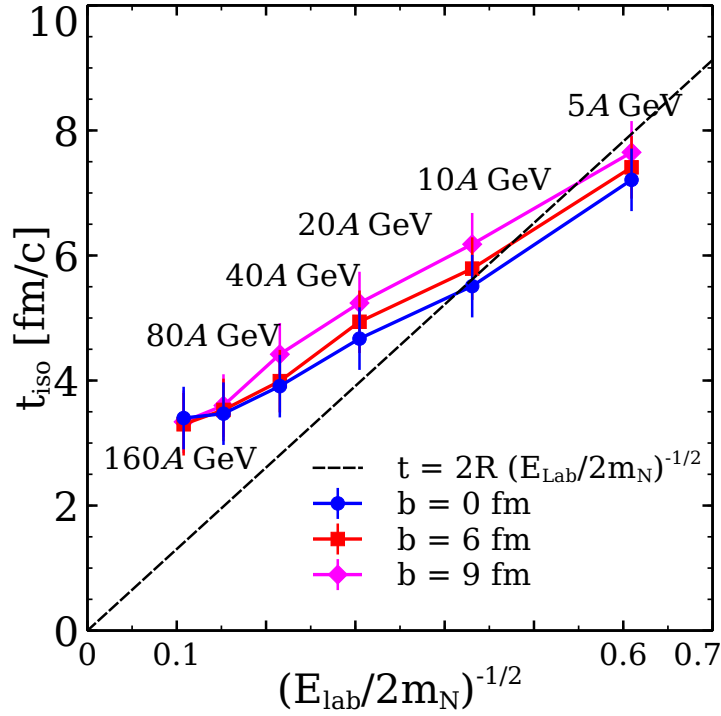


Figure 3.8.: Isotropization time t_{iso} (see definition in the text) versus energy and centrality.

geometrical criterion in Fig. 3.8. One can see that the isotropization time decreases with energy, but remains larger than the geometrical criterion for all energies except 5 A GeV. It is interesting to note that the isotropization time differs with centrality: for larger impact parameters b it slightly increases. One might assume that this has a pure geometrical reason: $t_0 = 0$ is chosen in UrQMD as a moment when nuclei touch each other in a central collision. However, for peripheral collisions the nuclei will only touch at $t_0(b) = \frac{R}{\gamma v} (1 - \sqrt{1 - (b/2R)^2})$. In Fig. 3.9 one can see that this naive expectation yields the right trend: t_{iso} rises with centrality and the rise is smaller for higher energies. However, quantitatively it overestimates t_{iso} for large impact parameters.

Let us compare the above findings to the study by Bravina et al. [240], where one central cell of $(5 \times 5 \times 5) \text{ fm}^3$ was chosen to study the pressure anisotropy of the energy-momentum tensor in Au+Au collisions. An isotropization time was defined, and it did not change significantly after zooming into the central cell to $(1 \times 1 \times 1) \text{ fm}^3$. This allowed for the conclusion that isotropization happens rapidly in a large volume. The isotropization time determined in this study also decreases with collision energy. All of these results are confirmed in the present study. However, our isotropization

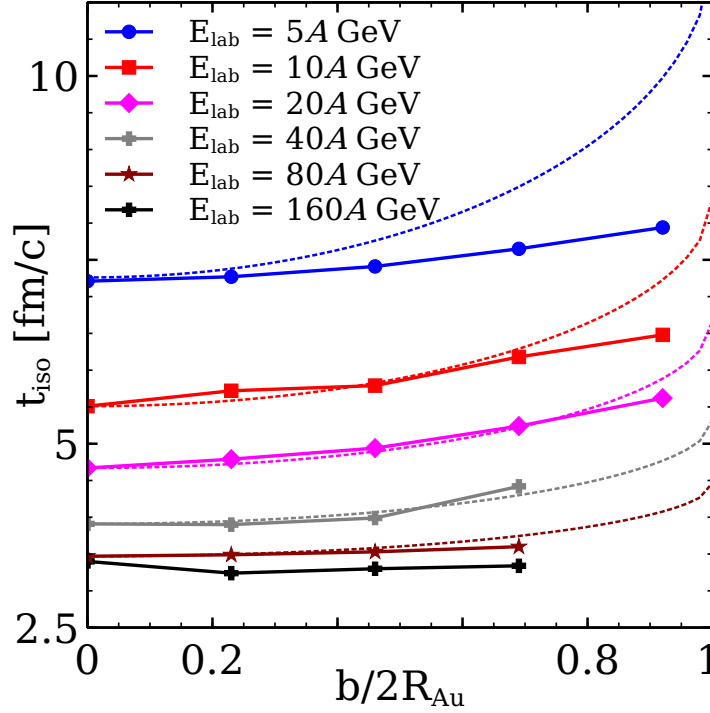


Figure 3.9.: Isotropization time t_{iso} (see definition in the text) versus centrality. The dotted lines represent the naive expectation from the collision geometry: $t_{iso}(b) = t_{iso}(b=0) + \frac{R}{\gamma v} (1 - \sqrt{1 - (b/2R)^2})$.

times are smaller than the ones obtained by Bravina et al. There are two possible reasons for that. First, the criterion for isotropization used here is less strict: while here at least 50% of event plane area to have $X < 0.3$ is required, the central cell study demands $p_z/p_x - 1 < 0.1$ in the whole cell, which corresponds to $X < 0.065$. Secondly, here only the deviation of the energy-momentum tensor from equilibrium is considered, but in the study [240] also deviations of hadron multiplicities from equilibrium are taken into account.

3.3.2. Off-diagonality of $T^{\mu\nu}$ in the local rest frame

The off-diagonality $Y = \frac{3(|T_L^{12}| + |T_L^{23}| + |T_L^{13}|)}{T_L^{11} + T_L^{22} + T_L^{33}}$ characterizes the size of the off-diagonal components of the stress tensor compared to the pressure. In ideal hydrodynamics $Y = 0$. For the applicability of viscous hydrodynamics it is necessary that $Y \ll 1$. Here $Y_{crit} = 0.3$ is considered as a value, after which viscous hydrodynamics is hardly applicable. An example for the space-time evolution of Y is given in Fig. 3.10. From this Fig. it can be seen that in the central region Y is always small. On the boundaries

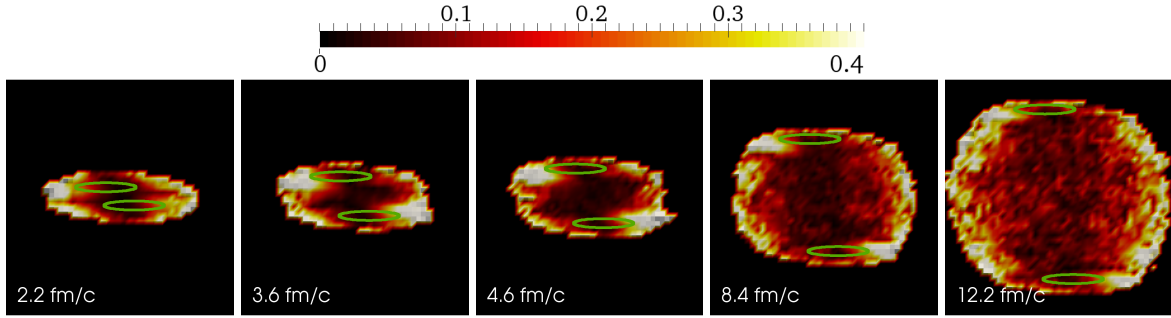


Figure 3.10.: Space-time evolution of the off-diagonality $Y = \frac{3(|T_L^{12}|+|T_L^{23}|+|T_L^{13}|)}{T_L^{11}+T_L^{22}+T_L^{33}}$ (see color scale above the Fig.) for collision energy $E_{\text{lab}} = 80 A \text{ GeV}$ and impact parameter $b = 6 \text{ fm}$. If the value of Y exceeds color map maximum, it is marked with the same color as maximum. Solid lines mark the positions of the nuclei, if they would not interact.

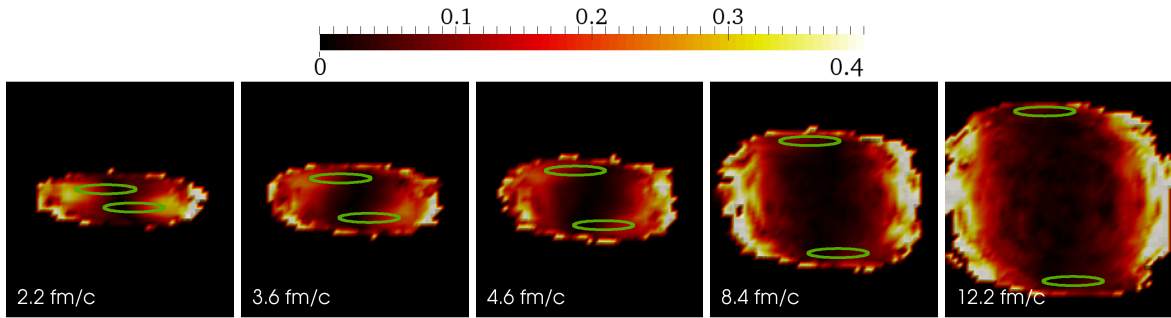


Figure 3.11.: Space-time evolution of relative velocity between Landau and Eckart frames $v_{LE} = \sqrt{(j_L^1)^2 + (j_L^2)^2 + (j_L^3)^2} / j_L^0$ (see color scale above the Fig.) for collision energy in lab frame $E = 80A \text{ GeV}$, centrality $b = 6 \text{ fm}$. If the value of v_{LE} exceeds color map maximum, it is marked with the same color as maximum. Solid lines mark the positions of the nuclei, if they wouldn't interact.

Y is typically large due to statistical effects. A quantitative study similar to the study of the pressure isotropy X shows that for all considered energies and centralities more than 80% of the event plane area have $Y < 0.3$ for the whole time of the evolution.

3.3.3. Relative velocity between Landau and Eckart frames

The relative velocity between Landau and Eckart frames for the baryon charge v_{LE} is shown in Fig. 3.11. At high enough statistics the relative velocity between Eckart and Landau frames is not an important factor. It is significant only on the borders of the system, where the density is small and statistical effects play a role. But in all the rest of the volume, for all the considered time evolution it remains small.

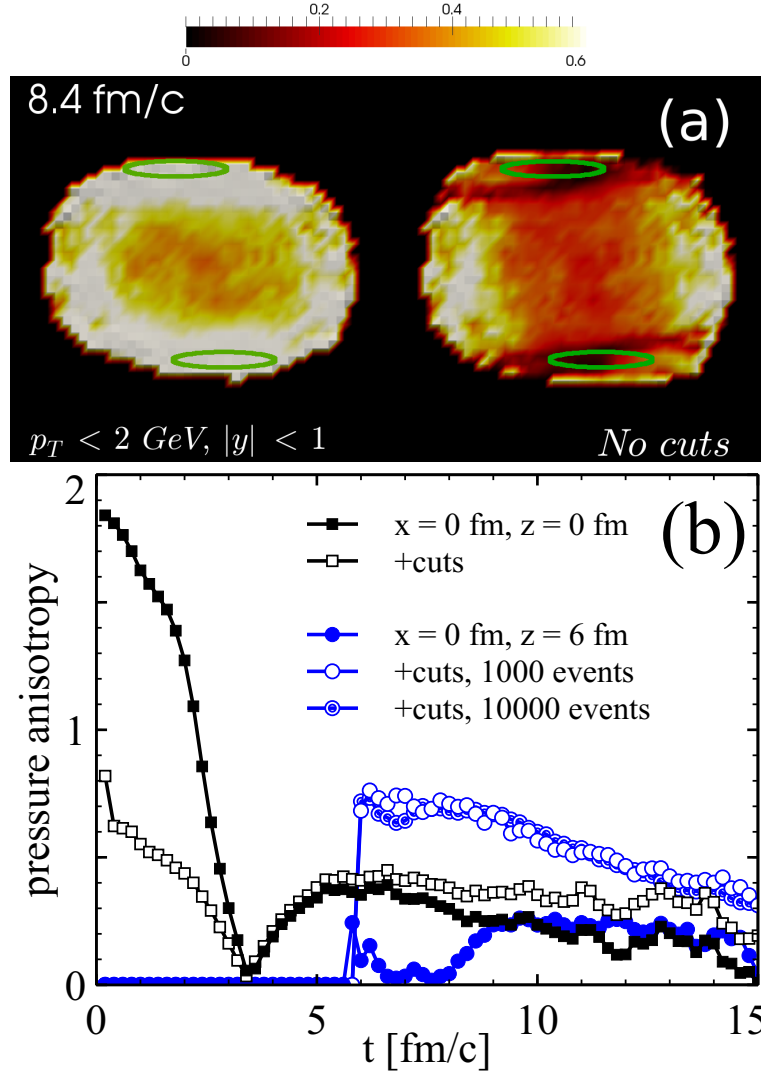


Figure 3.12.: The effect of $p_T < 2 \text{ GeV}$ and $|y| < 1$ cuts on the space distribution of the pressure anisotropy $X = \frac{|T_L^{11} - T_L^{22}| + |T_L^{22} - T_L^{33}| + |T_L^{33} - T_L^{11}|}{T_L^{11} + T_L^{22} + T_L^{33}}$ (see color scale above the Fig.) for collision energy $E_{\text{lab}} = 80 A \text{ GeV}$ and impact parameter $b = 6 \text{ fm}$. If the value of X exceeds color map maximum, it is marked with the same color as maximum. Solid lines mark the positions of the nuclei, if they would not interact.

3.3.4. The effect of momentum-space cuts

Previously, all participants were included into the $T^{\mu\nu}$ calculation. However, it is generally believed that soft particles at midrapidity thermalize faster, therefore it might be insightful to impose cuts in momentum space, if one wants to obtain a more isotropic $T^{\mu\nu}$. On the other hand, applying transverse momentum p_T and rapidity y cuts on a perfectly symmetric distribution results in an asymmetry. In addition, these

cuts decrease the statistics, which leads to an increase of the anisotropy. To study the effect of the kinematic cuts on the space distribution of the pressure anisotropy X , $T^{\mu\nu}$ was constructed only from particles with $p_T < 2 \text{ GeV}$ and $|y| < 1$. The effect of cuts on X over space is shown in Fig. 3.12. The statistical effect does not play a significant role, because the results do not change after increasing the number of events from $N_{ev} = 10^3$ to 10^4 . The large anisotropy at very early times decreases after imposing cuts. But the anisotropy at later times is strikingly larger with cuts, first of all in the regions behind the nuclei. While without cuts it was possible to introduce an "isotropization time", when X is smaller than 0.3 at more than 50% of the area, with the cuts the anisotropy is so high all over the space that the isotropization time cannot be introduced anymore.

3.4. Summary and discussion

The assumption of rapid equilibration was tested at $E_{\text{lab}} = 5\text{--}160 A \text{ GeV}$ using the coarse-grained UrQMD transport approach. The energy-momentum tensor was studied locally in space and time and its deviation from the ideal fluid form was quantified with two numbers: the pressure anisotropy X and the off-diagonality Y . First of all, it was shown that X and Y depend on the number of UrQMD events N_{ev} used to construct $T^{\mu\nu}$. Low statistics implies large deviations, even if the underlying distribution function is completely thermal and isotropic. An initial state constructed from less than a few hundred events (or a few hundred testparticles equivalently) is bound to deviate strongly from the ideal fluid form. The off-diagonality appears to be mostly produced by this statistics effect. For large statistics Y tends to be small in all the collision region at all times. The pressure anisotropy does not vanish with large statistics, it is a physical effect related to the anisotropy of the underlying distribution function $f(\vec{r}, \vec{p})$. As a consequence, the initial state from UrQMD with enough statistics is suitable for anisotropic hydrodynamics.

Unfortunately, all the results depend on the smearing parameter σ . With larger σ isotropization is reached later, but the degree of isotropization is higher. From a practical point of view that means that selecting large σ one has to take larger fluidization time. This is in agreement with conclusion of [254] that a larger fluidization time should be taken for larger σ to obtain the same pion yield. However, strictly speaking, the physical limit is $\sigma \rightarrow 0$, $\sigma^3 \rho N_{ev} \rightarrow \infty$. It was found that at small σ the isotropization time approaches the time of geometrical criterion $t_{geom} = 2R(E_{\text{lab}}/2m_N)^{-1/2}$, so the rapid isotropization at the time of geometrical overlap is partly justified, but only

in the above mentioned limit. In the existing models the smearing parameters and statistics are such that at t_{geom} the anisotropies are very high.

For the pressure anisotropy X it was observed, that it exhibits a similar pattern for all the considered collision energies and centralities: there is a narrow interval of time, when it rapidly drops in a considerable volume. This feature allowed us to introduce and study the isotropization time t_{iso} . The time t_{iso} can be considered as the time, when UrQMD starts to be compatible with viscous hydrodynamics. At $t < t_{\text{iso}}$ the pressure anisotropy X is too high for viscous hydrodynamics to be applied. Isotropization time decreases with collision energy, following the same trend as the geometrical overlap time. Based on this finding a new fluidization criterion is suggested: $t_{\text{iso}} = t_{\text{geom}}(E) + \Delta t_0(\sigma)$, where Δt_0 depends only on the Gaussian smearing σ and can be determined from Fig. 3.4. A slight dependence of the isotropization time on centrality was observed: it increases with impact parameter, but the slope of this increase becomes smaller and smaller for higher energies. This behaviour has a simple geometrical interpretation.

Chapter 4.

Cooper-Frye contributions in Au+Au collisions at $E_{\text{lab}} = 5\text{--}160 A \text{ GeV}$

In most heavy ion collision simulations involving relativistic hydrodynamics, the Cooper-Frye formula (see section 2.3) is applied to transform the hydrodynamical fields to particles. As it was discussed in section 2.3, under certain circumstances Cooper-Frye formula can produce negative numbers of particles, the so-called negative contributions. Here the magnitude of negative contributions is investigated as a function of the hadron mass, collision energy in the range of $E_{\text{lab}} = 5\text{--}160 A \text{ GeV}$, collision centrality and the energy density transition criterion defining the particlization hypersurface. The microscopic results are compared to negative contributions expected from hydrodynamical treatment assuming local thermal equilibrium. This chapter is based on publication [1].

4.1. Methodology

The calculation is based on the hadronic transport approach - Ultra-relativistic Quantum Molecular Dynamics (UrQMD 3.3p2) [197,253], already introduced in chapter 3. In this study no long-range potentials are included and particle trajectories between collisions are always straight lines. Au + Au collisions are simulated with UrQMD at laboratory frame energies $E_{\text{lab}} = 5, 10, 20, 40, 80$ and $160 A \text{ GeV}$. This energy region is chosen because UrQMD provides a reasonable description of the collision dynamics at those energies, and the Cooper-Frye negative contributions are expected to become significant in this energy range.

The general procedure for our calculations is:

1. Generate many UrQMD events and coarse-grain them on a 3+1D Cartesian space-time grid. The energy-momentum tensor $T^{\mu\nu}$ and baryon four-current j_B^μ are computed as described in the section 2.1. The grid cell sizes need to be small enough, so that gradients of all relevant physical quantities within the cell are small. On the other hand, if the cell sizes are too small one needs to generate infeasibly many events to damp statistical fluctuations of the $T^{\mu\nu}$ components from cell to cell, and obtain a smooth surface Σ . To satisfy these conditions and to ensure energy conservation precisely we choose $\Delta x = \Delta y = 1 \text{ fm}$, $\Delta z = 0.3 \text{ fm}$ and time step $\Delta t = 0.1 \text{ fm}$. For the highest collision energy, $E_{\text{lab}} = 160A \text{ GeV}$, the gradients are larger, so even smaller grid sizes were taken: $\Delta x = \Delta y = 0.3 \text{ fm}$ and $\Delta z = 0.1 \text{ fm}$. This choice is further discussed in the section 4.2, where the sensitivity of results to the grid size is studied. As discussed further in the section 4.2 $N = 1500$ events are enough to obtain stable results.
2. Find the local energy density in the Landau rest frame of each grid cell, $\epsilon_{\text{LRF}}(t, x, y, z)$, and the collective flow velocity in each cell, $\vec{v}(t, x, y, z)$ as described in section 2.2, according to Eq. (2.37). To apply the Cooper-Frye formula one needs the temperature T and chemical potentials, which do not exist in the microscopic picture. Strictly speaking they make sense only in the vicinity of thermal and chemical equilibrium, which may not be the case in our UrQMD simulation. Nevertheless, the Landau rest frame energy density and net baryon density obtained from UrQMD are substituted to the ideal hadron resonance gas equation of state (Eqs. 2.58-2.60) to obtain T and chemical potentials, as in the case when deviations from equilibrium are small. The particle list in the equation of state coincides with the list of particles in UrQMD. Zero strangeness density is assumed, even if UrQMD itself allows local non-zero strangeness.
3. Construct the hypersurface Σ of a constant energy density $\epsilon_{\text{LRF}}(t, x, y, z) = \epsilon_c$. In this way the transition surface in hybrid models is mimicked, which is typically constructed at energy densities $\epsilon_c = 0.3\text{--}1 \text{ GeV}/\text{fm}^3$ [230]. The isosurface is constructed using the Cornelius subroutine [230], that provides a continuous surface without holes and avoids double counting of hypersurface pieces. The subroutine provides the normal four-vectors $d\sigma_\mu$ of the hypersurface. The physical quantities on the grid, *i.e.*, the energy, net baryon density and the flow velocity, are linearly interpolated to the geometrical centers of the hypersurface elements.

4. Calculate the particle spectra on Σ by using the Cooper-Frye formula and by counting the actual UrQMD particles that cross Σ . To obtain these spectra and to compare them to each other is the goal of the computation.

This procedure mimics switching from hydrodynamics to transport in a hybrid model, but here the "hydrodynamical" picture is obtained by averaging over particle distributions on a space-time grid. Since all the information is still available in the underlying microscopic approach, it was possible to compare the negative Cooper-Frye contributions to the spectrum of actual backscattered particles.

Cooper-Frye formula is applied on the hypersurface. The spectrum from the Cooper-Frye formula is split into positive and negative parts:

$$\frac{dN_{CF}^+}{p_T dp_T d\varphi dy} = \frac{g}{(2\pi)^3} \int_{\sigma} \frac{\Theta(p^\mu d\sigma_\mu) p^\mu d\sigma_\mu}{e^{(p^\nu u_\nu - \mu)/T} \pm 1} \quad (4.1)$$

$$\frac{dN_{CF}^-}{p_T dp_T d\varphi dy} = \frac{-g}{(2\pi)^3} \int_{\sigma} \frac{\Theta(-p^\mu d\sigma_\mu) p^\mu d\sigma_\mu}{e^{(p^\nu u_\nu - \mu)/T} \pm 1} \quad (4.2)$$

To evaluate dN/dy or $dN/p_T dp_T$ the integrations are performed numerically, applying the 36×36 points Gauss-Legendre method to integrals transformed to finite limits.

For comparison with the Cooper-Frye calculation we count the actual microscopic particles crossing the same hypersurface Σ that is used for Cooper-Frye calculations. Inward and outward crossings are counted separately. Note that $\epsilon > \epsilon_c$ inside the surface and $\epsilon < \epsilon_c$ outside of it. This is used to find where a particle trajectory crosses Σ : the energy density is interpolated to the particle trajectory to find the point where $\epsilon - \epsilon_c$ changes sign. Each crossing of Σ is counted as positive, if the particle streams outward and negative, if the particle flies toward higher energy densities.

Both the Cooper-Frye calculation and the particle counting start at the same time t_{start} , which depends on the collision energy. Following the prescription from hybrid models, $t_{\text{start}} = \frac{2R}{v\gamma}$ is taken. This is the time two nuclei need to pass through each other. Numerical values are shown in Tab. 4.1. The same t_{start} is used for all centralities.

E_{lab}, A GeV	$t_{\text{start}}, \text{fm}/c$
5	8.0
10	5.6
20	4.0
40	2.8
80	2.0
160	1.4

Table 4.1.: The geometrical overlap time t_{start} versus collision energy E_{lab} . Both the Cooper-Frye calculation and the particle counting start at the time $t_{\text{start}} = \frac{2R}{v\gamma}$.

4.2. Sensitivity to internal parameters and fulfillment of conservation laws

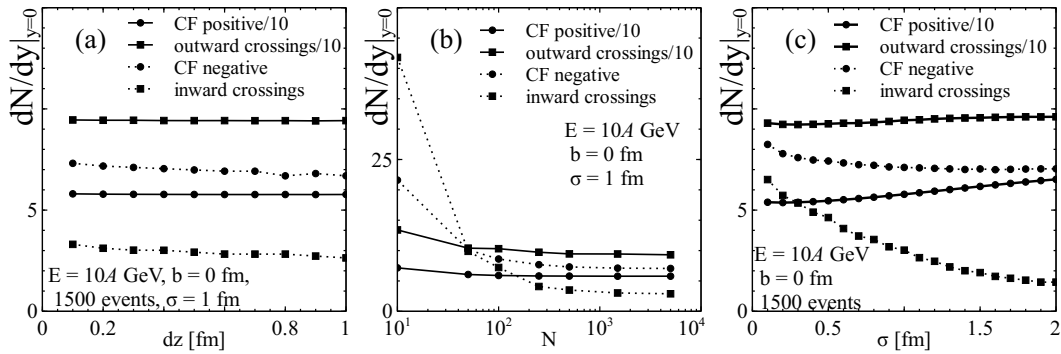


Figure 4.1.: Sensitivity of results to internal parameters of the simulation: grid spacing along z axis, dz (a), number of events, N (b) and the width σ of Gaussian smearing (c).

Besides physical parameters like the beam energy, E_{lab} , and centrality of the collision controlled by the impact parameter b , our simulation contains internal parameters like grid spacing, the width of the smearing Gaussian σ , and the number of events N . Ideally, one should work in a region of internal parameters, where the results are independent of them. To see how sensitive our results are to these internal parameters, the positive and negative contributions to the pion yield at midrapidity, $\frac{dN}{dy}|_{y=0}$, at different values of these parameters are evaluated.

The calculation is more sensitive to the grid spacing in z direction, dz , than to the spacings in x and y directions, dx and dy , since gradients of $T^{\mu\nu}$ are largest in the longitudinal direction. Although, as shown in Fig. 4.1 a), even the sensitivity to dz

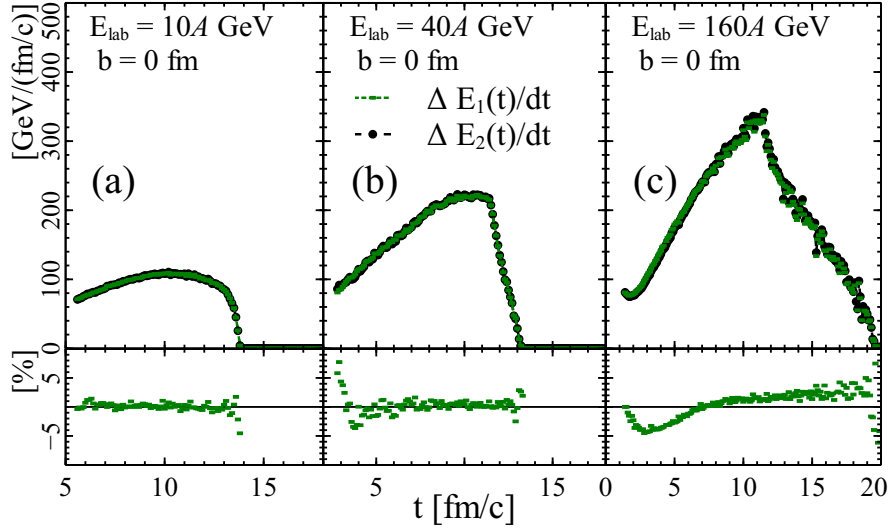


Figure 4.2.: Energy flux through the surface at different times evaluated as actual flow, $\Delta E_1(t)/dt = \int_{t-dt}^t T^{\mu 0} d\sigma_\mu/dt$ (circles), and as a difference in energy within the surface at different times, $\Delta E_2(t)/dt = (E_{in}(t) - E_{in}(t - dt))/dt$ (rectangles). Lower panel shows the relative difference between these two measures in %, and thus the conservation of energy in the calculation.

is weak over a reasonable range of values. The main motivation for choosing the grid spacing and time step comes in fact from the requirement of energy conservation discussed later.

The results are very sensitive to the small number of events (see Fig. 4.1 b), but already $N = 500$ events provides sufficient statistics for stable results. To be on the safe side, we have analyzed $N = 1500$ events for our final results. Unfortunately, our results are not completely independent of the width σ of the Gaussian smearing, as shown in Fig. 4.1 c). The number of inward crossing UrQMD pions is most sensitive to σ . Two effects play a role here: for small σ the surface still has large statistical fluctuations and small scale structures, “lumps” (See Fig. 2 of Ref [226]), whereas at large σ the smearing pushes transition surface further out in space. Further out the densities are smaller, and the UrQMD particle distributions are further away from equilibrium so that especially the number of particles moving toward the center is strongly reduced. We choose $\sigma = 1$ fm as a reasonable value for our calculations, but keep in mind that varying σ in the range from 0.6 fm to 1.4 fm causes $\sim 20\%$ difference in the number of inward crossings. We consider this a systematic error in our analysis, but fortunately this uncertainty does not affect our main conclusions.

To check that energy is conserved in the coarse-graining procedure, we evaluate the energy flow through the surface during the time step dt , $\Delta E_1(t) = \int_{t-dt}^t T^{\mu 0} d\sigma_\mu$, and compare it to the change in energy within the surface during the same time step, $\Delta E_2(t) = E_{\text{in}}(t) - E_{\text{in}}(t - dt)$, where E_{in} is total energy of particles inside the surface. Ideally $\Delta E_1(t) = \Delta E_2(t)$ for any dt , but finite cell sizes limit the precision and break the conservation of energy. The accuracy of $\Delta E_1 \approx \Delta E_2$ improves when grid spacing and time step are decreased. Fig. 4.2 shows the energy flux through the surface and the relative difference between $\Delta E_1(t)$ and $\Delta E_2(t)$ in central collisions at energies $E_{\text{lab}} = 10, 40, 160A \text{ GeV}$. To achieve better than 5% percent accuracy at all times, small grid spacing is used with $\Delta x = \Delta y = 1 \text{ fm}$, $\Delta z = 0.3 \text{ fm}$, and time step $\Delta t = 0.1 \text{ fm}/c$ in collisions with $E_{\text{lab}} \leq 80A \text{ GeV}$, and an even finer grid with $\Delta x = \Delta y = 0.3 \text{ fm}$, and $\Delta z = 0.1 \text{ fm}$ for collisions at $E_{\text{lab}} = 160A \text{ GeV}$. When integrated over the whole collision time, the violation of energy conservation is less than 1% at all collision energies. A similar check was performed for the net baryon charge, and similar results were obtained.

4.3. Magnitude of negative Cooper-Frye contributions estimated from the coarse-grained transport approach

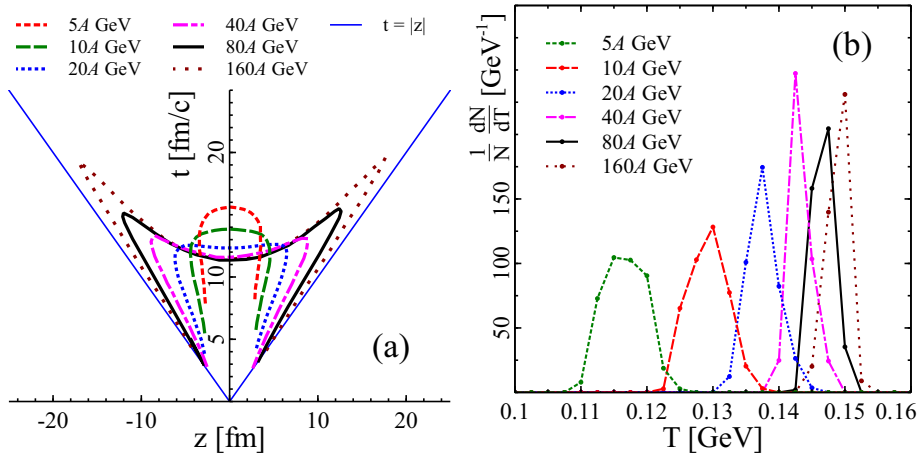


Figure 4.3.: Upper panel: Hypersurface of constant LRF energy density $\epsilon(t, 0, 0, z) = \epsilon_c = 0.3 \text{ GeV}/\text{fm}^3$. Lower panel: The fraction of hypersurface elements with (apparent) temperature T in central Au+Au collisions at the collision energy of $E_{\text{lab}} = 5, 10, 20, 40, 80, 160A \text{ GeV}$.

Let us start by investigating the properties of the transition hypersurface itself as a function of beam energy. Figure 4.3 depicts the surface Σ in longitudinal direction

along the x axis. One can see that with increasing energy, the lifetime of the system increases. This indicates longer lasting surface emission (from space-like parts of the surface), which might lead to larger negative contributions. On the other hand, with increasing energy the longitudinal expansion leads to a larger volume of the final volume emission (from time-like parts of the surface), which indicates smaller negative contributions. Thus there are two competing effects, and one has to carry out the actual calculation to find out how the negative contributions depend on energy.

Distributions of the (apparent) temperature of the hypersurface elements are shown on the right panel of Fig. 4.3. At each collision energy the temperature distribution is rather narrow, which means that the constant energy density surface approximately coincides with a constant temperature surface. As well, the average temperature increases with increasing collision energy as expected from thermal model fits to particle yields [143].

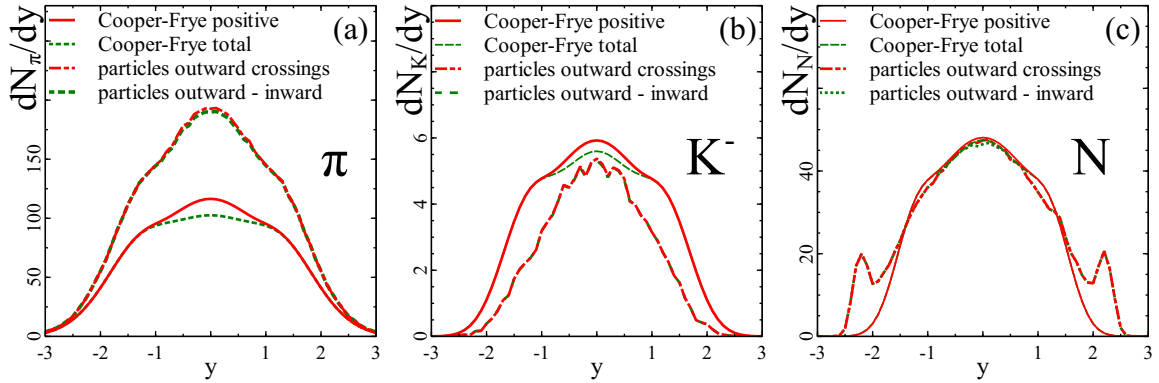


Figure 4.4.: Rapidity distribution of identified particles obtained from Cooper-Frye formula on the surface Σ and from explicit counting of particles that cross the same surface. Positive contributions and the net distribution, *i.e.*, positive-negative, are shown separately. Central Au+Au collisions at $E_{\text{lab}} = 40$ A GeV

Fig. 4.4 compares rapidity spectra of identified particles in Au+Au collisions at $E_{\text{lab}} = 40$ A GeV obtained by Cooper-Frye calculation and by counting of the microscopic particles. Even though, the results only for one collision energy are shown, all results are qualitatively the same at all other energies. If UrQMD is close to equilibrium on a surface at $\epsilon_c = 0.3$ GeV/fm³, both approaches should yield similar distributions. At midrapidity this is the case for nucleons, and with a lesser accuracy for kaons. Δ 's, Λ 's, ρ 's and η 's which are not shown in the figure depict a behavior similar to nucleons. However, the pion yields are wildly different indicating that pions are—and thus the entire system is—far away from chemical equilibrium at least. To cancel the effect

of non-equilibrium and to visualize the differences in momentum distributions we consider not the absolute value of the negative contributions, but the ratio of negative to positive ones, $(dN^-/dy)/(dN^+/dy)$ or $(dN^-/dp_T)/(dN^+/dp_T)$. From Fig. 4.4 it is also apparent that the magnitude of the negative contributions is always small compared to the positive ones as expected.

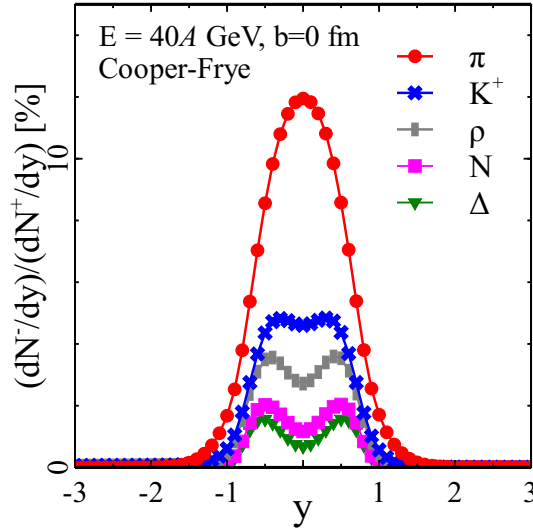


Figure 4.5.: Rapidity distribution of the ratio of negative to positive contributions for different hadron species: pions (circles), K^+ (crosses), ρ (bars), nucleons (rectangles), and deltas (triangles). Cooper-Frye calculation in central Au+Au collisions at $E_{\text{lab}} = 40A$ GeV.

The dependence of the ratio $(dN^-/dy)/(dN^+/dy)$ on the hadron type is illustrated in Fig. 4.5 by the Cooper-Frye results. Since for all cases, the microscopic negative contributions of backstreaming particles are much smaller than the Cooper-Frye ones we concentrate on showing the maximal effect. Surface temperature and velocity profiles are identical for all hadrons, so the plot demonstrates first of all the effect of particle mass. One can see that the average value of $(dN^-/dy)/(dN^+/dy)$ decreases with particle mass. This can be understood by considering a small volume of fluid in its rest frame, and a space-like surface moving through it with a velocity $0 < v_{\text{surf}} < c$ so that lower density, *i.e.*, outside, is in the negative direction. To be counted as a negative contribution, a particle must enter the fluid, and thus have a larger velocity than the surface. Average thermal velocity decreases with increasing mass, and therefore the heavier the particle, the fewer of them cross the surface inward. Since relative negative contributions for pions are several times larger than for other hadrons, in the following only pions will be considered.

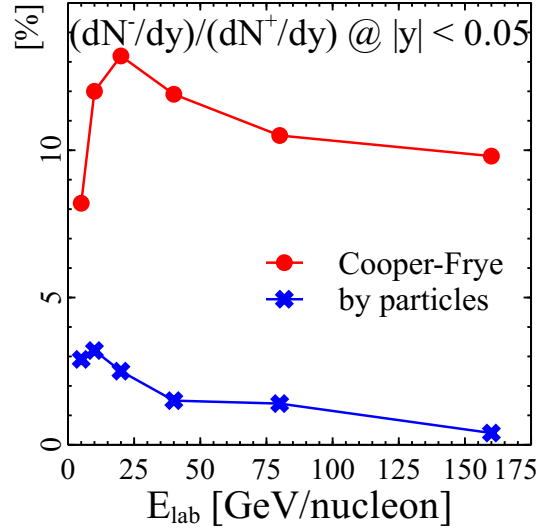


Figure 4.6.: The ratio of negative to positive contributions on the $\epsilon(t, x, y, z) = \epsilon_c = 0.3$ GeV/fm³ surface for pions at midrapidity in central Au+Au collisions at various collision energies. Circles depict Cooper-Frye result and rectangles the explicit counting of UrQMD particles.

As could be seen in Fig. 4.4, imposing equilibrium for Cooper-Frye calculation leads to significantly larger negative to positive contribution ratio at midrapidity than the counting of UrQMD particles. As shown in Fig. 4.6 this holds for all the considered energies, showing that the system is out of not only chemical, but also of kinetic equilibrium. Either the collective flow velocity of pions is different from the collective velocity of other particles [255, 256] or the dissipative corrections to pion distribution are very large. It was also checked that the relative microscopic negative contributions are much smaller in UrQMD at all centralities, for all particle species, and on isosurfaces of energy density $\epsilon_c = 0.3$ and 0.6 GeV/fm³.

On the other hand, the trend as a function of collision energy in Cooper-Frye and UrQMD calculations is the same: both curves have a maximum at 10-20A GeV and then decrease with increasing energy. This behavior is a result of a complicated interplay of several factors: temperature, relative velocities between surface and fluid, and relative amounts of volume and surface emission, *i.e.*, emission from the time- and space-like parts of the surface. To gain some insight all these factors are considered separately. The same argument used to explain the sensitivity of negative contributions to particle mass, explains why larger temperature leads to larger negative contributions. Temperature on the constant density surface grows with increasing collision energy (see Fig. 4.3), which would lead one to expect an increase of negative contributions

with increasing collision energy. On the other hand, larger relative velocity between the fluid and surface reduces the negative contributions (again the same argument), and one can see that the average relative velocity increases with increasing collision energy. Finally, as argued when discussing Fig. 4.3, the larger the collision energy, the larger the fraction of volume emission. Which, as mentioned, reduces the negative contributions.

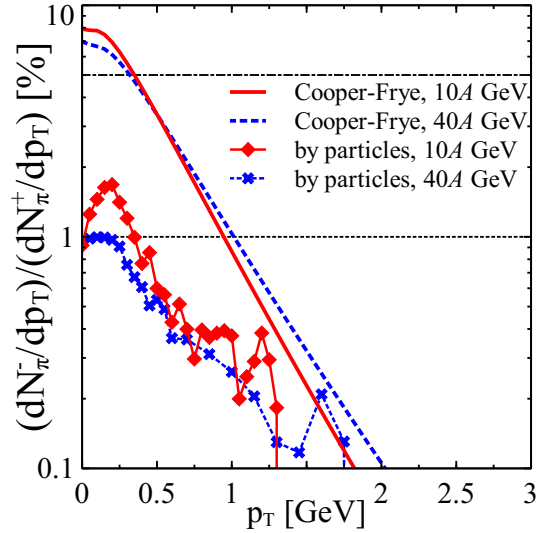


Figure 4.7.: The ratio of negative to positive pion contributions as a function of transverse momentum at midrapidity in central Au+Au collisions at $E_{\text{lab}} = 5, 10, 20, 40, 80 A \text{ GeV}$.

It is instructive to evaluate the negative contributions as function of transverse momentum p_T as well, as shown in Fig. 4.7 for Cooper-Frye calculation and "by particles". One can see that the largest negative contributions are located at small p_T , which means that one can reduce the uncertainty caused by the negative contributions by a low p_T cut. Also as a function of transverse momentum, the amount of microscopically backward streaming particles is much smaller than in an equilibrium scenario.

When discussing Fig. 4.6 it was mentioned that, independent of the energy density of the surface, the negative contributions are much smaller when counting the UrQMD particles. Furthermore, in Cooper-Frye calculations the strength of the negative contributions depends on the value of ϵ_c where the distributions are evaluated as shown in Fig. 4.8. Larger ϵ_c leads to larger negative contribution at midrapidity and lower at back- and forward rapidities. This result arises from interplay of two factors: larger temperature and smaller average v_{rel} for larger energy density. Quite surprisingly the negative contributions evaluated by counting the UrQMD particles is almost in-

dependent of the value of ϵ_c . This indicates that even in much higher temperature $T \sim 155\text{--}160 \text{ MeV}$ the microscopic system is not fully thermalised.

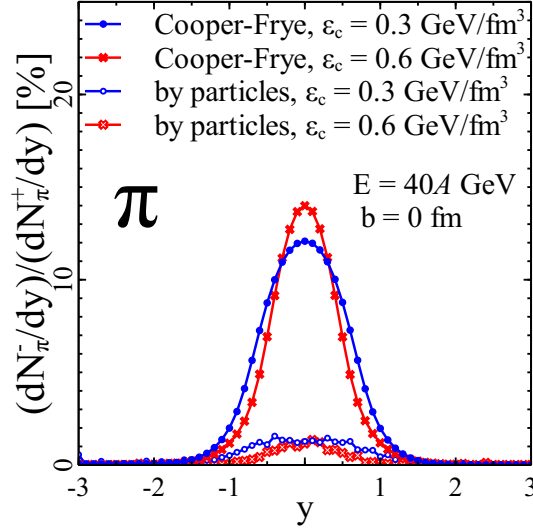


Figure 4.8.: Rapidity distribution of the ratio of negative to positive contributions for pions on $\epsilon(t, x, y, z) = \epsilon_c = 0.3 \text{ GeV}/\text{fm}^3$ (circles) and $\epsilon_c = 0.6 \text{ GeV}/\text{fm}^3$ (crosses) surfaces in central Au+Au collisions at $E_{\text{lab}} = 40 A \text{ GeV}$. Full symbols correspond to Cooper-Frye calculation and open symbols to explicit counting of UrQMD particles.

The dependence of the contribution ratio on centrality is shown in Fig. 4.9. The negative contributions decrease with decreasing centrality because the more peripheral the collision, the larger the fraction of time-like hypersurface elements. This behavior is illustrated in the right panel of Fig. 4.9. In the limit of very peripheral collisions the lifetime of the system becomes zero, and thus the surface is time-like everywhere and there are no negative contributions at all. Temperature and relative velocities appear to be less important factors in this case than the relative amount of time-like and space-like hypersurface elements.

Let us finally compare our results to previous studies. In [230] negative contributions were evaluated on the $\epsilon = 0.3 \text{ GeV}/\text{fm}^3$ transition surface of a hybrid model at SPS and RHIC energies— $E_{\text{lab}} = 160 A \text{ GeV}$ and $\sqrt{s_{\text{NN}}} = 200 \text{ GeV}$, respectively—and found to be around $(dN_{\pi^-}/dy)/(dN_{\pi^+}/dy) \simeq 13\%$ and 9% at $y = 0$. The negative contributions for $160 A \text{ GeV}$ are slightly larger than in our calculation. The reason for this discrepancy lies in the difference of the velocity profiles on the hypersurfaces: In hydrodynamics the average relative velocity between flow and surface is smaller than in our transport-based approach, which leads to larger negative contributions.

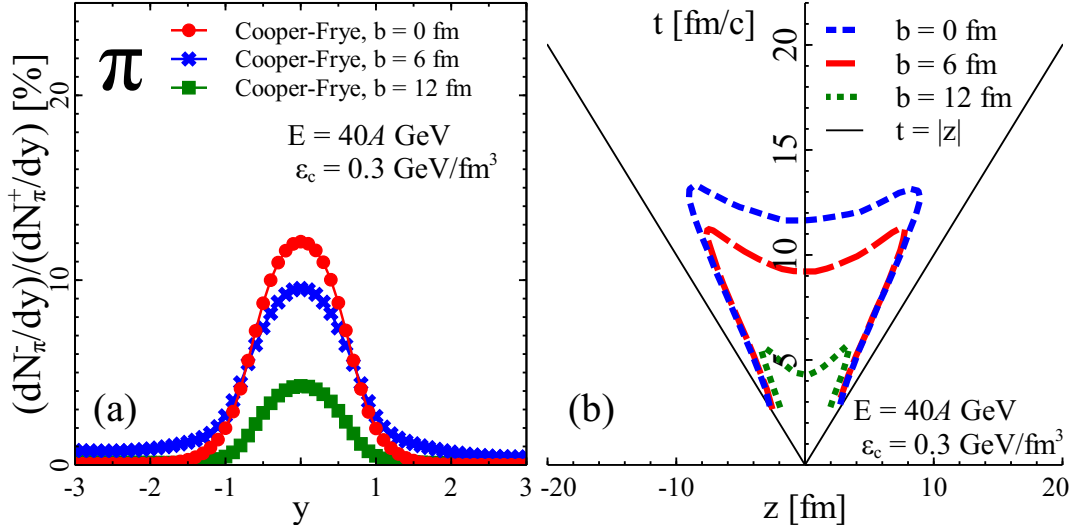


Figure 4.9.: Upper panel: Rapidity distribution of the ratio of negative to positive contributions for pions in Au+Au collisions at $E_{\text{lab}} = 40$ A GeV at various centralities: $b = 0$ (circles), $b = 6$ fm (crosses) and $b = 12$ fm (rectangles). Lower panel: hypersurfaces along the z axis in the same collisions at the same centralities.

4.4. Summary and discussion

The assumptions of hybrid and hydrodynamical approaches at the end of the hydrodynamical evolution lead to the appearance of Cooper-Frye negative contributions - negative numbers of particles produced by the Cooper-Frye formula at particlization on the hypersurface elements with a space-like normal. At high collision energies at midrapidity — the kinematic region probed by RHIC and LHC — the Cooper-Frye negative contributions are negligible. However, at intermediate energies they were not studied before.

Here negative Cooper-Frye contributions and backscattering were investigated using a coarse-grained transport approach. Au+Au collisions at $E_{\text{lab}} = 5\text{--}160$ A GeV energies have been simulated with UrQMD, and a hypersurface Σ of constant Landau rest frame energy density has been constructed. On this surface two quantities were computed: The ratio of Cooper-Frye negative to positive contributions, which assumes local thermal equilibrium, and the ratio of UrQMD particles crossing Σ inward to crossing Σ outward, which assumes no equilibrium.

It was found that at all collision energies the ratio of inward to outward moving particles calculated counting the UrQMD particles is much smaller than the same ratio calculated assuming equilibrium, *i.e.*, the Cooper-Frye negative to positive ratio. This

finding poses a question to the construction of hybrid models, and the treatment of freeze-out in hydrodynamical models: If the cascade leads to distributions nowhere near equilibrium, how are the hydrodynamical and cascade stages to be connected in a consistent fashion? On the other hand, this result shows that an ideal fluid dynamics hybrid approach contains the worst case scenario for negative contributions and even then they are on the order of max. 15% for the pion yield at midrapidity. What remains to be seen, however, is whether one could get closer to the UrQMD result with dissipative corrections to the distribution function of Cooper-Frye, or whether the deviations from equilibrium are so large that dissipative expansion is not feasible.

The largest observed impact of negative contributions is to pion rapidity spectrum at midrapidity in central collisions. In thermally equilibrated Cooper-Frye calculations it constitutes 8–13%, but only 0.5–4% in the counting of UrQMD particles. The Cooper-Frye value roughly agrees with the values obtained previously for hydrodynamics at 160 GeV. Several systematic features were found in these ratios. They are smaller for larger hadron mass and therefore largest for pions. The relative negative contributions decrease as a function of collision energy and by going from central to peripheral collisions. On the other hand, they increase if a higher energy density is chosen as a surface criterion. The small scale structures on the surface, its “lumpiness”, play a significant role: If the surface is not smooth enough both ratios can increase dramatically. Therefore, an interesting future study could be to compare single fluctuating events to the averaged result.

Chapter 5.

SMASH transport approach: implementation and testing

This chapter is largely based on [5]. A significant part of the work on this thesis was devoted to developing a new transport approach, SMASH (Simulating Many Accelerated Strongly-interacting Hadrons), which is described in this chapter. SMASH is used for an investigation carried out in chapter 6. Conceptually the approach is similar to UrQMD, which was used in chapters 3 and 4. The main difference is that SMASH is a transport approach of a BUU type, while UrQMD is of QMD type (see section 1.3.5 for BUU vs. QMD discussion). This difference mainly matters for the treatment of potentials and in the studies of this thesis potentials are not included. The reasons to use SMASH in the following investigation are rather technical than physical: SMASH is developed from scratch under version control, it is written in C++, it undergoes continuous testing (both from programming and physics side) and the implementation of forced thermalization approach appeared to be technically easier in SMASH. The current version of SMASH is 1.0rc, however the studies in chapter 6 were performed with an earlier version SMASH-0.9rc.

As a transport approach SMASH solves a coupled set of Boltzmann equations (1.20,1.24) via the Monte-Carlo method with the test-particle ansatz

$$f(x, p) = \frac{1}{N_{test}} \sum \delta^{(3)}(x - x_i) \delta^{(3)}(p - p_i). \quad (5.1)$$

Here every physical particle is represented by N_{test} testparticles, which sample the distribution function. To simulate the left part of the BUU equation (1.20) it is enough

to propagate particles according to their equations of motion. The collision integral (1.24) is solved via simulating particle collisions and decays.

The testparticle ansatz also requires that interaction cross-sections are modified:

$$\sigma \mapsto \sigma \cdot N_{test}^{-1} \quad (5.2)$$

$$N \mapsto N \cdot N_{test} \quad (5.3)$$

In this way the average scattering rate (number of collisions per unit time per particle) remains unchanged. The testparticle ansatz has three effects. Firstly, the more testparticles are used the more precisely the distribution function $f(x, p)$ is sampled. Due to the geometrical treatment of cross-sections, particles in SMASH can interact at non-zero distance in contrast to field theory, where all the interactions are local. So, secondly, the larger N_{test} the smaller are the non-locality effects introduced by the collision criterion. Thirdly, as shown in [257], experimental observables such as particle spectra and flow obtained using transport models depend on N_{test} and saturate when N_{test} is sufficiently large (in case of [257] $N_{test} = 16$ was large enough for saturation).

5.1. Degrees of freedom

The degrees of freedom entering BUU equations in SMASH are hadrons and strings. The number of coupled BUU equations coincides with the number of degrees of freedom.

5.1.1. Hadrons in SMASH

All hadrons consisting of the light quarks listed in the Review of Particle Properties [13], which have an experimental status "****" or "*****", are taken into account in SMASH. This notation for status means that the existence of these hadrons is experimentally confirmed with high reliability.

The classification of light quark hadrons by quark content using the SU(3) flavour group is shown in appendix C. These hadrons and their total angular momentum and radial excitations constitute the hadron spectrum in SMASH.

Currently SMASH has 46 unflavoured mesons, 12 mesons with open strangeness, 17 N baryons, 8 Δ baryons, 14 Λ baryons, 10 Σ baryons, 6 Ξ baryons and 2 Ω baryons. In this counting scheme the whole isospin group is considered as one particle, for

example proton and neutron are counted as one baryon or the group $\Delta^{++}, \Delta^+, \Delta^0$ and Δ^- is also counted as one Δ baryon. Antiparticles are also included.

All of these particles are unstable except the proton, but every combination of (anti-) quarks in a strong-interaction ground state lives long enough, so that in our simulations it may be considered as stable. A particle is treated as stable, if its width does not exceed 10 keV (such as the lightest $\pi, \eta, K, N, \Lambda, \Sigma, \Xi, \Omega$).

Every particle is characterized by the following parameters taken from experimental data [13]: the pole mass, the width at the pole mass, quantum numbers, decay channels and branching ratios. Branching ratios are assumed to be independent of mass.

5.1.2. Hadron spectral function

Every unstable hadron is characterized by a spectral function $\mathcal{A}(m^2)$ - the probability to find it in a state with mass m , given that it has pole mass M_0 . In SMASH this is implemented by sampling the mass m from the spectral function, when the resonance is produced. The particular form of $\mathcal{A}(m^2)$ used in SMASH, called relativistic Breit-Wigner function, can be understood from the following considerations.

The quantum field theory propagator of the particle, including interactions can be written according to Dyson-Schwinger equation as

$$\mathcal{G}(p) = \frac{1}{\mathcal{G}_0^{-1}(p) + \Sigma(p)}, \quad (5.4)$$

where $G_0(p)$ is the propagator of non-interacting particle and $\Sigma(p)$ is the so-called self-energy containing quantum loop corrections to the propagator. For the scalar field

$$\mathcal{G}_0(p) = \frac{1}{p^\mu p_\mu - m_{bare}^2}, \quad (5.5)$$

where m_{bare} is the bare mass in Lagrangian. For the Lorentz group representations different from scalars (spinors, vector particles, etc) the propagator is still proportional to the propagator of the scalar field. Splitting the self-energy $\Sigma(p)$ into real and imaginary part, one can rewrite the full propagator as

$$\mathcal{G}(p) = \frac{1}{p^\mu p_\mu - M_0^2 + i \text{Im}(\Sigma(p))} \quad (5.6)$$

$$M_0^2 = m_{bare}^2 - \text{Re}(\Sigma(p)) \quad (5.7)$$

Here M_0 is the physical pole mass with interaction correction. This is the mass taken from experimental data. Now the time-dependent propagator is the inverse Fourier transformation

$$\mathcal{G}(t, \vec{p}) = \int \frac{dp^0}{2\pi} e^{ip^0 t} \frac{1}{p^\mu p_\mu - m_0^2 + i \text{Im}(\Sigma(p))}. \quad (5.8)$$

This expression can be interpreted to use in a transport code. The Monte-Carlo interpretation of the integral in Eq. (5.8) is the following: instead of propagating an off-shell particle one can propagate an on-shell particle with a mass chosen with probability

$$w(m) \sim |m^2 - m_0^2 + i\Gamma(m)|^{-2} \quad (5.9)$$

$$\Gamma(m) = \text{Im}(\Sigma(m)) \quad (5.10)$$

In general $\Sigma(p)$ depends on the medium surrounding the particle, which leads to the off-shell equations of motion [258]. However, in SMASH these in-medium effects are neglected (the effects of accounting them are discussed in [259] and are usually small for hadronic observables). Therefore all unstable particles (“resonances”) are assumed to have the shape of a relativistic Breit-Wigner for the spectral function, resulting in the probability of a resonance with mass m :

$$\mathcal{A}(m^2) = \frac{\mathcal{N}}{\pi} \frac{m\Gamma(m)}{(m^2 - M_0^2)^2 + m^2\Gamma(m)^2}, \quad (5.11)$$

where \mathcal{N} is a normalization factor chosen in such a way that

$$\int_0^\infty \mathcal{A}(m^2) dm^2 = \int_{m_{\min}}^\infty \mathcal{A}(m^2) dm^2 = 1 \quad (5.12)$$

5.1.3. Resonance width

The total width Γ in the previous expression is not constant, but given by the mass-dependent function $\Gamma(m)$. Each resonance has a minimum mass m_{\min} corresponding to the sum of masses of the lightest decay channels, below which the width, and thus also the spectral function, vanishes. The total width is computed as the sum of all partial widths:

$$\Gamma(m) = \sum_i \Gamma_i(m) \quad (5.13)$$

The computation of the decay widths follows the formalism of Manley et al. [260], where in general the width of a two-body decay $R \rightarrow ab$ is written as

$$\Gamma_{R \rightarrow ab} = \Gamma_{R \rightarrow ab}^0 \frac{\rho_{ab}(m)}{\rho_{ab}(M_0)}. \quad (5.14)$$

Here m is the actual off-shell mass of the resonance R , M_0 is its pole mass, $\Gamma_{R \rightarrow ab}^0 = \Gamma_{R \rightarrow ab}(M_0)$ is the partial width at the pole mass and the function ρ_{ab} is defined as

$$\begin{aligned} \rho_{ab}(m) = & \int dm_a^2 dm_b^2 \mathcal{A}_a(m_a^2) \mathcal{A}_b(m_b^2) \\ & \times \frac{p_{cm}}{m} B_L^2(p_{cm} R) \mathcal{F}_{ab}^2(m). \end{aligned} \quad (5.15)$$

In this formula, m_a and m_b denote the (off-shell) masses of the particles a and b (which are being integrated over), \mathcal{A}_a and \mathcal{A}_b are their spectral functions and p_{cm} is the absolute value of the final-state momentum of a and b in the center-of-mass frame, which is given by:

$$\vec{p}_{cm}^2(m, m_a, m_b) = \frac{(m^2 - (m_a + m_b)^2)(m^2 - (m_a - m_b)^2)}{4m^2} \quad (5.16)$$

Finally, L is the orbital angular momentum of a and b in the final state and B_L are the so-called 'Blatt-Weisskopf functions' [261]. The parameter R is usually called the 'interaction radius' and is assumed to have a universal value of $R = 1$ fm for all processes. The form factor \mathcal{F}_{ab} is only relevant for unstable decay products and will be discussed further.

The simplest case is that of a resonance R decaying into two stable daughter particles. Popular examples are $\Delta \rightarrow \pi N$ or $\rho \rightarrow \pi\pi$. In this case, the daughters have

fixed masses (i.e. their spectral functions are just δ functions), so that the integrals collapse:

$$\rho_{ab}(m) = \frac{p_{cm}}{m} B_L^2(p_{cm}R) \quad (5.17)$$

As an example, the width for the p-wave (L=1) decays of the ρ and Δ (mentioned above) becomes

$$\Gamma(m) = \Gamma_0 \frac{M_0}{m} \left| \frac{p_{cm}}{p_{cm,0}} \right|^3 \frac{p_{cm,0}^2 + \Lambda^2}{p_{cm}^2 + \Lambda^2}, \quad (5.18)$$

using $B_1^2(x) = x^2/(1+x^2)$. Here m and M_0 are the off-shell and pole mass, respectively, while p_{cm} and $p_{cm,0}$ denote the final-state momenta in the center-of-mass frame for mass m and M_0 , respectively. $\Lambda = 1/R$ can be viewed as a cut-off parameter. For an s-wave (L=0) decay like $\sigma \rightarrow \pi\pi$, the width simply becomes

$$\Gamma(m) = \Gamma_0 \frac{M_0}{m} \frac{p_{cm}}{p_{cm,0}}, \quad (5.19)$$

since $B_0^2 = 1$.

In the case that one of the daughter particles is itself a resonance, the width calculation becomes more difficult, since the mass of this daughter resonance is not fixed and needs to be integrated over. Examples for this case are $N^*(1440) \rightarrow \pi\Delta$ or $\omega \rightarrow \pi\rho$. As one of the daughters is stable, at least one of the two integrals collapses:

$$\rho_{ab}(m) = \int_{m_a^{\min}}^{m-m_b} dm_a^2 \mathcal{A}_a(m_a^2) \frac{p_{cm}}{m} B_L^2(p_{cm}R) \mathcal{F}_{ab}^2(m) \quad (5.20)$$

The remaining integral runs from the minimum allowed mass of particle a (i.e. the threshold of its lightest decay channel) up to the maximum possible mass of a in the decay process (given by $m - m_b$). The form factor \mathcal{F}_{ab} (by M. Post [262]) is used only if unstable decay products are involved and is defined as

$$\mathcal{F}_{ab}(m) = \frac{\lambda^4 + 1/4(s_0 - M_0^2)^2}{\lambda^4 + (m^2 - 1/2(s_0 + M_0^2))^2}, \quad (5.21)$$

where the cut-off factors given in the table 5.1 are used.

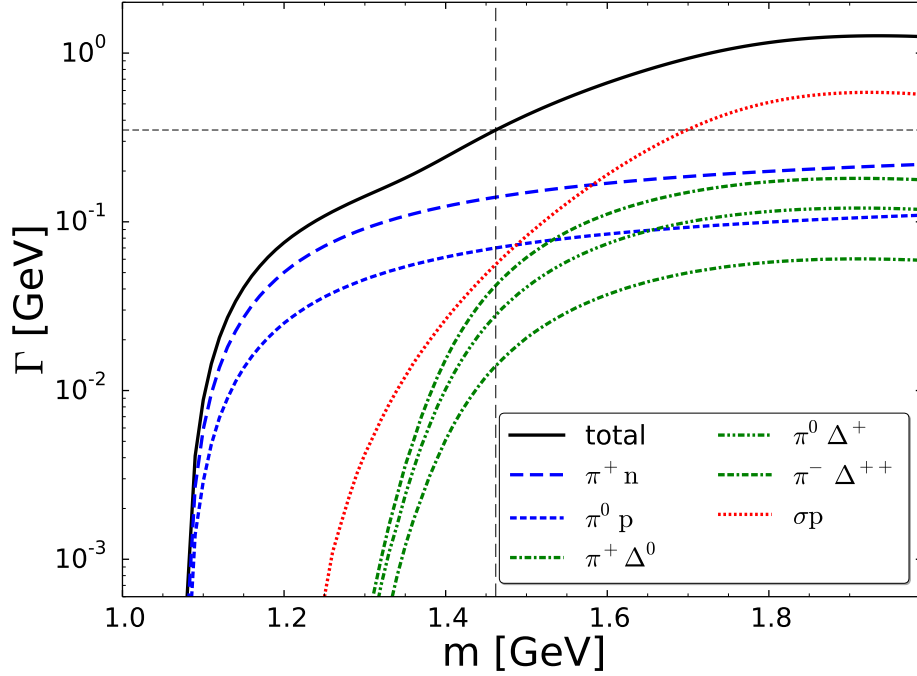


Figure 5.1.: Total and partial decay widths of the $N^*(1440)^+$ resonance as a function of mass. The vertical and horizontal dashed lines mark the pole mass and width.

Table 5.1.: Cut-off parameter λ for form factor in resonance decay widths.

decay	λ [GeV]
$\pi\rho$	0.8
unstable mesons (e.g. $\rho N, \sigma N$)	1.6
unstable baryons (e.g. $\pi\Delta$)	2.0
two unstable daughters (e.g. $\rho\rho$)	0.6

It is easy to see that $\mathcal{F}_{ab}(M_0) = \mathcal{F}_{ab}(\sqrt{s_0}) = 1$. Note that this form factor was not used by Manley originally, but was added only later in the GiBUU implementation. The effect of the form factor is that it suppresses the high-mass tail ($m > M_0$) and slightly enhances the low-mass tail ($m < M_0$). Both of these effects get stronger with decreasing λ ($\mathcal{F}_{ab} \rightarrow 1$ for $\lambda \rightarrow \infty$). In this aspect SMASH follows the GiBUU framework for the width parametrization of resonances, since it has been proven to give a good description of experimental data [200].

Table 5.2.: Woods-Saxon initialization parameters for some nuclei.

Nucleus	A	r_0 [fm]	d [fm]
U	238	6.86	0.556
Pb	208	6.67	0.54
Au	197	6.38	0.535
Cu	63	4.20641	0.597

To demonstrate the result of this formalism, in Fig. 5.1 the theoretical decay width of the $N^*(1440)$ resonance is shown as a function of mass. The total width is given as the sum of all partial widths. Each partial width has a threshold that is given by the sum of the minimal masses of the decay products. The branching ratios are fixed at the pole mass. One can see that all partial widths increase as a function of mass, since more phase space is available for heavier resonances. The lifetime correspondingly has an opposite trend and heavy particles decay faster than low-mass resonances. Since the width also enters in the production cross section, the production of such low-mass resonances becomes more unlikely.

5.1.4. Strings

At high \sqrt{s} hadron collisions are not described by resonance excitations anymore. In the regime of $\sqrt{s} \geq m_1 + m_2 + 2 \text{ GeV}$, where m_1 and m_2 are masses of colliding particles, SMASH adopts Lund string model [263] to describe multiparticle production in the hadron-hadron collisions. The used implementation of the Lund string model is PYTHIA 8 [264]. At the time, when the SMASH transport approach was applied for the studies relevant for this thesis (see chapter 6), strings were not yet implemented.

5.2. Initial conditions

5.2.1. Nucleus-nucleus collisions

Nucleon Distribution in coordinate space In SMASH a simple Woods-Saxon nucleon spatial distribution is implemented, as demonstrated in Fig. 5.2. The explicit form reads

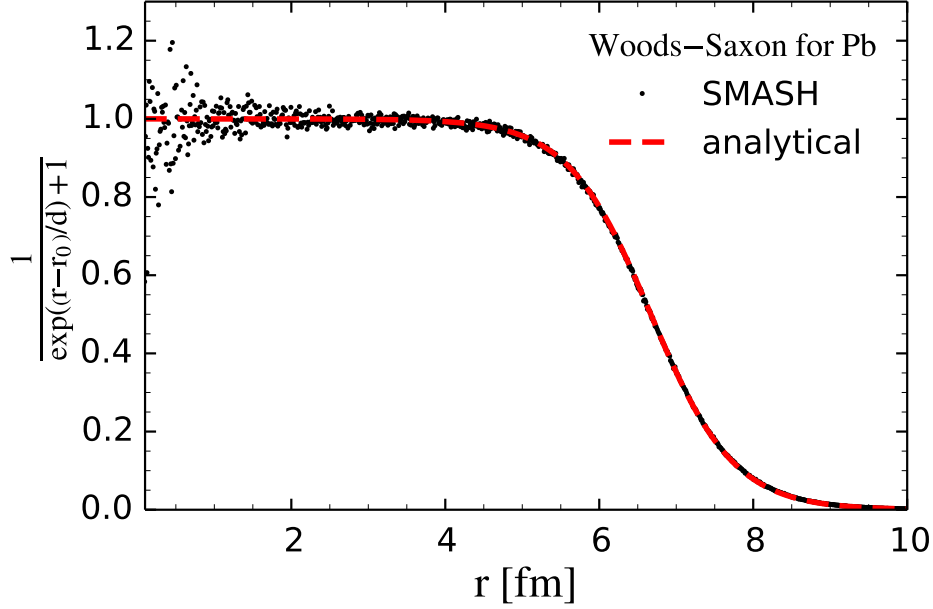


Figure 5.2.: Sampled coordinate space distribution of 208 nucleons is compared to the Woods-Saxon distribution with the parameters for a lead nucleus.

$$\frac{dN}{d^3r} = \frac{\rho_0}{\exp\left(\frac{r-r_0}{d}\right) + 1} \quad (5.22)$$

where r_0 is the nuclear radius and d is the diffusiveness, which controls the quick fall-off of the distribution. For $d \rightarrow 0$, the nucleus would be a hard sphere. The ground state density $\rho_0 \approx 0.168 \text{ fm}^{-3}$ emerges after A nucleons are sampled. The default value for the diffusiveness is $d = 0.545 \text{ fm}$, where more specific values are used for Au, Pb, Cu and U (see Table 5.2).

Within the sampling procedure nucleons are assumed to be independent. The finite size of the nucleons and nucleon-nucleon correlations [265] are neglected for simplicity, as are the neutron skin effects [266]. Deviations from sphericity can optionally be taken into account up to the quadrupole moment. No measures are taken to initialize the nucleus in the ground state, like it is done e.g. in [267].

The initial positions of nuclei and the time of initialization are chosen as shown in Fig. 5.3. Cartesian coordinates are used, where the z -direction corresponds to the beam direction and x is the impact parameter direction. At the initialization the projectile center is at xz -coordinates $(b/2, -\Delta z - \gamma_P^{-1}(R_P + d_P))$ and the target center is at $(-b/2, \frac{v_T}{v_P}\Delta z + \gamma_T^{-1}(R_T + d_T))$. Here $R_{P,T}$ are the projectile/target radii and $d_{P,T}$

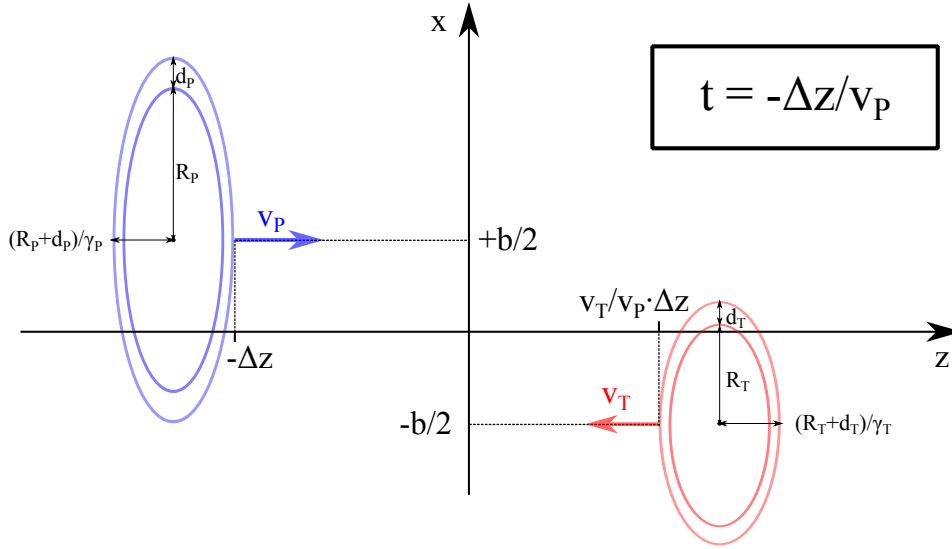


Figure 5.3.: Initial positions of nuclei such that contracted spheres of radii $(R + d)_{P,T}$ will touch at $t = 0$ in a central collision.

are the corresponding diffusiveness parameters from the Woods-Saxon distribution. By $v_{T,P}$ we denote absolute values of the velocities, while $\gamma_{P,T} = (1 - v_{P,T}^2)^{-1/2}$ are the associated gamma-factors. The separation of the centers of the nuclei in x -direction equals the impact parameter b . For deformed nuclei an additional rotation along all three angles is applied. In this way, the simulation is started at such an initial separation that the potential of one nucleus does not influence the other one yet, otherwise initialization in the ground state would not be justified. The initial coordinates and time are chosen in such a way that the Lorentz-contracted spheres of radii $(R + d)_{P,T}$ will touch at $t = 0$ in a central collision. An alternative definition would be that $t = 0$ fm corresponds to the maximal overlap of the two nuclei. The additional distance $\Delta z = 2$ fm is added to avoid missing any nucleon-nucleon collisions. Since the nucleons are distributed according to Woods-Saxon distributions, there is a small, but non-zero probability to position a nucleon at a large distance from the nucleus center. The initial separation distance Δz is chosen such that all collisions are taken into account. The initial time is $t_0 = \Delta z/v_p$, which implies that the projectile is always moving, $v_p > 0$, while the target can be at rest depending on the reference frame for the calculation.

Fermi motion In momentum space nucleons optionally get Fermi momenta, then target and projectile are boosted in z direction according to the chosen energy of the

reaction and computational frame. The gamma-factor of the boost is $\gamma = E_A/M_A$, where E_A is the energy of the nucleus and M_A is its mass. The velocity of the boost is $\beta = p_A/E_A$. Note that in E_A and M_A one has to account for the binding energy of the nucleus. For this an approximation used in the JAM transport code [199] is adopted, which assumes that all nucleons are equally bound. Thus, the energy of each nucleon in the rest frame of the nucleus is $E_i = M_A/A$, where A is the number of nucleons. With this assumption the boost of the longitudinal momenta p'_{iz} to the computational frame becomes

$$p'_{iz} = \gamma(p_{iz} + \beta E_i) = \gamma p_{iz} + \frac{p_A}{M_A} \frac{M_A}{A} = p_{\text{beam}} + \gamma p_{iz}, \quad (5.23)$$

where p_{beam} is the beam momentum per nucleon and p_{iz} are the momenta of nucleons in the rest frame of the nucleus. In our implementation p_{beam} and γ themselves are computed without accounting for binding energy. Note that there is no well-established procedure of boosting nuclei accounting for their binding energy. Codes like UrQMD [197], JAM [199] and GiBUU [200] apply different methods. Though the typical binding energy per nucleon is much smaller than the nucleon mass ($\simeq 8 \text{ MeV}/938 \text{ MeV} \approx 1\%$), the different methods of accounting for the binding energy produce small but noticeable differences in pion multiplicities and mean transverse momentum at low collision energies of $E_{\text{kin}} = 0.4 - 2A \text{ GeV}$.

The momentum distribution of nucleons in the ground state nucleus is generated in the Local Density Approximation (LDA). At every spatial point the momentum distribution is a uniformly filled Fermi sphere of radius

$$p_F(\vec{r}) = \hbar c(3\pi^2\rho(\vec{r}))^{1/3} \quad (5.24)$$

Here $\rho(\vec{r})$ is the density of nucleons at the point \vec{r} . A more detailed description of the density calculation is given in section 5.4. A typical value of $p_F \approx 300 \text{ MeV}$ corresponds to an energy of $p_F^2/(2m_N) \approx 45 \text{ MeV}$. The LDA is probably the easiest and most naive choice to implement. A more realistic treatment of Fermi motion includes Hartree-Fock mean-field calculation, which justifies LDA in the range of momenta from 0.5 to 1 fm^{-1} [268]. Similar conclusion can be made comparing Fig. 5.4 to experimentally measured momentum distributions [269].

In LDA the momentum distribution of the nucleons can be computed analytically. In the central part of the nucleus, where the density is almost constant, the momentum

distribution is just a Fermi sphere. This is indeed reproduced by SMASH, as shown in Fig. 5.4. For the whole nucleus one has to properly average over the density:

$$\frac{dN}{p^2 dp} \sim \int \frac{dN(r)}{p^2 dp} d^3r \sim \int_0^\infty \theta(p_F(r) - p) r^2 dr = r_{max}^3(p)/3, \quad (5.25)$$

where r_{max} is the root of the equation $p_F(r_{max}) = p$. Let us find this root.

$$\left(\frac{p}{\hbar c}\right)^3 \frac{1}{3\pi^2 \rho_0} = \frac{1}{1 + \exp((r - R)/d)} \quad (5.26)$$

$$(p_F^0/\hbar c)^3 = 3\pi^2 \rho_0 \quad (5.27)$$

$$r_{max}(p) = R + d \cdot \log \left(\left(\frac{p_F^0}{p} \right)^3 - 1 \right) \quad (5.28)$$

$$\frac{dN}{p^2 dp} \sim \left(1 + \frac{d}{R} \log[(p_F^0/p)^3 - 1] \right)^3 \theta(p_F^0 - p) \quad (5.29)$$

$$\frac{dN}{dp^3} = A \left(1 + \frac{d}{R} \log[(p_F^0/p)^3 - 1] \right)^3 \theta(p_F^0 - p) \frac{1}{(p_F^0)^3}, \quad (5.30)$$

where A is a dimensionless constant, which can be obtained from the normalization condition. Let us rewrite the previous equation with $\xi = \left(\frac{p}{p_F^0}\right)^3$:

$$\frac{dN}{d\xi} = A \left(1 + \frac{d}{R} \log[\xi^{-1} - 1] \right)^3 \theta(1 - \xi) \quad (5.31)$$

Integration results in

$$\int_0^1 \left(1 + \frac{d}{R} \log[\xi^{-1} - 1] \right)^3 d\xi = 1 + \left(\frac{\pi d}{R} \right)^2 \quad (5.32)$$

$$\frac{1}{N} \frac{dN}{d\xi} = \frac{1}{1 + \left(\frac{\pi d}{R} \right)^2} \left(1 + \frac{d}{R} \log[\xi^{-1} - 1] \right)^3 \theta(1 - \xi) \quad (5.33)$$

As Fig. 5.4 demonstrates, this theoretical expectation is matched by SMASH.

Including Fermi motion is only sensible, if potentials are turned on simultaneously. Otherwise, the nucleus will fly apart due to the finite transverse momenta of the nucleons that need to be compensated by the attractive mean field interaction.

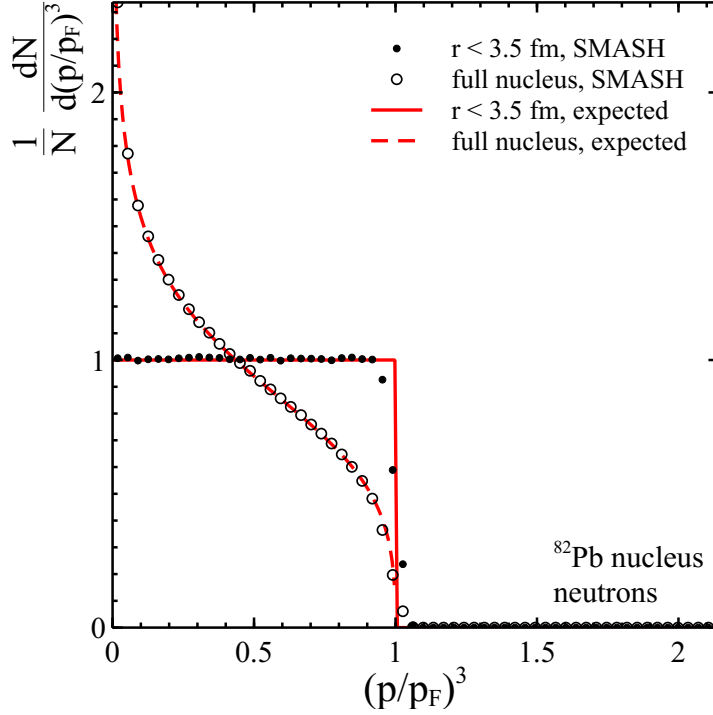


Figure 5.4.: Momentum space distribution of neutrons compared to the analytical expectation for a lead nucleus.

Alternatively, the so-called frozen Fermi approximation can be adopted, where the Fermi momenta are employed for the collisions, but not for the propagation.

5.2.2. Infinite matter (periodic box) calculations

To simulate infinite hadronic matter or other simple systems like an ideal massless or massive gas and investigate its thermodynamic properties, box calculations are performed. There are two initialization options. Firstly, the box can be initialized in the canonical ensemble with user-defined hadron multiplicities N_j of each hadron species. In this case N_j does not change from event to event. Secondly, multiplicities can be sampled from the Poisson distribution

$$N_j = Poi(n_j), \quad (5.34)$$

where $n_j(T, \mu_b, \mu_s)$ are the grand-canonical thermal multiplicities given by Eq. (2.61). The coordinates of the N particles (x_j, y_j, z_j) are sampled uniformly in the box. The momenta of the particles are sampled from the isotropic thermal Boltzmann distribution with temperature T :

$$w(\vec{p}) = \mathcal{N} \cdot \exp(-\sqrt{\vec{p}^2 + m^2}/T) p^2 dp \cdot \sin \theta d\theta d\varphi, \quad (5.35)$$

where $w(p)$ is a probability to generate momentum \vec{p} , θ and φ are angles in spherical coordinates and \mathcal{N} is a normalization factor. Let us denote the total momentum of N particles sampled from this distribution p_{tot} . One can see that the ensemble average of p_{tot} is zero,

$$\int \exp(-\sqrt{\vec{p}^2 + m^2}/T) d^3 p \cdot p_{x,y,z} = 0, \quad (5.36)$$

because it involves an integral over an odd function. However, in each single event $p_{tot} \neq 0$, which is corrected by changing the momentum of every particle $p_j \rightarrow p_j - p_{tot}/N$. After this procedure the thermal distribution is slightly spoiled, the total energy is changed and angle uniformity is disturbed. This is a small effect for large numbers of particles, because $\frac{p_{tot}}{E_{tot}} \sim \frac{1}{\sqrt{N}}$, where E_{tot} is the total energy of the particles. After letting the system thermalize, the temperature differs by 1-2% from the initialization temperature. One also has to note that the total energy is not the same from event to event, it is fluctuating, even without this momentum shift.

5.3. Interactions

5.3.1. Collisions

Collision Criterion

One of the challenges for solving the relativistic BUU equation is to define an appropriate collision criterion. The Kodama criterion [270] is a fully covariant collision criterion, but since it involves boosts of several four vectors it is rather inefficient. In the SMASH approach the geometrical criterion was chosen following the UrQMD (Ultra-relativistic Quantum Molecular Dynamics) approach [197]. The geometrical criterion is defined as follows:

$$d_{trans} < d_{int} = \sqrt{\frac{\sigma_{tot}}{\pi}} \quad (5.37)$$

with

$$d_{trans}^2 = (\vec{r}_a - \vec{r}_b)^2 - \frac{((\vec{r}_a - \vec{r}_b) \cdot (\vec{p}_a - \vec{p}_b))^2}{(\vec{p}_a - \vec{p}_b)^2} \quad (5.38)$$

where \vec{r} and \vec{p} are the coordinates and momenta of the two particles a and b in the center of mass frame of the binary collision. The time of the collision is determined as the time of the closest approach in the computational frame:

$$t_{coll} = -\frac{(\vec{r}_a - \vec{r}_b) \cdot (\vec{p}_a/E_a - \vec{p}_b/E_b)}{(\vec{p}_a/E_a - \vec{p}_b/E_b)^2} \quad (5.39)$$

where now all coordinate and momentum vectors have to be taken in the computational frame. The computational frame is usually chosen to be the equal velocity frame of the two nuclei, which is the same as the center of mass frame in case of symmetric systems. The computational system is the one that carries the clock that is relevant for ordering of the collisions, therefore it is crucial to transform the collision times to the same frame to decide which collision happens first.

An alternative option to include all relevant scatterings at high density is to implement the solution of the Boltzmann equation by stochastic rates [204, 271, 272]. This approach has the advantage that multi-particle scatterings can be taken into account in a straightforward way. On the hadronic level there are of course a lot of different possibilities that one would need to take into account in such an approach, therefore this is left for future work. Also, the stochastic rates approach is relying on having a large number of test particles in each cell, therefore it is not clear how to model event-by-event fluctuations properly.

Elastic and inelastic reactions

The elastic collisions can be truly elastic, where only momenta are exchanged between the particles, and pseudoelastic, which proceed through a resonance formations. In SMASH the meson-meson and baryon-meson reactions are assumed to be fully determined by resonance excitation and decay, e.g. $\pi N \rightarrow \Delta \rightarrow \pi N$ or $\pi\pi \rightarrow \rho \rightarrow \pi\pi$. For baryon-baryon collisions on the other hand the elastic cross sections are parametrized. The parametrizations of the elastic pp and pn cross sections in particular are taken from [273], eq. (44) and (45).

Inelastic interaction in SMASH are $2 \leftrightarrow 2$ collisions and $2 \rightarrow 1$ resonance formations. Many-particle reactions are not implemented, but an effective way to account for them

is discussed in chapter 6. Cross-sections of resonance formation are completely defined by the resonance properties and can be computed from the detailed balance principle using Eq. 5.77. The results of this treatment for $\pi^+\pi^-$ and πN cross-sections is demonstrated in Fig. 5.5. One can see the a resonant structure of both cross-sections.

Three groups of $2 \rightarrow 2$ reactions are implemented:

1. Single nucleon excitation reactions $NN \leftrightarrow NN$, $NN \leftrightarrow N\Delta$, $NN \leftrightarrow NN^*$ and $NN \leftrightarrow N\Delta^*$.
2. Double nucleon excitation reactions $NN \leftrightarrow \Delta\Delta$, $NN \leftrightarrow \Delta N^*$ and $NN \leftrightarrow \Delta\Delta^*$. Here N^* and Δ^* denote all possible excitations of nucleons and Delta-baryons.
3. Strangeness exchange reactions $K^- N \leftrightarrow \pi Y$ with $Y = \Lambda, \Sigma$.
4. $KN \leftrightarrow K\Delta$ and inelastic charge exchange $KN \leftrightarrow KN$

For the process $NN \leftrightarrow N\Delta$, the parametrized energy dependence is based on a fit to the Dmitriev one-boson-exchange (OBE) model [274]. For $NN \rightarrow NR$ and $NN \rightarrow \Delta R$ with $R = N^*, \Delta^*$, the matrix element is assumed to be independent of s , but can depend on the total isospin and the pole masses m_a and m_b of the outgoing particles. The same is true for the parametrizations of double resonance production $NN \rightarrow R_1 R_2$. For the parametrization details see [5]. The cross-sections are computed via Eq. 5.67, but additionally isospin factors are taken into account. The reverse reactions cross-sections are implemented via the detailed balance relations, see section 5.3.3. The resulting NN total cross-section is demonstrated in Fig. 5.5.

For the strangeness exchange reactions the explicit experimental cross-section parametrizations are taken from [275] and the reverse reactions are implemented via detailed balance. The $KN \leftrightarrow K\Delta$ and $KN \leftrightarrow KN$ cross-sections are also parametrized directly following the GiBUU and using expressions from the Appendix A.2.4 of [276].

Angular distributions

Anisotropic angular distributions are currently implemented only for $NN \rightarrow NN$, $NN \rightarrow N\Delta$ and $NN \rightarrow NR$ (with $R = N^*, \Delta^*$). For elastic nucleon-nucleon collisions the prescription by Cugnon et al. [279] is followed, using an exponential ansatz $d\sigma/dt \propto e^{-bt}$, with an energy-dependent parameter b which is fit to data. In the second case SMASH also follows Cugnon et al. [279], using the same ansatz as for elastic NN collisions. For the last case of $NN \rightarrow NR$ the ansatz $d\sigma/dt \propto t^{-a}$ is

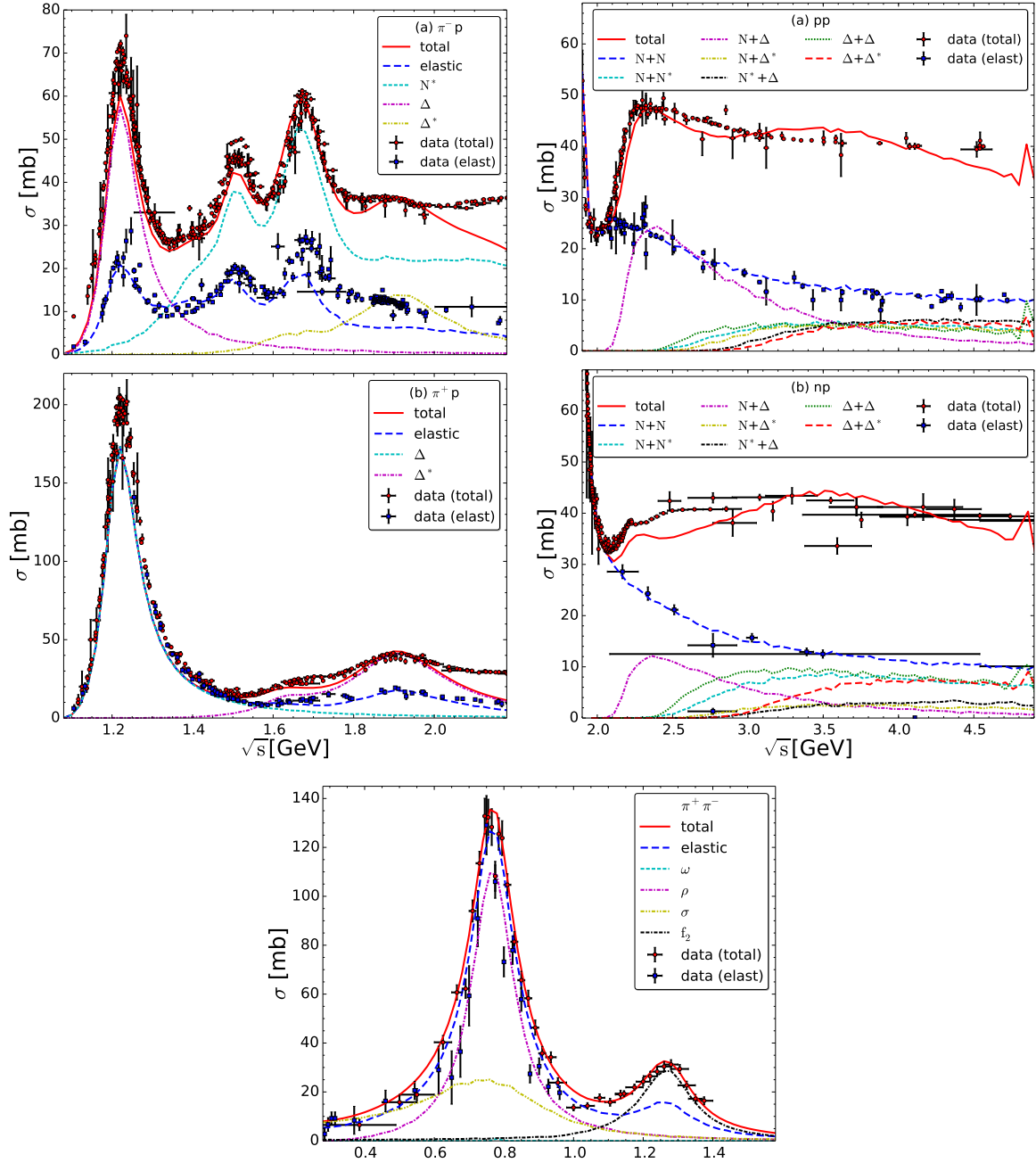


Figure 5.5.: Left upper panel: π^- -proton (a) and π^+ -proton (b) cross-sections compared to data from [13]. Right upper panel: Proton-proton (a) and proton-neutron (b) cross-sections compared to data from [13]. Lower panel: pion-pion cross-section compared to data from [277, 278].

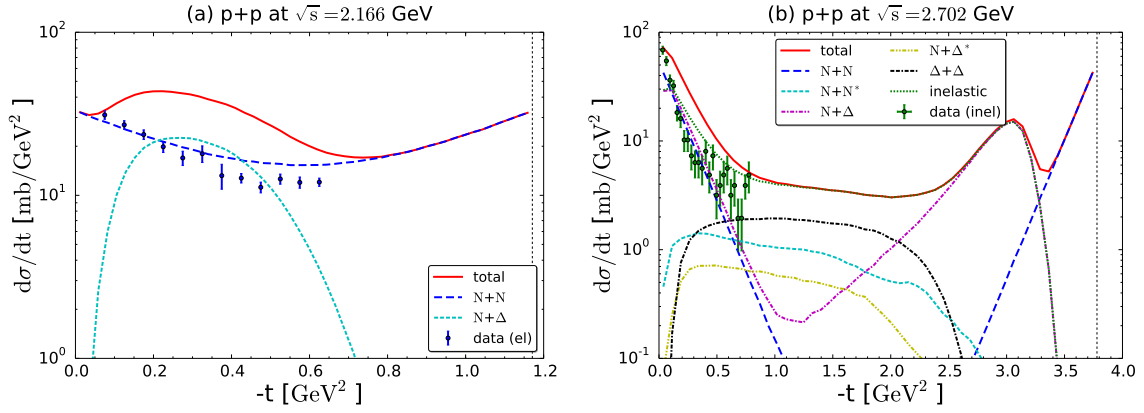


Figure 5.6.: Angular distributions for elastic and inelastic pp collisions at two different energies, compared to data from [281, 282].

used, with parameters a which fitted to HADES data [280]. Note that in the present implementation of SMASH all resonances decay isotropically.

In Fig. 5.6 two examples of angular distributions $d\sigma/dt$ in pp collisions are shown, t being the Mandelstam variable. The upper plot demonstrates a collision at a relatively low energy, where essentially only the elastic and single- Δ -production channels are open. The angular distribution of the elastic channel is of course symmetric in the allowed t -range and matches the data points rather well, even though the slope at this particular energy appears to be slightly too flat. The distribution for single- Δ production is not symmetric and restricted to a smaller range in t , due to the larger mass of the Δ in the final state. Unfortunately there is no inelastic data to compare to at this energy.

The lower plot in Fig. 5.6 shows a pp collision at a somewhat higher energy, where additional resonance production channels are open. In principle the distributions for all these channels are forward/backward-peaked (either exponential or power-law shaped). This forward/backward peaking is clearly visible for the NN and $N\Delta$ final states at least, while those final states with heavier resonances exhibit a more plateau-like structure, due to the limited phase space and the mass distributions of the resonances. Here the sum of all inelastic channels is compared to data and indeed shows a reasonable agreement, again with a slight tendency of being too flat.

5.3.2. Decays

In section 5.1.2 the time-dependent propagator (Eq. 5.8) was considered to derive the spectral function of hadrons. This propagator can be integrated for $t > 0$ by contour integration resulting in

$$\mathcal{G}(p, t) = \frac{i}{2\sqrt{\vec{p}^2 + M_0^2 - iM_0\Gamma}} \exp\left(-it\sqrt{\vec{p}^2 + M_0^2 - iM_0\Gamma}\right). \quad (5.40)$$

Assuming that $\Gamma \ll M_0$, one rewrites $\sqrt{\vec{p}^2 + M_0^2 - iM_0\Gamma} = E - \frac{iM_0\Gamma}{2E}$ and obtains

$$\mathcal{G}(p, t) = \frac{i}{2E} e^{-iEt} \exp\left(\frac{-M_0\Gamma}{2E} t\right) \quad (5.41)$$

Therefore the probability to find the resonance decays exponentially. The lifetime τ is determined according to

$$\tau = \frac{E}{M_0} \frac{1}{\Gamma(m)}. \quad (5.42)$$

The factor $\frac{E}{M_0}$ corresponds to the time dilation. In SMASH the lifetime of the particle is sampled from the exponential distribution:

$$P(\text{decay in the interval}(t, t + dt]) = \frac{dt}{\tau} e^{-t/\tau}. \quad (5.43)$$

The width $\Gamma(m)$ is computed according to section 5.1.3. SMASH has only 2-body decays to maintain detailed balance. All the resonance decays are assumed to be isotropic in the resonance rest frame.

5.3.3. Detailed balance

Detailed balance is an important principle that allows to express properties of the reverse reaction, if the properties of the forward reaction are known. Several equivalent statements are referred to as the principle of detailed balance:

- In thermal equilibrium the rate of forward reactions is equal to the rate of reverse reactions for every reaction in any region of phase space [283].

- Matrix elements of the forward reaction are equal to the matrix elements of the reverse reaction.
- A particular relation holds between the differential cross-sections of forward and reverse reaction or between the width of $1 \rightarrow 2$ and the cross-section of the reverse $2 \rightarrow 1$ reaction.

Time reversal and detailed balance principle

The equality of the matrix elements of the forward and reverse reaction can be derived from the time-reversal invariance of the S -matrix. Here for completeness the derivation given in different paragraphs of textbook [284] is put together. This reproduction is useful to

- introduce the concept of matrix elements and cross-sections, which are used throughout the text
- outline the connection between the time-reversal invariance and detailed balance
- set the stage for the derivation of the detailed balance relations for the reactions involving unstable particles

Let $|i\rangle$ be an initial state and $|f\rangle$ a final state wavefunctions of the scattering. The initial state can be written as

$$|i\rangle = \sum_f |f\rangle \langle i|S|f\rangle, \quad (5.44)$$

where the sum is taken over all possible final states. Here the operator S is connected to the Lagrangian via the formal solution of the equations of motion

$$S = T \exp \left(\int \mathcal{L}_{int} d^4x \right), \quad (5.45)$$

where $T \exp$ denotes time-ordered exponential, \mathcal{L}_{int} is interaction part of Lagrangian. This expression can be further expanded into formal series, where each term corresponds to Feynmann diagrams of a particular order. Matrix $S_{if} = \langle i|S|f\rangle$ is called scattering matrix or S -matrix. Quantities $|S_{if}|^2$ are probabilities to go from state $|i\rangle$ to state $|f\rangle$. Taking into account that for the absence of scattering $S_{if} = \delta_{if}$ and energy-momentum conservation, it is convenient to rewrite

$$S_{if} \equiv \langle i | f \rangle = \delta_{if} + i(2\pi)^4 \delta^{(4)}(P_i - P_f) T_{if}, \quad (5.46)$$

where factor $i(2\pi)^4$ is there just for further convenience, and P_i and P_f are the 4-momenta of the initial and final states. Computing $|S_{if}|^2$ one obtains the delta-function squared, a common artifact in field theory. One of the delta-functions can be rewritten as

$$\delta^{(4)}(P_i - P_f) = (2\pi)^{-4} \int e^{i(P_i - P_f)x} d^4x \quad (5.47)$$

Since first of delta functions sets $P_i = P_f$, this one can be interpreted as $(2\pi)^{-4} Vt$, where integration over d^4x is performed over the finite volume and time. So, for the non-diagonal elements

$$|S_{if}|^2 = (2\pi)^4 \delta^{(4)}(P_i - P_f) |T_{if}|^2 Vt \quad (5.48)$$

It turns out that in momentum representation wavefunctions that stand in T_{if} have structure like $(2EV)^{-1/2} (\hat{a}e^{-ipx} + \hat{a}^\dagger e^{ipx})$. Therefore, for reaction $p_1 + p_2 \rightarrow p'_1 + p'_2$ ¹ it is convenient to introduce

$$M_{if} = (2E_1V)^{-1/2} (2E_2V)^{-1/2} (2E'_1V)^{-1/2} (2E'_2V)^{-1/2} T_{if} \quad (5.49)$$

Object M_{if} is called the matrix element. For the strong interaction time reversal is a strict symmetry. This means that the S -matrix has the following property [285]:

$$S_{if} \equiv \langle i | f \rangle = e^{i(\varphi_i - \varphi_f)} \langle f | i \rangle = S_{fi} e^{i(\varphi_i - \varphi_f)} \quad (5.50)$$

From this relation it follows that

$$|M_{if}|^2 = |M_{fi}|^2 \quad (5.51)$$

Let us prove that Eq. (5.51) is enough for the rates of forward and reverse reactions to be identical in equilibrium. The proof is presented for $2 \rightarrow 2$ reactions, but it can be extended analogously for any other collisions. The probability to scatter with final momenta p'_1 and p'_2 per unit time follows from Eq. (5.48):

¹In this chapter capital P denotes 4-momenta, small p denotes 3-momenta.

$$dw = (2\pi)^4 \delta^{(4)}(P_i - P_f) |M_{if}|^2 \frac{1}{4E_1 E_2 V} \frac{d^3 p'_1}{2E'_1 (2\pi)^3} \frac{d^3 p'_2}{2E'_2 (2\pi)^3} \quad (5.52)$$

Additionally, there is a factor 1/2, if the particles in the final state are identical. It follows that the numbers of the forward and reverse reactions (denoting $d^4\Omega_p = \frac{d^3 p_1}{2E_1} \frac{d^3 p_2}{2E_2} \frac{d^3 p'_1}{2E'_1} \frac{d^3 p'_2}{2E'_2}$) are

$$dN_{\rightarrow} = (2\pi)^{-2} \delta^{(4)}(P_i - P_f) |M_{if}|^2 d^4\Omega_p f(p_1) f(p_2) \left(1 \pm f(p'_1)\right) \left(1 \pm f(p'_2)\right) \quad (5.53)$$

$$dN_{\leftarrow} = (2\pi)^{-2} \delta^{(4)}(P_i - P_f) |M_{if}|^2 d^4\Omega_p f(p'_1) f(p'_2) (1 \pm f(p_1)) (1 \pm f(p_2)) \quad (5.54)$$

In thermal equilibrium the parts of dN_{\rightarrow} and dN_{\leftarrow} related to the distributions are identical, therefore in thermal equilibrium

$$dN_{\rightarrow} = dN_{\leftarrow} \quad (5.55)$$

Finally, it is important to note that although this relation was derived from time-reversal invariance, it can also hold if the invariance is broken [285]. Further the detailed balance relation represented by Eq. (5.51) is linked to the cross-sections.

Detailed balance relations for 2 → 2 reactions

The cross-section σ is defined in the rest frame of the target via an expression for the number of interactions

$$dN_{inter} = \sigma v_{rel} n_1 n_2 dV dt \quad (5.56)$$

The factor after the cross-section is often called luminosity. This expression can be written for any frame in the Lorentz-invariant form [286]:

$$dN_{inter} = \sigma \sqrt{(\vec{v}_1 - \vec{v}_2)^2 + [\vec{v}_1 \times \vec{v}_2]^2} n_1 n_2 dV dt = \sigma \frac{\sqrt{(P_1 \cdot P_2)^2 - m_1^2 m_2^2}}{E_1 E_2} n_1 n_2 dV dt \quad (5.57)$$

The probability to scatter from Eq. (5.52) is connected to the cross-section via

$$dw = V^{-1} \sigma \sqrt{(\vec{v}_1 - \vec{v}_2)^2 + [\vec{v}_1 \times \vec{v}_2]^2}, \quad (5.58)$$

where $n_1 = n_2 = V^{-1}$ was assumed. Let us denote $I = \sqrt{(P_1 \cdot P_2)^2 - m_1^2 m_2^2}$. Then

$$d\sigma = (2\pi)^{-2} \delta^{(4)}(P_i - P_f) |M_{if}|^2 \frac{1}{4I} \frac{d^3 p'_1}{2E'_1} \frac{d^3 p'_2}{2E'_2} \frac{1}{1 + \delta_{1'2'}} \quad (5.59)$$

The last factor $\frac{1}{1 + \delta_{1'2'}}$ accounts for identical particles in the final state. The total cross-section is the integral of this expression. For the case where the outgoing particles are resonances the following trick from [287] is applied

$$\frac{d^3 p}{2E} = \delta(P^2 - m^2) d^4 p = \frac{d^3 p}{2E} \delta(M^2 - m^2) dM^2, \quad (5.60)$$

where a transformation from variables E, \vec{p} to $M^2 = E^2 - \vec{p}^2, \vec{p}$ was performed. For resonances in the final state one substitutes the spectral function of the resonance $\mathcal{A}(M^2)$ instead of δ -function. Therefore,

$$d\sigma = (2\pi)^{-2} \delta^{(4)}(P_i - P_f) |M_{if}|^2 \frac{1}{4I} \frac{d^3 p'_1}{2E'_1} \frac{d^3 p'_2}{2E'_2} \frac{1}{1 + \delta_{1'2'}} \mathcal{A}_1(M_1'^2) \mathcal{A}_2(M_2'^2) dM_1'^2 dM_2'^2 \quad (5.61)$$

The whole expression is Lorentz invariant and the integration over the momenta is easy to perform in the center of mass frame.

$$\delta^{(4)}(P_i - P_f) \frac{d^3 p'_1}{2E'_1} \frac{d^3 p'_2}{2E'_2} \rightarrow \delta(E_1 + E_2 - E'_1 - E'_2) \frac{d^3 p'_1}{4E'_1 E'_2} \quad (5.62)$$

$$d^3 p'_1 = p_{cm}^2 dp_{cm} d\Omega \quad (5.63)$$

$$d(E'_1 + E'_2) = d \left(\sqrt{p_{cm}^2 + M_1'^2} + \sqrt{p_{cm}^2 + M_2'^2} \right) = \left(\frac{1}{E'_1} + \frac{1}{E'_2} \right) p_{cm} dp_{cm} \quad (5.64)$$

Here p_{cm} is the momentum of the reaction products in the center of mass frame, which was introduced in Eq. (5.16). After the change of variables to $E'_1 + E'_2$ and integration over the remaining delta-function, taking into account that in the CM-frame $(E_1 + E_2)^2 = s$ and $I = p_{cm}(E_1 + E_2)$,

$$d\sigma/d\Omega = \frac{1}{64\pi^2 s} |M_{if}|^2 \frac{p_{cm}(s, M_1', M_2')}{p_{cm}(s, m_1, m_2)} \frac{1}{1 + \delta_{1'2'}} \mathcal{A}_1(M_1'^2) \mathcal{A}_2(M_2'^2) dM_1'^2 dM_2'^2 \quad (5.65)$$

Finally, in SMASH spin is not an explicit degree of freedom and one has to average matrix element over spins of the produced particles:

$$d\sigma/d\Omega = \frac{1}{64\pi^2 s} \frac{(2S'_1 + 1)(2S'_2 + 1)}{1 + \delta_{1'2'}} |M_{if}|^2 \frac{p_{cm}(s, M'_1, M'_2)}{p_{cm}(s, m_1, m_2)} \mathcal{A}_1(M_1'^2) \mathcal{A}_2(M_2'^2) dM_1'^2 dM_2'^2 \quad (5.66)$$

For numerical simulations it is useful to obtain expressions connecting the cross-section of the forward reaction to the one of the reverse reaction. It is assumed that in the forward reaction two incoming particles are stable with pole masses m_1 and m_2 and the outgoing particles are possibly unstable and their off-shell masses are not yet known, they will only be sampled after the cross-section is computed and the reaction takes place. In this way it is easy to understand why the forward reaction cross-section is averaged over the spectral functions of products.

$$d\sigma_{12 \rightarrow 1'2'}/d\Omega = \frac{1}{64\pi^2 s} \frac{(2S'_1 + 1)(2S'_2 + 1)}{1 + \delta_{1'2'}} |M_{if}(s)|^2 \times \frac{\int p_{cm}(s, M'_1, M'_2) \mathcal{A}_1(M_1'^2) \mathcal{A}_2(M_2'^2) dM_1'^2 dM_2'^2}{p_{cm}(s, m_1, m_2)} \quad (5.67)$$

In the reverse reaction incoming products already have particular off-shell masses M_1 and M_2 and they will form stable particles with masses m_1 and m_2 . Then for the reverse reaction

$$d\sigma_{1'2' \rightarrow 12}/d\Omega = \frac{1}{64\pi^2 s} \frac{(2S_1 + 1)(2S_2 + 1)}{1 + \delta_{12}} |M_{fi}(s)|^2 \frac{p_{cm}(s, m_1, m_2)}{p_{cm}(s, M_1, M_2)} \quad (5.68)$$

The matrix elements in Eqs. (5.67 - 5.68) are equal as discussed in section 5.3.3. Dividing the Eq. (5.67) over the Eq. (5.68) one obtains the detailed balance relation for cross-sections

$$\frac{d\sigma_{12 \rightarrow 1'2'}/d\Omega}{d\sigma_{1'2' \rightarrow 12}/d\Omega} = \frac{(2S'_1 + 1)(2S'_2 + 1)}{(2S_1 + 1)(2S_2 + 1)} \frac{1 + \delta_{12}}{1 + \delta_{1'2'}} \times \frac{p_{cm}(s, M_1, M_2) \int p_{cm}(s, M'_1, M'_2) \mathcal{A}_1(M_1'^2) \mathcal{A}_2(M_2'^2) dM_1'^2 dM_2'^2}{p_{cm}^2(s, m_1, m_2)} \quad (5.69)$$

Detailed balance relations for $2 \rightarrow 1$ reactions

Similarly to equation (5.61) for $2 \rightarrow 2$ reactions one can express the cross-section for $2 \rightarrow 1$ reactions $ab \rightarrow R$ with masses m_1, m_2 and M_R :

$$d\sigma = (2\pi)^{-2} \delta^{(4)}(P_i - P_f) |M_{if}|^2 \frac{1}{4I} \frac{d^3 p_R}{2E_R} \mathcal{A}_R(M_R^2) dM_R^2 \quad (5.70)$$

Performing the same transformations as for the $2 \rightarrow 2$ case and taking into account that $M_R^2 = s$ one arrives at

$$\sigma_{ab \rightarrow R} = \frac{\pi}{2} |M_{if}|^2 \frac{1}{\sqrt{s} p_{cm}(\sqrt{s}, m_1, m_2)} \mathcal{A}_R(s) \quad (5.71)$$

For the reverse decay $R \rightarrow ab$ with possibly unstable products the equation (5.52) for the probability to decay per unit time is rewritten in the same way as for $2 \rightarrow 2$ reactions resulting in

$$dw = \frac{d\Omega}{(2\pi)^2} |M_{fi}|^2 \frac{\int p_{cm}(\sqrt{s}, m'_1, m'_2) \mathcal{A}_1(m_1'^2) \mathcal{A}_2(m_2'^2) dm_1'^2 dm_2'^2}{8s} \frac{1}{1 + \delta_{ab}} \quad (5.72)$$

Integrating over $d\Omega$ and recalling that the probability to decay per unit time is the resonance width Γ one finds

$$\Gamma_{R \rightarrow ab} = \frac{|M_{fi}|^2}{8\pi s} \int p_{cm}(\sqrt{s}, m'_1, m'_2) \mathcal{A}_1(m_1'^2) \mathcal{A}_2(m_2'^2) dm_1'^2 dm_2'^2 \frac{1}{1 + \delta_{ab}} \quad (5.73)$$

Note that from this equation follows the expression for the off-shell width, Eq. (5.14), only without the Blatt-Weisskopf factor and the form factor. The latter originate from the matrix element, which here is assumed to depend only on s . Averaging matrix elements over spin and taking the ratio of Eq. (5.71) to Eq. (5.73) one obtains the detailed balance relation

$$\sigma_{ab \rightarrow R} = \Gamma_{R \rightarrow ab} \frac{2S_R + 1}{(2S_1 + 1)(2S_2 + 1)} (1 + \delta_{ab}) \frac{4\pi^2}{p_{cm}(\sqrt{s}, m_1, m_2) \rho(\sqrt{s})} \mathcal{A}_R(s) \quad (5.74)$$

$$\rho(\sqrt{s}) = \int \frac{p_{cm}(\sqrt{s}, m'_1, m'_2)}{\sqrt{s}} \mathcal{A}_1(m_1'^2) \mathcal{A}_2(m_2'^2) dm_1'^2 dm_2'^2 \quad (5.75)$$

With the additional Blatt-Weisskopf factor B_L and a form factor from Eq. (5.21) $\rho(\sqrt{s})$ is defined as in Eq. 5.15. Furthermore, one can introduce the so-called 'in-width':

$$\Gamma_{ab \rightarrow R}^{in} = \Gamma_{R \rightarrow ab}^0 \frac{p_{cm}(\sqrt{s}, m_1, m_2) B_L^2(p_{cm} R) \mathcal{F}_{ab}^2(\sqrt{s})}{\sqrt{s} \rho_{ab}(M_R^0)} \quad (5.76)$$

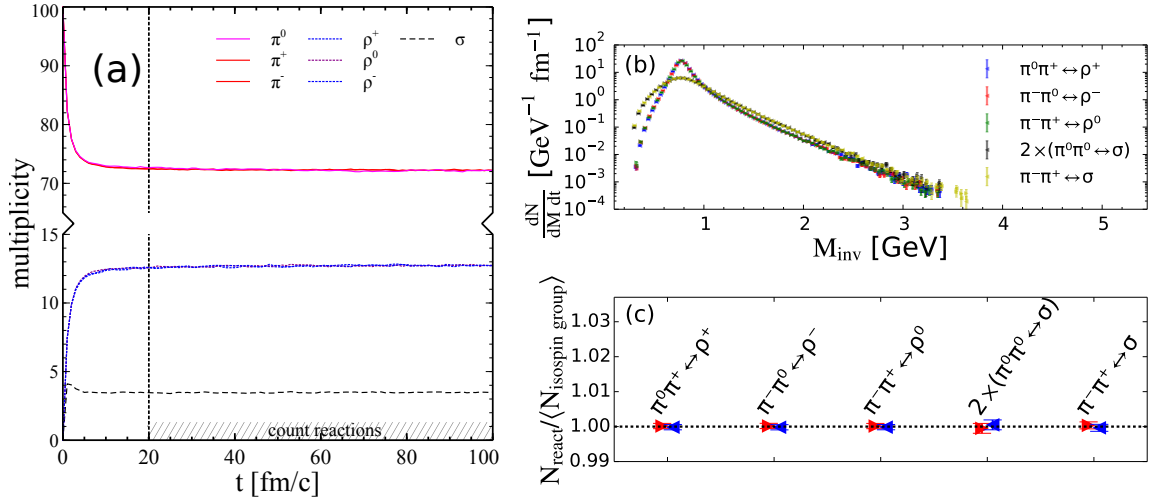


Figure 5.7.: Test of the detailed balance for the π - ρ - σ system in a box with periodic boundary conditions. Multiplicities versus time (a), scaled numbers of forward and backward reactions for $t > 20$ fm/c (c), and the same differentially versus the invariant mass of the reaction, which is equal to the resonance mass in this case (b).

Note that for stable decay products of the resonance it coincides with the resonance width. With this definition the detailed balance relation is rewritten in the following form:

$$\sigma_{ab \rightarrow R} = \Gamma_{R \rightarrow ab}^{in} \frac{2S_R + 1}{(2S_1 + 1)(2S_2 + 1)} (1 + \delta_{ab}) \frac{4\pi^2}{p_{cm}^2(\sqrt{s}, m_1, m_2)} \mathcal{A}_R(s) \quad (5.77)$$

Testing detailed balance in SMASH

In section 5.3.3 it was shown that from the time reversal symmetry of elementary interactions it follows that matrix elements of forward and reverse reactions are identical and in thermal equilibrium forward and reverse reaction rates should be equal. In SMASH cross-sections are implemented in such a way that the detailed balance principle is respected: if there is a forward reaction then the reverse one is always implemented and the cross-sections satisfy the detailed balance relations given in the section 5.3.3.

To test, if detailed balance actually holds in the calculations, a periodic box was initialized with multiple particle species. After the matter reaches equilibrium, it was verified that the rates of forward and backward reactions are identical within statistical errors. The fact that the box should reach equilibrium is granted by the H-theorem, which is derived assuming time reversal invariance and the hypothesis of molecular

chaos (Eq. 1.22). Strictly speaking, in a transport code both assumptions are valid only in the limit $N_{\text{test}} \rightarrow \infty$. At finite N_{test} the interactions are non-local due to the geometrical cross sections. In addition, while two particles with space coordinates \vec{r}_1 and \vec{r}_2 form a resonance at $(\vec{r}_1 + \vec{r}_2)/2$, the products of resonance decay obtain the same position as the decaying resonance. This breaks the time reversal invariance and may lead to a small violation of detailed balance, which vanishes at large N_{test} . This is indeed what occurs, as it is shown further.

For the test two configurations were used: a $\rho - \pi - \sigma$ box and a $N - \pi - \Delta$ box. The first one was initialized with a 100 π^+ , 100 π^- and 100 π^0 in a volume of $V = (10 \text{ fm})^3$. The reactions $\pi\pi \leftrightarrow \rho$ and $\pi\pi \leftrightarrow \sigma$ were allowed, while all the other possible reactions were switched off. From Fig. 5.7 one observes that the system has reached chemical equilibrium, since the particle multiplicities in the box have saturated after around $t = 20 \text{ fm}/c$. Starting from this time, forward and backward reactions were counted. The matrix elements of reactions in the same isospin group differ only by Clebsch-Gordan coefficients. Thus one expects, for example, that the number of reactions $N(\sigma \leftrightarrow \pi^+\pi^-) = 2N(\sigma \leftrightarrow \pi^0\pi^0)$. Therefore, the reaction numbers in Fig. 5.7 were scaled by the isospin and symmetry factors appropriately to make sure that this expectation is fulfilled. Detailed balance is valid not only for the total number of reactions, but it also has to be fulfilled differentially in momentum space. It is demonstrated in Fig. 5.7 that detailed balance is indeed fulfilled differentially in each invariant mass bin of the reaction. Note that for the $\rho - \pi - \sigma$ box detailed balance for the total (but not differential) number of reactions follows trivially from the multiplicity saturation.

However, this is not the case for the $N - \pi - \Delta$ system. The $N - \pi - \Delta$ box was initialized with 100 neutrons and 100 protons. The reactions $\Delta \leftrightarrow N\pi$, $NN \leftrightarrow N\Delta$ and $NN \leftrightarrow \Delta\Delta$ were allowed, with all the other reactions being forbidden. As demonstrated in Fig. 5.8 for $N_{\text{test}} = 100$ detailed balance is violated at maximum by 2%. For $N_{\text{test}} = 1$ this violation can reach 10% presumably because of the non-locality effect described above.

To see if the numbers of reactions within one isospin group relate as expected from Clebsch-Gordan factors, every number of reactions N_i is multiplied by a factor α_i that compensates for the isospin factors of this reaction. Let us denote $\langle N_{\text{isospin group}} \rangle = \frac{1}{k} \sum_{i=1}^k \alpha_i N_i$, where k is amount of reactions in the isospin group (forward + backward). If the SMASH result corresponds to the theoretical expectation, then $N_i / \langle N_{\text{isospin group}} \rangle$ should be strictly 1 for every reaction. One can extract from Fig. 5.7 and from Fig. 5.8

that SMASH matches this expectation. Table 5.3 shows the origin of compensating coefficients α_j . While most of the Clebsch-Gordan factors are simple, for $pn \leftrightarrow \Delta\Delta$ reactions they are less intuitive. The matrix element for $NN \leftrightarrow \Delta\Delta$ reaction is isospin dependent, namely $|M(I=0)|^2 = \kappa|M(I=1)|^2$, where $\kappa = \frac{8}{3}$. Here is one explicit example illustrating the calculation (where states beyond $I=1$ have been omitted, since they drop out):

$$|pn\rangle = \sqrt{\frac{1}{2}}|I=1\rangle + \sqrt{\frac{1}{2}}|I=0\rangle \quad (5.78)$$

$$|\Delta^-\Delta^{++}\rangle = \dots + \sqrt{\frac{9}{20}}|I=1\rangle - \sqrt{\frac{1}{4}}|I=0\rangle \quad (5.79)$$

$$\langle pn|\Delta^-\Delta^{++}\rangle^2 = \frac{9}{40}|M(I=1)|^2 + \frac{5}{40}|M(I=0)|^2 \quad (5.80)$$

$$\langle pn|\Delta^-\Delta^{++}\rangle^2 = \frac{5\kappa+9}{40}|M(I=1)|^2 \quad (5.81)$$

Therefore, the detailed balance in SMASH for a mesonic system and a more complex situation involving baryons and mesons is fulfilled.

5.3.4. Potentials

To create a more realistic simulation at low beam energies, a minimal version of mean-field potentials between nucleons is included in the BUU way (see section 1.3.5), i.e. with potentials dependent on local density rather than distances between particles. The equations of motions follow from the one-particle Hamiltonian H_i

$$H_i = \sqrt{\vec{p}_i^2 + m_{eff}^2} + U(\vec{r}_i), \quad (5.82)$$

where m_{eff} is the mass for stable hadrons and the effective mass for resonances in accordance with their mass distribution (e.g. Breit-Wigner). At this point, the potential depends only on the coordinates, but not on the momentum of the particles. The corresponding equations of motion are then

$$\frac{d\vec{r}_i}{dt} = \frac{\partial H_i}{\partial \vec{p}_i} = \frac{\vec{p}_i}{\sqrt{\vec{p}_i^2 + m_{eff}^2}}, \quad (5.83)$$

$$\frac{d\vec{p}_i}{dt} = -\frac{\partial H_i}{\partial \vec{r}_i} = -\frac{\partial U}{\partial \vec{r}_i}. \quad (5.84)$$

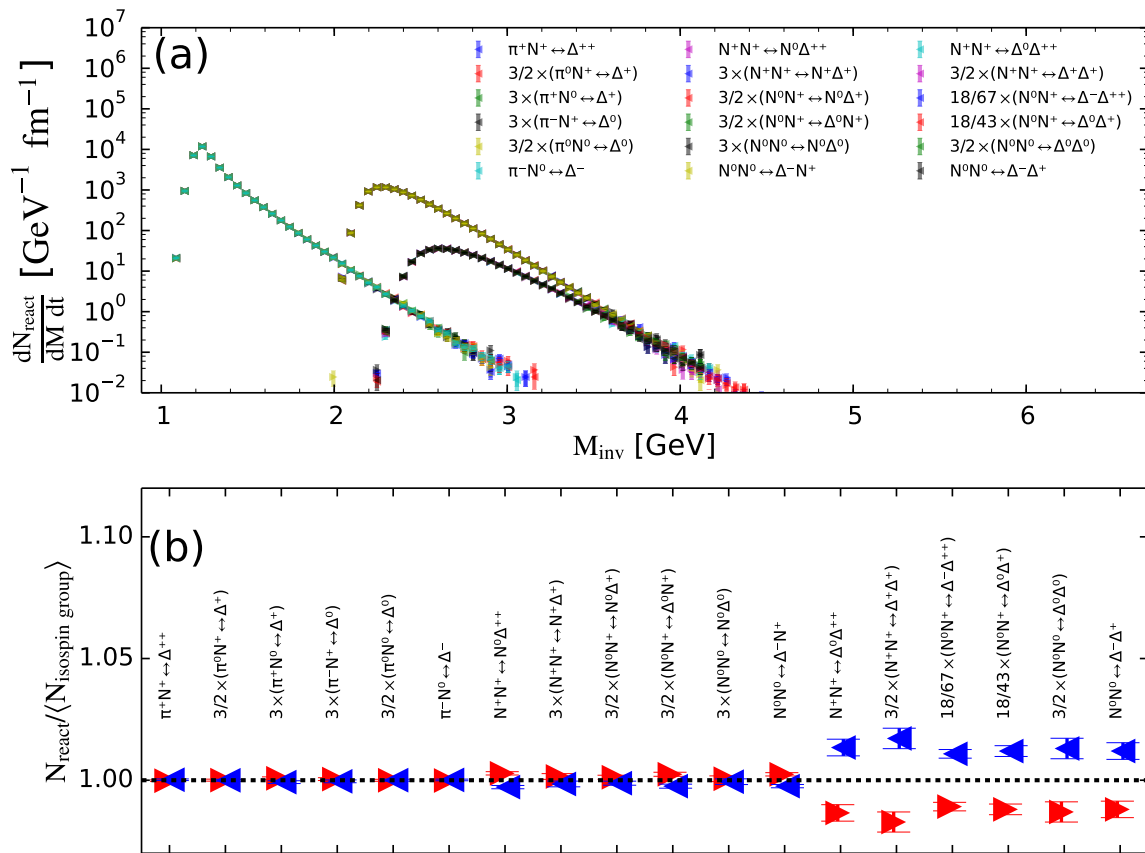


Figure 5.8.: Scaled numbers of forward (triangles right) and backward (triangles left) reactions for $t > 80 \text{ fm}/c$ π - N - Δ (b) and the same differentially in the invariant mass of reaction (a).

Reaction	Clebsch	Symmetry	Total
$\rho^+ \rightarrow \pi^+ \pi^0$	1/2	1	1/2
$\rho^- \rightarrow \pi^- \pi^0$	1/2	1	1/2
$\rho^0 \rightarrow \pi^0 \pi^0$	0	1/2	0
$\rho^0 \rightarrow \pi^+ \pi^-$	1/2	1	1/2
$\sigma \rightarrow \pi^+ \pi^-$	1/3	1	2/6
$\sigma \rightarrow \pi^0 \pi^0$	1/3	1/2	1/6
$p\pi^+ \rightarrow \Delta^{++}$	1	1	3/3
$p\pi^0 \rightarrow \Delta^+$	2/3	1	2/3
$p\pi^- \rightarrow \Delta^0$	1/3	1	1/3
$n\pi^+ \rightarrow \Delta^+$	1/3	1	1/3
$n\pi^0 \rightarrow \Delta^0$	2/3	1	2/3
$n\pi^- \rightarrow \Delta^-$	1	1	3/3
$pp \rightarrow p\Delta^+$	1/4	1/2	1/8
$pp \rightarrow n\Delta^{++}$	3/4	1/2	3/8
$pn \rightarrow n\Delta^+$	1/4	1	2/8
$pn \rightarrow p\Delta^0$	1/4	1	2/8
$nn \rightarrow p\Delta^-$	3/4	1/2	3/8
$nn \rightarrow n\Delta^0$	1/4	1/2	1/8
$pp \rightarrow \Delta^0 \Delta^{++}$	6/20	1/2	18/120
$pp \rightarrow \Delta^+ \Delta^+$	8/20	1/4	12/120
$pn \rightarrow \Delta^- \Delta^{++}$	67/120	1	67/120
$pn \rightarrow \Delta^+ \Delta^0$	43/120	1	43/120
$nn \rightarrow \Delta^+ \Delta^-$	6/20	1/2	18/120
$nn \rightarrow \Delta^0 \Delta^0$	8/20	1/4	12/120

Table 5.3.: Expected isospin and symmetry factors for number of reactions within isospin groups at equilibrium. The first numeric column is a Clebsch-Gordan factor, the second column is symmetry factor, the third one is their product.

In this formulation, as in any BUU approach, momentum conservation is fulfilled only on average. Event by event momentum conservation requires that $d\vec{p}_i/dt = -\partial H_{\text{tot}}/\partial \vec{r}_i$, where $H_{\text{tot}} = \sum_i H_i$. The potential is calculated as a function of the local density

$$U = a(\rho/\rho_0) + b(\rho/\rho_0)^\tau \pm 2S_{\text{pot}} \frac{\rho_{I3}}{\rho_0} \quad (5.85)$$

Here ρ is the Eckart rest frame baryon density and ρ_{I3} is the Eckart rest frame baryon isospin density of the relative isospin projection I_3/I . The density calculation is described in section 5.4. $\rho_0 = 0.1681/\text{fm}^3$ is the nuclear ground state density. Parameters for the Skyrme potential are by default set to $a = -209.2$ MeV, $b = 156.4$ MeV and $\tau = 1.35$, while $S_{\text{pot}} = 18$ MeV is the default value for the symmetry potential. These parameters were agreed on for a recent transport code comparison [207] and correspond to a rather soft potential with an incompressibility of $K = 240$ MeV. For the equations of motion one does not need the potential itself, but its gradient, $\partial U/\partial \vec{r}$. In the symmetry term the positive sign is applied for the potential acting on neutrons and the minus sign is applied for the potential acting on protons. Currently, the potential acts only on baryons. The potentials are always calculated after the actions are performed, right when the propagation happens.

Note that electromagnetic potentials (Coulomb and Lorentz force) are currently being neglected in the model, since they are typically much weaker than the hadronic mean fields (even if they are more long-ranged). The Coulomb potential can only play a role for collisions of large nuclei at very low energies and is completely negligible at higher energies (FAIR/RHIC/LHC).

Fig. 5.9 shows the nuclear stability over a large time range, much larger than what is actually relevant for a nucleus-nucleus collision. The nucleons fly apart as expected, if only Fermi motion without potentials to stabilize the nucleus are included. With potentials there is the expected oscillatory behavior: The nucleons drift apart due to Fermi motion and the potentials counteract and push them closer together again. One can also observe the oscillations of the nucleus during the propagation. This can be avoided if the nucleus is initialized in its ground state [267]. The observed oscillations are called a giant monopole resonance or a "breathing mode" of the nucleus.

Computations with potentials require that time step is small enough - the energy change per timestep should be much smaller than the energy of the particle:

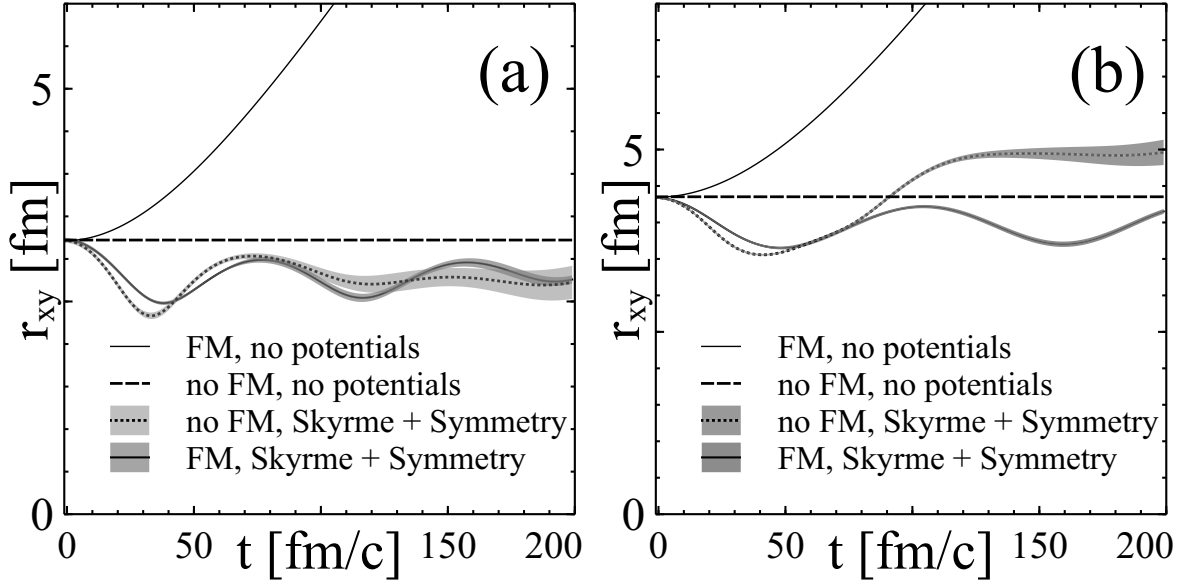


Figure 5.9.: Evolution of an average transverse radius $r_{xy} = \sqrt{\langle x^2 + y^2 \rangle}$ of a nucleus over 200 fm/c with different combinations of Fermi motion (FM) and potentials, ^{29}Cu nucleus (a) and ^{79}Au nucleus (b).

$$\frac{\Delta E}{E} \simeq \frac{|\partial U / \partial r| \Delta t}{E} \ll 1. \quad (5.86)$$

5.3.5. Pauli blocking

Pauli blocking is an effective way to obtain the solution of the quantum BUU equation, Eqs. (1.24-1.25), from classical molecular dynamics. Indeed, the BUU equations differ from the Boltzmann equations only by $(1 \pm f)$ factors in the collision integral. Here the plus sign is for bosons and the minus sign for fermions. One can interpret these factors as a multiplication of the cross sections by $\prod_i (1 \pm f_i)$, where the product is taken over all final states in the reaction and $f_i \equiv f(r_i, p_i, t)$ is the phase-space density of final-state particle i . This means that for bosons cross sections are effectively increased and for fermions cross sections are effectively decreased. This is called Bose enhancement and Pauli-blocking respectively. While Bose enhancement has been attempted to implement recently in a parton cascade [288], Pauli blocking is taken into account in many transport approaches. It is known to be especially important at low collision energies.

The implementation of Pauli blocking consists of two parts: the calculation of the phase-space density and the rejection of reactions with probability $1 - \prod_i (1 - f_i)$. For

the latter SMASH loops over all baryons in the final state after a collision has taken place and returns 'true' for blocking, if a uniformly distributed random number $r > f_i$. This means that the reaction is not blocked with probability $\prod_i(1 - f_i)$. In this way, no fermion should be produced or scatter into a phase space bin that is already occupied by another fermion.

The implementation of the phase space density calculation basically follows the method used in the GiBUU model, see section D.4.3 in [200]. By definition $N(\Delta V_r, \Delta V_p) = gf(r, p)\Delta V_r\Delta V_p$, where N is the number of (test)particles in a given phase-space volume $\Delta V_r\Delta V_p$ and g is the degeneracy. Theoretically, the size of the phase-space goes to zero $\Delta V_r, \Delta V_p \rightarrow 0$. In practice $\Delta V_r, \Delta V_p$ and the way of averaging are chosen to balance between the smoothness of the obtained distribution function and the resolution of coordinate and momentum space. This implementation relies on a large number of test particles ($N_{test} > 20$).

The phase-space density is calculated according to the following equations:

$$f_i(r_j, p) = \sum_{j:p_j \in V_p} \frac{1}{\kappa(2\pi\sigma^2)^{3/2}} \int_{\Delta V_r, |r-r_j| < r_c} d^3r \times \exp\left(-\frac{(r-r_j)^2}{2\sigma^2}\right) \quad (5.87)$$

with κ given as

$$\kappa = \frac{2\Delta V_r\Delta V_p N}{(2\pi)^3} \frac{4\pi}{(2\pi\sigma^2)^{3/2}} \int_0^{r_c} dr \times r^2 \exp\left(-\frac{r^2}{2\sigma^2}\right) \quad (5.88)$$

Here \vec{r}_j is a vector connecting the point, where f is calculated, and the position of the j -th particle. All these expressions can be analytically further evaluated for $r_c > r_r$. This is a reasonable assumption, because the Gaussian cut-off r_c has to be large enough, so that the results do not depend on it. If $r_c < r_r$ the whole method is hardly applicable. In GiBUU these integrals are computed numerically, but analytical expressions for them also exist (see appendix of [5]). For V_p a sphere of radius 80 MeV is taken.

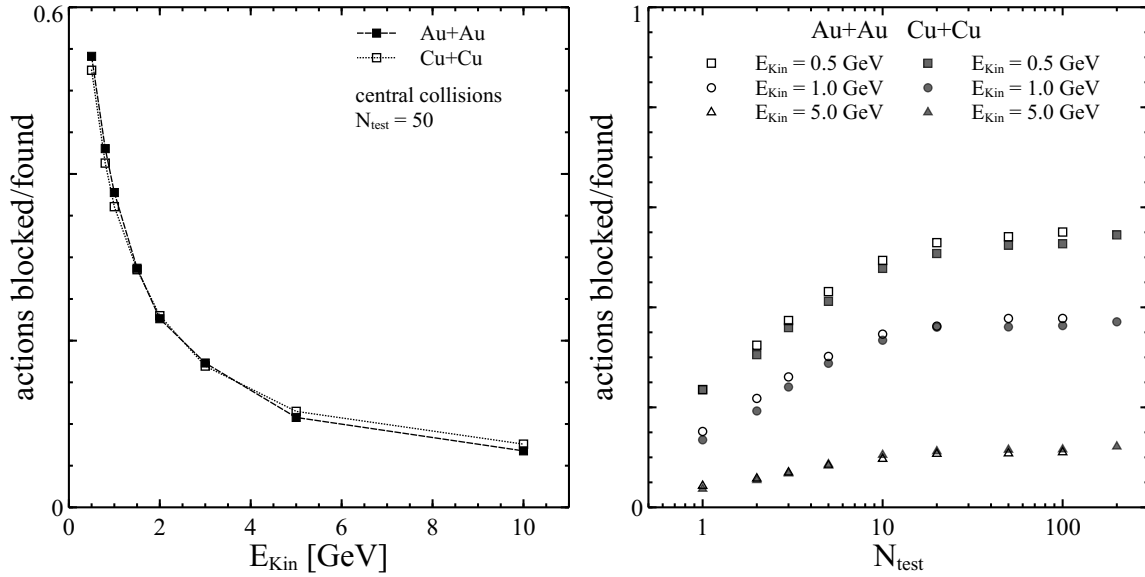


Figure 5.10.: Left panel: Ratio of Pauli blocked to total found actions in Cu+Cu and Au+Au collisions at different beam energies. For reference, the total number of found actions per event (both blocked and performed) in an Au+Au collision at $E_{\text{kin}} = 0.5 \text{ A GeV}$ is $0.99 \cdot 10^5$, for $E_{\text{kin}} = 5 \text{ A GeV}$ it constitutes $1.32 \cdot 10^5$. The number of test particles used in the simulation is $N_{\text{test}} = 50$. Right panel: Ratio of Pauli blocked to total found actions in Cu+Cu (filled symbols) and Au+Au (open symbols) collisions for different numbers of test particles.

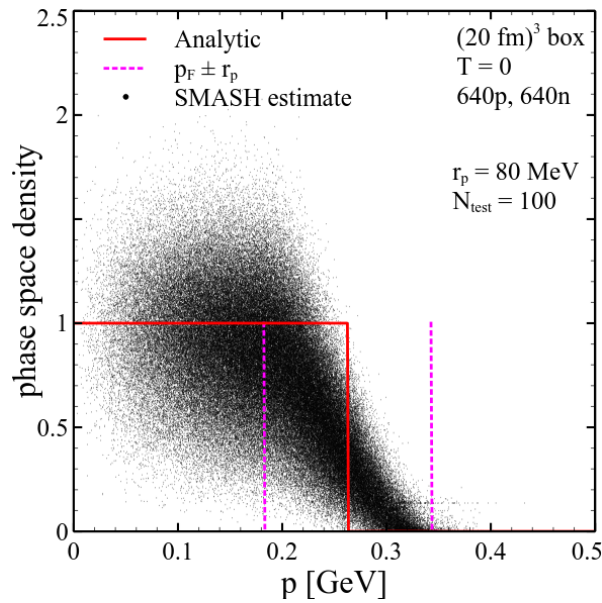


Figure 5.11.: Estimated distribution function at collision points is compared to analytical one. Periodic $(20 \text{ fm})^3$ box filled with 640 protons and 640 neutrons that are only allowed to collide elastically. The initial distribution is Fermi-Dirac distribution at zero temperature, so all the collisions should ideally be blocked.

In Fig. 5.10 the number of collisions that is blocked due to prior phase space occupation has been calculated in central Cu+Cu and Au+Au collisions as a function of beam energy. One can see that at very low energies there are as many blocked collisions compared to collisions taking place. The ratio drops rather fast and around $E_{kin} = 2A$ GeV only a quarter of the collisions are blocked. It then saturates around 10% for higher beam energies.

The right panel of Fig. 5.10 demonstrates the need for a decent number of test particles to obtain stable results. If the number of test particles is low the phase-space volume cannot be calculated with enough precision and therefore, there are too many collisions allowed. Saturation sets in around $N_{test} = 20$ and is very similar for Au+Au and Cu+Cu collisions.

One can notice from Fig. 5.10 that even for a very large number of testparticles there are collisions inside the nucleus, which should never happen in nature. To demonstrate how these collisions occur, a box with periodic boundaries is initialized with Fermi-Dirac distribution at zero temperature. In this case no collisions should be allowed, because analytically $f = 1$. The estimated values of the phase-space density f are shown in Fig. 5.11. The estimation of the phase-space density employs smearing, so the sharp boundary in momentum space is smeared and f is underestimated for $p < p_F$ and overestimated for $p > p_F$. This effect is significant within the momentum smearing radius $|p - p_F| < r_p$. For low momenta *in average* f is estimated correctly, but any underestimation in particular events unavoidably causes unwanted collisions.

Since collisions in the nucleus cannot be completely avoided using Pauli-blocking, sooner or later the nucleus thermalizes due to these collisions. To avoid this unwanted effect in SMASH collisions within a nucleus are explicitly forbidden unless the nucleon has already collided with some external particle.

5.4. Thermodynamics in the SMASH transport approach

5.4.1. Thermodynamic quantities from coarse-grained SMASH

Thermodynamic quantities such as net baryon density, total number density, energy density, temperature, chemical potentials (baryon, strangeness, isospin, etc) are necessary in several cases. Firstly, densities are used to compute potentials (see section 5.3.4). Secondly, they are needed for the forced thermalization (chapter 6). Thirdly,

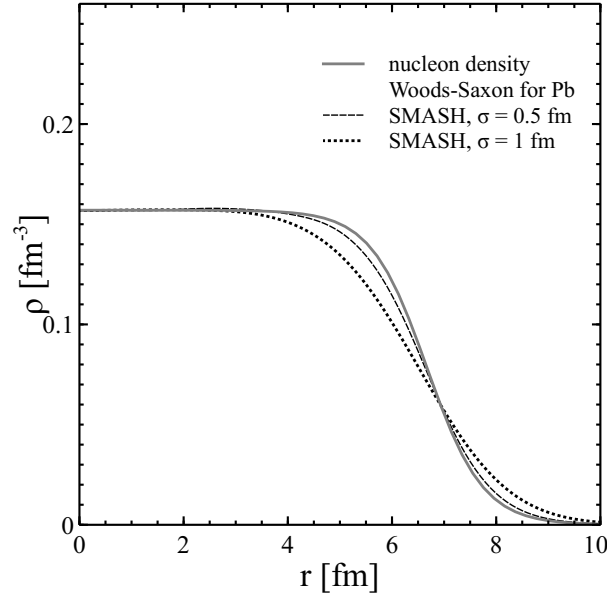


Figure 5.12.: Baryon density estimated in SMASH simulation with smearing $\sigma = 0.5$ fm (dashed line) and 1.0 fm (dotted line) is compared to the true density profile (solid line). Large $N_{\text{test}} = 1000$ for $\sigma = 1$ fm and $N_{\text{test}} = 10000$ for $\sigma = 0.5$ fm is taken to diminish fluctuations.

thermodynamic quantities are very useful to visualize heavy ion collisions, since they represent both coordinate and momentum space in an intuitively simple way.

The first step to compute thermodynamic quantities is constructing four-currents and energy-momentum tensor

$$T^{\mu\nu}(\vec{r}) = \frac{1}{N_{\text{ev}}N_{\text{test}}} \sum_{\text{events}} \sum_i \frac{p_i^\mu p_i^\nu}{p_i^0} K(\vec{r} - \vec{r}_i, p_i) \quad (5.89)$$

$$j^\mu(\vec{r}) = \frac{1}{N_{\text{ev}}N_{\text{test}}} \sum_{\text{events}} \sum_i \frac{p_i^\mu}{p_i^0} K(\vec{r} - \vec{r}_i, p_i), \quad (5.90)$$

where N_{ev} is the number of events and N_{test} is the test particle number. The formulas were derived in section 2.1, an explicit form of the used smearing kernel K (Eq. 2.26) is suggested and justified in the same section. In the limit of the smearing width $\sigma \rightarrow 0$ and $N_{\text{ev}}N_{\text{test}} \rightarrow \infty$ the full smooth quantities are obtained. This limit is numerically challenging, because when reducing the smearing width σ , one has to increase statistics, keeping $\sigma^3 N_{\text{ev}}N_{\text{test}} = \text{const}$. Therefore, one takes a reasonably small $\sigma = 1$ fm and keeps in mind the smearing effect, which is demonstrated in Fig. 5.12 for the density calculation of a Pb nucleus comparing $\sigma = 0.5$ fm and 1 fm.

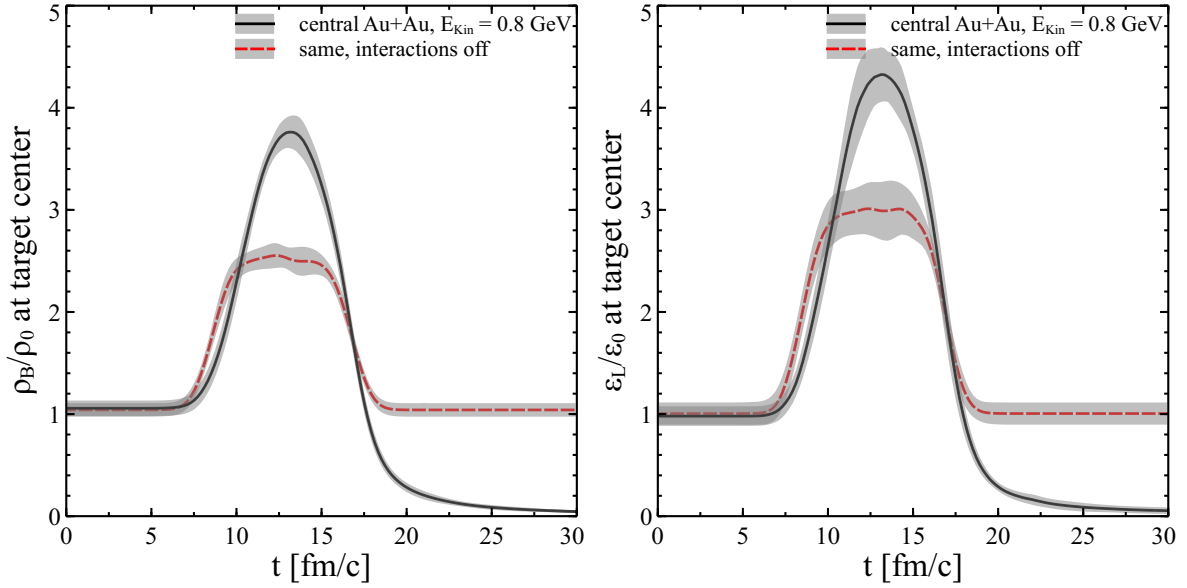


Figure 5.13.: Eckart rest frame net baryon density ρ_B (left panel) and Landau rest frame hadron density ϵ (right panel) at the target center in central Au+Au collision at $E_{\text{lab}} = 0.8$ A GeV in units of the ground state nuclear density ρ_0 / ground state nuclear energy density $\epsilon_0 = 0.150$ GeV/fm³. Simulation is performed in the fixed target frame. Time dependence for the full SMASH simulation (full line) is compared to the SMASH simulation with all interactions off (dashed line).

The next step is to transform $T^{\mu\nu}$ and j^μ to a local rest frame. In principle, there is a variety of possible rest frames, e.g. a frame of zero total/pion/baryon/etc momentum current; a frame of zero entropy current; a frame of zero total/baryon/electric/etc current; center of momentum frame and so on. All these frames only coincide in the case of ideal hydrodynamics. For a coarse-grained transport they are different in general.

SMASH uses three rest frames: Landau rest frame (zero total momentum current or equivalently $T^{0i} = 0$ for $i = 1, 2, 3$), net baryon Eckart frame (zero net baryon current of $j_B^{0i} = 0$ for $i = 1, 2, 3$) and net $\frac{I_3}{T}$ Eckart rest frame. The latter two are currently used to compute baryon density and net $\frac{I_3}{T}$ density, which stand in the expression for potentials (Eq. 5.85).

Since $j^\mu j_\mu$ is relativistically invariant, the Eckart rest frame density is obtained as $\rho_{\text{Eck}} = \sqrt{j^\mu j_\mu}$. For net baryon (charge, isospin projection) density a naive weighting of particles in Eq. (5.90) with their baryon numbers can give rise to $j^\mu j_\mu < 0$, meaning that Eckart frame is undefined. To avoid this, the density is computed as $\rho = \rho^+ - \rho^-$, where + corresponds to positive baryon number (charge, isospin projection) and -

corresponds to negative ones. In the left panel of Fig. 5.13 the dependence of the net baryon density versus time in the middle of the target in the central Au+Au collision at $E_{\text{kin}} = 0.8A$ GeV in the fixed-target frame is shown. The energy density in the Landau frame is depicted in the same figure on the right panel. From these plots one can see that the ground state baryon/energy density values are reproduced, when the collision term is disabled. Including interactions the baryon/energy density rises to about 4 times the nuclear ground state densities.

The Landau rest frame (LRF) quantities in SMASH are used for the forced thermalization. The advantage of the Landau rest frame is that it is always well-defined. By definition, $T_{\text{LRF}}^{0i} = 0$, the energy flow in the LRF is zero. To find the LRF, one has to find such a Lorentz boost that after it $T^{0i} = 0$. To achieve this the generalized eigenvalue problem

$$(T^{\mu\nu} - \lambda g^{\mu\nu})h_\nu = 0 \quad (5.91)$$

is solved, where $g^{\mu\nu}$ is the metric tensor. The eigenvectors are normalized so that $h^\mu h_\mu = 1$. Note that this generalized eigenvalue problem is equivalent to a usual eigenvalue problem for T_ν^μ , however T_ν^μ is neither symmetric nor positively defined, so numerical solvers look for complex eigenvalues. In contrast, the above generalized eigenvalue decomposition of $T^{\mu\nu}$ always gives real eigenvalues, since it is symmetric and positively defined:

$$T^{\mu\nu} = \Lambda^T \text{diag}(\lambda_{1-4}) \Lambda, \quad (5.92)$$

where Λ is a matrix consisting of eigenvectors h_μ . Note that this eigenvector decomposition is identical to the Lorentz transformation from the rest frame, where the upper row of the boost matrix (Eq. 1.17) is the required boost four-velocity u^μ . At the same time the upper row is one of the generalized eigenvectors h^μ of $T^{\mu\nu}$. Therefore, to find the required boost one just has to choose the right eigenvector from the four solutions of the eigenvalue problem.

Notice that the eigenvalue corresponding to u^μ is the LRF energy density ϵ , the rest of the eigenvalues of T_ν^μ are non-positive and smaller by magnitude. One can see this immediately assuming that T_ν^μ is computed from particles directly in the LRF. Therefore, the normalized eigenvector corresponding to the largest (and the only positive) eigenvalue is the required 4-velocity of the LRF.

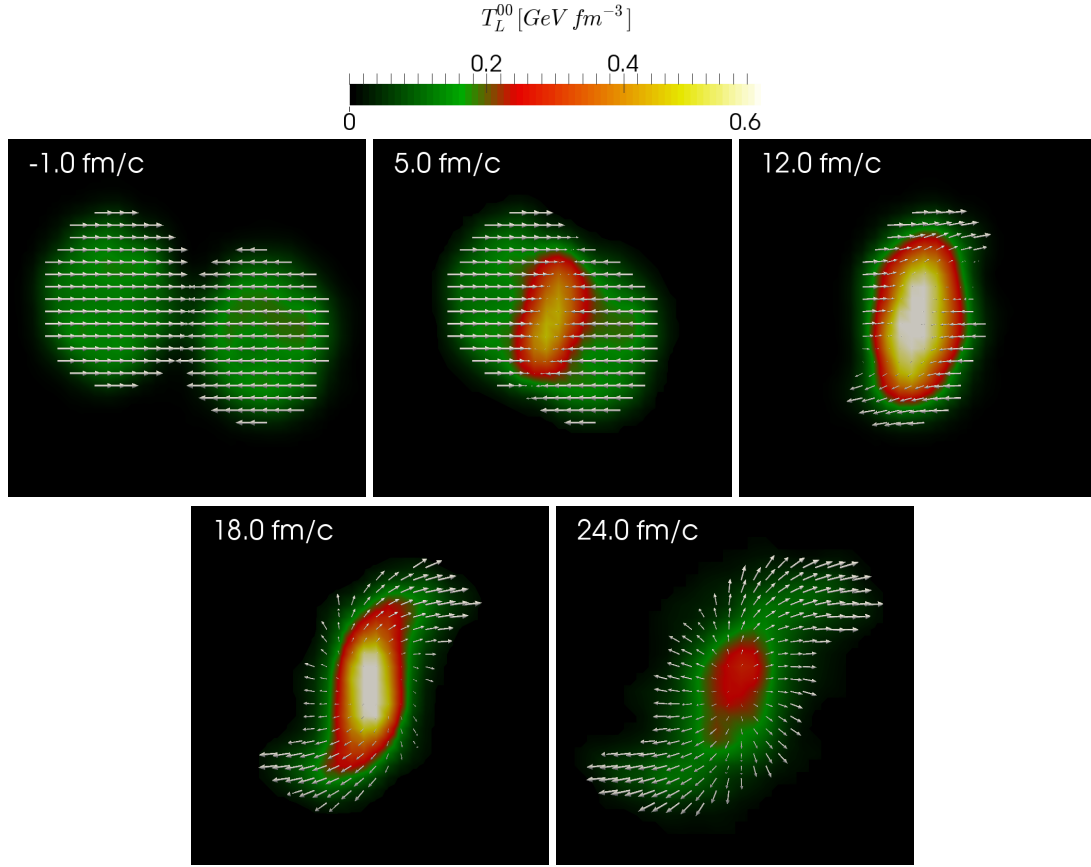


Figure 5.14.: Landau rest frame energy density T_L^{00} (background color) and velocity of Landau frame (arrows), both for baryons. Au+Au collision at $E_{\text{kin}} = 0.8A$ GeV with impact parameter $b = 3$ fm, $N_{\text{test}} = 20$. Color legend is given above. Velocity is proportional to the arrow length, maximal arrow length corresponds to velocity of $0.55 c$.

To demonstrate the result of this transformation the LRF energy density and collective velocities u^μ are plotted in the x - z -plane in Fig. 5.14 for a Au+Au collision. One can observe the onset of radial flow after the initial collision of the two nuclei. Note that the LRF energy density before collision reproduces again the nuclear ground state energy density.

5.4.2. SMASH equation of state

In Figure 5.15 the equation of state arising from SMASH is compared to UrQMD and to the parametrized lattice QCD equation of state from [289], which is used in many hydrodynamical calculations. The SMASH EoS is computed in two ways. First, the EoS of ideal gas consisting of all SMASH hadrons is calculated according to Eqs.

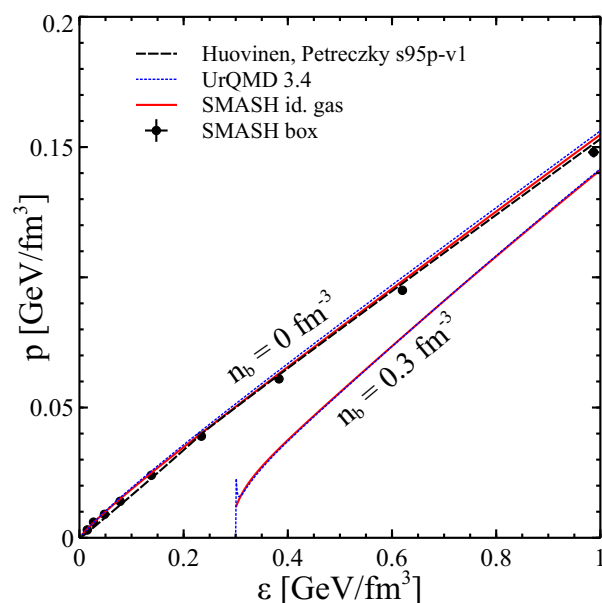


Figure 5.15.: Equation of State (EoS) comparison between ideal gas consisting of hadrons implemented in SMASH (solid lines), in UrQMD (dotted lines) and s95p-v1 QCD EoS from [289] (dashed line).

(2.58-2.60). This EoS does not take the effects of resonance widths into account. It is compared to SMASH EoS computed in a different way. A box with periodic boundary conditions is initialized with a set of hadrons, their multiplicities being computed according to an ideal gas EoS with pole masses. Then one waits for $1000 \text{ fm}/c$, until the mixture equilibrates (it is checked the hadron multiplicities saturate over time) and computes pressure and energy density. The results are plotted in Fig. 5.15: the SMASH box EoS only slightly deviates from the naive ideal gas EoS. The effects of non-zero widths tend to decrease pressure slightly at a given energy density.

Chapter 6.

Interpolating between hadronic transport and hydrodynamics using forced canonical thermalization

This chapter is based on [6]. As discussed in sections 1.3.4 and 1.3.5, the applicability of hydrodynamics requires that $l_{mfp} \ll L$ and the applicability of transport requires $l_{mfp} \gg \lambda_{Compton}$, where l_{mfp} denotes mean free path, L is size of the system and $\lambda_{Compton}$ is typical Compton wavelength. This complementarity of applicability regions of hydrodynamical and transport approaches makes hybrid approaches (see section 1.3.6) theoretically attractive, since in a hybrid approach each description is assumed to act in its region of applicability. Currently, the focus in heavy ion collision experiments is shifting towards intermediate collision energies (see section 1.2 for review of heavy ion experiments), at which the observation of the QCD critical point and the first order phase transition is expected. At the same time at intermediate energies the assumptions adopted by hybrid approaches become challenging.

A typical hybrid approach starts with generating an initial state, which can be highly anisotropic and includes event-by-event fluctuations. Then a rapid switch to relativistic hydrodynamics is performed, which neglects the initial anisotropy of the energy-momentum tensor. Hydrodynamical equations are solved in the forward light-cone until some late time. The particlization hypersurface (usually a constant temperature, energy density or Knudsen number hypersurface) is then determined, a Cooper-Frye particlization (section 2.3) is performed upon that surface, and particles are finally allowed to rescatter using hadronic transport. Note that in such approaches, hydrodynamical equations are solved even out of their region of applicability, where

the Knudsen number is large. The particlization hypersurface is determined a posteriori from hydrodynamics, but not from a dynamical condition considering both hydrodynamics and transport. Particles in the transport phase have no possibility to cause feedback to hydrodynamics, which leads to a well-known problem, the so-called negative Cooper-Frye contributions [1, 247, 248, 251]. At high collision energies, at midrapidity, which is the kinematical region studied by RHIC and LHC, negative Cooper-Frye contributions are negligible and the approximation adopted by hybrid approaches is justified. For lower energies they were estimated in the chapter 4 and can easily reach the level of 10% for hydrodynamics with smooth initial conditions. For event-by-event hydrodynamics they are practically unlimited.

Hydrodynamical and hybrid approaches could be completely substituted by transport models at low energies, but this presents two challenges. First, the equation of state does not explicitly enter the transport model, so it becomes impossible to study the equation of state directly, without specifying the degrees of freedom. Second, at high densities, multi-particle collisions and quantum interference effects gain importance, as the applicability condition $l_{mfp} \gg \lambda_{Compton}$ starts to be violated. As an example, the account of $p\bar{p}$ annihilations to many mesons and the inverse process of many-meson collisions is claimed to be essential to describe anti-proton and anti-Lambda yields at AGS [272], as well as yields at the LHC [290].

Here a simple approach that attempts to solve or avoid the above mentioned problems is explored. In a pure hadron transport model it is suggested to perform forced thermalization in the regions of high density. Physically, such thermalization corresponds to the extreme limit of N-particle collisions, so intense that thermalization happens rapidly, replacing the local distribution function by a thermal one. It follows from the H-theorem, that the thermalized state is unique and independent on the microscopic details of interaction, which makes it an easy case to consider. In fact such a treatment is conceptually very similar to a hybrid approach with Smoothed Particle Hydrodynamics [291], but here hydrodynamics and transport are dynamically coupled. Forced thermalization involves the EoS, thus allowing to explore the phase transition. The method is also similar to core-corona separation [217], but the thermalized and transport domains are coupled dynamically and transport can feedback to the thermalized regions. It remains applicable for small systems and at low collision energies, where hydrodynamics or hybrid approaches are not applicable. All this serves as a motivation to test and explore the implications of such an approach.

6.1. Performing forced canonical thermalization in SMASH

The forced canonical thermalization is implemented on top of the SMASH cascade approach described in detail in chapter 5 (specifically the version SMASH-0.9rc was used). The main assumption of this approach is that if the local rest frame energy density is high enough rapid thermalization occurs. In practice, the region Ω_{ϵ_c} where the local rest frame energy density ϵ is larger than some predefined ϵ_c is determined and particles in this region are substituted by new ones, sampled according to a thermal distribution conserving total energy, momentum and quantum numbers. In other words, the non-equilibrium distribution function is replaced by a thermal one in the transport approach at energy densities $\epsilon > \epsilon_c$. This treatment is ideologically similar to hybrid (hydrodynamical + transport) approaches, but here the boundary between the "hydrodynamical" and transport regions is found dynamically and not a posteriori; also negative Cooper-Frye contributions are not emerging in this approach.

Technically, forced thermalization consists of two steps - coarse-graining to determine the macroscopic densities and thermodynamic properties and the sampling of the new particles. To coarse-grain a Cartesian grid is spanned over the region of interest. The number of cells in each direction is a parameter, but its variation in a reasonable range does not influence results as shown later (see section 6.3). In each cell, the local energy-momentum tensor and the four-current are computed according to equations of section 2.1.3. In all simulations smearing width $\sigma = 1$ fm is taken, except for the simulations with the sphere setup, where $\sigma = 0.3$ fm is used to avoid too much smearing and allow for a reasonable comparison of the results to hydrodynamics. The rest-frame quantities are obtained using Eq. (2.36) with an ideal hadron gas equation of state (Eqs. 2.58-2.60). The list of hadrons in the equation of state coincides with the list of all hadrons available in SMASH. This equation of state is discussed in more detail in section 5.4.2.

After performing these steps, the information about the local rest-frame energy density $\epsilon(\vec{r})$, the temperature $T(\vec{r})$, the chemical potentials $\mu_B(\vec{r})$ and $\mu_S(\vec{r})$, and the local Landau rest frame velocity $v(\vec{r})$ is available in each cell of the grid. This allows to construct a region Ω_{ϵ_c} where $\epsilon > \epsilon_c$, from which particles are removed and new ones are sampled according to the local T , $\mu_{B,S}$ and v .

Since this sampling procedure is not uniquely defined, let us now discuss a few possible options. Denote the set of all conserved quantities (energy, momentum, baryon number, strangeness, electric charge, etc) in a given event in one cell by C_{cell} . The total conserved quantities in the thermalization region in this event are $C_{tot} = \sum C_{cell}$, where the sum goes over all thermalization cells.

The first option is to apply the Cooper-Frye formula to every cell, as it is done at the particlization in many hydrodynamical models. Then the conservation laws are fulfilled in every cell, but only in the event average. In the introduced notations, $\langle C_{cell}^{before} \rangle = \langle C_{cell}^{after} \rangle$, but $C_{cell}^{before} \neq C_{cell}^{after}$. The framework of a transport approach, used here, strictly respects conservation laws in each event, therefore it is desirable that the forced thermalization also follows conservation laws event-by-event.

Another option is to have exact event-by-event conservation laws, where $C_{tot}^{before} = C_{tot}^{after}$, but $C_{cell}^{before} \neq C_{cell}^{after}$ and $\langle C_{cell}^{before} \rangle \neq \langle C_{cell}^{after} \rangle$. This approach is applied for particlization in some hybrid models [163,230]. This method is applied here, because it is reasonably fast and provides a very good approximation to the next approach, when it goes about the distribution of total (not cell by cell) hadron multiplicities. In the next section the implications of this choice are investigated and its different algorithmic implementations are compared. Such a comparison makes this study useful for hybrid approaches, since it demonstrates how to perform particlization in a faster and more controlled way.

One more possibility is to perform microcanonical thermalization in each cell, so that $C_{cell}^{before} = C_{cell}^{after}$. This can in principle be done using the procedures described in [292] and [293] for every cell. In this case, it seems that T and μ are not necessary, but they are actually useful for initializing the Metropolis algorithm, as suggested in [293]. This method has two disadvantages: first, Metropolis sampling is slow and the need to perform it in $\sim 10^4$ of cells makes it almost not feasible. The other disadvantage is a sensitivity to the cell size and N_{test} : indeed, in the case of very small cells there is typically one or zero particles in the cell. Resampling this one particle conserving all quantum numbers will most probably lead to no change at all. At the same time, increasing N_{test} , one will find more than one particle in such a cell and thermalization results will change. So a combination of cell size and N_{test} becomes a physical parameter, characterizing a radius of interaction.

As mentioned, in this calculation the second method is used. The initial hadrons are substituted by a new set of hadrons distributed with probability

$$w(\vec{r}_i, p_i) \sim \prod_{\text{sorts}} \frac{1}{N_{\text{sort}}!} \prod_{i=1}^N \frac{d^3\vec{r}_i d^3\vec{p}_i}{(2\pi\hbar c)^3} e^{-(p_i^v u_v(\vec{r}_i) + \mu_i(\vec{r}_i))/T(\vec{r}_i)} \delta_E \delta_{\vec{p}} \delta_B \delta_S \delta_C, \quad (6.1)$$

where N_{sort} denotes the multiplicity of a hadron species. The δ -functions in this expression denote the conservation of total energy, momentum, baryon number, strangeness and electric charge. All these quantum numbers should be equal to the quantum numbers of initial particles in the region Ω_{ϵ} . Without the δ -functions, the sampling distribution from Eq. 6.1 is equivalent to a Cooper-Frye sampling on an isochronous hypersurface. In this case by integrating over $d^3\vec{r}_i d^3\vec{p}_i$ one can easily see that the distribution of a particular hadron yield in one cell is Poissonian:

$$w(N_i) \sim \frac{(V_{\text{cell}} \varphi_i)^{N_i}}{N_i!} \quad (6.2)$$

$$\varphi_i = \frac{g_i e^{\mu/T}}{(2\pi\hbar c)^3} \int d^3 p e^{-p^v u_v/T} \quad (6.3)$$

where φ_i is the average equilibrium density of a given hadron species in the cell. Strictly speaking, in a case with total energy- and momentum conservation this consideration is not applicable any more, because now momentum integrations involve additional global δ -functions, so the distribution in one cell may be different from Poissonian. However, it is assumed that there are many cells with many particles in them, so that the global conservation laws affect the local Poisson distributions only slightly. From these considerations it is clear, that the method prefers larger N_{test} and not too large cells to achieve reliable results. The details of the sampling algorithm and a test in a thermal box are discussed in the next section 6.2.

Here Boltzmann statistics was assumed instead of more realistic Fermi-Dirac and Bose-Einstein statistics. This is done intentionally to be consistent with the absence of Pauli-blocking or Bose-enhancement effects in the transport simulation. For quantum statistics the multiplicity distribution in a cell is not Poissonian anymore. For bosons the mean multiplicity increases due to quantum statistics and the variance decreases, for fermions it is the opposite. Here our model is applied for low collision energies in the high-density region, where the typical temperatures are around 110 MeV and typical baryon chemical potentials are of order 700 MeV (see Fig. 6.10). The correction for pions is then $\frac{1}{2} \frac{K_2(2m_\pi/T)}{K_2(m_\pi/T)} \approx 7\%$, for protons it is $\frac{1}{2} \frac{K_2(2m_p/T)}{K_2(m_p/T)} e^{\mu/T} \approx 4\%$ and for all the other hadrons it has to be smaller.

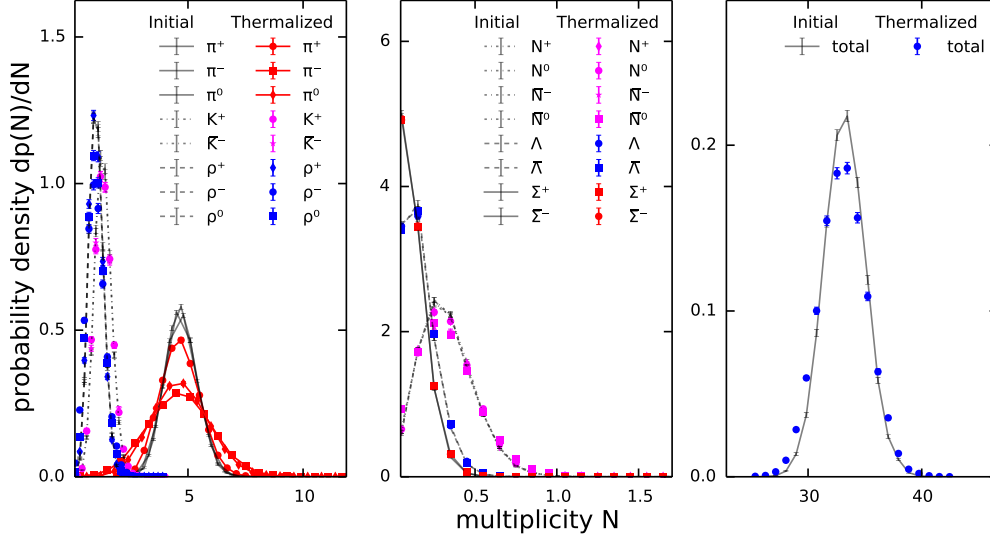


Figure 6.1.: Multiplicity distributions in a thermally initialized box are compared before and after additional forced thermalization. For a perfect thermalization algorithm these distributions should coincide. Here the thermalization algorithm is mode sampling.

The forced thermalization is performed every Δt_{th} starting from time t_{start} . Unless stated otherwise, $t_{start} = 0$ fm/c and $\Delta t_{th} = 1$ fm/c are taken. Further Δt_{th} is varied to see its effect on observables in Section 6.3. The system evolution before, between and after thermalizations follows the conventional SMASH cascade, with propagation, collisions and decays. It is assumed that the N-particle collisions happen momentarily, at a single point in time.

6.2. Thermal box - testing the sampling algorithm

Thermalization with global conservation of quantum numbers can be performed with different algorithms. In this section, three algorithms are compared within a thermal box containing infinite hadronic matter in equilibrium. First, a $V = (5 \text{ fm})^3$ box with periodic boundary conditions is created and initialized with thermally distributed hadrons that are available in SMASH. The multiplicities of each hadron species are $N_i = Poi(\phi_i)$, where Poi is a Poisson distribution and ϕ_i is the thermal multiplicity of i -th hadron species at a temperature of $T = 0.15$ GeV and zero chemical potential $\mu_B = 0$. The values of temperature and chemical potential are an arbitrary choice, but they correspond to the relevant conditions in hybrid approaches for heavy

ion reactions at high beam energies. The initial momenta are sampled from the Boltzmann distribution with the same temperature. The momenta in the box are centralized, so that total momentum of the box is zero, $p_i := p_i - \frac{1}{N} \sum_{j=1}^N p_j$. In this way a box with a thermalized hadron gas is obtained. The total energy and quantum numbers of such a box fluctuate from event to event.

As a second step the thermalization algorithm is applied, which conserves total energy, momentum and quantum numbers as described above in Section 6.1. The space-time grid consists of 10^3 cells. On this grid, the coarse graining as described above is performed, taking the periodic boundary conditions into account. After sampling new particles with three different algorithms the initial multiplicity and momentum distributions with the ones after forced thermalization are compared. If everything works as expected, the results are supposed to be identical.

The first algorithm under investigation is the mode sampling used for particlization in the UrQMD hybrid approach [230]. It consists of seven steps called "modes":

1. Choose a cell with probability $\frac{V_{cell}}{V}$. Sample particles in the cell according to the thermal distribution assuming a Poisson distribution around the mean, until the total energy exceeds E_{init} . Only particles with the positive strangeness are kept, reject all the other particles.
2. Compensate strangeness by sampling only particles with the negative strangeness.
3. Sample non-strange hadrons until the total energy exceeds E_{init} , keeping only non-strange baryons.
4. Compensate baryon charge by sampling only anti-baryons.
5. Sample non-strange mesons until the total energy exceeds E_{init} , keeping only positively charged non-strange mesons.
6. Compensate electric charge by sampling negatively-charged non-strange mesons.
7. Sample neutral mesons until the energy is conserved.

In this work, the original mode sampling algorithm has been improved to increase the computational speed. Choosing the cell with the probability $\frac{N_{cell}}{\sum_{cells} N_{cell}}$ and sampling one particle definitely in there helps to avoid rejections and samples the same distribution in a faster way. This improvement is especially noticeable at high baryon chemical potential, such as the one reached in low energy heavy ion collisions. The

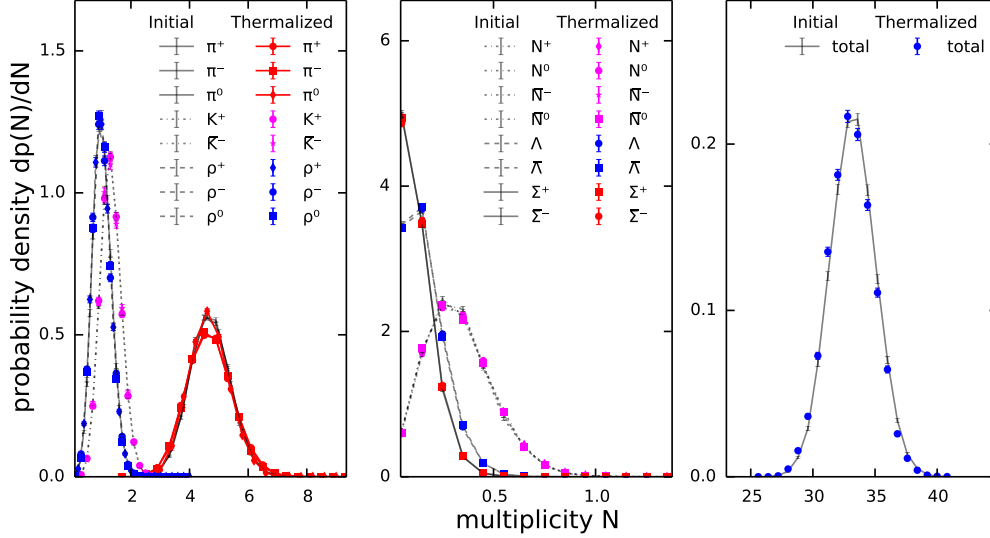


Figure 6.2.: Multiplicity distributions in a thermally initialized box are compared before and after additional forced thermalization. For a perfect thermalization algorithm these distributions should coincide. Here the thermalization algorithm is biased Becattini-Ferroni sampling with rejection by total energy.

average total number of anti-baryons can then be order of 10^{-5} . Sometimes one or two anti-baryons are needed to compensate the baryon number, but the probability to sample one in the original algorithm is 10^{-5} divided by number of cells. Therefore, many rejection steps are avoided with the newly defined probability.

Applying the mode sampling within the thermal box (see Fig. 6.1), one observes that the mean values of multiplicities are all reproduced and many multiplicity distributions are also reproduced. However, the π and ρ multiplicity distributions are wider than the initial ones, which results in a wider distribution for the total multiplicity. Moreover, the width of the multiplicity distribution follows $\Gamma(\pi^-) > \Gamma(\pi^0) > \Gamma(\pi^+)$, and similarly for ρ -mesons. To find the origin of this deviation from the expectation, the mode sampling order has been exchanged - instead of keeping only positively charged first and compensating with negative particles, only negatively charged are kept first and compensated with positive afterwards. Such reverse procedure results in $\Gamma(\pi^+) > \Gamma(\pi^0) > \Gamma(\pi^-)$. This demonstrates that the multiplicity distribution obtained from the mode sampling is sensitive to the internal algorithm realization, which is not physical.

The second considered algorithm is following the idea suggested by Becattini and Ferroni in [293], where one takes advantage of the fact that the sum of Poissonian variables is Poissonian itself. However, we implemented a biased version, different from the original Becattini and Ferroni suggestion. This version turns out to be numerically more efficient, while the bias is rather modest. The algorithm consists of the following steps:

1. Compute total average thermal numbers of baryons ν_B and anti-baryons $\nu_{\bar{B}}$. Sample N_B and $N_{\bar{B}}$ with probability

$$w(N_B, N_{\bar{B}}) \sim \frac{\nu_B^{N_B} \nu_{\bar{B}}^{N_{\bar{B}}}}{N_B! N_{\bar{B}}!} \delta(N_B - N_{\bar{B}} = B_{init}). \quad (6.4)$$

Such a distribution can be sampled very efficiently using the method discussed in the Appendix. Then the multiplicities of particular baryons and anti-baryons are sampled from the multinomial distribution.

2. Compute total thermal average for strange and anti-strange mesons: ν_S and $\nu_{\bar{S}}$. Then sample N_S and $N_{\bar{S}}$ with distribution

$$w(N_S, N_{\bar{S}}) \sim \frac{\nu_S^{N_S} \nu_{\bar{S}}^{N_{\bar{S}}}}{N_S! N_{\bar{S}}!} \delta(N_S - N_{\bar{S}} = S_{init} - S_{sampled}). \quad (6.5)$$

Then particular numbers of strange and anti-strange mesons are sampled from multinomial distribution.

3. Same procedure for charged non-strange mesons, in the distribution there is $\delta(N_C - N_{\bar{C}} = C_{init} - C_{sampled})$, where $C_{sampled}$ is the charge of the hadrons sampled in the previous steps.
4. Sample numbers of neutral mesons from Poissonian distributions.

Notice that for this version of the algorithm the distribution of the total number of particles is too wide. It turns out that this effect can be decreased, if one rejects all samples where the energy is too far away from the initial energy. Rejecting $|E_{sampled} - E_{init}|/E_{init} > 1\%$, one obtains the correct distribution for the total multiplicity, but the sampled distributions for π and ρ are slightly wider than the initial ones, see Fig. 6.2. This algorithm is so efficient, because of the fast method to generate pairs of Poisson-distributed numbers with fixed difference, described in the Appendix. The simple rejection method used for this purpose in the original paper by Becattini and

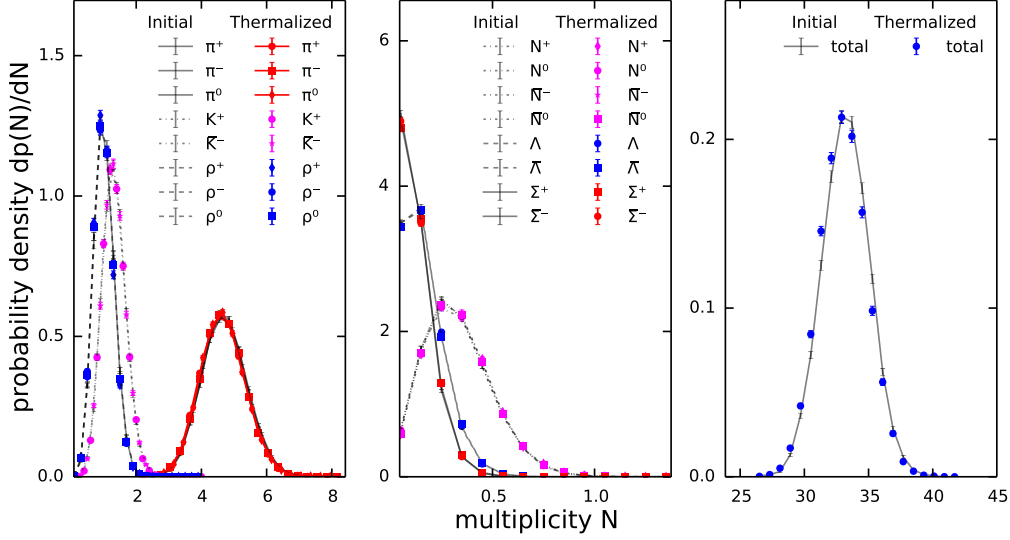


Figure 6.3.: Multiplicity distributions in a thermally initialized box are compared before and after additional forced thermalization. For a perfect thermalization algorithm these distributions should coincide. Here the thermalization algorithm is the unbiased Becattini-Ferroni sampling with rejection by total energy.

Ferroni is fast enough for the case of small chemical potential, but becomes slow for $\mu_B \simeq 0.7$ GeV reached in the Au+Au collisions at $\sqrt{s} = 3$ GeV - the energy relevant for our investigation.

Finally, the unbiased algorithm is tested, which is very similar to the previous one, except that rejection at any step requires the algorithm to start from scratch.

1. Identical to the first step of the biased algorithm.
2. Compute total thermal average for strange and anti-strange mesons: ν_S and $\nu_{\bar{S}}$. Then sample $N_S = Poi(\nu_S)$ and $N_{\bar{S}} = Poi(\nu_{\bar{S}})$. If $N_S - N_{\bar{S}} = S_{init} - S_{sampled}$, then proceed further, else start from the very beginning.
3. Similar to previous step for electric charge. If charge conservation not fulfilled, start over from the first step.
4. Sample neutral non-strange mesons.
5. Sample momenta for all particles, if total energy deviates more than 1% from the initial energy start over from the first step.

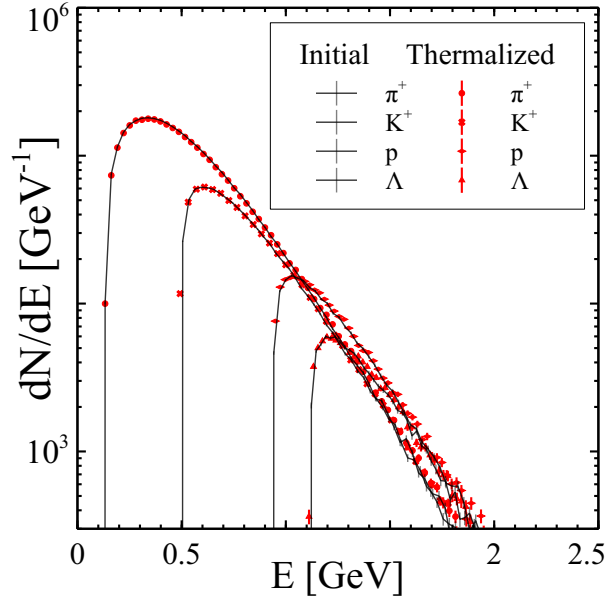


Figure 6.4.: Thermal box with the unbiased Becattini-Ferroni sampling with rejection by total energy: testing energy distribution

This algorithm produces the correct multiplicity distributions (see Fig. 6.3). Finally, Fig. 6.4 shows that the energy distributions are also appropriate using this algorithm.

In the following, the biased Becattini-Ferroni sampling is employed, since it is more efficient, the bias is small and it does not suffer from internal dependencies like the mode sampling. For a few cases, it was also checked that the unbiased algorithm produces identical results. In Fig. 6.5 we compare the performance of the considered algorithms on an Intel(R) Xeon(R) 2.5 GHz CPU. For the summary of algorithm properties see Tab. 6.1.

After the application of the sampling algorithm quantum numbers are conserved, but energy is only conserved with 1% precision and momentum conservation is only fulfilled on average. This shortcoming is addressed in two steps. First, the momenta are corrected to match the initial momentum, $p_i := p_i - \frac{1}{N}(\sum_{j=1}^N p_j - p_{init})$. Then, the particles are boosted to the rest frame of initialization with 3-velocity $-\frac{p_{init}}{E_{init}}$. In this frame the sum of momenta is zero, because in the previous step $\sum_{j=1}^N p_j = p_{init}$ was forced, so if one scales all momenta with the same factor, the sum will remain zero. Therefore, all momenta are scaled with a factor $(1 + a)$, such that

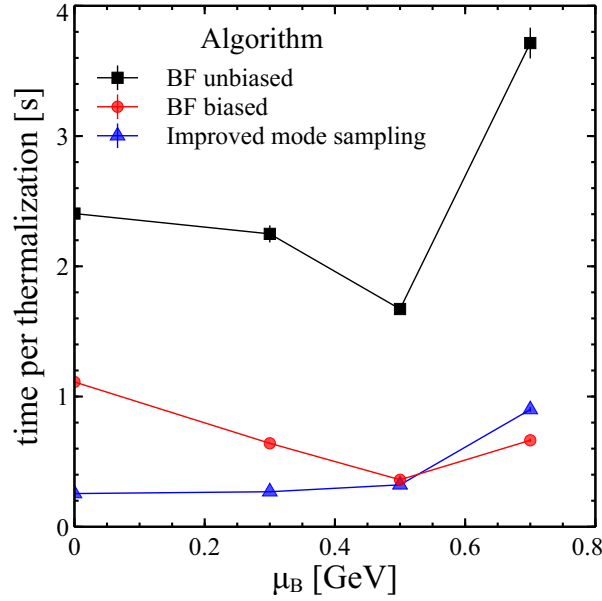


Figure 6.5.: Performance comparison of sampling algorithms: mode sampling, biased and unbiased Becattini-Ferroni sampling. Thermalization of the $(5 \text{ fm})^3$ thermal box with $T = 0.15 \text{ MeV}$, $N_{test} = 10$, $\mu_S = 0$, μ_B is varied.

Table 6.1.: Sampling algorithms with total quantum numbers conservation

Name	Bias on multiplicity distributions	Performance
Mode Sampling	Widths of distributions affected, bias dependent on implementation	fast
Biased Becattini-Ferroni	Widths of distributions affected, small bias observed	comparable to Mode Sampling
Unbiased Becattini-Ferroni	No bias observed	$\simeq 4$ times slower than previous

$$\sum_{j=1}^N \sqrt{m_j^2 + (1+a)^2 p_j^2} = E'_{init} \quad (6.6)$$

Finally the particles are boosted back to computational frame and now energy and momentum are exactly conserved. This procedure biases momentum distributions, but this bias decreases with higher numbers of sampled particles N . One can observe in Fig. 6.4, that if N is large enough, this bias is negligible.

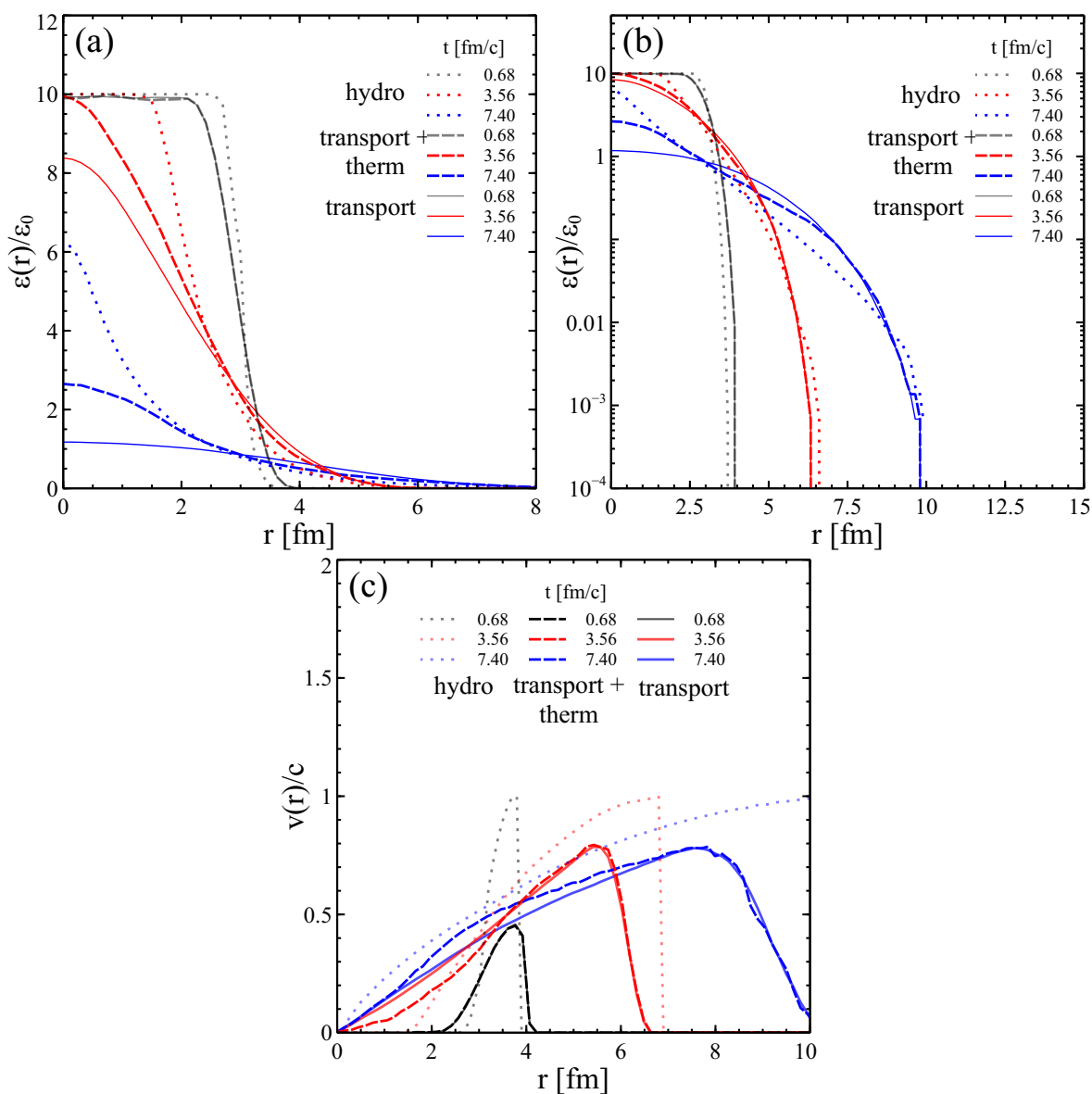


Figure 6.6.: The time evolution of an expanding sphere is compared for ideal hydrodynamics (SHASTA, dotted lines), hadron cascade (SMASH, solid lines) and the same hadron cascade enhanced by effective N-particle collisions using forced thermalization (SMASH+therm, dashed lines). Panels (a) and (b) depict the energy density in the local Landau rest frame versus radius. Panel (b) is exactly the same plot as panel (a) with a logarithmic scale, which allows to see the edges of the system. Panel (c) demonstrates the velocity of the Landau rest frame versus radius.

6.3. Interpolating between transport and hydrodynamics

After establishing the details of the algorithm to effectively include N-particle collisions in a transport approach, let us compare the influence on the time evolution

of an expanding system to pure transport and ideal fluid dynamics. The objective is to prove that this dynamically coupled approach interpolates between the two limits of kinetic theory. For this purpose, a simple scenario is chosen, namely an expanding sphere. The sphere of radius $R_0 = 3$ fm is initialized at an energy density of 10 times nuclear ground state energy densities, $\epsilon = 10\epsilon_0$, and at zero baryon density. In Fig. 6.6 the evolution of the local Landau rest frame energy density and velocity as a function of the radius r are compared. The ideal hydrodynamics code has been performed using the SHASTA [294] ideal fluid dynamics solver, which uses a 200^3 Cartesian grid with 0.1 fm grid spacing in each direction. The time step in SHASTA is 0.04 fm/c. In SMASH, the sphere is initialized with a thermal hadron gas with a temperature of $T \approx 191$ MeV, corresponding to energy density $\epsilon = 10\epsilon_0$. To minimize the effects of smoothing, the width of the Gaussian smearing kernel is taken to be $\sigma = 0.3$ fm. This is compensated by taking $N_{test} = 100$. In the version of SMASH with the effect of N-particle collisions, forced thermalization is performed every $\Delta t_{th} = 1$ fm/c in the region, where energy density is above $2\epsilon_0$. The thermalization grid has a cell spacing of 0.5 fm, which can seem rather large, but it was checked that decreasing it by factors of 2 and 3 does not change the results.

In Fig. 6.6 one immediately notices that transport and fluid dynamics do not produce identical results, as expected. At the time when, in fluid dynamics, the rarefaction wave has still not reached the center, in transport the energy density at the center has already dropped. To understand this difference, one has to consider the Knudsen number in the transport case. At small times, the scattering rate in SMASH is 0.73 fm^{-1} , so that the mean free path is $l_{mfp} \simeq 1.5$ fm and $Kn \simeq \frac{l_{mfp}}{R_0} \simeq 0.5$. At this Knudsen number hydrodynamics is already on the verge of applicability. Moreover, this number is averaged over space and over various hadron species. On the edges of the system one has to compare the mean free path not to R_0 , but to the distance to the edge. Furthermore, some hadron species have small interaction cross-sections with other particles, so their mean free path is large and they are in the ballistic regime, not in the hydrodynamic one. In Fig. 6.6, panel (c) shows that velocity at the edge in the hydrodynamics is c , while it is smaller in the transport model, because of massive particles being present.

SMASH including the effective treatment of N-particle collisions exhibits intermediate behaviour between hydrodynamics and pure transport. At the edges of the system, where forced thermalization is not happening, it behaves like transport, while in the center, it is closer to hydrodynamics. By forcing thermalization every $\Delta t_{th} = 1$

fm/c, the Knudsen number at the center is fixed for some time to $Kn \simeq \frac{\langle v_{therm} \rangle \Delta t_{th}}{R_0}$ for all hadron species. So even for hadrons with small cross-sections it becomes hard to escape the center too early. In fact, one can regulate this closeness to hydrodynamics by changing Δt_{th} . For smaller Δt_{th} one obtains smaller Knudsen number and the result is thus closer to hydrodynamics. It has to be underlined that the region of forced thermalization is coupled to the outside region: particles can move in both directions. This is different from hybrid approaches, where particles from transport have no chance to feedback to hydrodynamics. Overall, the introduction of effective N-particle collisions has the expected effect that it interpolates between pure transport and ideal hydrodynamics.

After studying the effect of forced thermalization in a simple controlled setup, one can investigate its implications in heavy ion collisions. To understand our results better, the influence of the thermalization parameters is also considered, such as the thermalization period Δt_{th} , the thermalization grid spacing and the energy density ϵ_c , above which the thermalization is enforced. In Fig. 6.7 one can see the effects of varying these parameters. The “default” ones are $N_{test} = 10$, $\Delta t_{th} = 1$ fm/c, thermalization grid spacing 0.5 fm in the beam direction and 1 fm in the transverse plane and $\epsilon_c = 0.3$ GeV/fm³. These parameters are varied one by one, keeping all the rest constant. As one can see in Fig. 6.7, the dependence of the multiplicities on the test particles number saturate at $N_{test} = 10$, which is the reason this number was chosen for further investigations. The grid spacing does not affect the final multiplicities, except a small effect on pions. The grid spacing has no physical meaning and ideally results do not depend on it. Surprisingly, Δt_{th} also plays a rather small role, even though multiplicities are decreasing with a larger thermalization period. This is in line with the naive expectation that larger Δt_{th} brings simulation results closer to a pure transport, where the multiplicity of the strange particles is typically below equilibrium values. The dependency on ϵ_c is also predictable - in the limiting case of high ϵ_c , no thermalization takes place at all, because such high energy densities are never reached in the collision. So for high ϵ_c SMASH with forced thermalization is equivalent to the normal SMASH cascade. This is also illustrated by Fig. 6.8. For low ϵ_c , a significant volume is thermalized during the evolution, which drastically increases strange particles multiplicities. This can be attributed to the fact that hadronic interactions do not provide as much strangeness production as a statistical model would predict. In Fig. 6.8 one can also see that the lifetime of the high-density region is prolonged due to the forced thermalization. This is in line with the previously

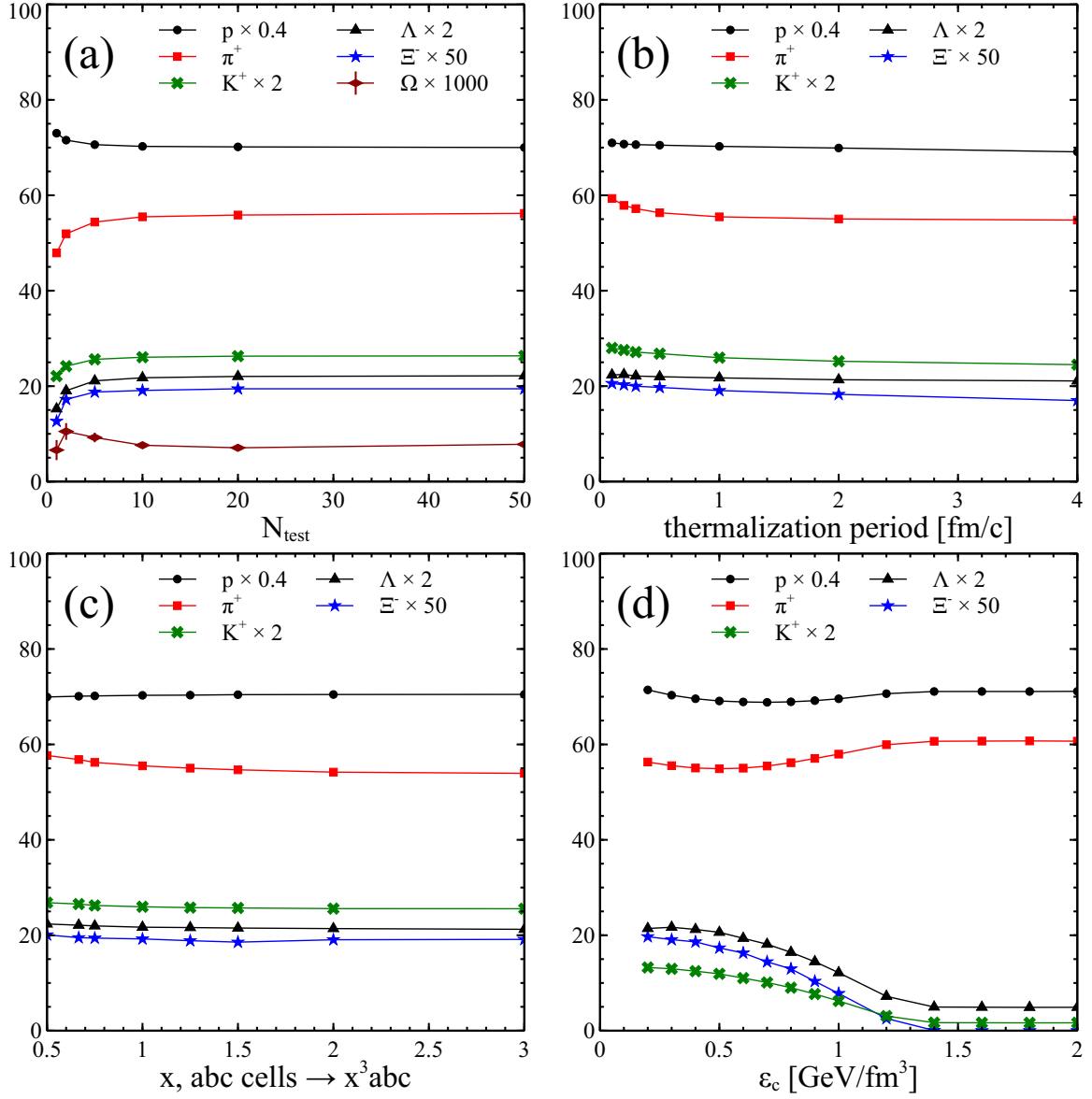


Figure 6.7.: Central AuAu collision at $\sqrt{s} = 3$ GeV calculated within SMASH with effective treatment of N-particle collisions. Final hadron multiplicities are shown versus test particle number (a), thermalization period Δt_{th} (b), grid spacing (panel c, x denotes the factor for number of cells in one dimension, $x = 2$ means that the grid is 8 times denser) and energy density ϵ_c , above which the thermalization is forced (d).

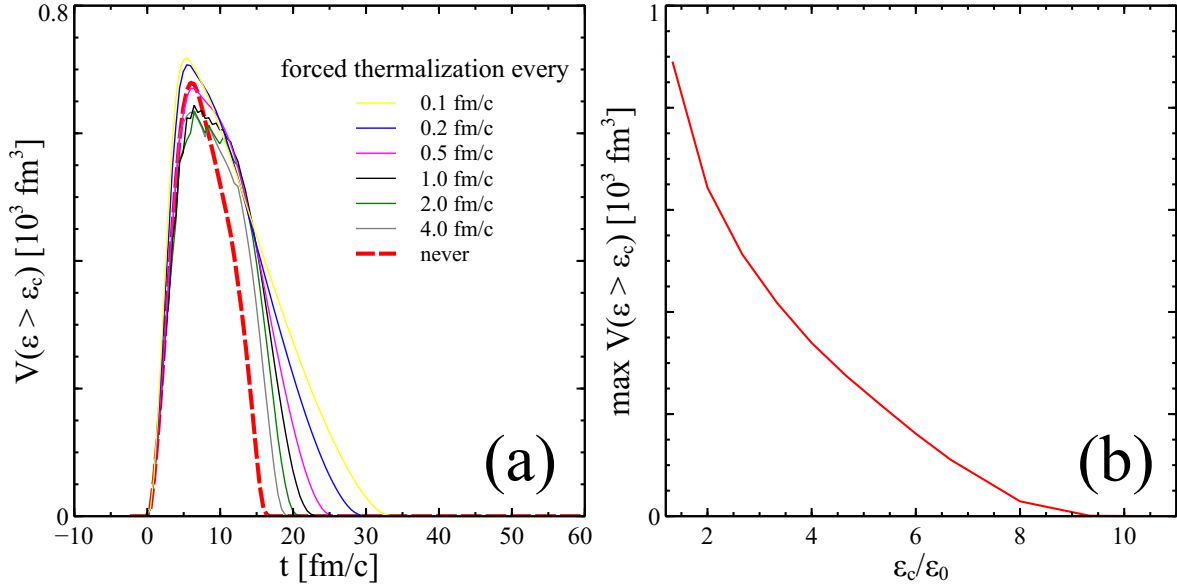


Figure 6.8.: Volume of thermalization region versus thermalization period Δt_{th} (a) and maximal volume versus ϵ_c (b). Central AuAu collisions at $\sqrt{s} = 3 \text{ GeV}$ simulated by SMASH with effective treatment of N-particle collisions.

described sphere scenario: transport with forced thermalization becomes closer to the hydrodynamical regime. The observable consequence of such behaviour may be larger HBT radii, compared to pure transport.

Another consequence of our model is a drastic increase of strangeness. This is not surprising, because in the pure transport strange particles are far from thermal equilibration. The effects of our forced thermalization on multiplicities are shown in Fig. 6.9, where 3 models are compared: SMASH, SMASH with thermalization, and UrQMD hybrid [163]. The starting time of the thermalization is taken to match that of the hybrid approach. Energy density ϵ_c is set to $2\epsilon_0$, in the UrQMD hybrid particleization energy density is also set to $2\epsilon_0$. One can see that in terms of multiplicities our model behaves similarly to the UrQMD hybrid approach, even though the underlying transport codes have significant differences in terms of resonance properties and strangeness production. From the Fig. 6.10 one can see that the average T and μ_B inside of thermalization/hydrodynamical region are similar in all three approaches, which makes comparison sensible.

One more consequence of the forced thermalization is that the pressures in the longitudinal and transverse directions rapidly equalize. This means that particles from larger rapidity are redirected to midrapidity and transverse momentum increases.

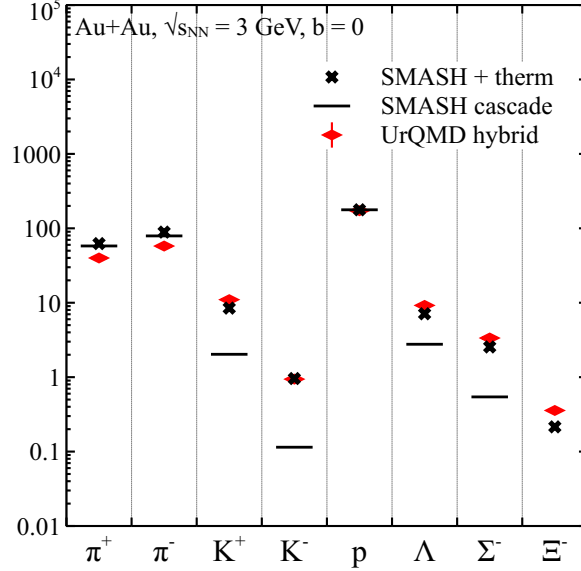


Figure 6.9.: Multiplicities in central AuAu collision at $\sqrt{s} = 3$ GeV are compared for SMASH, SMASH with thermalization, and UrQMD hybrid.

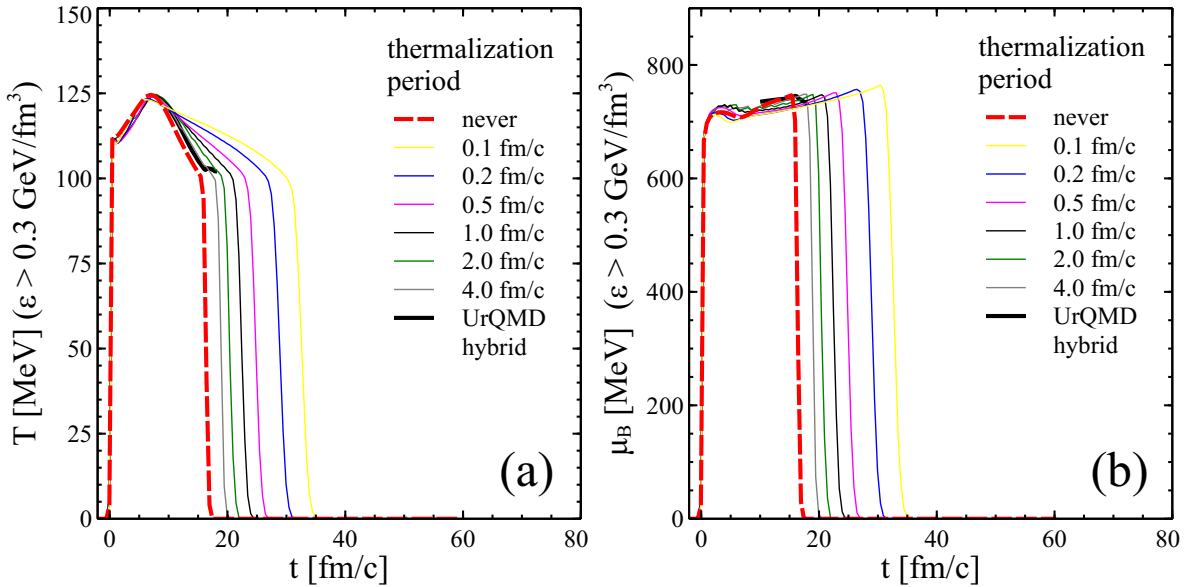


Figure 6.10.: Average temperature (a) and baryon chemical potential (b) inside of thermalization region for different thermalization periods. Averages are weighted with energy density, i.e. $\langle T \rangle = \sum_r T(r)\epsilon(r) / \sum_r \epsilon(r)$. Central AuAu collisions at $\sqrt{s} = 3$ GeV simulated by SMASH with (solid lines) or without (dashed lines) effective treatment of N-particle collisions. Black solid lines correspond to UrQMD hybrid approach.

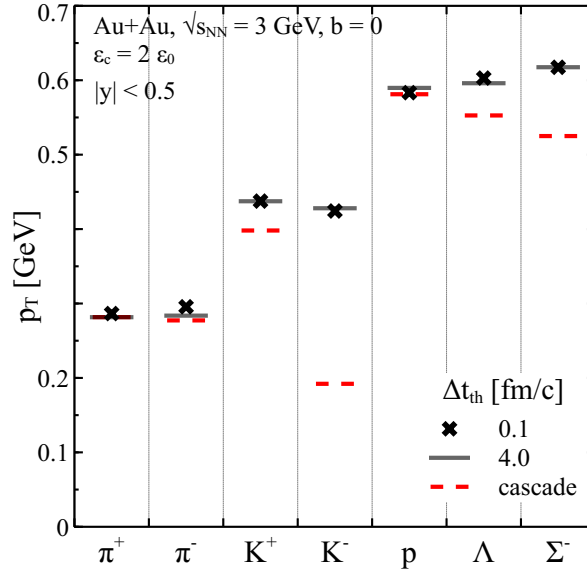


Figure 6.11.: Mean transverse momentum $p_T = \sqrt{p_x^2 + p_y^2}$ at midrapidity in central AuAu collision at $\sqrt{s_{NN}} = 3$ GeV. The model with the forced thermalization is compared to cascade.

This is illustrated by Fig. 6.11, which shows an increase of mean p_T for all particles. One can see that the mean p_T is insensitive to the thermalization period, but it is quite sensitive to the forced thermalization itself. The most dramatic effect can be seen for K^- . This is probably because, unlike K^+ that can be produced in $NN \rightarrow \Lambda K^+$ reactions, more than 80% of K^- are produced in the secondary strangeness exchange $\pi\Sigma \rightarrow NK^-$, $\pi\Lambda \rightarrow NK^-$ and $\Sigma^* \rightarrow NK^-$. Strangeness exchange reactions preferably deliver their products to high rapidities. Due to the forced thermalization K^- produced at high rapidities are redirected to midrapidity.

6.4. Discussion

A new approach was introduced, where canonical thermalization is performed in a pure hadronic transport in the regions of high energy density — the region, where hydrodynamics would be applied in the hybrid approaches. Unlike hybrid approaches, this approach automatically guarantees that the high density and the low density part can exchange particles and that transition hypersurface is determined dynamically. This approach was implemented and tested using the SMASH hadronic transport as a basis.

First, several algorithms for sampling particles respecting conservation laws for all quantum numbers were compared. The Becattini-Ferroni algorithm for sampling was found to be the most reliable one while its slightly biased version turned out to be reasonably efficient. In an expanding sphere scenario it was demonstrated that SMASH with the forced thermalization exhibits intermediate behaviour between hydrodynamics and transport. The closeness to hydrodynamics can be regulated by the thermalization frequency - the more often one thermalizes, the closer the result to hydrodynamics.

Within this novel approach heavy ion collisions were simulated and results were compared to transport and hybrid approaches. In the forced thermalization approach more strangeness is produced compared to pure transport, the mean transverse momentum is increased due to pressure isotropization and the high-density region lives longer. All these features are qualitatively similar to hybrid approaches. Note, however, that the problems of hybrid approaches at particlization (discussed in chapter 4) are absent in the forced thermalization approach. The dependency of final hadron multiplicities on model parameters was tested in the forced thermalization approach for Au+Au collisions. Grid spacing did not influence the multiplicities, the thermalization frequency changed them only slightly. An interesting behaviour was observed while varying the testparticles number N_{test} . For $N_{test} \geq 10$ multiplicities saturate. For smaller N_{test} one can see a difference that can be explained by canonical correction. If one increases energy density ϵ_c above which thermalization is forced, less particles are thermalized and therefore less strangeness is produced. Overall, the forced canonical thermalization approach leads to the expected results and the straightforward tests look promising.

In the thermalization procedure one needs the EoS to determine local temperature and chemical potentials. For this purpose a hadron gas EoS was applied, consistently with SMASH hadron content. One can also apply another EoS, for example an EoS with a phase transition, but between thermalizations the propagated degrees of freedom will be still hadrons, which seems inconsistent. If the quark-gluon plasma only exists at high energy densities and at the edges of the thermalized blobs the degrees of freedom are still hadronic, this might allow the direct investigation of EoS of strongly-interacting matter without explicit hydrodynamic evolution. In the future, these studies can be extended to higher collision energies and compared to existing experimental data and can provide predictions for upcoming experiments.

Chapter 7.

Summary

This thesis explores the limitations of traditional hybrid (hydrodynamics + transport) approaches for simulations of heavy ion collisions at beam energies $E_{\text{lab}} = 5\text{--}160 A \text{ GeV}$ and suggests a new forced thermalization approach, where some of these limitations are relaxed. After a brief introduction, which motivates heavy ion collisions as an experimental approach to study the phase diagram of a strongly-interacting matter, a small overview of experimental facilities is given. It demonstrates a continuing significant experimental interest to the intermediate energy range studied in this thesis.

Relativistic hydrodynamics and transport are introduced, mentioning that hydrodynamics is calibrated and describes experiments very well at highest RHIC and LHC energies, while hadronic transport is particularly good at low energies. A reliable approach at intermediate energies is an important goal: one can either extrapolate the hydrodynamical and hybrid approaches from higher energies or transport approaches from lower energies. In this thesis the approximations made by traditional hybrid approaches are tested and it is argued that they become challenging at intermediate energies.

Switching from transport to hydrodynamics requires certain degree of equilibration. Here the degree of local equilibration was quantified for Au+Au collisions at $E_{\text{lab}} = 5\text{--}160 A \text{ GeV}$ using coarse-grained transport approach. It was found that the most important contribution to deviation from equilibrium comes from pressure anisotropy. Other effects could be diminished if many events from transport code were used for fluidization. However, if one constructs an initial state for hydrodynamics from single transport events, not only pressure anisotropy is large, but also off-diagonal components of energy-momentum tensor deviate significantly from equilibrium. In

general, it is not obvious whether it is always the case that the degree of isotropization necessary to switch to hydrodynamics is reached in transport approach at any time. Here it was shown that it is indeed reached in a significant volume, although somewhat later than hybrid models typically perform fluidization. The isotropization time depends on the smearing parameter σ as $t_{iso} = t_{geom} + \alpha\sigma$, where t_{geom} is the time of geometrical overlap and α is a proportionality coefficient. It partially justifies the typical convention of hybrid approaches to perform fluidization at t_{geom} .

In the hybrid approaches hydrodynamical equations are solved in the whole forward light cone including those regions, where hydrodynamics is not applicable. The switching hypersurface is chosen a posteriori from the hydrodynamical evolution, but not from coupled hydrodynamical and transport equations. The particles from transport cannot cause any feedback to hydrodynamics. These approximations are manifested in the negative contributions to Cooper-Frye formula. Here it is shown that the negative Cooper-Frye contributions at midrapidity become significant for intermediate energies, which motivates new approaches, that avoid the negative Cooper-Frye contributions problem.

Such an approach was suggested as a main result of this thesis. In this novel approach conventional transport simulation is performed, but at the regions of high energy density, where traditional hybrid model would switch to hydrodynamics, a forced canonical thermalization is applied. The approach was tested in an artificial setup and in low energy heavy ion collisions and has shown reasonable results. The task still remains to apply it to intermediate energies confronting its results to experimental data.

Appendix A.

Glossary

A.1. Units and conventions

In this thesis a natural system of units is used, where $\hbar = c = k_B = 1$. In this system all the energies, masses and momenta and temperatures are given in electron-volts (eV, keV, MeV, GeV, TeV). Energy of 1 eV is the kinetic energy of electron accelerated by one volt, $1 \text{ eV} = 1.6 \cdot 10^{-19} \text{ J}$. The temperature of 1 eV corresponds in SI via $E = k_B T$ to 11604.5 K. The typical length scale in the thesis is 1 fm, so conversions between energy and length are convenient via

$$E = \frac{\hbar c}{L}, \quad (\text{A.1})$$

where $\hbar c = 0.19732 \text{ GeV} \cdot \text{fm}$.

The thesis adopts high-energy physics convention with metric tensor

$$g^{\mu\nu} = \text{diag}(1, -1, -1, -1). \quad (\text{A.2})$$

The terms “low energy”, “intermediate energy” and “high energy” are frequently used throughout the thesis. The ranges are defined only approximately, table 1.2 summarizes the convention adopted in the text.

A.2. Abbreviations

Abbreviations used in the thesis are collected in the following table.

BUU	Boltzmann-Ueling-Uhlenbeck (transport equations)
CGC	Color Glass Condensate [127, 128]
EoS	Equation of State
HBT	Hanbury-Brown Twiss correlations [76]
HI	Heavy Ion
HIC	Heavy Ion Collisions
HRG	Hadron Resonance Gas
QCD	Quantum Chromodynamics
QGP	Quark-Gluon Plasma
QMD	Quantum Molecular Dynamics
PDF	Parton Distribution Functions [129, 130]

Transport codes (1.3.4)

AMPT	A Multi-Phase Transport
BAMPS	Boltzmann Approach to Multi-Parton Scatterings
GiBUU	Gießen BUU
HSD	Hadron-String Dynamics
PHSD	Parton-Hadron-String Dynamics
RQMD	Relativistic Quantum Molecular Dynamics
SMASH	Simulating Many Strongly-interacting Hadrons
UrQMD	Ultrarelativistic Quantum Molecular Dynamics

HI centers (1.2)

BNL	Berkley National Laboratory (Berkley, USA)
BNL	Brookhaven National Laboratory (Brookhaven, USA)
CERN	Center for European Nuclear Research (Geneva, Switzerland)
GSI	Gesellschaft für Schwerionenforschung (Darmstadt, Germany)
JINR	Joint Institute for Nuclear Research (Dubna, Russia)
JPARC	Japan Proton Accelerator Research Complex (Tsukuba, Japan)

HI accelerators (1.2)

AGS	Alternating Gradient Synchrotron
HERA	Hadron-Electron Ring Accelerator
NICA	Nuclotron-based Ion Collider Facility
SIS	Schwerionensynchrotron
SPS	Super Proton Synchrotron
RHIC	Relativistic Heavy Ion Collider
LHC	Large Hadron Collider

Appendix B.

Sampling two Poissonian integers A and B with fixed $N = A - B$

In the algorithms described in chapter 6 one needs to sample N_1 and N_2 such that $w(N_1, N_2) \sim \frac{v_1^{N_1} v_2^{N_2}}{N_1! N_2!} \delta(N_1 - N_2 = N)$, $N > 0$. Let us rewrite it in terms of distribution for N_2 :

$$w(N_2) = \sum_{N_1=0}^{\infty} w(N_1, N_2) \sim \frac{v_1^{N_2+N} v_2^{N_2}}{(N_2 + N)! N_2!} \quad (\text{B.1})$$

$$w(N_2) = \text{const} \frac{(v_1 v_2)^{N_2}}{N_2! (N + N_2)!} \quad (\text{B.2})$$

Denoting $a = 2\sqrt{v_1 v_2}$ and normalizing probabilities, one obtains

$$w(N_2) = \frac{a^{2N_2+N}}{I_N(a) N_2! (N + N_2)!} \quad (\text{B.3})$$

This is the known Bessel distribution. The recommendations for sampling it are taken from the paper by Yuan and Kalbfleisch [295]. Maximal probability for the Bessel distribution is reached for

$$m = \frac{1}{2} \left(\sqrt{a^2 + N^2} - N \right) \quad (\text{B.4})$$

It is suggested by [295] that for $m > 6$ the Bessel distribution is very close to the Gaussian distribution, and for $m \leq 6$ probabilities can be computed explicitly and the

number can be sampled from a discrete distribution. Moments of $Y \sim \text{Bes}(N, a)$ can be computed as

$$EY = \frac{1}{2}aR_N(a) \quad (\text{B.5})$$

$$EY^2 = EY \left(1 + \frac{1}{2}aR_{N+1}(a) \right), \quad (\text{B.6})$$

Then the mean α and σ of the Gaussian are

$$\alpha = EY \quad (\text{B.7})$$

$$\sigma = \sqrt{EY^2 - (EY)^2} \quad (\text{B.8})$$

Here $R_N(a) = \frac{I_{N+1}(a)}{I_N(a)} = \left[\frac{2(N+1)}{a}, \frac{2(N+2)}{a}, \frac{2(N+3)}{a}, \dots \right]$, where $[a_1, a_2, a_3, \dots]$ denotes the continued fraction $\frac{1}{a_1 + \frac{1}{a_2 + \dots}}$.

An alternative method used by Becattini and Ferroni in [293] is to sample two numbers from Poissonian distributions and reject until the difference is the required one. Devroye points out that this method requires $\frac{e^a}{I_V(a)}$ rejections on average and is thus only acceptable for moderate values of a and N [296]. In terms of our purposes, it means that such method works well only for small enough chemical potentials. For completeness let us add that in response to the approximate sampling method by Yuan and Kalbfleisch, Devroye has suggested an exact method [296]. However, for the purposes of chapter 6 the approximate method is sufficient, as Fig. 6.3 demonstrates.

Appendix C.

Hadrons and the SU (3) group

Hadrons are the degrees of freedom implemented in transport models UrQMD and SMASH used throughout this thesis. In fact, hadrons are one of the main objects of study of the thesis. Nevertheless, two important questions about hadrons were omitted in the main part: "why only certain combinations of quarks and antiquarks occur as hadrons?" and "how are hadrons classified?" Both of them are answered with the help of SU (3) group. By definition SU (3) group is a group of 3×3 matrices U such that $UU^\dagger = \mathbb{1}$ and $\det U = 1$. In the following its role in hadron classification and in explaining color confinement (see section 1.1.3) is acknowledged.

Hadrons and quarks are microscopic objects, so their properties are defined by the quantum wavefunction $|\Psi\rangle$ - a complex function of spatial coordinate, spin and other variables of particle internal state. The squared module of wavefunction $|\Psi|^2$ is a probability to find particle at a given coordinate in a given state. Finding the wavefunction of the quantum system is enough to predict its properties.

For a single quark wavefunction is a product of color, flavor, spin and spatial parts:

$$|\Psi\rangle = |\Psi_{\text{color}}\rangle |\Psi_{\text{flavor}}\rangle |\Psi_{\text{spin}}\rangle |\Psi(x)\rangle \quad (\text{C.1})$$

Let us concentrate on the color part, which can be represented as a complex vector with 3 components. During propagation of the free quark color is conserved. According to Noether theorem, every conservation law corresponds to a symmetry, which in this case is invariance of interactions under multiplication of $|\Psi_{\text{color}}\rangle$ by matrices from SU (3) group, in other words invariance under color rotations.

In mathematical terms SU (3) is a Lie group and it is fully defined by its Lie algebra of infinitesimal color rotations: for every matrix U from SU (3)

$$U = \exp \left(\sum_{k=1}^8 i\alpha_k \lambda_k / 2 \right), \quad (\text{C.2})$$

where α_k are arbitrary real numbers and $\lambda_k/2$ matrices are called generators, which for SU (3) are known as Gell-Mann matrices. Explicitly expressed, λ_k are

$$\lambda_1 = \begin{pmatrix} 0 & 1 & 0 \\ 1 & 0 & 0 \\ 0 & 0 & 0 \end{pmatrix} \quad \lambda_2 = \begin{pmatrix} 0 & -i & 0 \\ i & 0 & 0 \\ 0 & 0 & 0 \end{pmatrix} \quad \lambda_3 = \begin{pmatrix} 1 & 0 & 0 \\ 0 & -1 & 0 \\ 0 & 0 & 0 \end{pmatrix} \quad (\text{C.3a})$$

$$\lambda_4 = \begin{pmatrix} 0 & 0 & 1 \\ 0 & 0 & 0 \\ 1 & 0 & 0 \end{pmatrix} \quad \lambda_5 = \begin{pmatrix} 0 & 0 & i \\ 0 & 0 & 0 \\ -i & 0 & 0 \end{pmatrix} \quad \lambda_6 = \begin{pmatrix} 0 & 0 & 0 \\ 0 & 0 & 1 \\ 0 & 1 & 0 \end{pmatrix} \quad (\text{C.3b})$$

$$\lambda_7 = \begin{pmatrix} 0 & 0 & 0 \\ 0 & 0 & -i \\ 0 & i & 0 \end{pmatrix} \quad \lambda_8 = \frac{1}{\sqrt{3}} \begin{pmatrix} 1 & 0 & 0 \\ 0 & 1 & 0 \\ 0 & 0 & -2 \end{pmatrix} \quad (\text{C.3c})$$

Choosing basis vectors in color space as

$$r = \begin{pmatrix} 1 \\ 0 \\ 0 \end{pmatrix} \quad g = \begin{pmatrix} 0 \\ 1 \\ 0 \end{pmatrix} \quad b = \begin{pmatrix} 0 \\ 0 \\ 1 \end{pmatrix} \quad (\text{C.4})$$

one can introduce ladder operators from non-diagonal Gell-Mann matrices and color isospin projection I_3^c and color hypercharge Y_c operators from diagonal matrices:

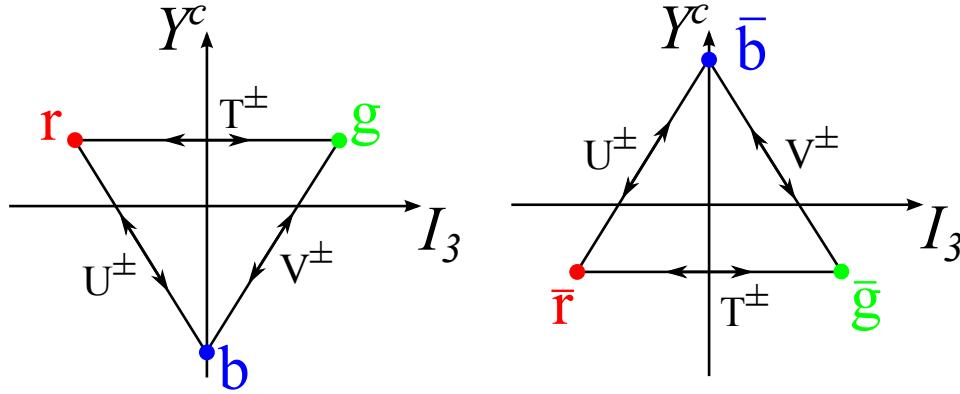


Figure C.1.: Ladder operators of SU(3) group in space of quark colors.

$$\begin{aligned}
 T^\pm &= \frac{1}{2} (\lambda_1 \pm i\lambda_2) \\
 V^\pm &= \frac{1}{2} (\lambda_4 \pm i\lambda_5) \\
 U^\pm &= \frac{1}{2} (\lambda_6 \pm i\lambda_7) \\
 I_3^c &= \frac{1}{2} \lambda_3 \\
 Y_c &= \frac{1}{\sqrt{3}} \lambda_8
 \end{aligned} \tag{C.5}$$

These operations turn quark and antiquark colors into each other, as illustrated in Fig. C.1. It is postulated that existing bound states are color singlets, meaning that acting with matrices C.5 on every single quark and antiquark turns the whole state into itself. It can be shown that this requirement defines color parts of meson and baryon wavefunctions uniquely:

$$|\Psi_c^{q\bar{q}}\rangle = \frac{1}{\sqrt{3}} (r\bar{r} + g\bar{g} + b\bar{b}) \tag{C.6}$$

$$|\Psi_c^{qqq}\rangle = \frac{1}{\sqrt{6}} (rgb - rbg + gbr - grb + brg - bgr) \tag{C.7}$$

Exactly the same mathematics is used for hadron classification, but now SU(3) is acting in flavor space of the lightest quarks: u , d and s . Note that SU(3) color symmetry is exact, but SU(3) flavor symmetry is only approximate, because the masses of light quarks are not identical.

Hadrons should be colorless, but they should not necessarily be flavorless. In the other words, all the flavor representations are allowed. It can be proven that

combinations of quarks split into irreducible representations of SU (3) in flavor space in the following way:

$$3 \otimes \bar{3} = 1 \oplus 8 \quad (\text{C.8})$$

$$3 \otimes 3 \otimes 3 = 10 \oplus 8 \oplus 8 \oplus 1 \quad (\text{C.9})$$

This means that there are 8 mesons (octet) that turn one into another under SU (3) flavor transformations and one meson that always turns into itself. As for baryons - 10 baryons (decuplet) transforming into each other and two physically equivalent octets. The singlet absent in nature, because strictly speaking one has to consider flavor and spin transformations together and in the representation of SU (3) \times SU (2) (the SU (2) group is here for spin transformations) flavor singlet is absent.

This explains classification of mesons into octet and singlet and baryons into decuplet and octet as shown in Figure C.2, which presents the lightest mesons and baryons consisting of u, d, s quarks and their antiquarks. Supplementing this picture by vector mesons, antibaryons and a tower of excitations and adding those for heavier quarks one gets a zoo of hadrons that observed in experiment. Few hadrons are discovered that may fall out of this classification scheme. They are supposed to be tetraquarks or 6-quark molecules.

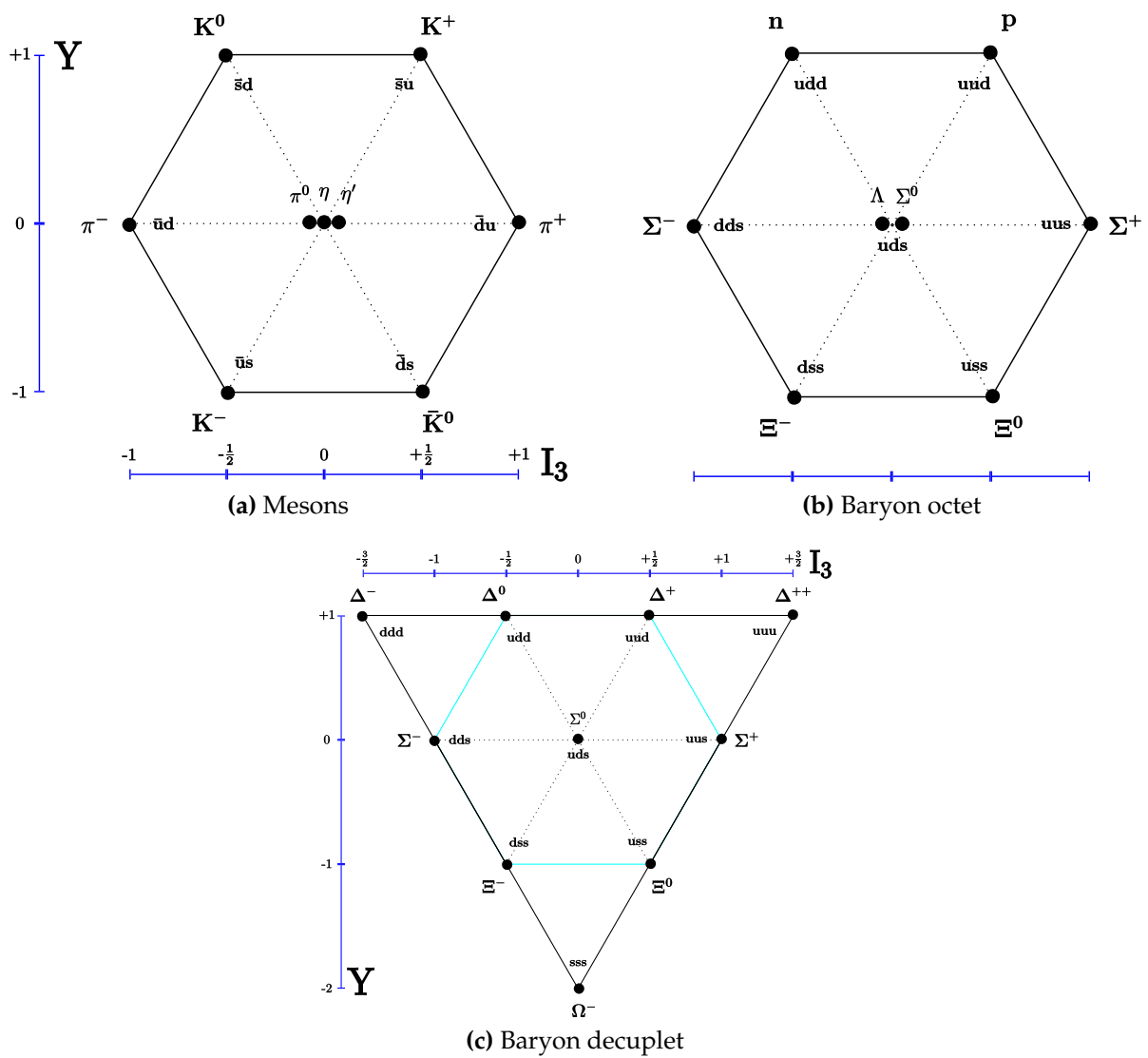


Figure C.2.: Classification of hadrons, consisting of light quarks, in the lowest energy state. The picture is taken from lectures in QCD by F. Jegerlehner.

Acknowledgements

First of all I would like to thank Hannah Petersen for the brilliant supervision, for being always kind, optimistic and full of ideas, for motivating me, for interesting discussions and for the help in all sorts of weird situations one can get into, while doing PhD abroad.

This work has inherited many ideas developed by Kyrill Bugaev and by Pasi Huovinen. I would like to thank them for that, as well as for insightful discussions and critical questions. I would also like to thank Pasi for providing the Cornelius code for hypersurface finding. The thesis is influenced by the excellent lectures in heavy ion physics by Elena Bratkovskaya and Igor Mishustin that I attended in the Institute of Theoretical Physics. Discussions during common lunches with Harri Niemi, Etele Molnar, LongGang Pang, Pasi Huovinen, Daisuke Satow, Shi Pu and many others were illuminating and certainly contributed to my understanding of heavy ion collisions.

Helmholtz Graduate School has supported my PhD studies, providing the travel money and excellent lectures. I would like to thank Henner Büsching and Sascha Vogel, who organized these lectures and motivated us to visit them. Due to the requirement of Helmholtz Graduate School to have a PhD committee I had a chance to discuss my work with Christian Sturm - he helped me not to lose the big picture behind technical details.

I would like to acknowledge funding by a Helmholtz Young Investigator Group VH-NG-822 from the Helmholtz Association and GSI.

For two years my PhD studies were supported by the stipend from Deutsche Telekom Stiftung. At the get-togethers of Deutsche Telekom Stiftung stipendiats I was introduced to a world of socially active students from natural sciences that changed my mentality. I would like to thank all fellow stipendiats for that, especially Arzu Yilmaz, Niklas Müller and Isabel Müller. The help and support of Christiane Frense-Heck, who is at the heart of organizational activities, cannot be overestimated.

It was exciting to be a part of the SMASH developers group. I want to thank all its members for a great collaboration. Besides co-developing SMASH, many have contributed to this thesis in different ways. Thanks to Matthias Kretz I have learned a lot about modern C++ programming. Vincent Steinberg and LongGang Pang were always willing to discuss scientific and technical issues, their support helped me to

avoid and correct many errors. I would like to thank Harri Niemi for his critical comments on the thesis, Anna Schäfer, Alba Ontoso and Sangwook Ryu for proof-reading different parts of the the thesis and Juan Torres-Rincon for correcting typos in formulas. Markus Mayer and Vinzent Steinberg have corrected my German in the summary (Zusammenfassung).

Significant part of the computations for this thesis was performed on the LOEWE-CSC computing cluster, which can be praised for its reliability and impressive computational power.

Finally, I would like to thank my parents, who always cared and worried that the author of this thesis is alive, healthy, fit, and has a good mood for some scientific research.

Bibliography

- [1] D. Oliinychenko, P. Huovinen, and H. Petersen, "Systematic Investigation of Negative Cooper-Frye Contributions in Heavy Ion Collisions Using Coarse-grained Molecular Dynamics," *Phys. Rev. C*, vol. 91, no. 2, p. 024906, 2015. [iii](#), [13](#), [35](#), [53](#), [69](#), [123](#)
- [2] —, "Cooper-Frye Negative Contributions in a Coarse-Grained Transport Approach," *J. Phys. Conf. Ser.*, vol. 599, no. 1, p. 012017, 2015. [iii](#)
- [3] D. Oliinychenko and H. Petersen, "Deviations of the Energy-Momentum Tensor from Equilibrium in the Initial State for Hydrodynamics from Transport Approaches," *Phys. Rev. C*, vol. 93, no. 3, p. 034905, 2016. [iii](#), [13](#), [35](#)
- [4] H. Petersen, D. Oliinychenko, J. Steinheimer, and M. Bleicher, "Influence of kinematic cuts on the net charge distribution," *Nucl. Phys.*, vol. A956, pp. 336–339, 2016. [iii](#)
- [5] J. Weil *et al.*, "Particle production and equilibrium properties within a new hadron transport approach for heavy-ion collisions," *Phys. Rev. C*, vol. 94, no. 5, p. 054905, 2016. [iii](#), [13](#), [82](#), [97](#), [114](#)
- [6] D. Oliinychenko and H. Petersen, "Forced canonical thermalization in a hadronic transport approach at high density," *J. Phys. G*, vol. 44, no. 3, p. 034001, 2017. [iii](#), [13](#), [35](#), [122](#)
- [7] —, "Effective dynamical coupling of hydrodynamics and transport for heavy-ion collisions," *J. Phys. Conf. Ser.*, vol. 832, no. 1, p. 012052, 2017. [iii](#)
- [8] H. Satz, *Extreme States of Matter in Strong Interaction Physics: An Introduction*, ser. Lecture Notes in Physics. Springer Berlin Heidelberg, 2012. [2](#)
- [9] [Online]. Available: https://commons.wikimedia.org/wiki/File:Standard_Model_of_Elementary_Particles.svg [4](#)
- [10] W. N. Cottingham and D. A. Greenwood, *An Introduction to the Standard Model of Particle Physics*. Cambridge University Press, 2007. [3](#)
- [11] V. F. Dmitriev and V. V. Flambaum, "Decays of Fourth Generation Bound States," *Int. J. Mod. Phys.*, vol. A27, p. 1250179, 2012. [6](#)
- [12] R. Aaij *et al.*, "Observation of $J/\psi p$ Resonances Consistent with Pentaquark States in $\Lambda_b^0 \rightarrow J/\psi K^- p$ Decays," *Phys. Rev. Lett.*, vol. 115, p. 072001, 2015. [7](#)

- [13] K. A. Olive *et al.*, “Review of Particle Physics,” *Chin. Phys. C*, vol. 38, p. 090001, 2014. [7](#), [83](#), [84](#), [98](#)
- [14] J. C. Collins and M. J. Perry, “Superdense Matter: Neutrons Or Asymptotically Free Quarks?” *Phys. Rev. Lett.*, vol. 34, p. 1353, 1975. [8](#)
- [15] E. V. Shuryak, “Theory of Hadronic Plasma,” *Sov. Phys. JETP*, vol. 47, pp. 212–219, 1978, [*Zh. Eksp. Teor. Fiz.*74,408(1978)]. [8](#)
- [16] J. Adams *et al.*, “Experimental and theoretical challenges in the search for the quark gluon plasma: The STAR Collaboration’s critical assessment of the evidence from RHIC collisions,” *Nucl. Phys. A*, vol. 757, pp. 102–183, 2005. [9](#), [17](#)
- [17] K. Adcox *et al.*, “Formation of dense partonic matter in relativistic nucleus-nucleus collisions at RHIC: Experimental evaluation by the PHENIX collaboration,” *Nucl. Phys. A*, vol. 757, pp. 184–283, 2005. [9](#), [17](#)
- [18] I. Arsene *et al.*, “Quark gluon plasma and color glass condensate at RHIC? The Perspective from the BRAHMS experiment,” *Nucl. Phys. A*, vol. 757, pp. 1–27, 2005. [9](#), [17](#)
- [19] B. B. Back *et al.*, “The PHOBOS perspective on discoveries at RHIC,” *Nucl. Phys. A*, vol. 757, pp. 28–101, 2005. [9](#), [17](#)
- [20] H. Song and U. W. Heinz, “Causal viscous hydrodynamics in 2+1 dimensions for relativistic heavy-ion collisions,” *Phys. Rev. C*, vol. 77, p. 064901, 2008. [9](#), [17](#)
- [21] K. Dusling and D. Teaney, “Simulating elliptic flow with viscous hydrodynamics,” *Phys. Rev. C*, vol. 77, p. 034905, 2008. [9](#), [17](#)
- [22] P. Romatschke and U. Romatschke, “Viscosity Information from Relativistic Nuclear Collisions: How Perfect is the Fluid Observed at RHIC?” *Phys. Rev. Lett.*, vol. 99, p. 172301, 2007. [9](#), [17](#), [28](#)
- [23] E. Shuryak, “Physics of Strongly coupled Quark-Gluon Plasma,” *Prog. Part. Nucl. Phys.*, vol. 62, pp. 48–101, 2009. [9](#)
- [24] P. Braun-Munzinger and J. Wambach, “The Phase Diagram of Strongly-Interacting Matter,” *Rev. Mod. Phys.*, vol. 81, pp. 1031–1050, 2009. [10](#)
- [25] S. Borsanyi, Z. Fodor, C. Hoelbling, S. D. Katz, S. Krieg, and K. K. Szabo, “Full result for the QCD equation of state with 2+1 flavors,” *Phys. Lett. B*, vol. 730, pp. 99–104, 2014. [10](#), [21](#)
- [26] A. Bazavov *et al.*, “Equation of state in (2+1)-flavor QCD,” *Phys. Rev. D*, vol. 90, p. 094503, 2014. [10](#), [21](#)
- [27] ———, “The QCD Equation of State to $\mathcal{O}(\mu_B^6)$ from Lattice QCD,” *Phys. Rev. D*, vol. 95, no. 5, p. 054504, 2017. [10](#), [21](#)

- [28] Y. Aoki, Z. Fodor, S. D. Katz, and K. K. Szabo, "The QCD transition temperature: Results with physical masses in the continuum limit," *Phys. Lett. B*, vol. 643, pp. 46–54, 2006. [10](#)
- [29] S. Borsanyi, Z. Fodor, C. Hoelbling, S. D. Katz, S. Krieg, C. Ratti, and K. K. Szabo, "Is there still any T_c mystery in lattice QCD? Results with physical masses in the continuum limit III," *JHEP*, vol. 09, p. 073, 2010. [10](#)
- [30] A. Bazavov *et al.*, "The chiral and deconfinement aspects of the QCD transition," *Phys. Rev. D*, vol. 85, p. 054503, 2012. [10](#)
- [31] P. de Forcrand, "Simulating QCD at finite density," *PoS L*, vol. AT2009, p. 010, 2009. [10](#)
- [32] M. A. Stephanov, "QCD phase diagram and the critical point," *Prog. Theor. Phys. Suppl.*, vol. 153, pp. 139–156, 2004, [Int. J. Mod. Phys.A20,4387(2005)]. [10](#)
- [33] R. A. Lacey, "Indications for a Critical End Point in the Phase Diagram for Hot and Dense Nuclear Matter," *Phys. Rev. Lett.*, vol. 114, no. 14, p. 142301, 2015. [10](#)
- [34] J. Berges and K. Rajagopal, "Color superconductivity and chiral symmetry restoration at nonzero baryon density and temperature," *Nucl. Phys. B*, vol. 538, pp. 215–232, 1999. [10](#)
- [35] A. M. Halasz, A. D. Jackson, R. E. Shrock, M. A. Stephanov, and J. J. M. Verbaarschot, "On the phase diagram of QCD," *Phys. Rev. D*, vol. 58, p. 096007, 1998. [10](#)
- [36] O. Scavenius, A. Mocsy, I. N. Mishustin, and D. H. Rischke, "Chiral phase transition within effective models with constituent quarks," *Phys. Rev. C*, vol. 64, p. 045202, 2001. [10](#)
- [37] N. G. Antoniou and A. S. Kapoyannis, "Bootstrapping the QCD critical point," *Phys. Lett. B*, vol. 563, pp. 165–172, 2003. [10](#)
- [38] Y. Hatta and T. Ikeda, "Universality, the QCD critical / tricritical point and the quark number susceptibility," *Phys. Rev. D*, vol. 67, p. 014028, 2003. [10](#)
- [39] M. A. Stephanov, "Non-Gaussian fluctuations near the QCD critical point," *Phys. Rev. Lett.*, vol. 102, p. 032301, 2009. [10](#)
- [40] M. A. Stephanov, K. Rajagopal, and E. V. Shuryak, "Event-by-event fluctuations in heavy ion collisions and the QCD critical point," *Phys. Rev. D*, vol. 60, p. 114028, 1999. [10](#)
- [41] A. D. Panagiotou, M. W. Curtin, H. Toki, D. K. Scott, and P. J. Siemens, "Experimental evidence for a liquid - gas phase transition in nuclear systems," *Phys. Rev. Lett.*, vol. 52, pp. 496–499, 1984. [11](#)
- [42] M. D'Agostino, M. Bruno, F. Gulminelli, F. Cannata, P. Chomaz, G. Casini,

- E. Geraci, F. Gramegna, A. Moroni, and G. Vannini, "Nuclear liquid-gas phase transition: Experimental signals," *Nucl. Phys. A*, vol. 749, pp. 55–64, 2005. [11](#)
- [43] M. G. Alford, K. Rajagopal, and F. Wilczek, "Color flavor locking and chiral symmetry breaking in high density QCD," *Nucl. Phys. B*, vol. 537, pp. 443–458, 1999. [11](#)
- [44] T. Schaefer, "Patterns of symmetry breaking in QCD at high baryon density," *Nucl. Phys. B*, vol. 575, pp. 269–284, 2000. [11](#)
- [45] K. Rajagopal, "Three flavor QCD at high density: Color flavor locking and chiral symmetry breaking," *Nucl. Phys. A*, vol. 642, pp. 26–38, 1998. [11](#)
- [46] A. Andronic, P. Braun-Munzinger, and J. Stachel, "Hadron production in central nucleus-nucleus collisions at chemical freeze-out," *Nucl. Phys. A*, vol. 772, pp. 167–199, 2006. [11](#), [23](#), [24](#)
- [47] J. Cleymans and K. Redlich, "Chemical and thermal freezeout parameters from 1-A/GeV to 200-A/GeV," *Phys. Rev. C*, vol. 60, p. 054908, 1999. [11](#)
- [48] J. Stachel, A. Andronic, P. Braun-Munzinger, and K. Redlich, "Confronting LHC data with the statistical hadronization model," *J. Phys. Conf. Ser.*, vol. 509, p. 012019, 2014. [11](#)
- [49] O. Kaczmarek, F. Karsch, E. Laermann, C. Miao, S. Mukherjee, P. Petreczky, C. Schmidt, W. Soeldner, and W. Unger, "Phase boundary for the chiral transition in (2+1) -flavor QCD at small values of the chemical potential," *Phys. Rev. D*, vol. 83, p. 014504, 2011. [11](#)
- [50] E. Witten, "Cosmic Separation of Phases," *Phys. Rev. D*, vol. 30, pp. 272–285, 1984. [12](#)
- [51] J. I. Kapusta, "Quark - gluon plasma in the early universe," in *Phase transitions in the early universe: Theory and observations. Proceedings, NATO ASI, International School of Astrophysics 'Daniel Chalonge', 8th Course dedicated to Andrei D. Sakharov, Erice, Italy, December 6-17, 2000*, 2000, pp. 103–121. [12](#)
- [52] S. Weinberg, *The First Three Minutes. A Modern View of the Origin of the Universe*, 1977. [12](#)
- [53] R. Xu, "Strange quark stars - A Review," 2002, [IAU Symp.214,191(2003)]. [12](#)
- [54] J. M. Lattimer, "The nuclear equation of state and neutron star masses," *Ann. Rev. Nucl. Part. Sci.*, vol. 62, pp. 485–515, 2012. [12](#)
- [55] P. Demorest, T. Pennucci, S. Ransom, M. Roberts, and J. Hessels, "Shapiro Delay Measurement of A Two Solar Mass Neutron Star," *Nature*, vol. 467, pp. 1081–1083, 2010. [12](#)
- [56] J. Antoniadis *et al.*, "A Massive Pulsar in a Compact Relativistic Binary," *Science*,

- vol. 340, p. 6131, 2013. 12
- [57] M. G. Alford, S. Han, and M. Prakash, "Generic conditions for stable hybrid stars," *Phys. Rev. D*, vol. 88, no. 8, p. 083013, 2013. 12
- [58] S. Benic, D. Blaschke, D. E. Alvarez-Castillo, T. Fischer, and S. Typel, "A new quark-hadron hybrid equation of state for astrophysics - I. High-mass twin compact stars," *Astron. Astrophys.*, vol. 577, p. A40, 2015. 12
- [59] J. Barale and et al., "Performance of the Bevalac," *IEEE Trans. Nucl. Sci.*, vol. 22, pp. 1672–1674, 1975. 15
- [60] J. R. Alonso, R. T. Avery, T. Elioff, R. J. Force, H. A. Grunder, H. D. Lancaster, J. R. Meneghetti, F. B. Selph, R. R. Stevenson, and R. B. Yourd, "Acceleration of uranium at the Bevalac," *Science*, vol. 217, pp. 1135–1137, 1982. 15
- [61] A. I. Malakhov, "The Main Physical Results at the Dubna Synchrophasotron," in *Proceedings, 11th International Workshop Relativistic Nuclear Physics: from Hundreds of MeV to TeV: Stara Lesna, Slovak Republik, June 17-23, 2012*, 2013, p. 6. 15
- [62] A. Kovalenko *et al.*, "Nuclotron at JINR: Operation Experience and Recent Development," in *Proceedings, 13th Heavy Ion Accelerator Technology Conference (HIAT2015): Yokohama, Japan, September 7-11, 2015*, 2016, p. MOPA19. 15
- [63] A. B. Kuznetsov, A. V. Tuzikov, and A. V. Philippov, "Gold ion beams induced desorption studies for Booster Nuclotron," *Phys. Part. Nucl. Lett.*, vol. 13, no. 7, pp. 982–987, 2016. 15
- [64] O. Kozlov, I. Meshkov, A. Sidorin, and G. Trubnikov, "Start-up configuration of the NICA collider equipment," *Phys. Part. Nucl. Lett.*, vol. 13, no. 7, pp. 934–936, 2016. 15
- [65] V. Kekelidze, R. Lednicky, V. Matveev, I. Meshkov, A. Sorin, and G. Trubnikov, "NICA project at JINR," *Phys. Part. Nucl. Lett.*, vol. 9, pp. 313–316, 2012. 15, 17
- [66] B. Friman, C. Höhne, J. Knoll, S. Leupold, J. Randrup, R. Rapp, and P. Senger, *The CBM Physics Book: Compressed Baryonic Matter in Laboratory Experiments*, ser. Lecture Notes in Physics. Springer Berlin Heidelberg, 2011. 15
- [67] [Online]. Available: <https://www.osti.gov/scitech/servlets/purl/6955779> 15
- [68] [Online]. Available: <http://www.rhichome.bnl.gov/RHIC/Runs/> 15, 16
- [69] H. G. Pugh, "Search for the quark - gluon plasma (1989): the NA35 experiment at the CERN SPS," *Phys. Scripta T*, vol. 32, pp. 208–217, 1990. 15, 16
- [70] N. Armesto and E. Scapparini, "Heavy-ion collisions at the Large Hadron Collider: a review of the results from Run 1," *Eur. Phys. J. Plus*, vol. 131, no. 3, p. 52, 2016. 15
- [71] H. Sako, "Future Heavy-Ion Program at J-PARC," *JPS Conf. Proc.*, vol. 8, p.

022010, 2015. 15, 18

- [72] G. E. Brown, "Heavy ion collisions at Bevalac energies," *Comments Nucl. Part. Phys.*, vol. 19, no. 4, pp. 185–208, 1990. 14
- [73] K. G. R. Doss *et al.*, "Nuclear Collective Flow as a Function of Projectile Energy and Mass," *Phys. Rev. Lett.*, vol. 57, pp. 302–305, 1986. 14
- [74] H. A. Gustafsson *et al.*, "Collective Flow Observed in Relativistic Nuclear Collisions," *Phys. Rev. Lett.*, vol. 52, pp. 1590–1593, 1984. 14
- [75] G. Roche *et al.*, "First Observation of Dielectron Production at the Bevalac," *Phys. Rev. Lett.*, vol. 61, pp. 1069–1072, 1988. 14
- [76] M. A. Lisa, S. Pratt, R. Soltz, and U. Wiedemann, "Femtoscscopy in relativistic heavy ion collisions," *Ann. Rev. Nucl. Part. Sci.*, vol. 55, pp. 357–402, 2005. 14, 17, 145
- [77] A. A. Kuznetsov, "Experiments at the Dubna synchrophasotron," *Nucl. Phys. A*, vol. 400, pp. 493C–524C, 1983. 14
- [78] W. Reisdorf *et al.*, "Systematics of pion emission in heavy ion collisions in the 1A- GeV regime," *Nucl. Phys. A*, vol. 781, pp. 459–508, 2007. 14
- [79] F. Laue *et al.*, "Medium effects in kaon and anti-kaon production in nuclear collisions at subthreshold beam energies," *Phys. Rev. Lett.*, vol. 82, pp. 1640–1643, 1999. 14
- [80] K. Wisniewski *et al.*, "Direct comparison of phase space distributions of K- and K+ mesons in heavy ion collisions at SIS energies: Evidence for in-medium modifications of kaons?" *Eur. Phys. J. A*, vol. 9, pp. 515–519, 2000. 14
- [81] X. Lopez *et al.*, "Subthreshold production of Sigma(1385) baryons in Al + Al collisions at 1.9A-GeV," *Phys. Rev. C*, vol. 76, p. 052203, 2007. 14
- [82] A. Mangiarotti *et al.*, "Sub-threshold phi-meson yield in central 58Ni+58Ni collisions," *Nucl. Phys. A*, vol. 714, pp. 89–123, 2003. 14
- [83] A. Andronic *et al.*, "Transition from in-plane to out-of-plane azimuthal enhancement in Au + Au collisions," *Nucl. Phys. A*, vol. 679, pp. 765–792, 2001. 14
- [84] J. Stroth, "Status and Plans of HADES," in *Workshop on Excited Hyperons in QCD Thermodynamics at Freeze-Out (YSTAR2016) Mini-Proceedings*, 2017, pp. 68–78. 14
- [85] G. Agakishiev *et al.*, "Dielectron production in Ar+KCl collisions at 1.76A GeV," *Phys. Rev. C*, vol. 84, p. 014902, 2011. 14
- [86] C. Franco, "Dilepton Results from HADES Using Au+Au Data at 1.23A GeV," *JPS Conf. Proc.*, vol. 13, p. 020003, 2017. 14
- [87] L. Ahle *et al.*, "An Excitation function of K- and K+ production in Au + Au

- reactions at the AGS," *Phys. Lett. B*, vol. 490, pp. 53–60, 2000. 14
- [88] —, "Centrality dependence of kaon yields in Si + A and Au + Au collisions at the AGS," *Phys. Rev. C*, vol. 60, p. 044904, 1999. 14
- [89] C. A. Ogilvie *et al.*, "Au + Au reactions at the AGS: Experiments E866 and E917," *Nucl. Phys. A*, vol. 638, pp. 57C–68C, 1998. 14
- [90] J. Barrette *et al.*, "Directed flow and particle production in Au + Au collisions from experiment E877 at the AGS," *Nucl. Phys. A*, vol. 590, pp. 259C–270C, 1995. 14
- [91] —, "Energy and charged particle flow in a 10.8-A/GeV/c Au + Au collisions," *Phys. Rev. C*, vol. 55, pp. 1420–1430, 1997, [Erratum: *Phys. Rev. C*56,2336(1997)]. 14
- [92] M. A. Lisa *et al.*, "Azimuthal dependence of pion interferometry at the AGS," *Phys. Lett. B*, vol. 496, pp. 1–8, 2000. 14
- [93] S. H. Kahana, D. E. Kahana, Y. Pang, and T. J. Schlagel, "Modeling relativistic heavy ion collisions at the AGS," *Ann. Rev. Nucl. Part. Sci.*, vol. 46, pp. 31–70, 1996. 14
- [94] P. Braun-Munzinger, J. Stachel, J. P. Wessels, and N. Xu, "Thermal equilibration and expansion in nucleus-nucleus collisions at the AGS," *Phys. Lett. B*, vol. 344, pp. 43–48, 1995. 16
- [95] J. P. Wessels *et al.*, "Latest results from CERES / NA45," *Nucl. Phys. A*, vol. 715, pp. 262–271, 2003. 16
- [96] L. Ramello *et al.*, "Results on leptonic probes from NA50," *Nucl. Phys. A*, vol. 715, pp. 243–251, 2003. 16
- [97] M. M. Aggarwal *et al.*, "Recent results on Pb + Pb collisions at 158-A-GeV from the WA98 experiment at CERN," *Nucl. Phys. A*, vol. 638, pp. 147–158, 1998. 16
- [98] G. E. Bruno, "New results from NA57 experiment," *J. Phys. G*, vol. 30, pp. S717–S724, 2004. 16
- [99] J. Bachler *et al.*, "Hadron production in nuclear collisions from the NA49 experiment at 158-GeV/c/A," *Nucl. Phys. A*, vol. 661, pp. 45–54, 1999. 16
- [100] M. Gazdzicki, M. Gorenstein, and P. Seyboth, "Onset of deconfinement in nucleus-nucleus collisions: Review for pedestrians and experts," *Acta Phys. Polon. B*, vol. 42, pp. 307–351, 2011. 16
- [101] A. Rustamov, "The Horn, Kink and Step, Dale: from few GeV to few TeV," *Central Eur. J. Phys.*, vol. 10, pp. 1267–1270, 2012. 16
- [102] E. L. Bratkovskaya, M. Bleicher, W. Cassing, M. van Leeuwen, M. Reiter, S. Soff, H. Stoecker, and H. Weber, "Strangeness dynamics in relativistic nucleus nucleus

- collision," *Prog. Part. Nucl. Phys.*, vol. 53, pp. 225–237, 2004. 16
- [103] M. Gazdzicki, "NA49/NA61: results and plans on beam energy and system size scan at the CERN SPS," *J. Phys. G*, vol. 38, p. 124024, 2011. 16
- [104] B. Alver *et al.*, "Phobos results on charged particle multiplicity and pseudorapidity distributions in Au+Au, Cu+Cu, d+Au, and p+p collisions at ultra-relativistic energies," *Phys. Rev. C*, vol. 83, p. 024913, 2011. 16
- [105] T. Chujo, "Results on identified hadrons from the PHENIX experiment at RHIC," *Nucl. Phys. A*, vol. 715, pp. 151–160, 2003. 16
- [106] L. Kumar, "Identified Hadron Production from the RHIC Beam Energy Scan," *J. Phys. G*, vol. 38, p. 124145, 2011. 16
- [107] G. Agakishiev *et al.*, "Energy and system-size dependence of two- and four-particle v_2 measurements in heavy-ion collisions at RHIC and their implications on flow fluctuations and nonflow," *Phys. Rev. C*, vol. 86, p. 014904, 2012. 16
- [108] R. A. Lacey, "Elliptic flow measurements with the PHENIX detector," *Nucl. Phys. A*, vol. 698, pp. 559–563, 2002. 16
- [109] P. F. Kolb, P. Huovinen, U. W. Heinz, and H. Heiselberg, "Elliptic flow at SPS and RHIC: From kinetic transport to hydrodynamics," *Phys. Lett. B*, vol. 500, pp. 232–240, 2001. 17
- [110] P. Huovinen, P. F. Kolb, U. W. Heinz, P. V. Ruuskanen, and S. A. Voloshin, "Radial and elliptic flow at RHIC: Further predictions," *Phys. Lett. B*, vol. 503, pp. 58–64, 2001. 17
- [111] T. Hirano and K. Tsuda, "Collective flow and two pion correlations from a relativistic hydrodynamic model with early chemical freezeout," *Phys. Rev. C*, vol. 66, p. 054905, 2002. 17
- [112] D. Teaney, J. Lauret, and E. V. Shuryak, "Hydro+cascade, flow, the equation of state, predictions and data," *Nucl. Phys. A*, vol. 698, pp. 479–482, 2002. 17
- [113] B. Betz, "Jet Quenching in Heavy-Ion Collisions - The Transition Era from RHIC to LHC," *Eur. Phys. J. A*, vol. 48, p. 164, 2012. 17
- [114] N. Xu, "Collective expansion in high-energy nuclear collisions: The search for the partonic EOS at RHIC," *Nucl. Phys. A*, vol. 751, pp. 109–126, 2005. 17
- [115] L. Adamczyk *et al.*, "Observation of an Energy-Dependent Difference in Elliptic Flow between Particles and Antiparticles in Relativistic Heavy Ion Collisions," *Phys. Rev. Lett.*, vol. 110, no. 14, p. 142301, 2013. 17
- [116] Y. Lu, M. Bleicher, F. Liu, Z. Liu, H. Petersen, P. Sorensen, H. Stoecker, N. Xu, and X. Zhu, "Anisotropic flow at RHIC: How unique is the number-of-constituent-quark scaling?" *J. Phys. G*, vol. 32, pp. 1121–1130, 2006. 17

- [117] L. Adamczyk *et al.*, “Energy Dependence of Moments of Net-proton Multiplicity Distributions at RHIC,” *Phys. Rev. Lett.*, vol. 112, p. 032302, 2014. [17](#)
- [118] K. Aamodt *et al.*, “Two-pion Bose-Einstein correlations in central Pb-Pb collisions at $\sqrt{s_{NN}} = 2.76$ TeV,” *Phys. Lett. B*, vol. 696, pp. 328–337, 2011. [17](#)
- [119] P. Spiller and G. Franchetti, “The FAIR accelerator project at GSI,” *Nucl. Instrum. Meth. A*, vol. 561, pp. 305–309, 2006. [17](#)
- [120] D. I. Kazakov, “Radiative Corrections, Divergences, Regularization, Renormalization, Renormalization Group and All That in Examples in Quantum Field Theory,” 2008. [20](#)
- [121] D. J. Gross, “Twenty five years of asymptotic freedom,” *Nucl. Phys. Proc. Suppl.*, vol. 74, pp. 426–446, 1999. [20](#)
- [122] D. J. Gross, R. D. Pisarski, and L. G. Yaffe, “QCD and Instantons at Finite Temperature,” *Rev. Mod. Phys.*, vol. 53, p. 43, 1981. [21](#)
- [123] M. Bruno, M. Dalla Brida, P. Fritzsche, T. Korzec, A. Ramos, S. Schaefer, H. Simma, S. Sint, and R. Sommer, “The Λ -parameter in 3-flavour QCD and $\alpha_s(m_Z)$ by the ALPHA collaboration,” *PoS*, vol. LATTICE2016, p. 197, 2016. [21](#)
- [124] S. Borsanyi, Z. Fodor, C. Hoelbling, S. D. Katz, S. Krieg, C. Ratti, and K. K. Szabo, “Recent results on the Equation of State of QCD,” *PoS*, vol. LATTICE2014, p. 224, 2015. [21](#)
- [125] A. Bashir, L. Chang, I. C. Cloet, B. El-Bennich, Y.-X. Liu, C. D. Roberts, and P. C. Tandy, “Collective perspective on advances in Dyson-Schwinger Equation QCD,” *Commun. Theor. Phys.*, vol. 58, pp. 79–134, 2012. [21](#)
- [126] A. V. Manohar, “Effective field theories,” *Lect. Notes Phys.*, vol. 479, pp. 311–362, 1997. [22](#)
- [127] F. Gelis, E. Iancu, J. Jalilian-Marian, and R. Venugopalan, “The Color Glass Condensate,” *Ann. Rev. Nucl. Part. Sci.*, vol. 60, pp. 463–489, 2010. [22](#), [43](#), [145](#)
- [128] E. Iancu and R. Venugopalan, “The Color glass condensate and high-energy scattering in QCD,” in *In *Hwa, R.C. (ed.) et al.: Quark gluon plasma** 249–3363, 2003. [22](#), [145](#)
- [129] J. Pumplin, D. R. Stump, J. Huston, H. L. Lai, P. M. Nadolsky, and W. K. Tung, “New generation of parton distributions with uncertainties from global QCD analysis,” *JHEP*, vol. 07, p. 012, 2002. [22](#), [145](#)
- [130] M. Gluck, E. Reya, and A. Vogt, “Dynamical parton distributions of the proton and small x physics,” *Z. Phys. C*, vol. 67, pp. 433–448, 1995. [22](#), [145](#)
- [131] M. Froissart, “Asymptotic behavior and subtractions in the Mandelstam representation,” *Phys. Rev.*, vol. 123, pp. 1053–1057, 1961. [22](#)

- [132] T. Hirano, U. W. Heinz, D. Kharzeev, R. Lacey, and Y. Nara, "Hadronic dissipative effects on elliptic flow in ultrarelativistic heavy-ion collisions," *Phys. Lett. B*, vol. 636, pp. 299–304, 2006. [23](#), [31](#)
- [133] A. Kurkela and Y. Zhu, "Isotropization and hydrodynamization in weakly coupled heavy-ion collisions," *Phys. Rev. Lett.*, vol. 115, no. 18, p. 182301, 2015. [23](#)
- [134] J. M. Maldacena, "The Large N limit of superconformal field theories and supergravity," *Int. J. Theor. Phys.*, vol. 38, pp. 1113–1133, 1999, [Adv. Theor. Math. Phys.2,231(1998)]. [23](#)
- [135] P. Kovtun, D. T. Son, and A. O. Starinets, "Viscosity in strongly interacting quantum field theories from black hole physics," *Phys. Rev. Lett.*, vol. 94, p. 111601, 2005. [23](#)
- [136] P. M. Chesler and W. van der Schee, "Early thermalization, hydrodynamics and energy loss in AdS/CFT," *Int. J. Mod. Phys. E*, vol. 24, no. 10, p. 1530011, 2015. [23](#)
- [137] I. Aref'eva, "Multiplicity and thermalization time in heavy-ions collisions," *EPJ Web Conf.*, vol. 125, p. 01007, 2016. [23](#)
- [138] R. Dashen, S.-K. Ma, and H. J. Bernstein, "S Matrix formulation of statistical mechanics," *Phys. Rev.*, vol. 187, pp. 345–370, 1969. [23](#)
- [139] D. R. Oliinychenko, K. A. Bugaev, and A. S. Sorin, "Investigation of Hadron Multiplicities and Hadron Yield Ratios in heavy Ion Collisions," *Ukr. J. Phys.*, vol. 58, no. 3, pp. 211–227, 2013. [23](#)
- [140] F. Becattini, J. Cleymans, A. Keranen, E. Suhonen, and K. Redlich, "Features of particle multiplicities and strangeness production in central heavy ion collisions between 1.7A-GeV/c and 158A-GeV/c," *Phys. Rev. C*, vol. 64, p. 024901, 2001. [24](#)
- [141] A. Andronic, P. Braun-Munzinger, K. Redlich, and J. Stachel, "Statistical hadronization of charm in heavy ion collisions at SPS, RHIC and LHC," *Phys. Lett. B*, vol. 571, pp. 36–44, 2003. [24](#)
- [142] J. Cleymans, H. Oeschler, K. Redlich, and S. Wheaton, "Comparison of chemical freeze-out criteria in heavy-ion collisions," *Phys. Rev. C*, vol. 73, p. 034905, 2006. [24](#)
- [143] A. Andronic, P. Braun-Munzinger, and J. Stachel, "Thermal hadron production in relativistic nuclear collisions: The Hadron mass spectrum, the horn, and the QCD phase transition," *Phys. Lett. B*, vol. 673, pp. 142–145, 2009, [Erratum: Phys. Lett.B678,516(2009)]. [24](#), [75](#)
- [144] A. Andronic, P. Braun-Munzinger, K. Redlich, and J. Stachel, "The thermal model on the verge of the ultimate test: particle production in Pb-Pb collisions at the LHC," *J. Phys. G*, vol. 38, p. 124081, 2011. [24](#)

- [145] R. Hagedorn and K. Redlich, "Statistical Thermodynamics in Relativistic Particle and Ion Physics: Canonical or Grand Canonical?" *Z. Phys. C*, vol. 27, p. 541, 1985. [24](#)
- [146] J. Cleymans, H. Oeschler, and K. Redlich, "Influence of impact parameter on thermal description of relativistic heavy ion collisions at (1-2) A-GeV," *Phys. Rev. C*, vol. 59, p. 1663, 1999. [24](#)
- [147] V. V. Begun, M. Gazdzicki, M. I. Gorenstein, M. Hauer, V. P. Konchakovski, and B. Lungwitz, "Multiplicity fluctuations in relativistic nuclear collisions: Statistical model versus experimental data," *Phys. Rev. C*, vol. 76, p. 024902, 2007. [24](#)
- [148] S. Hamieh, K. Redlich, and A. Tounsi, "Canonical description of strangeness enhancement from p-A to Pb Pb collisions," *Phys. Lett. B*, vol. 486, pp. 61–66, 2000. [24](#)
- [149] A. Andronic, F. Beutler, P. Braun-Munzinger, K. Redlich, and J. Stachel, "Thermal description of hadron production in e+e- collisions revisited," *Phys. Lett. B*, vol. 675, pp. 312–318, 2009. [24](#)
- [150] J. Rafelski, Ed., *Melting Hadrons, Boiling Quarks - From Hagedorn Temperature to Ultra-Relativistic Heavy-Ion Collisions at CERN*. Springer, 2016. [24](#)
- [151] R. Hagedorn, "Statistical thermodynamics of strong interactions at high-energies," *Nuovo Cim. Suppl.*, vol. 3, pp. 147–186, 1965. [24](#)
- [152] N. Cabibbo and G. Parisi, "Exponential Hadronic Spectrum and Quark Liberation," *Phys. Lett. B*, vol. 59, pp. 67–69, 1975. [24](#)
- [153] F. Cooper and G. Frye, "Comment on the Single Particle Distribution in the Hydrodynamic and Statistical Thermodynamic Models of Multiparticle Production," *Phys. Rev. D*, vol. 10, p. 186, 1974. [24](#), [51](#)
- [154] P. J. Siemens and J. O. Rasmussen, "Evidence for a blast wave from compress nuclear matter," *Phys. Rev. Lett.*, vol. 42, pp. 880–887, 1979. [24](#)
- [155] E. Schnedermann, J. Sollfrank, and U. W. Heinz, "Thermal phenomenology of hadrons from 200-A/GeV S+S collisions," *Phys. Rev. C*, vol. 48, pp. 2462–2475, 1993. [24](#)
- [156] M. Chojnacki, A. Kisiel, W. Florkowski, and W. Broniowski, "THERMINATOR 2: THERMal heavy IoN generATOR 2," *Comput. Phys. Commun.*, vol. 183, pp. 746–773, 2012. [24](#)
- [157] L. D. Landau, "On the multiparticle production in high-energy collisions," *Izv. Akad. Nauk Ser. Fiz.*, vol. 17, pp. 51–64, 1953. [25](#)
- [158] S. Z. Belenkij and L. D. Landau, "Hydrodynamic theory of multiple production of particles," *Nuovo Cim. Suppl. S*, vol. 310, p. 15, 1956, [*Usp. Fiz.*

- Nauk56,309(1955)]. [25](#)
- [159] J. D. Bjorken, “Highly Relativistic Nucleus-Nucleus Collisions: The Central Rapidity Region,” *Phys. Rev. D*, vol. 27, pp. 140–151, 1983. [25](#)
- [160] R. Derradi de Souza, T. Koide, and T. Kodama, “Hydrodynamic Approaches in Relativistic Heavy Ion Reactions,” *Prog. Part. Nucl. Phys.*, vol. 86, pp. 35–85, 2016. [25](#)
- [161] L.-G. Pang, K. Zhou, N. Su, H. Petersen, H. Stoecker, and X.-N. Wang, “An EoS-meter of QCD transition from deep learning,” 2016. [26](#)
- [162] P. Huovinen and P. V. Ruuskanen, “Hydrodynamic Models for Heavy Ion Collisions,” *Ann. Rev. Nucl. Part. Sci.*, vol. 56, pp. 163–206, 2006. [26](#)
- [163] H. Petersen, J. Steinheimer, G. Burau, M. Bleicher, and H. Stoecker, “A Fully Integrated Transport Approach to Heavy Ion Reactions with an Intermediate Hydrodynamic Stage,” *Phys. Rev. C*, vol. 78, p. 044901, 2008. [26](#), [31](#), [43](#), [44](#), [45](#), [125](#), [138](#)
- [164] I. A. Karpenko, P. Huovinen, H. Petersen, and M. Bleicher, “Estimation of the shear viscosity at finite net-baryon density from $A + A$ collision data at $\sqrt{s_{NN}} = 7.7 - 200$ GeV,” *Phys. Rev. C*, vol. 91, no. 6, p. 064901, 2015. [26](#), [28](#), [31](#), [43](#), [44](#), [45](#)
- [165] L. Pang, Q. Wang, and X.-N. Wang, “Effects of initial flow velocity fluctuation in event-by-event (3+1)D hydrodynamics,” *Phys. Rev. C*, vol. 86, p. 024911, 2012. [26](#), [43](#), [44](#), [45](#), [46](#)
- [166] T. Lappi and R. Venugopalan, “Universality of the saturation scale and the initial eccentricity in heavy ion collisions,” *Phys. Rev. C*, vol. 74, p. 054905, 2006. [26](#)
- [167] B. Schenke, P. Tribedy, and R. Venugopalan, “Fluctuating Glasma initial conditions and flow in heavy ion collisions,” *Phys. Rev. Lett.*, vol. 108, p. 252301, 2012. [26](#)
- [168] C. Gale, S. Jeon, B. Schenke, P. Tribedy, and R. Venugopalan, “Event-by-event anisotropic flow in heavy-ion collisions from combined Yang-Mills and viscous fluid dynamics,” *Phys. Rev. Lett.*, vol. 110, no. 1, p. 012302, 2013. [26](#), [43](#), [44](#), [45](#), [46](#)
- [169] J. L. Albacete, A. Dumitru, and Y. Nara, “CGC initial conditions at RHIC and LHC,” *J. Phys. Conf. Ser.*, vol. 316, p. 012011, 2011. [26](#)
- [170] H. J. Drescher and Y. Nara, “Effects of fluctuations on the initial eccentricity from the Color Glass Condensate in heavy ion collisions,” *Phys. Rev. C*, vol. 75, p. 034905, 2007. [26](#)
- [171] M. L. Miller, K. Reygers, S. J. Sanders, and P. Steinberg, “Glauber modeling in high energy nuclear collisions,” *Ann. Rev. Nucl. Part. Sci.*, vol. 57, pp. 205–243, 2007. [26](#)

- [172] W. Broniowski, M. Rybczynski, and P. Bozek, "GLISSANDO: Glauber initial-state simulation and more.." *Comput. Phys. Commun.*, vol. 180, pp. 69–83, 2009. [26](#)
- [173] C. Loizides, J. Nagle, and P. Steinberg, "Improved version of the PHOBOS Glauber Monte Carlo," *SoftwareX*, vol. 1-2, pp. 13–18, 2015. [26](#)
- [174] C. E. Coleman-Smith, H. Petersen, and R. L. Wolpert, "Classification of initial state granularity via 2d Fourier Expansion," *J. Phys. G*, vol. 40, p. 095103, 2013. [26](#)
- [175] F. G. Gardim, F. Grassi, M. Luzum, and J.-Y. Ollitrault, "Mapping the hydrodynamic response to the initial geometry in heavy-ion collisions," *Phys. Rev. C*, vol. 85, p. 024908, 2012. [27](#)
- [176] J. Auvinen and H. Petersen, "Evolution of elliptic and triangular flow as a function of $\sqrt{s_{NN}}$ in a hybrid model," *Phys. Rev. C*, vol. 88, no. 6, p. 064908, 2013. [27](#)
- [177] J. Noronha-Hostler, "Resolving the R_{AA} to v_n puzzle," in *8th International Conference on Hard and Electromagnetic Probes of High-energy Nuclear Collisions: Hard Probes 2016 (HP2016) Wuhan, Hubei, China, September 23-27, 2016*, 2016. [27](#)
- [178] C. Eckart, "The Thermodynamics of irreversible processes. 3.. Relativistic theory of the simple fluid," *Phys. Rev.*, vol. 58, pp. 919–924, 1940. [28](#)
- [179] L. D. Landau and E. M. Lifshitz, *Fluid Mechanics*. Pergamon Press, 1959. [28](#)
- [180] W. Israel and J. M. Stewart, "Transient relativistic thermodynamics and kinetic theory," *Annals Phys.*, vol. 118, pp. 341–372, 1979. [28](#)
- [181] G. S. Denicol, H. Niemi, E. Molnar, and D. H. Rischke, "Derivation of transient relativistic fluid dynamics from the Boltzmann equation," *Phys. Rev. D*, vol. 85, p. 114047, 2012, [Erratum: *Phys. Rev.D*91,no.3,039902(2015)]. [28](#)
- [182] D. Teaney, "The Effects of viscosity on spectra, elliptic flow, and HBT radii," *Phys. Rev. C*, vol. 68, p. 034913, 2003. [28](#)
- [183] M. Luzum and P. Romatschke, "Conformal Relativistic Viscous Hydrodynamics: Applications to RHIC results at $s(NN)^{1/2} = 200\text{-GeV}$," *Phys. Rev. C*, vol. 78, p. 034915, 2008, [Erratum: *Phys. Rev.C*79,039903(2009)]. [28](#)
- [184] B. Schenke, S. Jeon, and C. Gale, "Elliptic and triangular flow in event-by-event (3+1)D viscous hydrodynamics," *Phys. Rev. Lett.*, vol. 106, p. 042301, 2011. [28](#)
- [185] H. Song and U. W. Heinz, "Suppression of elliptic flow in a minimally viscous quark-gluon plasma," *Phys. Lett. B*, vol. 658, pp. 279–283, 2008. [28](#)
- [186] E. Molnar, H. Holopainen, P. Huovinen, and H. Niemi, "Influence of temperature-dependent shear viscosity on elliptic flow at backward and forward

- rapidities in ultrarelativistic heavy-ion collisions," *Phys. Rev. C*, vol. 90, no. 4, p. 044904, 2014. 28
- [187] H. Niemi, K. J. Eskola, R. Paatelainen, and K. Tuominen, "Pinning down QCD-matter shear viscosity in $A\bar{A}$ collisions via EbyE fluctuations using pQCD + saturation + hydrodynamics," *Nucl. Phys. A*, vol. 956, pp. 312–315, 2016. 28
- [188] M. Strickland, "Anisotropic Hydrodynamics: Three lectures," *Acta Phys. Polon. B*, vol. 45, no. 12, pp. 2355–2394, 2014. 28, 33, 43
- [189] D. Bazow, U. W. Heinz, and M. Strickland, "Second-order (2+1)-dimensional anisotropic hydrodynamics," *Phys. Rev. C*, vol. 90, no. 5, p. 054910, 2014. 28, 33
- [190] S. R. De Groot, W. A. Van Leeuwen, and C. G. Van Weert, *Relativistic Kinetic Theory*. North-Holland Publishing Company, 1980. 28
- [191] J. Aichelin and H. Stoecker, "Quantum molecular dynamics. A Novel approach to N body correlations in heavy ion collisions," *Phys. Lett. B*, vol. 176, pp. 14–19, 1986. 30
- [192] C. M. Ko, "Relativistic Vlasov-Uehling-Uhlenbeck Model for High-energy Heavy Ion Collisions," *Nucl. Phys. A*, vol. 495, pp. 321C–336C, 1989. 30
- [193] Y. Pang, T. J. Schlagel, and S. H. Kahana, "Cascade calculation of Au + Au collisions at 11.7-GeV/c," in *1992 Meeting of the Division of Nuclear Physics of the American Physical Society (Preceded by 2 Workshops both on Oct 14: New Vistas in Physics with High-energy Pion Beams and Neutrons - Their Use for Nuclear Physics and Fundamental Symmetry Tests) Santa Fe, New Mexico, October 15-17, 1992, 1992*. 30
- [194] C. Hartnack, Z. X. Li, L. Neise, G. Peilert, A. Rosenhauer, H. Sorge, H. Stoecker, W. Greiner, and J. Aichelin, "Quantum Molecular Dynamics: A Microscopic Model From Unilac to CERN Energies," *Nucl. Phys. A*, vol. 495, pp. 303C–320C, 1989. 30
- [195] W. Cassing, V. Metag, U. Mosel, and K. Niita, "Production of energetic particles in heavy ion collisions," *Phys. Rept.*, vol. 188, pp. 363–449, 1990. 30
- [196] H. Sorge, H. Stoecker, and W. Greiner, "Relativistic quantum molecular dynamics approach to nuclear collisions at ultrarelativistic energies," *Nucl. Phys. A*, vol. 498, pp. 567C–576C, 1989. 30
- [197] S. A. Bass *et al.*, "Microscopic models for ultrarelativistic heavy ion collisions," *Prog. Part. Nucl. Phys.*, vol. 41, pp. 255–369, 1998, [*Prog. Part. Nucl. Phys.* 41,225(1998)]. 30, 54, 69, 92, 95
- [198] W. Cassing, E. L. Bratkovskaya, and S. Juchem, "Excitation functions of hadronic observables from SIS to RHIC energies," *Nucl. Phys. A*, vol. 674, pp. 249–276,

2000. [30](#)

- [199] Y. Nara, N. Otuka, A. Ohnishi, K. Niita, and S. Chiba, “Study of relativistic nuclear collisions at AGS energies from p + Be to Au + Au with hadronic cascade model,” *Phys. Rev. C*, vol. 61, p. 024901, 2000. [30](#), [92](#)
- [200] O. Buss, T. Gaitanos, K. Gallmeister, H. van Hees, M. Kaskulov, O. Lalakulich, A. B. Larionov, T. Leitner, J. Weil, and U. Mosel, “Transport-theoretical Description of Nuclear Reactions,” *Phys. Rept.*, vol. 512, pp. 1–124, 2012. [30](#), [88](#), [92](#), [114](#)
- [201] K. Geiger and B. Muller, “Dynamics of parton cascades in highly relativistic nuclear collisions,” *Nucl. Phys. B*, vol. 369, pp. 600–654, 1992. [30](#)
- [202] D. Molnar and P. Huovinen, “Dissipation and elliptic flow at RHIC,” *Phys. Rev. Lett.*, vol. 94, p. 012302, 2005. [30](#)
- [203] B. Zhang, “ZPC 1.0.1: A Parton cascade for ultrarelativistic heavy ion collisions,” *Comput. Phys. Commun.*, vol. 109, pp. 193–206, 1998. [30](#)
- [204] Z. Xu and C. Greiner, “Thermalization of gluons in ultrarelativistic heavy ion collisions by including three-body interactions in a parton cascade,” *Phys. Rev. C*, vol. 71, p. 064901, 2005. [30](#), [96](#)
- [205] W. Cassing and E. L. Bratkovskaya, “Parton transport and hadronization from the dynamical quasiparticle point of view,” *Phys. Rev. C*, vol. 78, p. 034919, 2008. [30](#)
- [206] Z.-W. Lin, C. M. Ko, B.-A. Li, B. Zhang, and S. Pal, “A Multi-phase transport model for relativistic heavy ion collisions,” *Phys. Rev. C*, vol. 72, p. 064901, 2005. [30](#)
- [207] J. Xu *et al.*, “Understanding transport simulations of heavy-ion collisions at 100A and 400A MeV: Comparison of heavy-ion transport codes under controlled conditions,” *Phys. Rev. C*, vol. 93, no. 4, p. 044609, 2016. [31](#), [112](#)
- [208] S. A. Bass and A. Dumitru, “Dynamics of hot bulk QCD matter: From the quark gluon plasma to hadronic freezeout,” *Phys. Rev. C*, vol. 61, p. 064909, 2000. [31](#)
- [209] D. Teaney, J. Lauret, and E. V. Shuryak, “A Hydrodynamic description of heavy ion collisions at the SPS and RHIC,” 2001. [31](#)
- [210] C. Nonaka and S. A. Bass, “Space-time evolution of bulk QCD matter,” *Phys. Rev. C*, vol. 75, p. 014902, 2007. [31](#)
- [211] K. Werner, I. Karpenko, T. Pierog, M. Bleicher, and K. Mikhailov, “Event-by-Event Simulation of the Three-Dimensional Hydrodynamic Evolution from Flux Tube Initial Conditions in Ultrarelativistic Heavy Ion Collisions,” *Phys. Rev. C*, vol. 82, p. 044904, 2010. [31](#), [43](#), [44](#), [45](#), [46](#)

- [212] H. Song, S. A. Bass, U. Heinz, T. Hirano, and C. Shen, “200 A GeV Au+Au collisions serve a nearly perfect quark-gluon liquid,” *Phys. Rev. Lett.*, vol. 106, p. 192301, 2011, [Erratum: *Phys. Rev. Lett.*109,139904(2012)]. [31](#)
- [213] I. A. Karpenko, Yu. M. Sinyukov, and K. Werner, “Uniform description of bulk observables in the hydrokinetic model of $A + A$ collisions at the BNL Relativistic Heavy Ion Collider and the CERN Large Hadron Collider,” *Phys. Rev. C*, vol. 87, no. 2, p. 024914, 2013. [31](#)
- [214] T. Hirano, P. Huovinen, K. Murase, and Y. Nara, “Integrated Dynamical Approach to Relativistic Heavy Ion Collisions,” *Prog. Part. Nucl. Phys.*, vol. 70, pp. 108–158, 2013. [31](#)
- [215] J. Auvinen, K. Redlich, and S. A. Bass, “Multi-strange hadrons and the precision extraction of QGP properties in the RHIC-BES domain,” *J. Phys. Conf. Ser.*, vol. 779, no. 1, p. 012045, 2017. [31](#)
- [216] H. Petersen, “Anisotropic flow in transport + hydrodynamics hybrid approaches,” *J. Phys. G*, vol. 41, no. 12, p. 124005, 2014. [31](#)
- [217] J. Steinheimer and M. Bleicher, “Core-corona separation in the UrQMD hybrid model,” *Phys. Rev. C*, vol. 84, p. 024905, 2011. [32](#), [123](#)
- [218] K. A. Bugaev, “Relativistic kinetic equations for finite domains and freezeout problem,” *Phys. Rev. Lett.*, vol. 90, p. 252301, 2003. [33](#), [53](#)
- [219] Yu. M. Sinyukov, S. V. Akkelin, and Y. Hama, “On freezeout problem in hydro kinetic approach to $A+A$ collisions,” *Phys. Rev. Lett.*, vol. 89, p. 052301, 2002. [33](#)
- [220] S. V. Akkelin, Y. Hama, I. A. Karpenko, and Yu. M. Sinyukov, “Hydro-kinetic approach to relativistic heavy ion collisions,” *Phys. Rev. C*, vol. 78, p. 034906, 2008. [33](#)
- [221] L. P. Csernai, V. K. Magas, E. Molnar, A. Nyiri, and K. Tamosiunas, “Freeze out and the Boltzmann transport equation,” 2004. [33](#)
- [222] E. Molnar, L. P. Csernai, V. K. Magas, A. Nyiri, and K. Tamosiunas, “Covariant description of kinetic freeze out through a finite space-like layer,” *Phys. Rev. C*, vol. 74, p. 024907, 2006. [33](#)
- [223] A. K. S. Tiwari and S. Hardt, “A particle–particle hybrid method for kinetic and continuum equations,” *Journal of Computational Physics*, vol. 228, no. 18, pp. 7109 – 7124, 2009. [33](#)
- [224] T. Tuckmantel, A. Pukhov, J. Liljo, and M. Hochbruck, “Three-dimensional relativistic particle-in-cell hybrid code based on an exponential integrator,” *IEEE Transactions on Plasma Science*, vol. 38, no. 9, pp. 2383–2389, 2010. [33](#)
- [225] A. A. F.H. Harlow and J. Nix, “Three-dimensional relativistic particle-in-cell hybrid code based on an exponential integrator,” *J. Comp. Phys.*, vol. 20, p. 119,

1976. [34](#)

- [226] P. Huovinen, M. Belkacem, P. J. Ellis, and J. I. Kapusta, “Dileptons and photons from coarse grained microscopic dynamics and hydrodynamics compared to experimental data,” *Phys. Rev. C*, vol. 66, p. 014903, 2002. [35](#), [73](#)
- [227] S. Endres, H. van Hees, J. Weil, and M. Bleicher, “Coarse-graining approach for dilepton production at energies available at the CERN Super Proton Synchrotron,” *Phys. Rev. C*, vol. 91, no. 5, p. 054911, 2015. [35](#)
- [228] L. D. Landau and E. M. Lifshitz, *Field theory*. Pergamon Press, 1959. [37](#)
- [229] Sutherland, “Energy-momentum tensor for a field and particle in interaction,” *arXiv:1509.00001*, 2015. [37](#)
- [230] P. Huovinen and H. Petersen, “Particlization in hybrid models,” *Eur. Phys. J. A*, vol. 48, p. 171, 2012. [41](#), [53](#), [70](#), [79](#), [125](#), [128](#)
- [231] V. V. Skokov and V. D. Toneev, “Semi-central In-In collisions and Brown-Rho scaling,” *Phys. Rev. C*, vol. 73, p. 021902, 2006. [43](#), [44](#), [45](#)
- [232] R. Andrade, F. Grassi, Y. Hama, T. Kodama, O. Socolowski, Jr., and B. Tavares, “Nexsphere results on elliptic flow at RHIC and connection with thermalization,” *Eur. Phys. J. A*, vol. 29, pp. 23–26, 2006. [43](#), [44](#), [45](#), [46](#)
- [233] R. S. Bhalerao, A. Jaiswal, and S. Pal, “Collective flow in event-by-event partonic transport plus hydrodynamics hybrid approach,” *Phys. Rev. C*, vol. 92, no. 1, p. 014903, 2015. [43](#), [44](#), [45](#), [46](#)
- [234] U. W. Heinz, “Thermalization at RHIC,” *AIP Conf. Proc.*, vol. 739, pp. 163–180, 2005, [163(2004)]. [43](#)
- [235] M. Strickland, “Thermalization and isotropization in heavy-ion collisions,” *Pramana*, vol. 84, no. 5, pp. 671–684, 2015. [43](#)
- [236] M. P. Heller, R. A. Janik, and P. Witaszczyk, “The characteristics of thermalization of boost-invariant plasma from holography,” *Phys. Rev. Lett.*, vol. 108, p. 201602, 2012. [43](#)
- [237] W. van der Schee, P. Romatschke, and S. Pratt, “Fully Dynamical Simulation of Central Nuclear Collisions,” *Phys. Rev. Lett.*, vol. 111, no. 22, p. 222302, 2013. [43](#)
- [238] T. Lappi, “Small x physics and RHIC data,” *Int. J. Mod. Phys. E*, vol. 20, no. 1, pp. 1–43, 2011. [43](#)
- [239] P. B. Arnold, J. Lenaghan, G. D. Moore, and L. G. Yaffe, “Apparent thermalization due to plasma instabilities in quark-gluon plasma,” *Phys. Rev. Lett.*, vol. 94, p. 072302, 2005. [43](#)
- [240] L. V. Bravina *et al.*, “Microscopic models and effective equation of state in nuclear collisions at FAIR energies,” *Phys. Rev. C*, vol. 78, p. 014907, 2008. [43](#), [50](#), [63](#), [64](#)

- [241] J. Liu, C. Shen, and U. Heinz, “Pre-equilibrium evolution effects on heavy-ion collision observables,” *Phys. Rev. C*, vol. 91, no. 6, p. 064906, 2015, [Erratum: *Phys. Rev.C*92,no.4,049904(2015)]. 44
- [242] H. J. Drescher, S. Ostapchenko, T. Pierog, and K. Werner, “Initial condition for QGP evolution from NEXUS,” *Phys. Rev. C*, vol. 65, p. 054902, 2002. 45
- [243] Y. Hama, T. Kodama, and O. Socolowski, Jr., “Topics on hydrodynamic model of nucleus-nucleus collisions,” *Braz. J. Phys.*, vol. 35, pp. 24–51, 2005. 45
- [244] V. V. Skokov and V. D. Toneev, “Dilepton production from hydrodynamically expanding fireball,” *Acta Phys. Slov.*, vol. 56, pp. 503–510, 2006. 44
- [245] C. Shen, G. Denicol, C. Gale, S. Jeon, A. Monnai, and B. Schenke, “A hybrid approach to relativistic heavy-ion collisions at the RHIC BES energies,” in *26th International Conference on Ultrarelativistic Nucleus-Nucleus Collisions (Quark Matter 2017) Chicago, Illinois, USA, February 6-11, 2017*, 2017. 44
- [246] D. H. Rischke, “Fluid dynamics for relativistic nuclear collisions,” 1998, [Lect. Notes Phys.516,21(1999)]. 52
- [247] K. A. Bugaev, “Shock - like freezeout in relativistic hydrodynamics,” *Nucl. Phys. A*, vol. 606, pp. 559–567, 1996. 53, 123
- [248] C. Anderlik, Z. I. Lazar, V. K. Magas, L. P. Csernai, H. Stoecker, and W. Greiner, “Nonideal particle distributions from kinetic freezeout models,” *Phys. Rev. C*, vol. 59, pp. 388–394, 1999. 53, 123
- [249] C. Anderlik, L. P. Csernai, F. Grassi, W. Greiner, Y. Hama, T. Kodama, Z. I. Lazar, V. K. Magas, and H. Stoecker, “Freezeout in hydrodynamical models,” *Phys. Rev. C*, vol. 59, pp. 3309–3316, 1999. 53
- [250] S. Pratt, “Accounting for backflow in hydrodynamic-Boltzmann interfaces,” *Phys. Rev. C*, vol. 89, no. 2, p. 024910, 2014. 53
- [251] K. A. Bugaev and M. I. Gorenstein, “Particle freezeout in selfconsistent relativistic hydrodynamics,” 1999. 53, 123
- [252] K. A. Bugaev, “Boundary conditions of the hydro cascade model and relativistic kinetic equations for finite domains,” *Phys. Rev. C*, vol. 70, p. 034903, 2004. 53
- [253] M. Bleicher *et al.*, “Relativistic hadron hadron collisions in the ultrarelativistic quantum molecular dynamics model,” *J. Phys. G*, vol. 25, pp. 1859–1896, 1999. 54, 69
- [254] H. Petersen, C. Coleman-Smith, S. A. Bass, and R. Wolpert, “Constraining the initial state granularity with bulk observables in Au+Au collisions at $\sqrt{s_{NN}} = 200$ GeV,” *J. Phys. G*, vol. 38, p. 045102, 2011. 67
- [255] H. Sorge, “Temperatures and nonideal expansion in ultrarelativistic nucleus-

- nucleus collisions," *Phys. Lett. B*, vol. 373, pp. 16–22, 1996. [77](#)
- [256] S. Pratt and J. Murray, "Modeling the breakup stage of relativistic heavy ion collisions," *Phys. Rev. C*, vol. 57, pp. 1907–1919, 1998. [77](#)
- [257] S. Cheng, S. Pratt, P. Csizmadia, Y. Nara, D. Molnar, M. Gyulassy, S. E. Vance, and B. Zhang, "The Effect of finite range interactions in classical transport theory," *Phys. Rev. C*, vol. 65, p. 024901, 2002. [83](#)
- [258] W. Cassing and E. L. Bratkovskaya, "Parton-Hadron-String Dynamics: an off-shell transport approach for relativistic energies," *Nucl. Phys. A*, vol. 831, pp. 215–242, 2009. [85](#)
- [259] W. Cassing and S. Juchem, "Semiclassical transport of hadrons with dynamical spectral functions in A + A collisions at SIS / AGS energies," *Nucl. Phys.*, vol. A672, pp. 417–445, 2000. [85](#)
- [260] D. M. Manley and E. M. Saleski, "Multichannel resonance parametrization of pi N scattering amplitudes," *Phys. Rev. D*, vol. 45, pp. 4002–4033, 1992. [86](#)
- [261] J. M. Blatt and V. F. Weisskopf, *Theoretical Nuclear Physics*. Wiley, 1958. [86](#)
- [262] M. Post, S. Leupold, and U. Mosel, "Hadronic spectral functions in nuclear matter," *Nucl. Phys. A*, vol. 741, pp. 81–148, 2004. [87](#)
- [263] B. Andersson, G. Gustafson, G. Ingelman, and T. Sjostrand, "Parton Fragmentation and String Dynamics," *Phys. Rept.*, vol. 97, pp. 31–145, 1983. [89](#)
- [264] T. Sjostrand, S. Mrenna, and P. Z. Skands, "A Brief Introduction to PYTHIA 8.1," *Comput. Phys. Commun.*, vol. 178, pp. 852–867, 2008. [89](#)
- [265] M. Alvioli, H. J. Drescher, and M. Strikman, "A Monte Carlo generator of nucleon configurations in complex nuclei including Nucleon-Nucleon correlations," *Phys. Lett. B*, vol. 680, pp. 225–230, 2009. [90](#)
- [266] C. M. Tarbert *et al.*, "Neutron skin of ^{208}Pb from Coherent Pion Photoproduction," *Phys. Rev. Lett.*, vol. 112, no. 24, p. 242502, 2014. [90](#)
- [267] T. Gaitanos, A. B. Larionov, H. Lenske, and U. Mosel, "Breathing mode in an improved transport approach," *Phys. Rev. C*, vol. 81, p. 054316, 2010. [90](#), [112](#)
- [268] M. Jaminon, C. Mahaux, and H. NgÅt, "Effect of correlations on the momentum distribution of protons in ^{208}Pb ," *Nucl. Phys. A*, vol. 452, pp. 445–461, 1986. [92](#)
- [269] M. K. Gaidarov, A. N. Antonov, G. S. Anagnostatos, S. E. Massen, M. V. Stoitsov, and P. E. Hodgson, "Proton momentum distribution in nuclei beyond He-4," *Phys. Rev. C*, vol. 52, pp. 3026–3031, 1995. [92](#)
- [270] T. Kodama, S. B. Duarte, K. C. Chung, R. Donangelo, and R. A. M. S. Nazareth, "Causality and relativistic effects in intranuclear cascade calculations," *Phys. Rev. C*, vol. 29, pp. 2146–2152, 1984. [95](#)

- [271] P. Danielewicz and G. F. Bertsch, "Production of deuterons and pions in a transport model of energetic heavy ion reactions," *Nucl. Phys. A*, vol. 533, pp. 712–748, 1991. [96](#)
- [272] W. Cassing, "Anti-baryon production in hot and dense nuclear matter," *Nucl. Phys. A*, vol. 700, pp. 618–646, 2002. [96](#), [123](#)
- [273] J. Weil, "Vector Mesons in Medium in a Transport Approach," Ph.D. dissertation, Giessen U., 2013. [Online]. Available: <http://geb.uni-giessen.de/geb/volltexte/2013/10253/> [96](#)
- [274] V. Dmitriev, O. Sushkov, and C. Gaarde, " Δ Formation in the ^1H (^3He , ^3H) Δ^{++} Reaction at Intermediate-energies," *Nucl. Phys. A*, vol. 459, pp. 503–524, 1986. [97](#)
- [275] G. Graef, J. Steinheimer, F. Li, and M. Bleicher, "Deep sub-threshold Ξ and Λ production in nuclear collisions with the UrQMD transport model," *Phys. Rev. C*, vol. 90, p. 064909, 2014. [97](#)
- [276] M. Effenberger. (1999) Eigenschaften von hadronen in kernmaterie in einem vereinheitlichten transportmodell, ph.d. thesis, justus-liebig-universitaet giessen. [Online]. Available: http://www.uni-giessen.de/fbz/fb07/fachgebiete/physik/einrichtungen/theorie/inst/theses/dissertation/previous/effenberger_diss [97](#)
- [277] S. D. Protopopescu, M. Alston-Garnjost, A. Barbaro-Galtieri, S. M. Flatte, J. H. Friedman, T. A. Lasinski, G. R. Lynch, M. S. Rabin, and F. T. Solmitz, " $\pi\pi$ Partial Wave Analysis from Reactions $\pi^+p \rightarrow \pi^+\pi^-\Delta^{++}$ and $\pi^+p \rightarrow K^+K^-\Delta^{++}$ at 7.1 GeV/c," *Phys. Rev. D*, vol. 7, p. 1279, 1973. [98](#)
- [278] E. A. Alekseeva, A. A. Kartamyshev, V. K. Makarin, K. N. Mukhin, O. O. Patarakin, M. M. Sulkovskaya, A. F. Sustavov, L. V. Surkova, and L. A. Chernysheva, "Use of $\pi p \rightarrow \pi\pi N$ reactions to study $\pi\pi$ scattering in the elastic interaction region," *Sov. Phys. JETP*, vol. 55, pp. 591–600, 1982, [*Zh. Eksp. Teor. Fiz.*82,1007(1982)]. [98](#)
- [279] J. Cugnon, J. Vandermeulen, and D. L'Hote, "Simple parametrization of cross-sections for nuclear transport studies up to the GeV range," *Nucl. Instrum. Meth. B*, vol. 111, pp. 215–220, 1996. [97](#)
- [280] G. Agakishiev *et al.*, "Baryon resonance production and dielectron decays in proton-proton collisions at 3.5 GeV," *Eur. Phys. J. A*, vol. 50, p. 82, 2014. [99](#)
- [281] T. C. Bacon, F. M. Bomse, T. B. Cochran, W. J. Fickinger, E. R. Goza, H. W. K. Hopkins, and E. O. Salant, "Comparison of Isobar Production in pp and pn Interactions at 2.8 GeV/c," *Phys. Rev.*, vol. 162, pp. 1320–1322, 1967. [99](#)
- [282] B. A. Ryan, A. Kanofsky, T. J. Devlin, R. E. Mischke, and P. F. Shepard, *Proton - proton differential cross section from 600 MeV/c to 1800 MeV/c*, 1969. [99](#)
- [283] E. M. Lifshitz and L. P. Pitaevskiy, *Physical kinetics*. Pergamon Press, 1981. [100](#)

- [284] V. B. Berestetskii, E. M. Lifshitz, and L. P. Pitaevskiy, *Quantum Electrodynamics*. Pergamon Press, 1982. [101](#)
- [285] R. G. Sachs, *The Physics of Time Reversal*. The University of Chicago Press, 1987. [102](#), [103](#)
- [286] L. D. Landau and E. M. Lifshitz, *The Classical Theory of Fields*. Pergamon Press, 1971. [103](#)
- [287] G. Wolf, W. Cassing, and U. Mosel, "Eta and dilepton production in heavy-ion reactions," *Nucl. Phys. A*, vol. 545, pp. 139–150, 1992. [104](#)
- [288] Z. Xu, K. Zhou, P. Zhuang, and C. Greiner, "Thermalization of gluons with Bose-Einstein condensation," *Phys. Rev. Lett.*, vol. 114, no. 18, p. 182301, 2015. [113](#)
- [289] P. Huovinen and P. Petreczky, "QCD Equation of State and Hadron Resonance Gas," *Nucl. Phys. A*, vol. 837, pp. 26–53, 2010. [120](#), [121](#)
- [290] Y. Pan and S. Pratt, "Baryon annihilation and regeneration in heavy ion collisions," *Phys. Rev. C*, vol. 89, no. 4, p. 044911, 2014. [123](#)
- [291] C. E. Aguiar, T. Kodama, T. Osada, and Y. Hama, "Smoothed particle hydrodynamics for relativistic heavy ion collisions," *J. Phys. G*, vol. 27, pp. 75–94, 2001. [123](#)
- [292] K. Werner and J. Aichelin, "Microcanonical treatment of hadronizing the quark-gluon plasma," *Phys. Rev. C*, vol. 52, pp. 1584–1603, 1995. [125](#)
- [293] F. Becattini and L. Ferroni, "Statistical hadronization and hadronic microcanonical ensemble. 2." *Eur. Phys. J. C*, vol. 38, pp. 225–246, 2004, [Erratum: *Eur. Phys. J.* 66,341(2010)]. [125](#), [130](#), [147](#)
- [294] D. H. Rischke, S. Bernard, and J. A. Maruhn, "Relativistic hydrodynamics for heavy ion collisions. 1. General aspects and expansion into vacuum," *Nucl. Phys. A*, vol. 595, pp. 346–382, 1995. [135](#)
- [295] L. Yuan and J. D. Kalbfleisch, "On the Bessel Distribution and Related Problems," *Annals of the Institute of Statistical Mathematics*, vol. 52, no. 3, pp. 438–447, 2000. [146](#)
- [296] L. Devroye, "Simulating Bessel random variables," *Statistics and Probability Letters*, vol. 57, no. 3, pp. 249–257, 2002. [147](#)

Lebenslauf

Name: Dmytro Oliinychenko
Adresse: Augustenburgstr. 6, 60488 Frankfurt am Main
Geburtsdatum: 8. November 1990
Geburtsort: Dnepropetrovsk, Ukraine
Nationalität: ukrainisch
Familienstand: ledig

Ausbildung

9/1997 - 7/2004 Rivne State Classical Gymnasium
9/2004 - 7/2007 Lyceum at Kiev National University
9/2007 - 7/2013 Moscow Institute for Physics and Technology

- B. S. in Physik, Summa Cum Laude
Undergraduate Thesis: "Description of particle multiplicities in heavy ion collisions data using thermal model with hard-core potential including Lorentz contraction"
- M. S. in Physik, Summa Cum Laude
Graduate Thesis: "Investigation of Multiplicities in Heavy Ion Collisions"

seit 10/2013 Doktorand in Physik an der J.W.-Goethe Universität Frankfurt

Stipendien und Auszeichnungen

2006 Zweiter Preis in der Ukrainischen Physik Olympiade (Nationalniveau)
2007 Stipendium des Präsidenten der Ukraine für Gewinner der Schullolympiaden
2010, 2012, 2013 Gewinner/"Best reporter" des Internationalen Physiker-Turniers
2008 - 2013 Stipendium des Dekanats für ausgezeichnete Prüfungsleistung
2012 - 2013 Stipendium vom D. Zimin "Dynasty"-Stiftung für junge Forscher
2013 M. M. Bogoliubov Stipendium für junge Forscher vom JINR, Dubna
2015 Giersch Excellence Award
2015 - 2016 Stipendium der Deutsche Telekom Stiftung

Veröffentlichungen

In referierten Zeitschriften

1. A. I. Ivanytskyi *et al.*, *Physical properties of Polyakov loop geometrical clusters in SU(2) gluodynamics*, Nucl. Phys. A **960**, 90-113 (2017).
2. D. Oliinychenko and H. Petersen, *Forced canonical thermalization in a hadronic transport approach at high density*, J. Phys. G **44**, no. 3, 034001 (2017).
3. K. A. Bugaev *et al.*, *Separate chemical freeze-outs of strange and non-strange hadrons and problem of residual chemical non-equilibrium of strangeness in relativistic heavy ion collisions*, Ukr. J. Phys. **61**, 659 (2016).
4. J. Weil *et al.*, *Particle production and equilibrium properties within a new hadron transport approach for heavy-ion collisions*, Phys. Rev. C **94**, no. 5, 054905 (2016).
5. K. A. Bugaev, V. V. Sagun, A. I. Ivanytskyi, D. R. Oliinychenko, E. M. Ilgenfritz, E. G. Nikonov, A. V. Taranenko and G. M. Zinovjev, *New Signals of Quark-Gluon-Hadron Mixed Phase Formation*, Eur. Phys. J. A **52**, no. 8, 227 (2016).
6. H. Petersen, D. Oliinychenko, J. Steinheimer and M. Bleicher, *Influence of kinematic cuts on the net charge distribution*, Quark Matter 2016 proceedings, Nucl. Phys. A **956**, 336 (2016).
7. D. Oliinychenko and H. Petersen, *Deviations of the Energy-Momentum Tensor from Equilibrium in the Initial State for Hydrodynamics from Transport Approaches*, Phys. Rev. C **93**, no. 3, 034905 (2016).
8. K. A. Bugaev, A. I. Ivanytskyi, D. R. Oliinychenko, V. V. Sagun, I. N. Mishustin, D. H. Rischke, L. M. Satarov and G. M. Zinovjev, *Thermodynamically Anomalous Regions and Possible New Signals of Mixed Phase Formation*, Eur. Phys. J. A **52**, no. 6, 175 (2016).
9. D. Oliinychenko, P. Huovinen, H. Petersen, *Systematic Investigation of Negative Cooper-Frye Contributions in Heavy Ion Collisions Using Coarse-grained Molecular Dynamics*, Phys. Rev. C **91** (2015) 2, 024906.
10. K. A. Bugaev, A. I. Ivanytskyi, D. R. Oliinychenko *et al.*, *Thermodynamically Anomalous Regions as a Mixed Phase Signal*, Phys. Part. Nucl. Lett. **12** (2015) 2, 238-245.
11. K. A. Bugaev, A. I. Ivanytskyi, D. R. Oliinychenko *et al.*, *Non-smooth Chemical Freeze-out and Apparent Width of Wide Resonances and Quark Gluon Bags in a Thermal Environment*, Ukr. J. Phys. **60** (2015) 3, 181-200.
12. V. V. Sagun, D. R. Oliinychenko, K. A. Bugaev *et al.*, *Strangeness enhancement at the hadronic chemical freeze-out*, Ukr. J. Phys. **59** (2014) 1043-1050.

13. D. R. Oliinychenko, V. V. Sagun, A. I. Ivanytskyi, K. A. Bugaev, *Separate chemical freeze-out of strange particles with conservation laws*, Ukr. J. Phys. **59** (2014) 1051-1059.
14. K. A. Bugaev, D. R. Oliinychenko, et al., *Chemical freeze-out of strange particles and possible root of strangeness suppression*, Europhys. Lett., **104** (2013) 22002.
15. K. A. Bugaev, D. R. Oliinychenko, A. S. Sorin, *A Scientific Analysis of the Preprint arXiv:1301.1828v1 [nucl-th]*, Ukr. J. Phys. **58** (2013) 10, 939-943.
16. K. A. Bugaev, A. I. Ivanytskyi, V. V. Sagun and D. R. Oliinychenko, *Is bimodality a sufficient condition for a first order phase transition existence?*, Phys. Part. Nucl. Lett. **10** (2013), 6, pp. 832-851.
17. K. A. Bugaev, D. R. Oliinychenko, A. S. Sorin, G. M. Zinovjev, *Simple Solution to the Strangeness Horn Description Puzzle*, Eur. Phys. J. A **49** (2013), 30–1-8.
18. D.R. Oliinychenko, K.A. Bugaev, A.S. Sorin, *Investigation of hadron multiplicities and hadron yield ratios in heavy ion collisions*, Ukr. J. Phys. **58** (2013), No. 3, 211-227.

Konferenz Proceedings

1. D. Oliinychenko and H. Petersen, *Effective dynamical coupling of hydrodynamics and transport for heavy-ion collisions*, J. Phys. Conf. Ser. **832**, no. 1, 012052 (2017).
2. A. Ivanytskyi et al., *Geometrical clusterization of Polyakov loops in SU(2) lattice gluodynamics*, J. Phys. Conf. Ser. **798**, no. 1, 012065 (2017)
3. V. V. Sagun, K. A. Bugaiev, A. I. Ivanytskyi, D. R. Oliinychenko and I. N. Mishustin, *Effects of Induced Surface Tension in Nuclear and Hadron Matter*, EPJ Web Conf. **137**, 09007 (2017)
4. D. Oliinychenko, H. Petersen, *Effective dynamical coupling of hydrodynamics and transport for heavy-ion collisions*, Hot Quarks 2016, to be published in Journal of Physics: Conference Series (JPCS).
5. V. V. Sagun, K. A. Bugaiev, A. I. Ivanytskyi, D. R. Oliinychenko and I. N. Mishustin, *Effects of Induced Surface Tension in Nuclear and Hadron Matter*, XII Quark Confinement and Hadron Spectrum Conference (CONF12), arXiv:1611.07071 [nucl-th].
6. V. V. Sagun, K. A. Bugaev, A. I. Ivanytskyi and D. R. Oliinychenko, *New irregularities at chemical freeze-out of hadrons*, 2015 International Young Scientists Forum on Applied Physics (YSF), doi:10.1109/YSF.2015.7333191
7. K. A. Bugaev, A. I. Ivanytskyi, V. V. Sagun, G. M. Zinovjev, D. R. Oliinychenko, V. S. Trubnikov and E. G. Nikonov, *A possible evidence of observation of two mixed phases in nuclear collisions*, EPJ Web Conf. **126**, 03003 (2016).

8. D. Oliinychenko, P. Huovinen, H. Petersen, *Cooper-Frye Negative Contributions in a Coarse-Grained Transport Approach*, FAIRNESS 2014, J. Phys. Conf. Ser. **599**, no. 1, 012017 (2015).
9. V. V. Sagun, A. I. Ivanytskyi, D. R. Oliinychenko and K. A. Bugaev, *Bimodality as a signal of the nuclear liquid-gas phase transition*, arXiv:1401.2881 [nucl-th].
10. V. V. Sagun, A. I. Ivanytskyi, K. A. Bugaev and D. R. Oliinychenko, *Bimodality Phenomenon in Finite and Infinite Systems Within an Exactly Solvable Statistical Model* Helmholtz International Summer School "Physics of Heavy Quarks and Hadrons", Dubna, Russia, July 15-28, 2013; arXiv:1311.7042 [nucl-th].
11. V. V. Sagun, A. I. Ivanytskyi, D. R. Oliinychenko and K. A. Bugaev, *Can bimodality exist without phase transition?*, XI International Scientific Conference of Students and Young Scientists "Shevchenkivska Vesna 2013", Kyiv, March 18-22, 2013; arXiv:1304.5997 [nucl-th].
12. K. A. Bugaev, D. R. Oliinychenko, A. S. Sorin, E.G. Nikonov, G. M. Zinovjev, *Adiabatic chemical freeze-out and wide resonance modification in a thermal medium*, PoS Baldin ISHEPP XXI (2012) **017**, 1-14; arXiv:1212.0132 [hep-ph].

Lehre

WS 2016

Tutorium, Theoretische Physik I

WS 2017

Tutorium, Theoretische Physik V (Statistische Physik)